Photocatalytic removal of toxic metal ions from water using functionalized gC_3N_4

Timothy Oladiran Ajiboye

orcid.org/0000-0001-5418-3234

Thesis submitted in fulfilment of the requirements for the degree *Doctor of Philosophy in Chemistry* at the North-West University

Promoter: Prof. D.C. Onwudiwe

Co-Supervisor: Dr. O. A. Oyewo

Graduation ceremony: November 24, 2022

Student number: 32480342

CERTIFICATION

This is to certify that the thesis titled "**Photocatalytic removal of toxic metal ions from water using functionalized gC_3N_4"** is an authentic research work carried out by TIMOTHY OLADIRAN AJIBOYE under the supervision of Prof. Damian Chinedu Onwudiwe at the Chemistry department of the North-West University, Faculty of Natural and Agricultural Sciences, South Africa.

Date: 21-10-2022

T.O. Ajiboye

Date: 21-10-2022

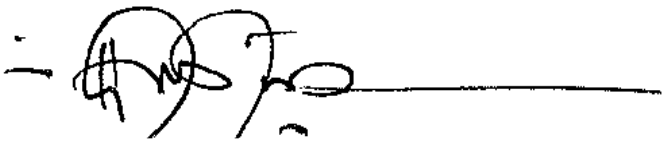

Prof. D.C. Onwudiwe

DECLARATION

I declare that this doctoral thesis titled: "**Photocatalytic removal of toxic metal ions from water using functionalized gC_3N_4"** is solely owned by me, and has not been submitted to any other institution for the purpose of obtaining a degree or qualification, and all sources cited are acknowledged by comprehensive referencing where any information has been derived from other sources.

21-10-2022

Signature: ……

Timothy Oladiran Ajiboye

DEDICATION

This thesis is dedicated to the Almighty God for the mercy that I am receiving daily. Also to my immediate family, Titilope Tinu Ajiboye and Toluwanimi Hephzibah Ajiboye, for the co-operation and patience during the time of the research.

ACKNOWLEDGEMENT

My first appreciation goes to the Almighty God for showing me mercy and giving me the grace and wisdom to complete this stage successfully. I will be an ingrate if I fail to appreciate the guidance of my supervisor (Prof. Damian C. Onwudiwe) throughout the course of the research work. I also appreciate the wonderful contributions of my co-supervisor (Dr. Opeyemi A. Oyewo). The contributions of Prof. Alex Kuvarega in editing some of the publications is appreciated. My gratitude also goes to all laboratory and academic staff of the Chemistry Department, North-West university, Mafikeng Campus, South Africa for their assistance throughout the period of research. I have been encouraged by working with the intellectuals in the FNAS and the Inorganic and Materials chemistry research group of the North-West Universit, South Africa.

The support of my wife (Titilope Tinu) and my child (Toluwanimi) is highly appreciated. Without their support, this achievement might not have been possible. The prayer supports of my families (Ajiboyes and Olatunjis) and siblings have been the fuel propelling me to break the barriers. I also appreciate the Akinsolas for taking good care of my boy during the period of research.

I cannot forget the efforts of friends like Akinola Tosin, Timothy Wasiu, Jerry Adeyemi, Taiwo Yetunde, Fadipes (Micheal and Fisayo), Akinmade Tosin, Olatunde Olalekan and my Supervisor's wife (Precious Onwudiwe) for their efforts towards ensuring that I secured admission and settled down on time for my studies. Also, the advice of late Prof. Jire Adegoke, Prof. Tunde Lawal, Prof. Olubukola Babalola, Rev. Segun Akande, Rev. Dr. Job Adeyemo and Dr. Hazel Mufthandu has helped me to continue against the storm of weariness. The trust that Prof. David Aworinde, Bro and Sis. Abikoye and Mr. Jide Alade Areo had in me that made them to release their account statements for my permit processing cannot be forgotten.

I will also not forget to mention the contributions of my friends at El-Shaddai Baptist Church, Agbowo, Ibadan, Nigeria; RCCG God's Heritage Arena parish, Moshawane, South Africa;2002 Alumni of the School of Science, Ogbomoso; 2010 "Cations and anions" LAUTECH Alumni and 2014 Chemistry Postgraduate Alumni of the University of Ibadan, Nigeria. My last appreciation still goes to the Almighty God who is the Alpha and Omega.

LIST OF PUBLICATIONS

1. **Timothy O. Ajiboye**, Stephen O. Babalola and Damian C. Onwudiwe -Photocatalytic Inactivation as a Method of Elimination of E. coli from Drinking Water- Appl. Sci.**2021**, 11, 1313. https://doi.org/10.3390/app11031313

2. **Timothy O. Ajiboye**, Opeyemi A. Oyewo and Damian C. Onwudiwe -The performance of bismuth-based compounds in photocatalytic applications- Surfaces and Interfaces, Volume 23, April **2021**, 100927- https://doi-org/10.1016/j.surfin.2021.100927

3. **Timothy O. Ajiboye**, Opeyemi A. Oyewo and Damian C. Onwudiwe-Simultaneous removal of organics and heavy metals from industrial wastewater: A review- Chemosphere, Volume 262, January **2021**, 128379- https://doi-org./10.1016/j.chemosphere.2020.128379

4. **Timothy O. Ajiboye**, Alex T.Kuvarega and Damian C. Onwudiwe- Graphitic carbon nitride-based catalysts and their applications: A review- Nano-Structures & Nano-Objects, Volume 24, October **2020**, 100577- https://doi-org/10.1016/j.nanoso.2020.100577

5. **Ajiboye, T.O.**, Oyewo, O.A. & Onwudiwe, D.C. Conventional and Current Methods of Toxic Metals Removal from Water Using g-C_3N_4-Based Materials. J Inorg Organomet Polym **31**, 1419–1442 **(2020)**. https://doi-org/10.1007/s10904-020-01803-3
6. **Timothy O. Ajiboye**, Alex T.Kuvarega and Damian C. Onwudiwe -Recent Strategies for Environmental Remediation of Organochlorine Pesticides- Appl. Sci. **2020**, 10, 6286; https://doi:10.3390/app10186286

7. Jerry O. Adeyemi, **Timothy O. Ajiboye** and Damian C. Onwudiwe -Mineralization of antibiotics in waste water via photocatalysis- Water, Air, & Soil Pollution.**2021,** 232 (5), 1-28; https://doi.org/10.1007/s11270-021-05167-3

8. **Timothy O. Ajiboye** and Damian C. Onwudiwe -Bismuth sulfide based compounds: Properties, synthesis and applications- Results in Chemistry,Volume 3, January **2021**, 100151; https://doi.org/10.1016/j.rechem.2021.100151

9. **Timothy O. Ajiboye**, Opeyemi A. Oyewo and Damian C. Onwudiwe- Photocatalytic removal of parabens and halogenated products in wastewater: a review- Environmental Chemistry Letters (**2021**). https://doi.org/10.1007/s10311-021-01263-2

10. **Timothy O. Ajiboye**, Opeyemi A. Oyewo and Damian C. Onwudiwe- Adsorption and photocatalytic removal of Rhodamine B from wastewater using carbon-based materials- FlatChem, Volume 29, September **2021**, 10027. https://doi.org/10.1016/j.flatc.2021.100277

11. **Timothy O. Ajiboye**, Bukola O.Oluwarinde, Peter K.Montso, Collins N.Ateba, Damian C. Onwudiwe-Antimicrobial activities of Cu(II), In(III), and Sb(III) complexes of N-methyl-N–phenyl dithiocarbamate complexes- Results in Chemistry-Volume 3, January **2021**, 100241. https://doi.org/10.1016/j.rechem.2021.100241

12. **T.O. Ajiboye**, T.T. Ajiboye, R. Marzouki, D.C. Onwudiwe, The Versatility in the Applications of Dithiocarbamates, International Journal of Molecular Sciences, 23 (**2022**) 1317. https://doi.org/10.3390/ijms23031317

13. Emmanuel E.Imade, **Timothy O.Ajiboye**, Ayomide E.Fadiji, Damian C.Onwudiwe, Olubukola O.Babalola-Green synthesis of zinc oxide nanoparticles using plantain peel extracts and the evaluation of their antibacterial activity- Scientific African, Volume 16, July **2022**, e01152 - https://doi.org/10.1016/j.sciaf.2022.e01152

14. **Timothy O. Ajiboye**, Emmanuel E. Imade, Opeyemi A. Oyewo, and Damian C. Onwudiwe-Silver functionalized g-C_3N_4: photocatalytic potency for chromium(VI) reduction, and evaluation of the antioxidant and antimicrobial properties. Journal of Photochemistry & Photobiology, A: Chemistry- Volume 432, 1 November **2022**, 114107- https://doi.org/10.1016/j.jphotochem.2022.114107

15. **Timothy O. Ajiboye**, Olutobi D. Ogunbiyi, Elizabeth O. Omotola, Wale J. Adeyemi, Olayinka O. Agboola and Damian C. Onwudiwe, Urine: Useless or useful waste? Results in Engineering.**2022**- https://doi.org/10.1016/j.rineng.2022.100522

16. **Timothy O. Ajiboye**, Opeyemi A. Oyewo, Youssef Ben Smida, and Damian C. Onwudiwe (**2022)**-Visible light-driven photocatalytic reduction of monovalent silver using a composite of $Ni_3Bi_2S_2$ incorporated into O-doped gC_3N_4. Results in Engineering 15, 100540. https://doi.org/10.1016/j.rineng.2022.100540.

17. **Ajiboye, Timothy O.,** Opeyemi A. Oyewo, Riadh Marzouki, and Damian C. Onwudiwe-Photocatalytic reduction of hexavalent chromium using $Cu_{3.21}Bi_{4.79}S_9$/g-C_3N_4 composite. Catalysts **2022**, 12(10), 1075; https://doi.org/10.3390/catal12101075.

18. **Timothy O. Ajiboye**, Opeyemi A. Oyewo, Riadh Marzouki, Ameni Brahmi, Damian C. Onwudiwe **(2022)** -Synthesis of $AgBiS_2/gC_3N_4$ and its application in the photocatalytic reduction of Pb(II) in the matrix of methyl orange, crystal violet and methylene blue dyes. *Ceramics International.* https://doi.org/10.1016/j.ceramint.2022.10.187.

19. Synthesis and characterization of Ag_2S using silver (I) complex of *N*-methyl-*N*-phenyl-dithiocarbamate as single-source precursor. Accepted for publication by *Journal of Nano Research*-Scientific.Net (In-print).

Conference papers/Symposiums/Presentations

1. **Timothy O. Ajiboye** and Damian C. Onwudiwe**,** Simultaneous removal of toxic metal ions and organic pollutants from water using functionalized g-C_3N_4 Photocatalysts, 2nd Commonwealth Chemistry -Building Networks to Address the Goals-30 September-1 October **2021**, (*Oral presentation*).

2. **Timothy O. Ajiboye** and Damian C. Onwudiwe, Removal of heavy metals from water using functionalized g-C_3N_4-Green Chemistry Postgraduate Summer School held on 4-9 July, **2021**. Venice, Italy, (*Oral Presentation*)

ABSTRACT

Heavy metal ions in the environment are increasing geometrically, because the existing conventional wastewater treatment techniques are grossly deficient in the treatment of these toxic pollutants. Photocatalysis is the preferred method to eradicate the toxic effects of these heavy metal ions in water by converting the heavy metals in the toxic oxidation states to less-toxic and more useful oxidation states. Also, it is cost effective, environmentally friendly and perform maximally without generating secondary waste. However, a photocatalytic process requires photocatalysts that are thermally stable, insoluble and that can absorb in the visible region of the electromagnetic spectrum. Therefore, the synthesis of novel photocatalysts for the removal of toxic metal ions from water has inspired different studies. Bismuth-based ternary metal sulphides of the form M-Bi-S (where M = Ni, Ag and Cu) are good semiconductors with good structural and optical properties. Despite their good properties, utilization of bismuth-based ternary metal sulphides as photocatalysts is still very limited due to the fact that they are difficult to synthesize in their pure stoichiometry phase. In this study, the synthesis of $AgBiS_2$ and $Ni_2Bi_2S_3$ were achieved through a one-pot synthetic route. The synthesis of the non-stoichiometric phase of the copper bismuth sulphide ($Cu_{3.21}Bi_{4.79}S_9$) was first carried out through heat-up method by using copper(II)- and bismuth(III)- complexes of *N*-methyl-*N*-phenyldithiocarbamate complexes and oleylamine as the capping agent. The suitability of the dithiocarbamate complex as single source precursors were examined by the preparation of the respective binary sulphides from the complexes. Silver(I) sulphide (Ag_2S) was prepared as a model binary sulphide from *N*-methyl-*N*-phenyl dithiocarbamate complex. The obtained ternary metal bismuth sulphides were incorporated into graphitic carbon nitride to form nanocomposites. Graphitic carbon nitride was not only utilized as a support material for these sulphides, but also as a semiconductor that is stable to heat with band gap energy of 2.70 eV. Apart from these bismuth-based ternary nanocomposites, metallic silver was also composited into graphitic carbon nitride *in-situ*. Metallic silver was used due to its higher surface plasmon resonance compared to other metals. The four functionalized graphitic carbon nitrides ($Cu_{3.21}Bi_{4.79}S_9/gC_3N_4$, $AgBiS_2/gC_3N_4$ $Ni_2Bi_2S_3/O\text{-}gC_3N_4$ and Ag/gC_3N_4) were investigated for the photocatalytic reduction of heavy metal ions in water. As such, the graphitic carbon nitride functionalized with silver and copper bismuth sulphides were investigated for the photocatalytic reduction of Cr(VI). The graphitic carbon nitride functionalized with nickel bismuth sulphide and silver bismuth sulphide were investigated for

the photocatalytic reduction of Ag(I) and Pb(II) respectively. The Ag(I), Pb(II) and Cr(VI) were chosen as a model for the monovalent, divalent and multivalent toxic metal ions.

About 92.77% reduction of Cr(VI) was achieved at pH 2 using 10 mg of the $Cu_{3.21}Bi_{4.79}S_9/gC_3N_4$ photocatalyst and 10 mg/L of the solution of Cr(VI) under the visible light irradiation. The pseudo-first order rate constant of photocatalysis was found to be 0.0393 min^{-1}, which was 1.37 and 5.17 folds higher than that of gC_3N_4 and $Cu_{3.21}Bi_{4.79}S_9$ respectively. The presence of bisphenol A and other heavy metal ions including Ag(I) and Pb(II) (as secondary pollutants) in the photocatalytic system reduced the rate of photocatalysis from 0.0393 min^{-1} to 0.0019 min^{-1} and 0.0039 min^{-1} respectively. The performance of photocatalytic reduction of Cr(VI) was 66.87% even after 2 h of visible light irradiation in the presence of Ag/gC_3N_4 photocatalyst. This implies that functionalization of graphitic carbon nitride with metallic silver is not as effective as functionalization with ternary copper bismuth sulphide. The use of 25 mg of $Ni_2Bi_2S_3/O\text{-}gC_3N_4$ reduced about 93.08% (pseudo-first order rate constant of 0.0460 min^{-1}) of Ag(I) within 1 h under the visible light. Mixed organic pollutants and persulfate were found to have inhibitory effects on the rate of photocatalytic reduction.

In a bid to better understand the influence of other additives on the rate of photocatalytic reduction of Pb(II) using functionalized graphitic carbon nitride, $AgBiS_2/gC_3N_4$ was used as photocatalyst for the reduction of Pb(II) in the presence different additives. The results revealed that the presence of easily-oxidizable organics has synergistic effects on the photocatalytic reduction of Pb(II), while persulfate displayed an inhibitive effect on Pb(II) reduction. The removal of Pb(II) in dye' s matrix was influenced by the type of dyes that were present in the water. The rate of Pb(II) reduction was reduced in the presence of methylene blue and methyl orange, but crystal violet displayed synergistic effects. Finally, the rate of degradation of dyes in the presence of Pb(II) was also investigated. The rate of photocatalytic reduction of Pb(II) decreased from 0.0045 min^{-1} to 0.0036 min^{-1} and 0.0016 min^{-1} in the matrix of methyl orange and methylene blue respectively. On the contrary, there was an increase in the rate of photocatalytic reduction of Pb(II) from 0.0045 to 0.0096 min^{-1} in the matrix of crystal violet. In general, the use of functionalized graphitic carbon nitride as the photocatalyst is a promising and sustainable alternative for the removal of toxic heavy metal ions from water.

TABLE OF CONTENT

PREFACE

This thesis was written following the article format. All experimental works and drafting of initial manuscript were done by Timothy O. Ajiboye, while the supervision of the research work and proof reading of manuscripts were carried out by Prof. D. C. Onwudiwe. The project was co-supervised by Dr. Opeyemi A. Oyewo. A total of nineteen (19) published articles and two (2) conference proceedings were combined in compiling the thesis.

All manuscripts have been included in this thesis with permission from the journal Editors and Co-authors.

LIST OF FIGURES

Chapter two

Chapter three

Chapter four

Chapter five

Chapter six

Chapter seven

LIST OF TABLES

CHAPTER ONE

Introduction and general background

1.0 Problem statement

The applications of heavy metals in several industrial, domestic, agricultural, medical and for technological purposes remain the major source of these toxic metals in water bodies and the environment. This has raised concerns on their potential effects on human health and the environment. Chromium and lead are ranked among the priority metals that are of great concern to public health because of their high degree of toxicity (Wilbur et al., 2012). They are also classified as human carcinogens (known or probable) according to the U.S. Environmental Protection Agency (USEPA) and the International Agency for Research on Cancer (IARC) (Chen and K. Ray, 2001). These elements exist in ionic forms in solution, and the following oxidation states: Cr(VI) and Pb(II) have been reported to be very toxic among the metal ions present in the environment (Chen and K. Ray, 2001; Litter, 2009). Hence, their removal from the environment is very important.

Several techniques, which include physical, chemical and biological routes have been developed for the removal of these pollutants and the alleviation of their negative impact on the environment. For example, coagulation/flocculation process is an age-long water treatment technique, which has proven to be cost-effective and an efficient operating unit in separation technology. However, generation of secondary waste that poses disposal problems through the voluminous sludge produced remains the major drawback.

Heterogeneous photocatalysis is preferred for the removal of toxic metals because it offers the advantage of destroying the pollutants, in contrast to conventional techniques such as adsorption and ion exchange that only transfer the contaminants from one phase to another. Several semiconductors such as TiO_2, ZnS and ZnO have been investigated as potential photocatalysts. However, they have some disadvantages: large band gap energy, require UV light to achieve electron excitation, are unstable in an aqueous phase, and undergo rapid recombination of photo-generated electron-hole pairs. Thus, photo-stable and effective photocatalysts under visible light are highly required (Jing et al., 2001; Chen et al., 2012). Graphitic carbon nitride (g-C_3N_4), a polymeric semiconductor, has recently attracted attention, due to its unique properties, which include excellent chemical stability, tunable electronic structure, and medium band gap (2.7 eV) (Yang et al., 2011). Therefore, this study focuses on

the remediation of toxic metal ions from water using heterojunction systems synthesized from graphitic-C_3N_4 incorporated with ternary nanoparticles as photocatalysts**.**

1.1 Motivation and rationale

The effectiveness of the photocatalytic process largely depends on the properties of the photocatalysts utilized among other factors. The need to synthesize photocatalysts that can absorb in the visible region of the solar system and arestable and easy to separate has inspired a lot of interest in the synthesis of ternary bismuth-based sulphides. The bismuth-based semiconductor has attracted interest resulting in several applications recently (Griffith et al., 2021). This is due the fact that bismuth has low reactivity to biological species, high melting point, high density, easy to functionalize, diamagnetic and able to resist magnetic field. Although ternary bismuth sulphide, Particularly, possesses low band gap energy and high absorption coefficient but the focus has been on binary bismuth sulphide (Fazal et al.,2022). This is because the synthesis of pure phase ternary bismuth sulphide is difficult to achieve. The utilization of these ternary bismuth materials as photocatalysts is therefore grossly inadequate. There is need to combine these materials with graphitic carbon nitride to produce a better nanocomposite photocatalyst. The combination is necessary because pure graphitic carbon nitride displays fast hole and electron recombination, small surface area, and insufficient light absorption. The utilization of these graphitic carbon nitride functionalized with ternary bismuth sulphide as photocatalyst in water treatment has not been significantly explored. Specifically, their usage as the photocatalysts for the photocatalytic reduction of heavy metal ions is lacking. The need to explore them as photocatalysts for the reduction of heavy metal ions to non-toxic species is therefore important.

1.2 Research aim and objectives

The aim of the proposed research is to remove toxic metal ions from water using novel synthesized graphitic carbon nitride incorporated with ternary nanomaterials composed of ear th abundant elements.

The objectives are to:

- synthesize novel precursor complexes of dithiocarbamate,
- synthesize bismuth based ternary nanoparticles,
- synthesize graphitic carbon nitride decorated with bismuth based ternary nanoparticle s
- characterize the composite materials using FTIR, X Ray diffraction, scanning electron microscopy, transmission electron microscopy, UV visible spectroscopy,
- investigate the photocatalytic removal of selected heavy metal ions from aqueous solution using prepared composite at different concentration, pH, and dosage of the solution,
- compare the removal efficiency of the composite with that of ordinary graphitic carbon nitride,
- investigate the effect of sacrificial and easily oxidizable organics on photocatalysis.

REFERENCES

Chen, D., K. Ray, A., 2001. Removal of toxic metal ions from wastewater by semiconductor photocatalysis. Chemical Engineering Science 56, 1561-1570.

Chen, H., Nanayakkara, C.E., Grassian, V.H., 2012. Titanium dioxide Photocatalysis in Atmospheric Chemistry. Chemical Reviews 112, 5919-5948.

Fazal, T., Iqbal, S., Shah, M., Bahadur, A., Ismail, B., Abd-Rabboh, H.S.M., Hameed, R., Mahmood, Q., Ibrar, A., Nasar, M.S., Ehsan, Y., Shah Saqib, A.N., Adnan, Qayyum, M.A., 2022. Deposition of bismuth sulfide and aluminum doped bismuth sulfide thin films for photovoltaic applications. Journal of Materials Science: Materials in Electronics 33, 42-53.

Griffith, D.M., Li, H., Werrett, M.V., Andrews, P.C., Sun, H., 2021. Medicinal chemistry and biomedical applications of bismuth-based compounds and nanoparticles. Chemical Society Reviews 50, 12037-12069

Jing, L., Xu, Z., Sun, X., Shang, J., Cai, W., 2001. The surface properties and photocatalytic activities of ZnO ultrafine particles. Applied Surface Science 180, 308-314.

Litter, M., 2009. Treatment of Chromium, Mercury, Lead, Uranium, and Arsenic in Water by Heterogeneous Photocatalysis. Advances in Chemical Engineering 36, 37-67.

Wilbur, S., Abadin, H., Fay, M., Yu, D., Tencza, B., Ingerman, L., 2012. Toxicological Profile for Chromium. Atlanta (GA): US Department of Health and Human Services. Public Health Service, Agency for Toxic Substances and Disease Registry 24049864.

Yang, S., Feng, X., Wang, X., Müllen, K., 2011. Graphene-Based Carbon Nitride Nanosheets as Efficient Metal-Free Electrocatalysts for Oxygen Reduction Reactions. Angewandte Chemie (International ed. in English) 50, 5339-5343.

CHAPTER TWO

2.0 Photocatalysis and photocatalyts

The continuous search for new strategies for the environmental and water remediation from pollutants led to the emergence of heterogeneous catalysis as one of the preferred water remediation techniques. Photocatalysis utilizes solar light which is abundantly available, and it is efficient and cost effective compared to other existing water treatment techniques. In addition, it can degrade pollutants at ambient pressure and temperature instead of transferring them from one medium to another, which could lead to secondary pollution problem. It is one of the advanced oxidation processes, which require the use of a suitable photocatalyst. As shown in Fig. 2.1, an ideal photocatalyst should be chemically and biologically inert, stable to photo corrosion, utilizable in the visible or near UV light region, cheap, non-toxic, and photoactive (Bhatkhande, 2011). Examples of semiconductors that have been utilized as photocatalysts are metal oxides, metal sulphides, noble metals, graphene oxide, graphitic carbon nitride or their composites.

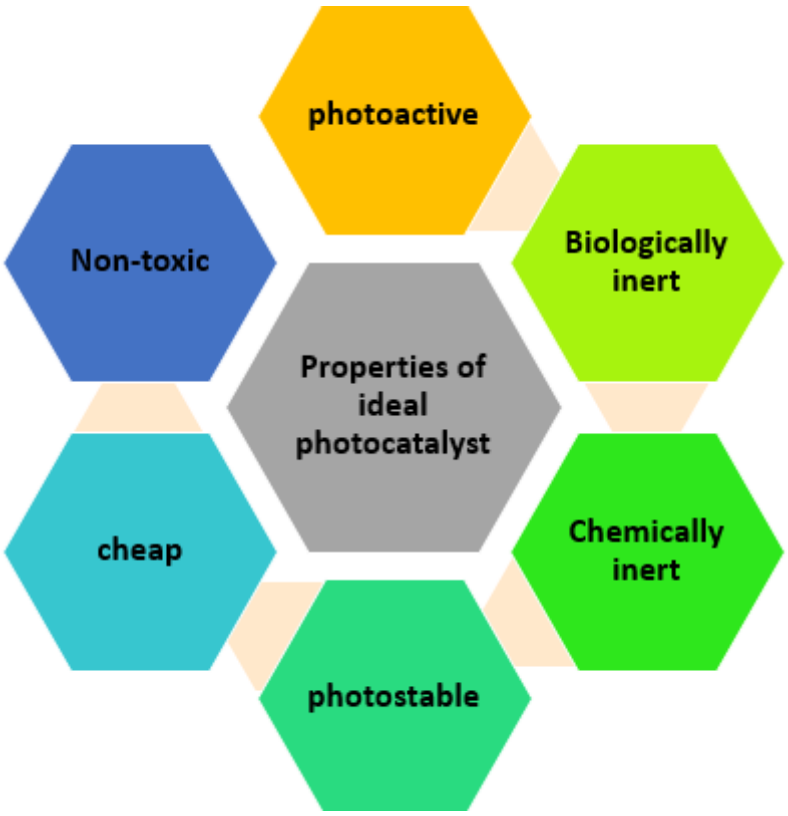

Figure 2.1: Properties of ideal photocatalysts.

2.1 Graphitic carbon nitride as photocatalyst

The use of g-C_3N_4 as visible-light-responsive photocatalysts has been well applauded in recent times (Akhundi et al., 2019). The discovery of the compound was the result of the quest for non-metal containing materials that could efficiently absorb within the solar spectrum and maximally utilize the solar energy. A large part of about 46% solar spectrum falls in the visible light region, while only 5% falls within the ultraviolet region (Lokhande et al., 2019). Due to their very wide band gap energy, most photocatalysts absorb in the UV region. Therefore, solar energy is not fully utilized. According to the studies conducted by Wang et. al., (2009), quite a number of g-C_3N_4 based nanocomposites have been developed as photocatalysts, signalling a new area of applications. Some of these applications have been reviewed by various groups (Masih D, 2017; Chi Zhang, 2018; Mousavi et. al., 2018; Zhang et al., 2018; Akhundi et al., 2019; Chan et al., 2019; Mishra et al., 2019; Prasad et al., 2019).

Historically, studies involving graphitic carbon nitride started in the 1830s, when Liebig and Berzelius discovered "melon". It contains tri-s-triazines monomer that is connected through tertiary amine. The historical trend is summarized in Table 2.1 (Cao et al., 2015). However, g-C_3N_4 was introduced into heterogeneous catalysis in 2006 (Goettmann et al., 2006). Particularly, the use of graphitic carbon nitride as photocatalyst for water splitting has been reported (Masih D, 2017).

Table 2.1: Historical exploration and the evolutionary process of g-C_3N_4

Year	Works on g-C_3N_4	References
1834	Berzelius made synthetic polymer which was a derivative of carbon nitride. Leibig named it as "melon" in 1834.	(Liebig, 1834)
1835	Sulphur and potassium ferricyanide was heated together in a crucible to make potassium hydromelanote by Gmelin.	(Gmelin, 1835)
1922	The term "carbonic nitride" was introduced and it was found to be formed as the last product of several ammonocarbonic acids using melon as the starting material by Franklin	(Franklin, 1922)

1937	Tri-s-triazine was suggested as repeat monomer unit of graphitic carbon nitride by Sturdivant and Pauling.	(Pauling and Sturdivant, 1937)
1940	Resemblance between graphite and melon was pointed out by Lucas and Redemann. They were both planar and very large.	(Redemann and Lucas, 1940)
1982	Derivatives of cyameluric were obtained as the pioneer crystal structure by Leonard *et al.,*	(Hosmane et al., 1982)
1990	Sp^3-bonded β-C_3N_4 was theoretically predicted to have hardness and bulk modulus that is either equal or greater than that of diamond.	(Cohen, 1985; Maya et al., 1991)
1996	Although by calculation methods, graphitic carbon nitride was shown to have five structural types by Hemley and Teter.	(Chan, 2019)
2001	Species having high crystallinity which was believed to be melon possessing high molecular weight was reported by Komatsu.	(Komatsu, 2001)
2003	Melam and melem derivatives were isolated and identified as the crystalline structure of heptazine by Schnick *et al.,*	(Jürgens et al., 2003; Lotsch and Schnick, 2007)
2006	g-C_3N_4 was discovered to be a heterogeneous photocatalyst without containing metals.	(Goettmann et al., 2006)
2007	Milan *et al.,* converted dicyandiamide to imide phase carbon nitride.	(E. Horvath-Bordon, 2007)
2009	Semiconductor without metal-based hydrogen generation by Wang using g-C_3N_4.	(Masih D, 2017)

2.1.1 *Structure and properties of g-C_3N_4*

Seven phases of carbon nitride have been identified, which include g-h-heptazine, g-o- triazine, g-h-triazine, pseudo-cubic C_3N_4, cubic C_3N_4, β-C_3N_4 and α-C_3N_4 (Teter and Hemley, 1996). Among these phases, g-C_3N_4 is unique due to its band gap, which is considered appropriate (2.7 eV) for low energy activation, and it is also the phase with the least band gap energy among all. The relatively low band gap allows it to absorb light in the visible range of the solar spectrum (450−460 nm) (Dong et al., 2013). The low band gap of g-C_3N_4 could be because of nitrogen and sp^2-hybridized carbon, which resulted in the electronic structures that contain π-conjugated systems (Maeda et al., 2009). The basic units of g-C_3N_4 are triazine(C_3N_3) (shown in Fig. 2.2a) and heptazine or tri-s-triazine(C_6N_7) rings (Fig. 2.2b). Tri-s-triazine- based g-C_3N_4 is not only the most stable phase, but it is also the most favoured under room conditions when energy is put into consideration (Zheng et al., 2015). Consequently, tri-s-triazine, which is also called melem, is being considered to be the unit on which graphitic carbon nitride was built.

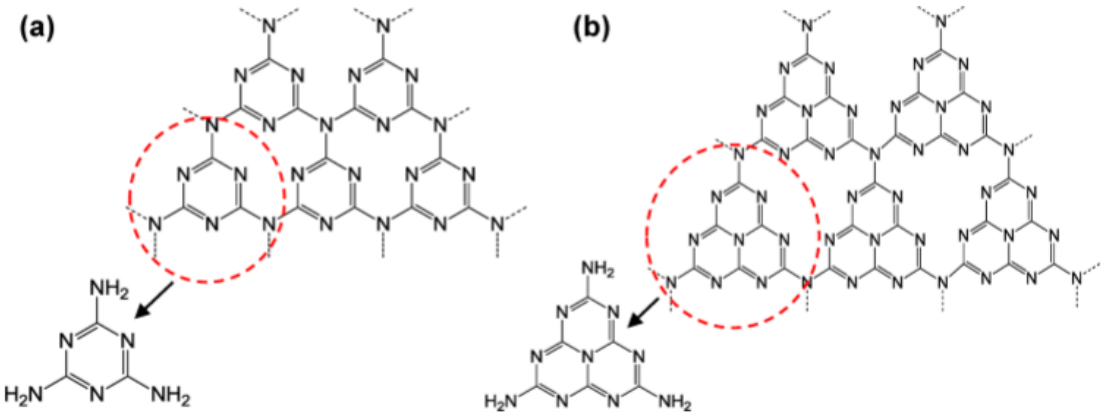

Figure 2.2: Graphitic carbon nitride structures: (a) Triazine and (b) heptazine also called tri-s-triazine (Ong et al., 2016). Copyright (2016), with permission from American Chemical Society.

Tri-s-triazine-based carbon nitride has the highest stability among the allotropes of carbon nitride (Ou et al., 2017). It can also withstand heat without breaking down even at 600 °C in air, as evidenced in the thermogravimetric analysis (TGA) (Wang et al., 2012a). At 750 °C, graphitic carbon nitride decomposes completely in oxygen atmosphere to give oxides of nitrogen and carbon without leaving any residue (Lin et al., 2015; Elshafie et al., 2020). Graphitic carbon nitride also has good chemical stability, it is insoluble in common solvents such as toluene, diethylether, tetrahydrofuran, dimethylformamide, alcohols and water (Martin et al., 2014). It is easy to prepare because it contains two earth-abundant elements (carbon and

nitrogen) (Wang et al., 2012b). The surface of this interesting 2D-conjugated polymer can easily be modulated at the molecular level by surface engineering without changing the composition significantly (Ong et al., 2016; Prasad et al., 2019). It is the robust and visible-light-active photocatalyst used in the fields of environmental remediation and conversion of solar energy (Zhang et al., 2018).

2.1.2. *The photocatalytic property of g-C_3N_4*

g-C_3N_4, has displayed a very good photocatalytic activity due to its suitable band gap energy and ability to absorb within the solar spectrum. The polymeric nature of the material is another important factor, which contributes to its use as photocatalyst in either environmental remediation from toxic inorganic and organic compounds, or in water splitting to generate hydrogen. Other properties, which made g-C_3N_4 a better choice as photocatalyst, include its non-toxic nature, availability, and low cost. In addition, g-C_3N_4 is stable under the light; it cannot be easily degraded by heat, biological microbes cannot break it down and it cannot be dissolved in most solvents (Bhatkhande, 2011). Apart from exfoliation that is necessary to get the stack layer, it is equally important to boost the photocatalytic performance of g-C_3N_4 by adopting various strategies.

The photocatalytic activities of g-C_3N_4 is inadequate because of low surface area, which alters the creation of textured pores (Qamar et al., 2021). This could also be due to the high degree of monomer condensation during synthesis. Fast photogenerated electron-hole pairs recombination rate is another challenge. In addition, the particle boundary effect interrupts the delocalization of electron and there is low effectiveness of electron-hole separation. Synthesis of special structures and morphologies including mesoporous structures, ultra-thin two-dimensional g-C_3N_4 nanosheet were adopted with the aim of enhancing the photocatalytic performance (Dong et al., 2015; Lin et al., 2020). Another step forward is the adoption of modified techniques (Prasad et al., 2019), which has been used to improve the photocatalytic performance of graphitic carbon nitride. Examples of such techniques are coupling g-C_3N_4 to another photocatalyst, joining carbon nanomaterials with g-C_3N_4, deposition of noble metal and addition of heteroatoms, which may be metal or non-metal into the framework of graphitic carbon nitride.

2.1.3 *Photocatalytic improvement strategies for g-C_3N_4*

Doping of metals such as noble metals, rare earth metals or alkali metals into g-C_3N_4 enhances photocatalytic efficiency of g-C_3N_4. This is advantageous because it leads to bandgap narrowing and surface area improvement. There is also an improvement in the band structure and the separation of charge is properly fine-tuned (Nemiwal et al.,2021). The problem with this strategy is the formation of secondary pollutants as a result of leaching of metal ions Viet et al., (2019) fabricated g-C_3N_4 doped with noble metal by using heat condensation method. The noble metal used was silver, and a reduction in particle size as well as the energy of the band gap was reported. In addition, there was a reduction in the recombination rate of electron and hole. The separation of charge carriers was also significantly enhanced. The study further examined the removal efficiency of oxytetracycline from water, and the highest removal was reported with the use of graphitic carbon nitride loaded with 7% of silver. The photocatalyst remained stable even after five times reuse, indicating good re-usability property.

The doping of g-C_3N_4 with non-metals is another strategy that has been employed to improve the efficiency of g-C_3N_4 (Nemiwal et. al., 2021). Unlike metallic doping, this cannot lead to secondary pollution. It also absorbs visible light better and there is an enhancement of charge separation. Doping with non-metal elements is an important way of tunning g-C_3N_4 structure. Non-metallic doping occurs by replacing either carbon or nitrogen atoms in graphitic carbon nitride structure, this then affects both the valence bond and the conduction band. On the contrary, doping with metal involves inserting metal into graphitic carbon nitride framework. Most of the time, it leads to reduction in the bandgap which consequently elongates its ability to absorb light. This strategy is flexible because the quantity of the elements can be varied, as well as the identity of the elements based on the desired position of the band during bandgap engineering (Cao et al., 2015). However, recombination centres may be formed when doped with non-metals since non-metals cannot participate in the movement of charge. Chen et al (2018b) reported a cheap pathway for doping g-C_3N_4 with carbon, thereby giving a porous structure with nitrogen vacancy.

The nano particulate forms of noble metals such as Pd, Au, Pt and Cu deposited on g-C_3N_4 is also one of the explored methods. This strategy was applauded because the presence of the metal has positive influence on the photocatalytic activity before reaching the optimum loading (Mafa et al.,2022). The demerit of this strategy is that when the metal ions are more than necessary, they could become a centre where holes and electrons pairs could recombine,

especially after reaching the maximum metal carrying capacity. Gao et al., (2015) reported the use of a precursor and a sacrificial template made from supramolecular network of 2D melamine/copper to innovatively made graphitic carbon nitride doped with copper. The specific surface area of the prepared sample (40.86 m^2 g^{-1}) was found to be seven times more than that of ordinary graphitic carbon nitride. It also showed better visible light absorption and at near infrared region, and also exhibited high photocatalytic activity.

Another strategy involves the formation of hybrids of g-C_3N_4 and carbon-based nanomaterial such as reduced graphene oxide (rGO), graphene oxide (GO), carbon nanosphere (CNS) and carbon nanotubes (CNTs). The resulting nanocomposite usually possesses high heat and high electrical conductivity, and absorbs both inorganic and organic compounds better. The major demerit is the reduction in the light penetration to the photocatalyst because excessive amount of carbon nanomaterials, particularly reduced graphene oxide, and can absorb a lot of molecules of dyes onto the surface of the catalyst (Chen et al., (2016). Wu et al.(2018) combined graphene oxide with graphitic carbon nitride and molybdenum sulphide. An improvement in photocatalytic removal of dyes was observed, in addition to being able to effectively reduce Cr(VI) to Cr(III) in the water sample. Finally, more than one semiconductors could be coupled to form a heterojunction of semiconductors with a better stability and enhanced utilization of visible light. Charge separation and transfer also becomes better and formation of the oxidizing species becomes more efficient. The only challenge of this strategy is that it is not easy to get a suitable semiconductor photocatalyst with appropriate position of band edge. The common heterojunction systems are type I, II, III and Z-scheme (Singh et al., 2020). The Z-scheme is one of the commonly adopted heterojunction systems (Di et al., 2017b; Jourshabani et al., 2017; Singh et al., 2020). This is because it is effective in surmounting the challenges encountered when a single component heterogeneous photocatalyst is used (Di et al., 2017b).

2.1.4 *Analytical Identification of graphitic carbon nitride*

Different techniques have been used to study the chemical identity of g-C_3N_4, including X-ray diffraction (XRD) and X-ray photoelectron spectroscopy (XPS), which are very useful in indexing peaks to particular features of the g-C_3N_4. The XRD pattern of graphitic carbon nitride shows two noticeable peaks at *ca*. 13.0 and 27.4° (Fig. 2.3a). The second peak is indexed as the 002 peak and it is the peak from the stacking of intralayer repeated aromatic units (Jin et al., 2018), while the first peak is the 100 peak which is for the separation between the planes

(Wang et al., 2009; Cao et al., 2015; Yan et al., 2020). The atomic status of the nitrogen (Figure 2.3c) and carbon (Fig. 2.3b) in graphitic carbon nitride could be determined by XPS. This pattern showed that carbon-carbon peak for sp^2 hybridized carbon is around 284.6 eV whereas the sp^2 bonded carbon attached to nitrogen, N–**C**=N, is around 288.1 eV. Also, the sp^2-bonded nitrogen, C–**N**=C, (i.e the nitrogen directly bonded to a sp^2 hybridized carbon) is around 398.7 eV, amino group (which is a product of imperfect polymerization, C–**N–H)** is found around 401.4 eV. The XPS pattern also showed tertiary nitrogen groups, **N**R_3 whose peak appears around 400.3 eV (Zhang et al., 2012; Cao et al., 2015). The percentage of carbon and nitrogen, as well as the ratio of carbon to nitrogen are derived from the elemental analysis. To estimate its band gap energy, UV– vis diffuse reflectance spectra is employed. The band gap energy could be approximately calculated by dividing 1240 by the value of the absorption band edge of a particular sample, λ (nm) (Cao et al., 2015).

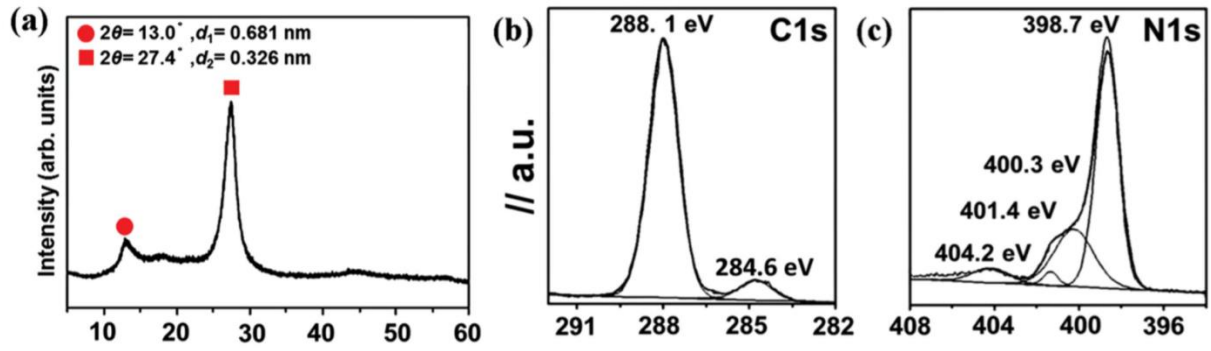

Figure 2.3: (a) X-ray diffraction pattern of graphitic carbon nitride. High-resolution XPS spectra of (b) C1s and (c) N1s of graphitic carbon nitride (Cao et al., 2015). Copyright (2015), with permission from Wiley Interscience.

The optical characterization is carried out using photoluminescence (PL) and UV/Vis absorption spectroscopic techniques. Depending on the atoms and variation in structure, g-carbon nitride polymer could have a band gap as high as 5 eV, based on theoretical calculations. At around 420 nm, common C_3N_4 has absorption pattern that is typical of semiconductors (Wang et al., 2012b) as shown in Fig. 2.4. TGA is used to confirm the stability of graphitic carbon nitride, and its thermal stability is useful in determining the suitability of the compound as a catalyst.

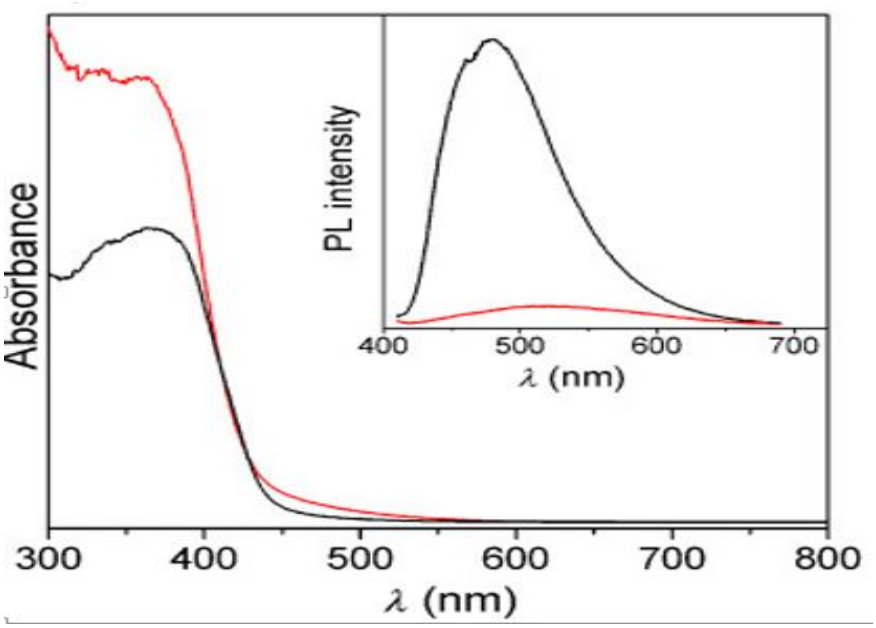

Figure 2.4: Diffuse reflectance absorption and photoluminescence spectra (insert) of g-C_3N_4 at 420 nm excitation wavelength (Wang et al., 2012b). Black is bulk g-C_3N_4 and red is mesoporous g-C_3N_4. Copyright (2012), with permission from Wiley Interscience.

2.1.5 *Methods of g-C_3N_4 preparation*

The g-C_3N_4 can easily be prepared by heat treatment of precursors that are rich in nitrogen including thiourea, urea, cyanamide, dicyanamide, and melamine (Ong et al., 2016). Thermal polymerization of cyanamide, dicyanamide and urea can be carried out at 550 ^{o}C. The pyrolysis temperature for thiourea is between 450-650 ^{o}C, while melamine is between 500-580 ^{o}C. Other precursors are ammonium thiocyanate, guanidine thiocyanate, carbamide powder with thiocyanate, sulphur-mixed melamine and sulphuric acid-mixed melamine (Cao et al., 2015; Hao et al., 2020; Wang et al., 2020b). Some factors such as the process used for its modification, preparation defects, packing, temperature used for condensation and the type of precursor used during preparation can affect the adsorption edge of C_3N_4 (Ong et al., 2016). Fig. 2.5A shows the effect of type of precursor used on the photoluminescence property of obtained g-C_3N_4. When graphitic carbon nitride is excited at 365nm, it shows four peaks in the visible regime as shown in Figure 2.5B (Wang et al., 2017).

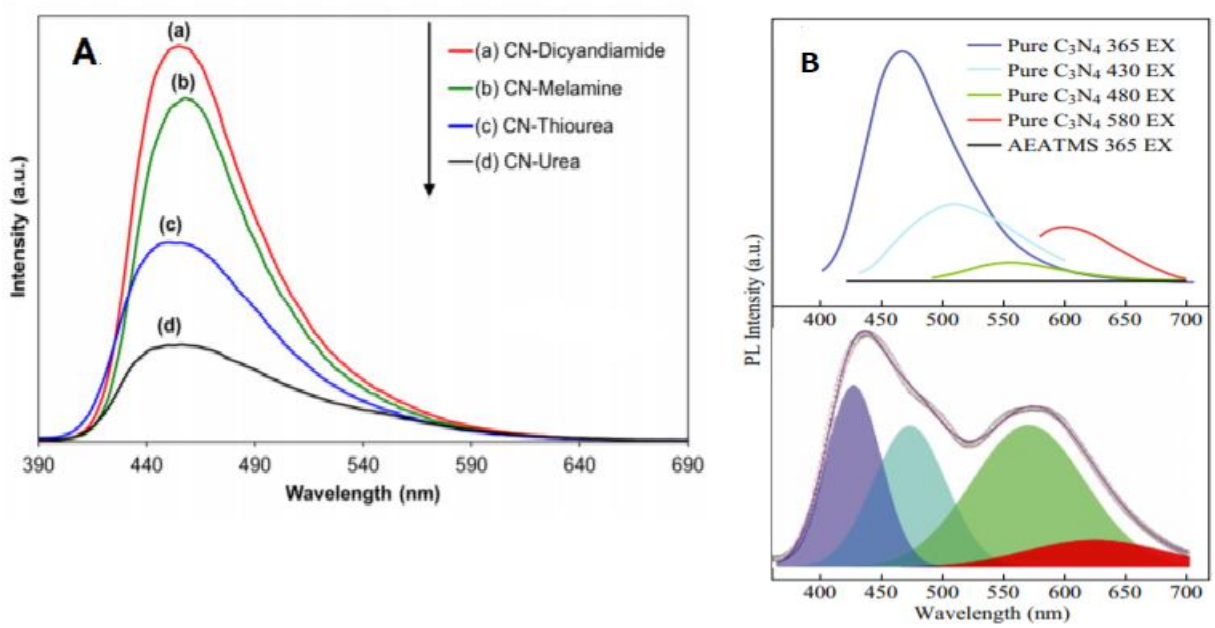

Figure 2.5: (A) PL spectra of synthesized graphitic carbon nitride by changing the precursors used (Ong, 2015). Copyright (2015), with permission from Royal Society of Chemistry (RSC). (B) PL spectrum of the g-C_3N_4/silica gels, excited at 365 nm displaying four peaks (430, 480, 580, and 627 nm) in the visible regime. Reprinted with permission from (Wang et al., 2017). Copyright (2017) Springerlink.

It is important to note that synthesizing an ideal graphitic carbon nitride with exact theoretical carbon-to-nitrogen ratio is quite tedious. Furthermore, the presence of amine group could slightly lower the non-reactive nature of the surface of graphitic carbon nitride, which favors its reaction with the desired reactants. However, when the carbon-to-nitrogen ratio is stoichiometrically too low, charge migration and separation may be negatively impacted because of condensation not being completed due to too many defects. This should be prevented since it compromises its activity (Cao et al., 2015). Another important note is that the condition used for the synthesis, as well as, the precursors used determines the specific surface area of g-C_3N_4. For example, when melanine was used as precursor for a typical g-C_3N_4, the surface area was reported to be small (ca. 8 m^2 g^{-1}) (Yan, 2009).

2.1.6 *Synthetic pathways*

The synthesis route for urea self-polymerization is similar to that of thiourea precursor (Chen et al.,2016). One of the similarities is the liberation of ammonia during the polymerization process. The major difference is that thiourea condensation involves elimination of carbon disulphide and hydrogen sulphide, but urea polymerization involves the elimination of carbon dioxide and water (Fig. 2.6). The gasses generated during this heat treatment process (either ammonia liberated at low temperature below 200 °C or carbon dioxide at high temperature) are extremely important for good porous graphitic carbon nitride processing (Ong et al., 2016). Another difference is that their polymerization involves different intermediates.

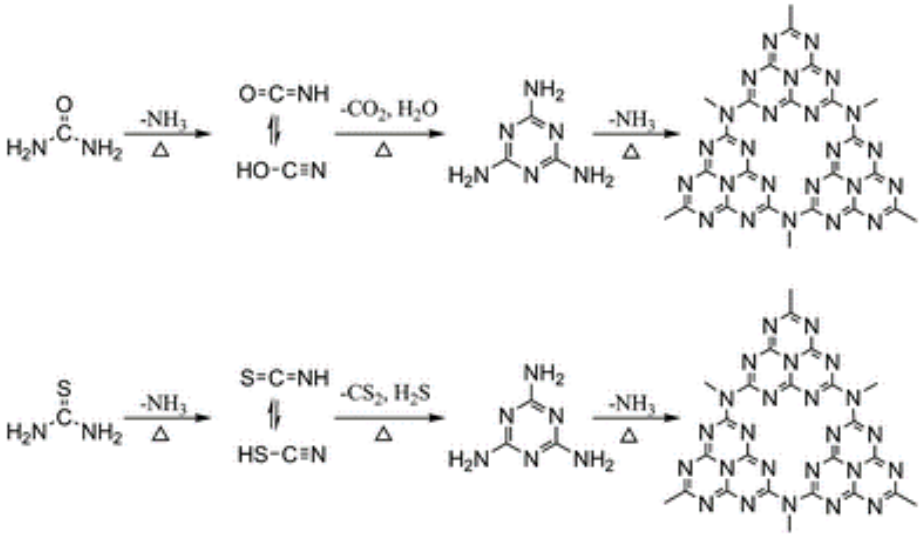

Figure 2.6: High temperature self-polymerization of urea and thiourea in air to form graphitic carbon nitride (Zhang et al., 2012). Copyright (1996), with permission from Royal Society of Chemistry.

The use of cyanamide as precursor for g-C_3N_4 was pioneered by Wang et al., (2009). In their report, both XRD and TGA were employed for intermediate species' characterization. Condensation reaction occurred at 203 and 234 °C, leading to the formation of dicyandiamide and melamine respectively. This condensation later led to the removal of ammonia gas, and at 335 °C in all the products that were based on melamine. Increasing the temperature to 390 °C, led to the tri-s-triazine units' formation because of melamine rearrangement as shown in Fig. 2.7. Continuous heating and condensation at 520 °C led to the formation of polymeric form of graphitic carbon nitride. However, the polymer became unstable when the temperature was increased to 600 °C. Finally, at temperatures greater than 700 °C, the whole polymer of

graphitic carbon nitride disappeared forming fragments of cyano and nitrogen without leaving any residue.

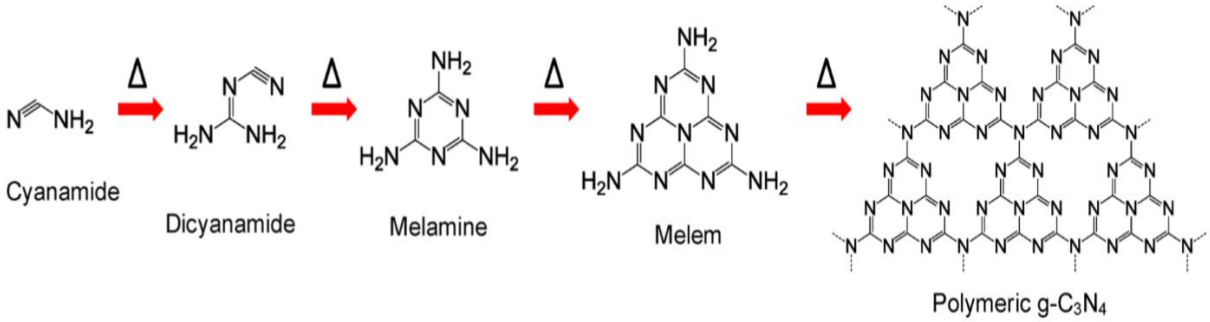

Figure 2.7: Graphitic carbon nitride synthesis pathway using cyanamide precursor (Ong et al., 2016). Copyright (2016), with permission from American Chemical Society.

The search for a more novel precursor led to the discoveries of guanidinium-based precursors. The use of heat condensation of guanidinium dicyanamide and guanidinium tricyanomelaminate for the synthesis of graphitic carbon nitride was reported by Schnick et al., (2005). It was confirmed that melamine was one of the important intermediates during the synthesis. Hence, chemicals that are based on guanidinium could be changed to the building block of graphitic carbon nitride and then subjected to heat treatment to undergo cross-linking. In a similar work, Long et al.,(2014) used heat induced desulphurization and subsequent condensation to convert guanidinium thiocyanate to thiocyanic acid (as the first product) and guanidine as shown in Figure 2.8a. Both products reacted at the same time to give a series of products. Guanidinium thiocyanate is readily available and very cheap. Shi et al., (2014) also used a different compound that is based on guanidine to make mesoporous graphitic carbon nitride. The compound used was guanidine hydrochloride, and the synthesis was carried out at 650 °C while the polymerization reaction employed was initiated by heat. As shown in the reaction pathway in Fig. 2.8b, the intermediates involved are melon, melem and melamine, and the final product is polymeric graphitic carbon nitride.

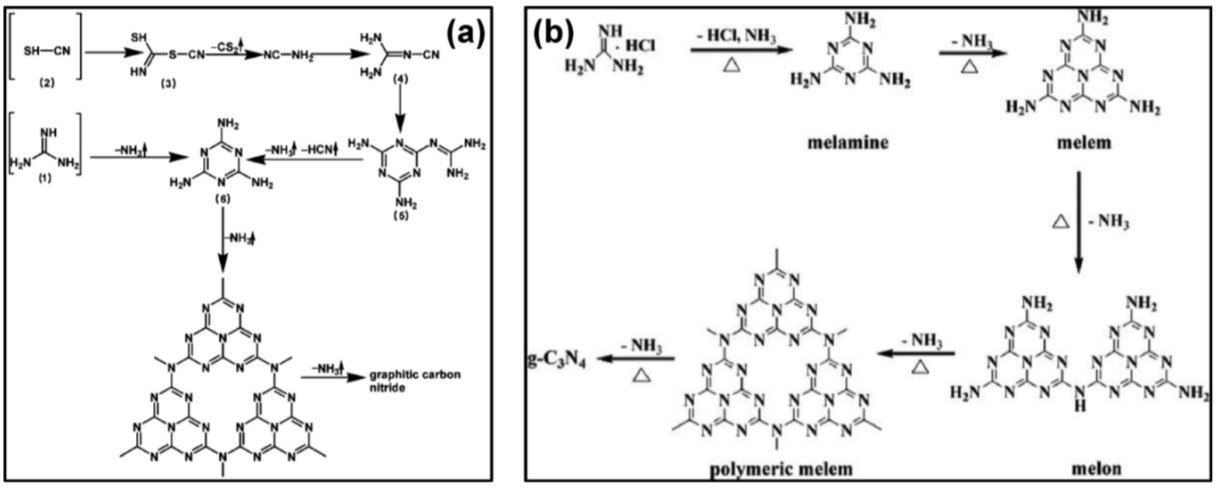

Figure 2.8: Thermal graphitic carbon nitride self-polymerization synthesis route for (a) guanidine thiocyanate and (b) guanidine hydrochloride (Long, 2014; Shi, 2014). Copyright (2014), with permission from Royal Society of Chemistry.

2.1.7 *Exfoliation of bulk graphitic carbon nitride*

Polymeric stacking of the bulk graphitic carbon nitride layer leads to low specific surface area, low efficiency of charge separation and insufficient active site on its surface (Cui et al., 2018). Therefore, it is extremely important to find means of separating the stack layers in order to get high surface area (Cao et al., 2015), good ability to transport electrons, large exposed edges number and narrow band gap for maximum use of g-C_3N_4, (Cui et al., 2018). In a bid to achieving these, the use of sonication to achieve exfoliation in liquid phase has been proposed by Yang et al., (2013). It was reported that bulk g-C_3N_4 can be converted to thin-layer using this method. To improve the exfoliation, low boiling point solvent such as isopropyl alcohol was proposed to be the best solvent, with the constant sonication assistance. Kumar et al., (2014) reported another study involving the use of sonication to convert melamine to graphitic carbon nitride by using a mixture of water and ethanol as solvent. The surface area of the resultant graphitic carbon nitride mesoporous (112 m^2g^{-1}) was far greater than that obtained in bulk g-C_3N_4 (8 m^2g^{-1}). Apart from using organic solvents for exfoliation, there are recent reports on the use of solution of either base or acid. One of the reports involved the use of sonication and addition of concentrated H_2SO_4 mixed with deionized water for the exfoliation of graphitic carbon nitride derived from dicyandiamide (Xu et al., 2013). In a similar work, Niu et al., (2012) carried out the exfoliation of bulk g-C_3N_4 using thermal oxidation method. The g-C_3N_4 made from dicyandiamide exhibited improved surface area (2 nm) after the

exfoliation. Summarily, thermal or liquid-type exfoliation is possible, and the utilized liquid could be acid, base or organic solvents. Irrespective of the method used for the exfoliation, the resultant g-C_3N_4 will possess improved efficiency of charge separation, enhanced transport ability of electrons and there will be an increase in specific surface area (Cao et al., 2015).

2.1.8 *Different forms of g-C_3N_4 nanostructures*

Different nanostructures of g-C_3N_4 now exist such as porous g-C_3N_4, hollow spheres and 1D nanostructures (Cao et al., 2015). These forms are discussed below:

Porous g-C_3N_4: The presence of high surface area and mass diffusion via several channels has boosted the interest in the use of porous materials as photocatalysts. In addition to these very good properties, the separation and migration of charges is uniquely interesting. They are usually made by either soft or hard templating techniques. This is because the method gives room for tuning, which implies that different templates could be chosen. Silica hard templates such as KIT-6, KCC-1 and SBA-15 are usually employed in order to get nanostructures of graphitic carbon nitride (Ong et al., 2016). Other methods employed the use of soft templates, such as the bubble-forming templates (like urea and thiourea) and pluronic P123 (Yan, 2012). Porous graphitic carbon nitride could also be hard template, and this has been used to prepare nanoparticles such as Ta_3N_5, which were well arranged and with tunable sizes (Fukasawa et al., 2011). The common precursors for this design were cyanamide, dicyanamide and melamine. In a typical design, the first step was to infuse the silica template mesopore with precursors. The product obtained was condensed after calcination to give graphitic carbon nitride inside a silica template. HF or NH_4HF_2 was then used to remove the template, and the final product was nanostructured graphitic carbon nitride that was well ordered. The preparation of porous graphitic carbon nitride without the use of templates has been reported. One of the works was carried out by Gu et al., (2015) where post-heating handling of solvothermal techniques without the use of templates was reported. The sample prepared was shown to have similar composition as that of bulk g-C_3N_4 but with nanoporous surface. The prepared sample also possessed lower resistance and narrow bandgap. These properties favoured better separation and transport of photogenerated charge carriers as well as efficient light harvesting in the visible region.

Hollow spheres: Hollow sphere photocatalysts are also a good form because the structure allows better harvesting of incident light and it is a better carrier of photo induced charges. The

major problem that is associated with them is the possibility of collapsing during preparation. Initially, the hard template methods were being used for their preparation, where structured silica core-shells were used as hard template. The preparation of hollow structured graphitic carbon is currently carried out by utilizing the triazine molecules based on supramolecular chemistry. This thus involves the gathering of the triazine molecules, leading to the formation of a supramolecular network held together by hydrogen bonding. The precursor commonly employed in this process is a complex made from both melamine and cyanuric acid. There are different forms of hollow spheres, including hollow boxes, mesoporous hollow sphere and hollow 3D assemblies, that all have good photocatalytic activity (Cao et al., 2015). From recent studies, it is now possible to prepare hollow sphere through non-templating method. For instance, one-step solvothermal techniques have been used for preparing hollow spheres g-C_3N_4 without the use of template (Cui et al., 2015). Both Fourier transform infrared (FTIR) and XRD results showed that heptazine-based structure and graphitic structure are present in the sample at different temperatures.

1D nanostructures: This could be nanotubes, nanoribbon, nanobelts, nanowires and nanorods. The nanostructures have attracted preference because of their outstanding electronic, optical and chemical properties, which lead to the optimum activity of the catalyst. These properties can be improved by tuning both diameter and length (Cao et al., 2015; Ong et al., 2016). In addition, 1D nanostructures are associated with charge carrier mobility and specificity in the surface area. One of the mostly used template for its synthesis is SBA-15. The non-templating technique has been reported by Bai et al., (2020). The graphitic carbon nitride nanorods was synthesized by heat treatment using graphitic carbon nitride nanoplates as precursors. This synthesis was carried out in a mixture of water and methanol through a simple reflux process. Other morphological forms of graphitic carbon nitrides are shown in Fig. 2.9.

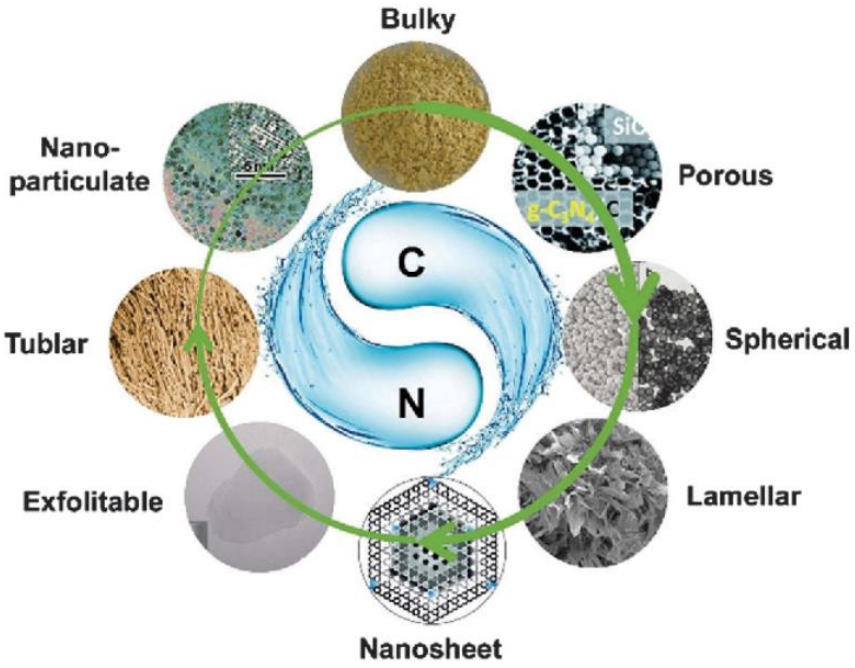

Figure 2.9: Different morphologies of g-C_3N_4 with dimension ranging from quantum dot to bulk (Liu et al., 2016). Published by the Royal Society of Chemistry (under creative common license).

2.2 Dithiocarbamates as precursors for material synthesis

Dithiocarbamates are amides formed from dithiocarbamic acid and have the ability to form stable metal complexes because of their exceptional coordination properties (Adeyemi and Onwudiwe, 2020). They could generally be classified as heterocyclic dithiocarbamates, symmetric dithiocarbamates, unsymmetric dithiocarbamates, dialkyldithioc arbamates and monoalkyldithiocarbamates (Cvek and Dvorak, 2007). Several methods have been used to synthesize dithiocarbamate compounds. However, the synthesis is commonly achieved by the reaction of carbon disulphide and amine (primary or secondary). The reaction is usually carried out in the presence of electrophiles such as imines, transition metals, epoxides, and alkyl halides (Shinde et al., 2020). The synthesis could be effected without a catalyst or in the presence of an appropriate alkali as shown in Fig. 2.10 through (equation a-n). Their ligands can form complexes with octahedral, square planar or tetrahedral geometry depending on the type of metal ion and also the ratio of the metal-to-ligand (Cvek and Dvorak, 2007). Dimers of dithiocarbamate are also formed by using dilauroyl peroxide as the oxidizing agent (Chen et al., 2015) (equation o). Other polyfunctional ligands of dithiocarbamate exist

but they are rare compared to other forms of dithiocarbamate compounds (Tan et al., 2021). Both the dithiocarbamate ligands and complexes are useful in several applications. Although, when both ligands and complexes found relevance in similar applications, the complexes appear to be more potent than the ligands. For instance, dithiocarbamate complexes are more active against microbes than the ligands from which the complexes are formed (Ejelonu et al., 2018). The choice of dithiocarbamates compared to other related compounds is attributed to their poor solubility in water, ease of preparation under laboratory conditions, and formation of more stable compounds than several complexes made from other common analytical ligands (Kanchi et al., 2014).

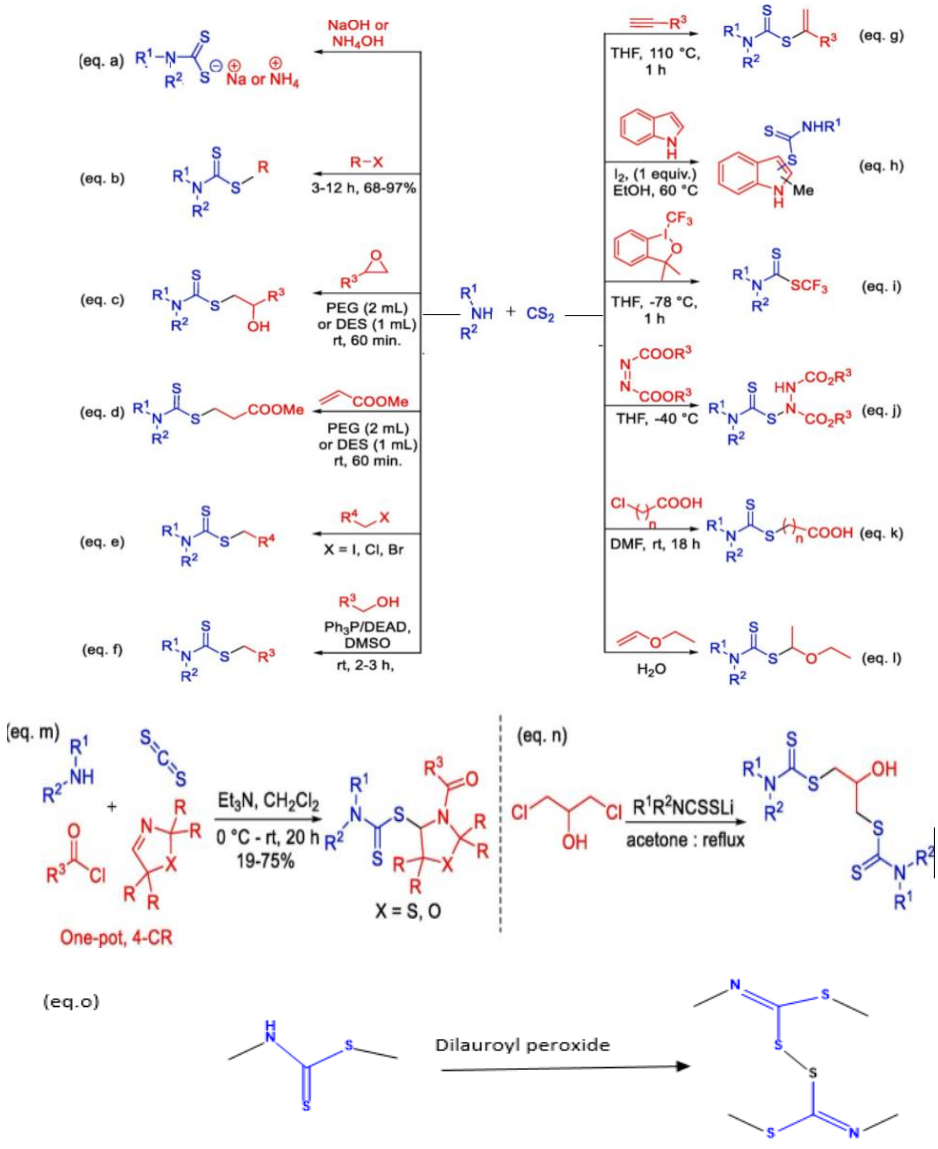

Figure 2.10: Various routes for the synthesis of dithiocarbamates. *Adapted from* (Shinde et al., 2020). *Copyright (2020), with permission from Elsevier*

Different synthetic methods have been used to produce metal sulphide nanoparticles and one of these methods involve the use of metal complexes as single source precursors (SSP). Among the metal complexes used as SSP, dithiocarbamate complexes have been the most explored complexes. Dithiocarbamate complexes are thermolysed to generate metal sulphides (Olatunde and Onwudiwe, 2021b). Some of these nanoparticles especially the bismuth-based have been reviewed by Ajiboye et al., (2021). The use of dithiocarbamate complexes for the synthesis of these nanoparticles is preferred since dithiocarbamate is rich in sulphur, hence the use of a separate sulphur-source will not be required (Srinivasan, 2019). Generally, the synthesis of dithiocarbamate complexes using the solvothermal method requires the use of capping agents, and the commonly used are oleylamine, octadecene, dodecane thiol, ethylene glycol, and hexadecylamine. Their presence in the system controls the growth of the nanoparticles (Sarker and Hogarth, 2021), while some of these capping agents (such as oleylamine) can also function as reducing agents, solvents or surfactants in the material synthesis (Mourdikoudis and Liz-Marzán, 2013). Table 2.2 highlights other examples of nanoparticles made from dithiocarbamate.

Table 2.2: Application of dithiocarbamates in nanoparticle(s) synthesis

Dithiocarbamate precursor used	Nanoparticle(s) obtained	Temp. used	Particle size and (band gap)	Ref.
Bis(N-ethylphenyldithiocarbamato) palladium(II)	Palladium sulphide	160, 200 and 240 °C resp.	2.01–2.50 nm, 4.00–4.86 nm and 2.53–4.12 nm (4.90–5.02 eV)	(Paca and Ajibade, 2021)
Bis(N,N-di(4-fluorobenzyl)dithiocarbamato-S,S′)M(II) (M = Cd)	Cadmium sulphide (CdS)	-	-(3.29 eV)	(Eswari et al., 2021)
Cu(II) bis N-methyl-N-phenyl Dithiocarbamate	Copper sulphide (CuS and Cu_5S_9)	≥240 °C	34.7 ± 13.3 nm	(Olatunde and

			width size(1.85 eV)	Onwudiwe, 2021a)
Dithiocarbamate complexes with varied Ag/In/Ga/Zn ratios	Quinary Ag-In-Ga-Zn-S quantum dots	220 °C	2.0 ± 0.4 nm	(Galiyeva et al., 2021)
Molybdenum dithiocarbamates	Molybdenium sulphide (MoS_2)	-	40 nm	(Tanabe et al., 2021)
N-alkyldithiocarbamate copper(II) complexes with $NaBH_4$	Copper sulphide (Cu_9S_5 and Cu_2S)	180 °C	-(3.0 eV)	(Duran-García et al., 2021)
copper(ii) bis-(2,2′-(dithiocarboxyazanediyl)diacetic acid)	Copper sulphide (CuS)	90 °C	8 ± 1 nm	(Mann et al., 2019)
bis(diethyldithiocarbamato)disulfidothioxo tungsten(VI)	chromium-doped tungsten disulphide (WS_2)	450 °C	-	(Murtaza et al., 2018)
tetrakis(N,N-diethyldithiocarbamato)molybdenum(IV)	Molybdenum sulphide(MoS_2)	450 °C	flake thickness of ∼10 nm	(Zeng et al., 2019)
$[V_2S_4(nBu_2dtc)_4]$(dtc=dithiocarbamate)	Vanadium sulphide(VS_2)	150 °C	-	(Fomenko et al., 2018)
Manganese diethyldithiocarbamate trihydrate	Manganese sulphide(MnS)	290 °C	(3.3 eV)	(Peng et al., 2012)
Tris-(piperidinedithiocarbamato) iron(III) and tris-(tetrahydroquinolinedithiocarbamato)iron(III)	Iron sulphide($Fe_{0.975}S$ and Fe_3S_4 phases)	350–450 °C	(0.95–2.0 eV)	(Mlowe et al., 2016)

lead(II) complexes of morpholine dithiocarbamate	Lead sulphide((PbS)	160 °C	(13.86–36.06 nm)	(Dong et al., 2021)

2.3 Photocatalytic performance of bismuth-based ternary sulphide photocatalysts

Recently, bismuth-containing compounds have been a subject of investigation as a replacement for commercial photocatalysts due to their unique properties. They possess highly efficient photocatalytic capacity, good antibacterial action, non-toxic, have the ability to convert light to heat, and can strongly absorb at near infra-red region. Bismuth can also be regarded as cost-effective and stable chemical, easy to functionalize, able to resist magnetic field, good electrical and diamagnetic properties with sufficient surface area (Shahbazi et al., 2020). It has low reactivity to biological species, which makes it efficient as a constituent of some pharmaceutical products such as Pepto-Bismo and Kaopectate (Miller and Bernechea, 2018). Metallic bismuth has a rhombohedral crystal structure, melting point of 271 $^{\circ}$C and density of 9.7 gcm^{-3} (Karen et al., 2020; Shahbazi et al., 2020). Trivalent bismuth has been reported as the most stable oxidation state of bismuth (Jiang et al., 2020) and it is mostly used in photocatalysts development. It was discovered that the trivalent bismuth-containing catalysts mostly displayed better photocatalytic performance compared to commercial titanium oxide photocatalyst in the visible or UV light.

Several studies (William et al., 2018; Xu et al., 2019) have reported the performance of bismuth-based chalcogenides and compared them with the photocatalytic activities of titanium oxide in the removal of pollutants from environmental samples. Ternary bismuth-based nanoparticles and their composites have been exploited as light responsive catalysts due to their low cost and effectiveness (Wu et al., 2017). Some of these ternary sulphide photocatalysts and various photocatalytic applications are discussed in this section.

2.3.1 *Copper bismuth sulphides ($Cu_4Bi_4S_9$, $CuBiS_2$ and Cu_3BiS_3)*

Copper-bismuth sulphides has not been thoroughly investigated as a photocatalyst despite that the elements are not only abundantly available world-wide but are also non-toxic. Ternary copper bismuth sulphides can display different properties and different stoichiometries. There are 13 known phases of copper bismuth sulphide. However, three phases including Cu_4BiS_9, $CuBiS_2$ (emplectite) and Cu_3BiS_3 (wittichenite) are stable and viable phases (Todor Serafimovski et al., 2015). They have coefficient of optical absorption (α) with the band gap energy of ~1.5 eV (Chakraborty et al., 2019). They are all crystalline with orthorhombic structure and they possess p-type character and high absorption coefficients ranging from 104 –105 cm^{-1}. The reported bandgaps range from 1.2 to 1.84 eV for Cu_3BiS_3, 1.5 to 2.62 eV for $CuBiS_2$, and 0.88 to 1.14 eV for $Cu_4Bi_4S_9$ (Deshmukh S.G. and V.Kheraj, 2017; Bernechea, 2018; Miller and Bernechea, 2018). The most reported work on $Cu_4Bi_4S_9$ is on synthesis of one-dimensional nanobelts or nanoribbon structure and its application as solar cells.

$CuBiS_2$ has an indirect bandgap that ranges from 1.4 to 1.7 eV as evidenced from the theoretical calculation; the difference between the energies of direct and indirect bandgap is just between 0.1 to 0.3eV, this could be attributed to flat lowest conduction band (CB) (Kumar and Persson, 2013). $CuBiS_2$ possesses high absorption coefficients (0.93 to 1.5×10^5 cm^{-1}) (Kumar and Persson, 2014). The $CuBiS_2$ density of states shows that the hole carriers' formation will trigger the Cu^+ to Cu^{2+} oxidation. This may impact the hole transport in $CuBiS_2$ and it also implies that allowing a number of copper deficiencies may be of benefit to $CuBiS_2$. Theoretical studies have also revealed that Cu_3BiS_3 shows a fundamental indirect bandgap range of 1.5 to 1.7 eV (Miller and Bernechea, 2018), and its direct band gap energy ranges between 1.6 and 1.8 eV (Kumar and Persson, 2013). The structural morphology of the copper bismuth sulphide also influences the band gap energy. The appropriate band gap energy of copper bismuth sulphide rendered it suitable for several photocatalytic applications. It was reported that the photovoltaic was fabricated from heterojunction made from copper bismuth sulphide heterojunction (Yanbo Yang, 2019).

2.3.2 *Silver bismuth sulphide ($AgBiS_2$)*

$AgBiS_2$ crystallizes in symmetrical crystalline structures unlike Bi_2S_3 and the copper-bismuth sulphide families and is temperature dependent (Miller and Bernechea, 2018; Ganguly et al., 2019). These materials possess pseudo-cubic rock salt structure at high temperatures while they have hexagonal structure at low temperatures. $AgBiS_2$ has been reported as an n-type material with a direct bandgap ranging from 1.0 to 1.4 eV (Wang et al., 2007; Miller and Bernechea, 2018; Ganguly et al., 2019). The two known phases of silver bismuth sulphide are α-$AgBiS_2$ which is a cubic structure obtained under high temperature conditions and β-$AgBiS_2$ which has a hexagonal structure and is obtained at low temperature (Bellal et al., 2017; Ganguly et al., 2019). Some of the synthetic methods that were reported for synthesizing silver bismuth sulphides are sonochemical techniques, polyol method, solvothermal route, hydrothermal process, microwave-assisted method, flux techniques, solid solution method and solid state reaction method (Wang et al., 2007; Thongtem et al., 2009; Zhong et al., 2013; Ganguly et al., 2019).

The factors limiting the performance of $AgBiS_2$ are trap-assisted recombination processes, poor carrier transport, recombination without complete extraction and low extraction of carriers' efficiency at elevated intensities of light. Some of the remedies that could be utilized is to introduce schemes that could trap light, efficient passivation of nanocrystal which could be via the treatment of ligand or surface, improvements in the synthesis, or the active layer nanostructuring. The solvothermal method has been used for the synthesis of $AgBiS_2$ (Bernechea, 2018). Thereafter, the production of films of $AgBiS_2$ was being carried out through spray pyrolysis (Hu L. et al., 2018; Pai et al., 2018) and the slow cooling method has been used to grow a single crystal of $AgBiS_2$ successfully as reported by Nakamura et al., (2015). The stoichiometric composition of the $AgBiS_2$ was found to be equivalent to the congruent melt composition as shown by XRD measurement and composition analysis. The pattern obtained from Laue X-ray backscattering has proved that the grown $AgBiS_2$ crystal was a single crystal. Analysis results from DTA indicated that $AgBiS_2$ melts at 805 °C. The grown crystal by this group showed hole mobility of 1.1 cm^2/V s, the electrical resistivity of 2.1 Ω cm, a carrier concentration of 2.6×10^{18} cm^{-3} and n-type conductivity at room temperature (Nakamura et al., 2015).

$AgBiS_2$ fabricated at low temperature was used as light sensitive solar cells due to their good photocatalytic efficiency and good absorption coefficient (10^5) (van Embden and Della

Gaspera, 2019). In a similar research, $AgBiS_2$ synthesized at 550°C from bismuth sulphide and silver sulphide in an ampoule made from pyrex. Its photo electrochemical properties were studied under illumination and in the dark (Bellal et al., 2017). Embden and Della (2019)., prepared silver bismuth sulphide and investigated its photocatalytic performance by measuring light-conducting ability of electrodes used for solar cell design. Silver bismuth sulphide-titanium oxide composite was used for several photocatalytic applications by Ganguly et al., (2019). This composite photocatalyst showed 95% doxycycline degradation within 3 h. It also displayed 3-log removal of two bacteria strains (*S. aureus* and *E.coli*). Finally, the photocatalyst was reported to be enhanced by 1000 times for hydrogen generation via water splitting (Ganguly et al., 2019).

2.3.3 *Indium bismuth sulphide ($InBiS_3$)*

One of the photocatalytic applications involving the use of indium bismuth sulphide is in the fabrication of solar cells (Ali et al., 2018). In-BiS_3 was found to be suitable for this application due to high optical coefficient of absorption (around 10^5 cm^{-1}) coupled with change in electrical resistivity and band gap energy as the temperature varied under visible light (Ali et al., 2018). In a similar investigation, Daraz et al., (2019), synthesized composite of $InBiS_3$-In_2S_3-Bi_2S_3 through the mixture of thiocyanate-based precursors of bismuth and indium dispersed in the mixture of chloroform and toluene. The synthesized nanocomposite was investigated for photocurrent generation, which is a light-based application.

2.3.4 *Bismuth sulphur iodide ($Bi_{13}S_{18}I_2$)*

This compound could be produced with the reaction of flux mixture of iodine/sulphur and bismuth ion (Groom et al., 2017). Raman spectroscopy and thermal decomposition studies showed the formation of this compound. The optical bandgap was later determined to be 0.3 eV by optical reflectance study and electronic structure calculation (Groom et al., 2017). Xu et al., (2006) reported 1.8 eV as the bandgap obtained from UV-Vis-NIR spectra which was clearly different from the band gap energy derived from the electronic structure calculation. Typically, a hydrothermal process was used to synthesize iodine bismuth sulphide where I_2, $(NH_2)_2CS$ and $BiCl_3$, were reacted at high temperature and thereafter double washed with deionized water (Su et al., 2006). Bismuth sulphur iodide has been used to boost the photo voltage of the solar cells. The presence of iodide and sulphide in this material led to a spike in the value of photocurrent (Kazyrevich et al., 2019). Thin film of $Bi_{13}S_{18}I_2$ microrod was also

investigated for photo-electrochemical solar cell applications and it was found to be appropriate even over a wide temperature variation (Hahn et al., 2012). In addition, Bismuth sulphur iodide and bismuth selenide iodide were investigated for photovoltaic application due to their good solar absorbing capacities (Hahn et al., 2012). $Bi_{13}S_{18}I_2$ has been loaded on nanotube along with BiOI and used as visible light photocatalyst to degrade more than 90% of malachite green dyes (Bargozideh et al., 2020). $Bi_{13}S_{18}I_2/MoS_2$ was used to destroy crystal violet dyes in the presence of visible light with a better performance than when neat molybdenium sulphide and neat bismuth sulphur iodide was used (Bargozideh and Tasviri, 2018).

2.3.*5 Zinc bismuth sulphide ($Zn_xBi_2S_{3+x}$)*

$Zn_xBi_2S_{3+x}$ is ternary nanoparticle composed of zinc, bismuth and Sulphur. It was used to form a shell structure with WO_3 photo electrode and thereafter utilized for the photocatalytic generation of hydrogen gas. This photocatalyst was found to display high hydrogen evolution efficiency during photo-electrochemical process, and its photo activity was better than the material synthesized with WO_3 and Bi_2S_3 only (Liu et al., 2015).

2.3.6 Antimony bismuth sulphide

One of the phases of antimony bismuth sulphide that was reported for photocatalytic application is $Bi_{1.09}Sb_{0.91}S_3$. Patra et al., (2017) reported $Bi_{1.09}Sb_{0.91}S_3$ nanotube synthesized from trivalent antimony and trivalent bismuth precursors. The synthesized photocatalyst was transformed to nanorod by a facile crystal growth mechanism known as chemical filling. The resultant nanorod composite was utilized to photo-electrocatalytically split water. The rate of water splitting was enhanced by doping $Bi_{1.09}Sb_{0.91}S_3$ with gold (Patra et al., 2017). In a related study, $Bi_{0.536}Sb_{1.464}S_3$ nanorod was used under visible light radiation to destroy rhodamine B dyes (Dashairya et al., 2020). Other phases that were fabricated were $Bi_{1.68}Sb_{0.32}S_3$ and $Bi_{1.09}Sb_{0.91}S_3$. Similar photocatalytic performance was reported for both catalysts in the degradation of Rhodamine under the same operating condition. As confirmed by Differential Reflectance Spectroscopy, they all have band gap energies around 2.3 eV (Dashairya et al., 2020).

2.3.7 *Alkali metal bismuth sulphide* (*$MBiS_2$ (M = Li, Na, K))*

Based on experimental results, the lattice crystal structure of $MBIS_2$ was discovered to resemble the lattice crystal structure of NaCl with M occupying sodium sub lattice in NaCl and sulphur occupying chlorine sub-lattice. Different environments for each atom arise from ions alternation in the sub lattice of the cation (Gabrel'yan et al., 2008). Apart from $LiBiS_2$, Nakhal et al., (2016) reported $LiBi_3S_5$ as another phase of lithium bismuth sulphide. Lithium NMR relaxometry and topological analyses of this other phase of lithium bismuth sulphide showed that the diffusion of lithium ion takes place along the b direction channel with 0.662 eV activation energy (Nakhal et al., 2016).

2.3.8 *Sodium bismuth sulphide ($NaBiS_2$)*

One of the reported methods for the synthesis of $NaBiS_2$ is the alkaline-conditioned hydrothermal method. Its nanosheet usually has atomic configuration on its surface, which may also include nano-domain that is amorphous and amorphous clusters when analysed with high-resolution transmission electron microscopy (Wang et al., 2020a). It has a direct band gap of 1.32 eV and an indirect band gap of 1.02 eV. Wang et al., (2020a) used this bismuth ternary to destroy methyl blue dyes in the presence of UV light. About 99.6% of the dye was degraded after 1 h 20 min of continuous light irradiation. In addition, $NaBiS_2$ has also found use as photovoltaic and has been used to photocatalytically generate hydrogen through water splitting (BaQais et al., 2019).

2.4 Heavy metal ions reduction using functionalized graphitic carbon nitride

Photoreduction of heavy metal ions have been carried out by using g-C_3N_4 –containing photocatalyst. Approximately 90% rhodamine B and 85% Cr(VI) have been simultaneously removed from water using photocatalysts made from g-C_3N_4 and red phosphorus by Liu et al., (2019). This photocatalyst remains active even after it has been utilized for four runs of reactions. Similarly, photocatalyst made from the g-C_3N_4 nanosheet, Bi_4O_7 and Ag has been reported, and was used to successfully reduced hexavalent chromium to trivalent chromium under visible light. The good charge separation that resulted in better photocatalytic performance was attributed to the presence of g-C_3N_4 (Ye, 2019). Photocatalytic removal of Cr(VI) and As(III) has been successfully carried out using pyromellitic diimide-doped g-C_3N_4 as photocatalyst (Wang et al., 2019). This was achieved with the use of visible light and addition of hydrogen peroxide. Removal of hexavalent chromium took place by reduction while trivalent arsenic removal took

place by oxidation to pentavalent arsenic. Photogenerated electrons, superoxide radical, effected this synergistic removal and photogenerated holes (Wang et al., 2019). Formate anion coupled with g-C_3N_4 has been used to photocatalytically reduce Cr(VI) to Cr(III) (Dong and Zhang, 2013). Also, oxidation of sulfisoxazole and photoreduction of hexavalent chromium has been jointly achieved (Song et al., 2019). Finally, g-C_3N_4 synthesized from urea via solvent treatment has been used to remove highly potent cancer-causing Cr(VI) from an aqueous solution in the presence of light (Hu et al., 2019). The most studied ion is hexavalent chromium, and some reported studies involving the reduction of hexavalent chromium to trivalent species using g-C_3N_4 as photocatalyst are shown in Table 2.3.

Table 2.3: Photocatalytic reduction of chromium(VI) by using g-C_3N_4-based photocatalysts.

Photocatalysts	Fabrication method	Heavy metal ions reduced	Light used	Performance	Ref.
CeO_2/g-C_3N_4/V_2O_5 heterojunction	simple hydrothermal	Cr(VI)	infra-red and visible light	99% reduced within 1h 40 mins	(Kumar et al., 2020)
CoS_2/g-C_3N_4-rGO	one-pot solvothermal	Cr(VI)	visible light	99.8% reduction of Cr(VI) in 2h	(Wang et al., 2020c)
g-C_3N_4/UiO-66	ball-milling	Cr(VI)	white light irradiation	Better than neat g-C_3N_4 and UiO-66	(Ma et al., 2019)
Nanosheets of Ag/Bi_4O_7/g-C_3N_4	-	Cr(VI)	visible light	Better than pure g-C_3N_4	(Ye et al., 2018)
g-C_3N_4/graphene oxide sheets	-	Cr(VI)	visible light	Complete removal in 1.5h	(Hu et al., 2018)

2.5 Photocatalytic degradation of both organic and heavy metals pollutants from water

Photocatalysts are light-sensitive semiconductors that possess band gap where no energy levels are present. When the semiconductor absorbs photon (ultraviolet or visible light), an electron (e^-) is excited from the valence band to the conduction band, provided that the energy of the

photon is more than or equal to the bandgap energy of the photocatalyst (Cao et al., 2015). Positively charged holes (h^+) are also known as electron vacancies, and they are simultaneously generated in the valence band. The pair of holes and the electron generated may recombine and generate heat energy (Bhatkhande, 2011) or a redox reaction may occur with both heavy metals and organic contaminants at once. The second phenomenon leads to the mineralization of the organics and transformation of heavy metal ions to less harmful products. Furthermore, hydroxyl radical could also be generated from the interaction of water with a hole (Kabra et al., 2004). In a similar manner, superoxide may be formed as a result of interaction of oxygen with the generated electron. These reactive oxygen species (hydroxyl radicals and superoxide radicals) also destroy the organic pollutants (Kabra et al., 2004). The mechanism of the entire process is illustrated in Figure 2.11. Some of the parameters that affect the photocatalytic process are pH, size and structure of the photocatalysts, surface area of the photocatalysts, reaction temperature, initial pollutants concentration, nature of pollutants, dopants used on photocatalysts, light intensity, light source, irradiation time and the dose of photocatalysts used (Topare and Patil, 2013; Kumar A and G., 2017; Danyliuk et al., 2020).

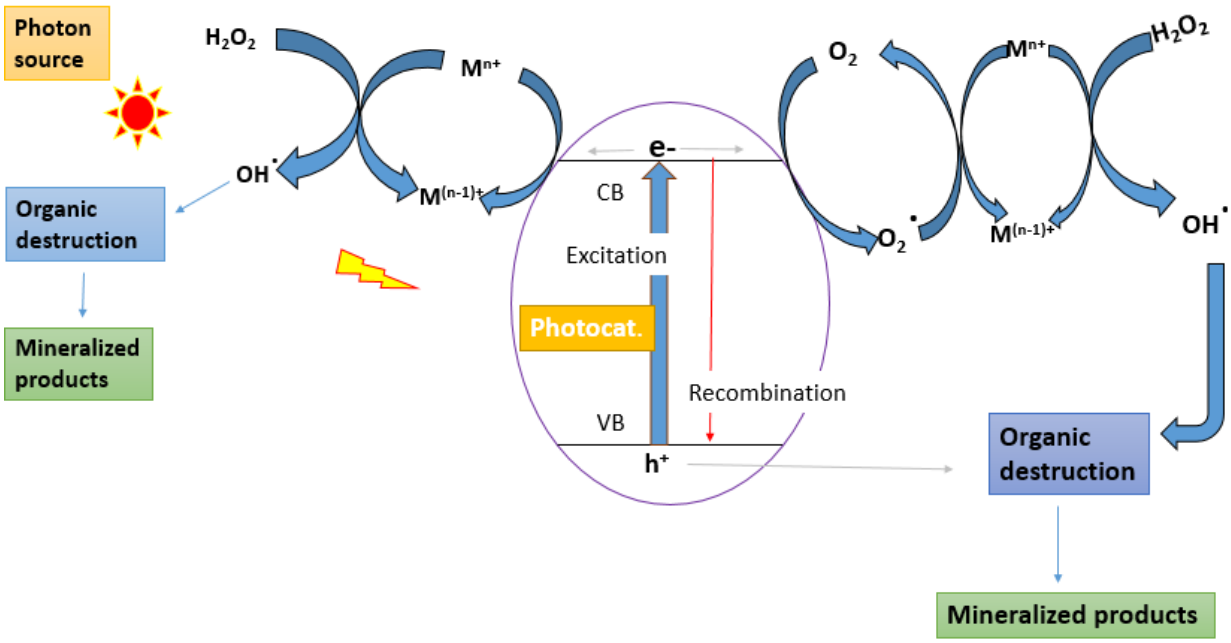

Figure 2. 11: Mechanism of photocatalysis for joint organic and heavy metals removal.

Simultaneous removal of heavy metal ions in the presence of organic compounds has been demonstrated to be better than the removal of the metal ions alone through the use of photocatalysts. Reduction of chromium (VI) to Cr(III) in the presence of humic acid using

titanium oxide as a photocatalyst was reported by Yang et al., (2006b). The photocatalytic efficiency of the titanium oxide was reported to increase with increase in the amount of humic acid. An increase in the pH level enhanced the removal of the humic acid but reduced the photoreduction of chromium(VI) to chromium(III). The increase in photocatalyst dosage also increased the removal efficiencies of both humic acid and the heavy metal ions (Yang and Lee, 2006a). The study suggests that simultaneous removal of toxic organic pollutants and heavy metal ions is feasible. Several studies have reported the removal of hexavalent chromium along with different organic contaminants. Some of the studies on the simultaneous removal of organic and heavy metals pollutants using photocatalysts are shown in Table 2.4. The organics mostly removed with heavy metals are pesticides, dyes, drugs and phenol.

Table 2.4: Photocatalytic removal of organic pollutants and heavy metals

Method	**Photocatalyst used**	**Organic pollutant**	**Heavy metal**	**Light used**	**Organic removal technique**	**Heavy metals removal technique**	**Ref.**
Photocatalysis	g-C_3N_4	2,4,6-trichlorophenol	Cr(VI)	Visible	Oxidation	Reduction	(Hu et al., 2014)
Photocatalysis (assisted by adsorption)	TiO_2-fly ash composite	Methylene blue and surfactants	Cu(II)	UV and Visible	Oxidation	Reduction	(Visa et al., 2016)
Photocatalysis	TiO_2	Luranzol S Kong dye	Cr(VI)	UV	Oxidation	Reduction	(Schrank et al., 2002)
Photocatalysis	TiO_2 doped with both nitrogen and Fluorine	Benzoic acid	Cr(VI)	Visible	Oxidation	Reduction	Giannakas et al., 2016)
Photocatalysis	TiO_2 doped with gold nanoparticles	Methylene blue	Cr(VI)	UV	Oxidation	Reduction	(A. Pandikumar and R. Ramaraj, 2012)

Photocatalysis	TiO_2 functionalized with metal deposits	Methylene blue	Cr(VI)	UV	Reduction	Reduction	(Batool et al., 2014b)
Photocatalysis	TiO_2	Di-n-butyl phthalate	Cr(VI)	UV	-	Reduction	(Batool et al., 2014a)
Photocatalysis	TiO_2	Salicyclic acid	Cr(VI)	UV	Oxidation	Reduction	(Wang and I. M. C. Lo, 2009)
Photocatalysis	TiO_2 sensitized with polymer	Phenol	Cr(VI)	UV	Oxidation	Reduction	(Batool et al., 2014a)
Photocatalysis	TiO_2	Acid Orange 20	Cr(VI)	UV	Reduction	Reduction	(Batool et al., 2014a)
Photocatalysis	TiO_2	Acid orange 7	Cr(VI)	UV	Reduction	Reduction	(H. Kyung et al., 2005)
Photocatalysis	Nanotube of TiO_2 functionalized with gold	Acid Orange 7	Cr(VI)	Visible	Oxidation	Reduction	(H. Kyung et al., 2005)

2.5.1 *Photocatalytic reduction of pesticides and heavy metals from water using various catalysts*

Photocatalytic reduction of hexavalent chromium using g-C_3N_4 photocatalyst with the simultaneous destruction of toxic organochlorine (2, 4, 6-trichlorophenol) under visible light has been reported (Swenson and Stadie, 2019). The effects of different kinetic parameters such as the pH, dissolved oxygen and initial concentrations of pollutants were studied (Hu et al., 2014). The presence of oxygen significantly enhanced the dual removal process of organochlorine and heavy metals. In addition, there was a synergistic reduction-oxidation reaction mechanism during the joint removal process (Hu et al., 2014). Nanosheet of ultrathin graphitic carbon nitride doped with phosphorus displayed enhanced photoreduction for hexavalent chromium and simultaneous degradation of toxic pesticides (2,4-dichlorophenol). The phosphorus doping and the nanosheet pore structure extended the region of visible light and affected the number of active sites respectively, which resulted in a better photocatalytic

reaction process. In addition, dissolved oxygen and low pH promoted the oxidation of the pesticide and at the same time reduced heavy metal ions (Deng et al., 2017).

2.5.2 *Photocatalytic reduction of dyes and heavy metals from water using various catalysts*

Titanium oxide incorporated into fly ash has been used as a photocatalyst for the reduction of copper(II) ions, dodecyl benzenesulfonate surfactants and methylene blue dye (Visa et al., 2016). Shrank et al., (2002) treated tannery wastewater by photocatalytically degrading Luranzol S Kong dye and at the same time photoreduced chromium(VI). The concentration of both pollutants and the pH significantly influenced the rate of photocatalysis under UV light. Synergistic effect was more noticed in the photocatalytic performance than the removal of a single contaminant.

2.5.3 *Photocatalytic reduction of pharmaceutical contaminants and heavy metals from water using various catalysts*

A z-scheme ternary heterojunction system of $BiVO_4$/AgBr/Ag photocatalyst was used to remove both ciprofloxacin and chromium(VI) under visible light. The electron spin resonance measurement showed that hydroxyl radical, peroxyl ion radical and the hole influenced the degradation of ciprofloxacin. However, peroxyl ion radicals and electrons are involved in the photoreduction of chromium(VI) (Chen et al., 2018a). Both pentavalent and trivalent form of arsenics were removed along with ibuprofen by Di et al.(2017a). The photocatalyst used was a mixed metal oxide of zinc and iron. All the ibuprofen was completely degraded after 12 h and the total concentration of arsenic dropped significantly from 1000 to 1.61 $\mu g \cdot L^{-1}$ (Di et al., 2017a). In a similar study, Ibuprofen was photocatalytic destroyed from polluted water using titanate and zinc oxide under UV light and solar radiation. The degradation performance was observed to be better under solar irradiation at pH of 7 (Tanveer et al., 2019).

2.5.4 *Photocatalytic reduction of phenol and heavy metals from water using various catalysts*

Phenol is a benzene-containing compound, and apart from glycosyl, the benzene ring is the next expanded chemical species that naturally occurs (Bayat et al., 2019). The chemical and physical stability of benzene compounds (including phenol) can be attributed to the properties of the π orbitals in the benzene ring. The stability property can be utilized in the fabrication of

chemical materials without considering its possible environmental impact when it finds its way to the surface water. The quantity of phenol and other aromatics that are discharged into the environment is increasing geometrically (Bayat et al., 2019). Photocatalysis was considered as an option to remove phenol and heavy metals from wastewater.

Titanium oxide sensitized with polymer (poly (fluoro-co-thiophene)) has been utilized for the oxidation of phenol and reduction of hexavalent chromium under visible light. The polymer functioned as both sensitizer and electron donor for hexavalent chromium because the electrons in the polymer migrated to the conduction band of titanium oxide. A synergistic effect exists due to the combined removal of phenol and the heavy metal ions from the wastewater (Qiu et al., 2012). These pollutants have also been removed from water using bismuth oxide, where both phenol oxidation and chromium reduction occurred simultaneously on the different crystal surfaces in the presence of light (Yu et al., 2018).

REFERENCES

Pandikumar, R. Ramaraj, 2012. Titanium dioxide-gold nanocomposite materialsembedded in silicate sol-gel filmcatalyst for simultaneous photodegradation of hexavalentchromium and methylene blue. Journal of Hazardous Materials, vol. 203-204, pp. 244–250, 2012. 203-204, 244-250.

Adeyemi, J.O., Onwudiwe, D.C., 2020. Chemistry and Some Biological Potential of Bismuth and Antimony Dithiocarbamate Complexes. Molecules 25, 305.

Ajiboye, T.O., Oyewo, O.A., Onwudiwe, D.C., 2021. The performance of bismuth-based compounds in photocatalytic applications. Surfaces and Interfaces 23, 100927.

Akhundi, A., Habibi-Yangjeh, A., Abitorabi, M., Rahim Pouran, S., 2019. Review on photocatalytic conversion of carbon dioxide to value-added compounds and renewable fuels by graphitic carbon nitride-based photocatalysts. Catalysis Reviews 61, 595-628.

Ali, N., Hussain, A., Ahmed, R., Omar, M.F.B., Sultan, M., Fu, Y.Q., 2018. Crystallized InBiS3 thin films with enhanced optoelectronic properties. Applied Surface Science 436, 293-301.

BaQais, A., Tymińska, N., Le Bahers, T., Takanabe, K., 2019. Optoelectronic Structure and Photocatalytic Applications of $Na(Bi,La)S_2$ Solid Solutions with Tunable Band Gaps. Chemistry of Materials 31, 3211-3220.

Bargozideh, S., Tasviri, M., 2018. Construction of novel $BiSI/MoS_2$ nanocomposite with enhanced visible-light driven photocatalytic performance. New Journal of Chemistry 42.

Bargozideh, S., Tasviri, M., Ghabraei, M., 2020. Effect of carbon nanotubes loading on the photocatalytic activity of BiSI/BiOI as a novel photocatalyst. Environmental Science and Pollution Research, 1-11.

Batool, S., Akib, S., Ahmad, M., Balkhair, K.S., Ashraf, M.A., 2014a. Study of Modern Nano Enhanced Techniques for Removal of Dyes and Metals. Journal of Nanomaterials 2014, 1-20.

Bayat, M., Tehrani, M.S., Kobarfard, F., Husain, S.W., Yazdanpanah, H., 2019. Validation of an Analytical Method for Simultaneous Determination of 18 Persistent Organic Pollutants in Trout Using LLE Extraction and GC-MS/MS. Iran J Pharm Res 18, 1224-1238.

Bellal, B., Berger, M.H., Trari, M., 2017. Physical and photoelectrochemical properties of spherical nanoparticles of α-$AgBiS_2$. Journal of Solid State Chemistry 254, 178-183.

Cates, N., Bernechea, M., 2018. Research Update: Bismuth based materials for photovoltaics. APL Materials 6, 084503.

Bhatkhande, D.S., Pangarkar, V.G., Beenackers, AA. , 2011. Photocatalytic degradation for environmental applications:a review. J. Chem. Tech. Bio. 77, 102-116.

Cao, S., Low, J., Yu, J., Jaroniec, M., 2015. Polymeric photocatalysts based on graphitic carbon nitride. Adv Mater 27, 2150-2176.

Chakraborty, M., Thangavel, R., Komninou, P., Zhou, Z., Gupta, A., 2019. Nanospheres and nanoflowers of copper bismuth sulphide (Cu_3BiS_3): Colloidal synthesis, structural, optical and electrical characterization. Journal of Alloys and Compounds 776, 142-148.

Chan, M.-H., Liu, R.-S., Hsiao, M., 2019. Graphitic carbon nitride-based nanocomposites and their biological applications: a review. Nanoscale 11, 14993-15003.

Chan, M., Liu, R., Hsiao, M., 2019. Graphitic carbon nitride-based nanocomposites and their biological applications: a review. Nanoscale, 11, 14993.

Chen, F., Yang, Q., Wang, Y., Yao, F., Ma, Y., Huang, X., Li, X., Wang, D., Zeng, G., Yu, H., 2018a. Efficient construction of bismuth vanadate-based Z-scheme photocatalyst for simultaneous Cr(VI) reduction and ciprofloxacin oxidation under visible light: Kinetics, degradation pathways and mechanism. Chemical Engineering Journal 348, 157-170.

Chen, N., Zhong, X., Li, P., Xu, J., 2015. A Mild Radical Method for the Dimerzation of Dithiocarbamates. European Journal of Organic Chemistry 2015, 802-809.

Chen, Z., Fan, T.-T., Yu, X., Wu, Q.-L., Zhu, Q.-H., Zhang, L.-Z., Li, J.-H., Fang, W.-P., Yi, X.-D., 2018b. Gradual carbon doping of graphitic carbon nitride towards metal-free visible light photocatalytic hydrogen evolution. Journal of Materials Chemistry A 6, 15310-15319.

Chi Zhang, Y.L., Danmeng Shuai, Yun Shen, Wei Xiong, Linqiong Wang,, 2018. Graphitic carbon nitride (g-C_3N_4)-based photocatalysts for water disinfection and microbial control: A review, . j.chemosphere.

Cohen, M.L., 1985. Calculation of bulk moduli of diamond and zinc-blende solids. Physical Review B 32, 7988-7991.

Cui, L., Liu, Y., Fang, X., Yin, C., Li, S., Sun, D., Kang, S., 2018. Scalable and clean exfoliation of graphitic carbon nitride in NaClO solution: enriched surface active sites for enhanced photocatalytic H2 evolution. Green Chemistry 20, 1354-1361.

Cui, Y., Tang, Y., Wang, X., 2015. Template-free synthesis of graphitic carbon nitride hollow spheres for photocatalytic degradation of organic pollutants. Materials Letters 161, 197-200.

Cvek, B., Dvorak, Z., 2007. Targeting of nuclear factor-κB and proteasome by dithiocarbamate complexes with metals. Current pharmaceutical design 13, 3155-3167.

Danyliuk, N.V., Tatarchuk, T.R., Shyichuk, A.V., 2020. Batch microreactor for photocatalytic reactions monitoring. Physics and Chemistry of Solid State 21, 338-346.

Daraz, U., Ansari, T.M., Arain, S.A., Mansoor, M.A., Mazhar, M., 2019. Study of solvent effect on structural and photoconductive behavior of ternary chalcogenides $InBiS_3$-In_2S_3-Bi_2S_3 composite thin films deposited via AACVD . Main Group Metal Chemistry. 42, 102.

Dashairya, L., Mehta, A., Saha, P., Basu, S., 2020. Visible-light-induced enhanced photocatalytic degradation of Rhodamine-B dye using $BixSb_2$-xS_3 solid-solution photocatalysts. Journal of Colloid and Interface Science 561, 71-82.

Deng, Y., Tang, L., Zeng, G., Zhu, Z., Yan, M., Zhou, Y., Wang, J., Liu, Y., Wang, J., 2017. Insight into highly efficient simultaneous photocatalytic removal of Cr(VI) and 2,4-diclorophenol under visible light irradiation by phosphorus doped porous ultrathin g-C_3N_4 nanosheets from aqueous media: Performance and reaction mechanism. Applied Catalysis B: Environmental 203, 343-354.

Deshmukh S.G. and V.Kheraj, 2017. "A comprehensive review on synthesis and characterizations of Cu_3BiS_3 thinfilmsforsolar photovoltaics,". Nanotechnol. Environ. Eng.2.

Di, G., Zhu, Z., Zhang, H., Zhu, J., Lu, H., Zhang, W., Qiu, Y., Zhu, L., Küppers, S., 2017a. Simultaneous removal of several pharmaceuticals and arsenic on Zn-Fe mixed metal oxides: Combination of photocatalysis and adsorption. Chemical Engineering Journal 328.

Di, T., Zhu, B., Cheng, B., Yu, J., Xu, J., 2017b. A direct Z-scheme g-C_3N_4/SnS_2 photocatalyst with superior visible-light CO_2 reduction performance. Journal of Catalysis 352, 532-541.

Dong, F., Zhao, Z., Sun, Y., Zhang, Y., Yan, S., Wu, Z., 2015. An Advanced Semimetal–Organic Bi Spheres–g-C_3N_4 Nanohybrid with SPR-Enhanced Visible-Light Photocatalytic Performance for NO Purification. Environmental Science & Technology 49, 12432-12440.

Dong, F., Zhao, Z., Xiong, T., Ni, Z., Zhang, W., Sun, Y., Ho, W.-K., 2013. In Situ Construction of g-C_3N_4/g-C_3N_4 Metal-Free Heterojunction for Enhanced Visible-Light Photocatalysis. ACS Applied Materials & Interfaces 5, 11392-11401.

Dong, G., Zhang, L., 2013. Synthesis and Enhanced Cr(VI) Photoreduction Property of Formate Anion Containing Graphitic Carbon Nitride. The Journal of Physical Chemistry C 117, 4062-4068.

Dong, Z., Jiang, T., Xu, B., Li, Q., Zhong, H., Yang, Y., 2021. Selective flotation of galena using a novel collector S-benzyl-N-ethoxycarbonyl thiocarbamate: An experimental and theoretical investigation. Journal of Molecular Liquids 330.

Duran-García, E.I., Martínez-Santana, J., Torres-Gómez, N., Vilchis-Nestor, A.R., García-Orozco, I., 2021. Copper sulfide nanoparticles produced by the reaction of N-

alkyldithiocarbamatecopper(II) complexes with sodium borohydride. Materials Chemistry and Physics 269.

Horvath-Bordon, R.R., P. F. McMillan, P. Kroll, G. Miehe, P. A. van Aken, A. Zerr, P. Hoppe, O. Shebanova, I. McLaren, S. Lauterbach, E. Kroke, R. Boehler, , 2007. Angew. Chem. Int. Ed 46, 1476-1480.

Ejelonu, B.C., Olagboye, S.A., Oyeneyin, O.E., Ebiesuwa, O.A., Bada, O.E., 2018. Synthesis, characterization and antimicrobial activities of sulfadiazine Schiff base and phenyl dithiocarbamate mixed ligand metal complexes. Open Journal of Applied Sciences 8, 346.

Elshafie, M., Younis, S.A., Serp, P., Gad, E.A.M., 2020. Preparation characterization and non-isothermal decomposition kinetics of different carbon nitride sheets. Egyptian Journal of Petroleum 29, 21-29.

Eswari, S., Selvaganapathi, P., Thirumaran, S., Ciattini, S., 2021. Effect of solvent used for crystallization on structure: Synthesis and characterization of bis(N,N-di(4-fluorobenzyl)dithiocarbamato-S,S′)M(II) (M = Cd, Hg) and usage as precursor for CdS nanophotocatalyst. Polyhedron 206, 115330.

Fomenko, I.S., Gushchin, A.L., Nadolinny, V.A., Efimov, N.N., Laricheva, Y.A., Sokolov, M.N., 2018. Dinuclear Vanadium Sulfide Clusters: Synthesis, Redox Behavior, and Magnetic Properties. 2018, 2965-2971.

Franklin, E.C., 1922. The Ammono Carbonic Acids. Journal of the American Chemical Society 44, 486-509.

Fukasawa, Y., Takanabe, K., Shimojima, A., Antonietti, M., Domen, K., Okubo, T., 2011. Synthesis of ordered porous graphitic-C_3N_4 and regularly arranged Ta_3N_5 nanoparticles by using self-assembled silica nanospheres as a primary template. Chemistry, an Asian journal 6, 103-109.

Gabrel'yan, B.V., Lavrentiev, A.A., Nikiforov, I.Y., Sobolev, V.V., 2008. Electronic energy structure of $MBiS_2$ (M = Li, Na, K) calculated with allowance for the difference between the M-S and Bi-S bond lengths. Journal of Structural Chemistry 49, 788-794.

Galiyeva, P., Rinnert, H., Balan, L., Alem, H., Medjahdi, G., Uralbekov, B., Schneider, R., 2021. Single-source precursor synthesis of quinary AgInGaZnS QDs with tunable photoluminescence emission. Applied Surface Science 562, 150143.

Ganguly, P., Mathew, S., Clarizia, L., Kumar R, S., Akande, A., Hinder, S., Breen, A., Pillai, S.C., 2019. Theoretical and experimental investigation of visible light responsive $AgBiS_2$-TiO_2 heterojunctions for enhanced photocatalytic applications. Applied Catalysis B: Environmental 253, 401-418.

Gao, J., Wang, J., Qian, X., Dong, Y., Xu, H., Song, R., Yan, C., Zhu, H., Zhong, Q., Qian, G., Yao, J., 2015. One-pot synthesis of copper-doped graphitic carbon nitride nanosheet by heating Cu–melamine supramolecular network and its enhanced visible-light-driven photocatalysis. Journal of Solid State Chemistry 228, 60-64.

Giannakas, A.E., Antonopoulou, M., Daikopoulos, C., Deligiannakis, Y., Konstantinou, I., 2016. Characterization and catalytic performance of B-doped, B–N co-doped and B–N–F tri-doped TiO_2 towards simultaneous Cr(VI) reduction and benzoic acid oxidation. Applied Catalysis B: Environmental 184, 44-54.

Gmelin, L.A.P., 1835. Ueber einige Verbindungen des Melon's. 15, 252-258.

Goettmann, F., Fischer, A., Antonietti, M., Thomas, A., 2006. Chemical Synthesis of Mesoporous Carbon Nitrides Using Hard Templates and Their Use as a Metal-Free Catalyst for Friedel–Crafts Reaction of Benzene. 45, 4467-4471.

Groom, R., Jacobs, A., Cepeda, M., Drummey, R., Latturner, S.E., 2017. Bi13S18I2: (Re)discovery of a Subvalent Bismuth Compound Featuring [Bi2]4+ Dimers Grown in Sulfur/Iodine Flux Mixtures. Chemistry of Materials 29, 3314-3323.

Gu, Q., Liao, Y., Yin, L., Long, J., Wang, X., Xue, C., 2015. Template-free synthesis of porous graphitic carbon nitride microspheres for enhanced photocatalytic hydrogen generation with high stability. Applied Catalysis B: Environmental 165, 503-510.

H. Kyung, J. Lee, W. Choi, 2005. Simultaneous and synergistic conversion of dyes and heavy metal ions in aqueous TiO_2 suspensions under visible-light illumination. EnvironmentalScience and Technology 39, 2376-2382.

Hahn, N., Self, J., Mullins, C., 2012. BiSI Micro-Rod Thin Films: Efficient Solar Absorber Electrodes? The Journal of Physical Chemistry Letters 3, 1571-1576.

Hao, Q., Jia, G., Wei, W., Vinu, A., Wang, Y., Arandiyan, H., Ni, B.-J., 2020. Graphitic carbon nitride with different dimensionalities for energy and environmental applications. Nano Research 13, 18-37.

Hosmane, R.S., Rossman, M.A., Leonard, N.J., 1982. Synthesis and Structure of Tri-s-Triazine. J. Am. Chem. Soc. 104, 5497-5499.

Hu, C., Chu, Y.-C., Lin, Y.-R., Yang, H.-C., Wang, K.-H., 2019. Photocatalytic Dye and Cr((VI)) Degradation Using a Metal-Free Polymeric g-C_3N_4 Synthesized from Solvent-Treated Urea. Polymers (Basel) 11, 182.

Hu L. et al., 2018. “Enhanced optoelectronic performance in $AgBiS_2$ nanocrystals from an improved amine-based synthesis route,”. J. Mater. Chem. C 6, 731-737.

Hu, X., Ji, H., Chang, F., Luo, Y., 2014. Simultaneous photocatalytic Cr(VI) reduction and 2,4,6-TCP oxidation over g-C_3N_4 under visible light irradiation. Catalysis Today 224, 34-40.

Hu, X., Wang, W., Xie, G., Wang, H., Tan, X., Jin, Q., Zhou, D., Zhao, Y., 2018. Ternary assembly of g-C_3N_4/graphene oxide sheets /$BiFeO_3$ heterojunction with enhanced photoreduction of Cr(VI) under visible-light irradiation. Chemosphere 216.

Jiang, W.-x., Qi, J.-R., Liao, J.-s., Wan, Z.-l., Liang, W.-l., Huang, J.-y., Cao, Y., Xiao, J., Yang, X.-Q., 2020. Structural characterization of pectin-bismuth complexes and their

aggregation in acidic conditions. International Journal of Biological Macromolecules 154, 788-794.

Jin, Z., Zhang, Q., Chen, J., Huang, S., Hu, L., Zeng, Y.-J., Zhang, H., Ruan, S., Ohno, T., 2018. Hydrogen bonds in heterojunction photocatalysts for efficient charge transfer. Applied Catalysis B: Environmental 234, 198-205.

Jourshabani, M., Shariatinia, Z., Badiei, A., 2017. Controllable Synthesis of Mesoporous Sulfur-Doped Carbon Nitride Materials for Enhanced Visible Light Photocatalytic Degradation. Langmuir 33, 7062-7078.

Jürgens, B., Irran, E., Senker, J., Kroll, P., Müller, H., Schnick, W., 2003. Melem (2,5,8-Triamino-tri-s-triazine), an Important Intermediate during Condensation of Melamine Rings to Graphitic Carbon Nitride: Synthesis, Structure Determination by X-ray Powder Diffractometry, Solid-State NMR, and Theoretical Studies. Journal of the American Chemical Society 125, 10288-10300.

Kabra, K., Chaudhary, R., Sawhney, R.L., 2004. Treatment of Hazardous Organic and Inorganic Compounds through Aqueous-Phase Photocatalysis: A Review. Industrial & Engineering Chemistry Research 43, 7683-7696.

Kanchi, S., Singh, P., Bisetty, K., 2014. Dithiocarbamates as hazardous remediation agent: A critical review on progress in environmental chemistry for inorganic species studies of 20th century. Arabian Journal of Chemistry 7, 11-25.

Karen, V.G., Hernández-Gordillo, A., Oros-Ruiz, S., Rodil, S.E., 2020. Microparticles of α-Bi_2O_3 Obtained from Bismuth Basic Nitrate [$Bi_6O_6(OH)_2(NO_3)_4 \cdot 2H_2O$] with Photocatalytic Properties. Topics in Catalysis.

Kazyrevich, M., Ivashenka, D., Bondarenko, E., Streltsov, E., Kulak, A., 2019. Synthesis and photoelectrochemical properties of bismuth thioiodide. Proceedings of the National Academy of Sciences of Belarus, Chemical Series 54, 413-418.

Komatsu, T., 2001. Attempted chemical synthesis of graphite-like carbon nitride. Journal of Materials Chemistry 11, 799-801.

Kumar A, G., P., 2017. A review on the factors affecting the photocatalytic degradation of hazardous materials. Material Sci & Eng Int J. 1, 106-114.

Kumar, A., Sharma, S.K., Sharma, G., Naushad, M., Stadler, F.J., 2020. CeO_2/g-C_3N_4/V_2O_5 ternary nano hetero-structures decorated with CQDs for enhanced photo-reduction capabilities under different light sources: Dual Z-scheme mechanism. Journal of Alloys and Compounds 838, 155692.

Kumar, M., Persson, C., 2013. $CuSbS_2$ and $CuBiS_2$ as potential absorber materials for thin-film solar cells. Journal of Renewable and Sustainable Energy 5, 031616.

Kumar M and C. Persson, 2014. "Cu(Sb,Bi)$(S,Se)_2$ as indium-free absorber material with high optical efficiency,". EnergyProcedia 44, 176-183.

Kumar, M., Persson, C., 2013a. Cu_3BiS_3 as a potential photovoltaic absorber with high optical efficiency. Applied Physics Letters 102, 062109.

Kumar, S., Surendar, T., Kumar, B., Baruah, A., Shanker, V., 2014. Synthesis of highly efficient and recyclable visible-light responsive mesoporous g-C_3N_4 photocatalyst via facile template-free sonochemical route. RSC Adv. 4, 8132-8137.

Liebig, J., 1834. Uber Einige Stickstoff - Verbindungen. Ann. Pharm. 10, 1.

Lin, B., Chaturvedi, A., Di, J., You, L., Lai, C., Duan, R., Zhou, J., Xu, B., Chen, Z., Song, P., Peng, J., Ma, B., Liu, H., Meng, P., Yang, G., Zhang, H., Liu, Z., Liu, F., 2020. Ferroelectric-field accelerated charge transfer in 2D $CuInP_2S_6$ heterostructure for enhanced photocatalytic H_2 evolution. Nano Energy 76, 104972.

Lin, H.-P., Lee, W.-L., Lai, Y.-Y., Chen, J.-Y., Chen, Y.-Q., Fu, J.-Y., 2015. Synthesis of $SrFeO_3$-x/g-C_3N_4 heterojunction with improved visible-light photocatalytic activities in chloramphenicol and crystal violet degradation. RSC Adv. 6.

Liu, C., Yang, Y., Li, W., Li, J., Li, Y., Shi, Q., Chen, Q., 2015. Highly Efficient Photoelectrochemical Hydrogen Generation Using $Znx Bi_2 S_{3+x}$ Sensitized Platelike WO_3 Photoelectrodes. ACS Applied Materials & Interfaces 7, 10763-10770.

Liu, E., Du, Y., Bai, X., Fan, J., Hu, X., 2020. Synergistic improvement of Cr(VI) reduction and RhB degradation using RP/g-C_3N_4 photocatalyst under visible light irradiation. Arabian Journal of Chemistry 13, 3836-3848.

Liu, J., Wang, H., Antonietti, M., 2016. Graphitic carbon nitride "reloaded": emerging applications beyond (photo)catalysis. Chemical Society reviews 45, 2308-2326.

Lokhande, A.C., Babar, P.T., Karade, V.C., Gang, M.G., Lokhande, V.C., Lokhande, C.D., Kim, J.H., 2019. The versatility of copper tin sulfide. Journal of Materials Chemistry A 7, 17118-17182.

Long, B.L., J.; Wang, X. , 2014. Thermally-Induced Desulfurization and Conversion of Guanidine Thiocyanate into Graphitic Carbon Nitride Catalysts for Hydrogen Photosynthesis. J. Mater. Chem. 2, 2942−2951.

Lotsch, B.V., Schnick, W., 2007. New Light on an Old Story: Formation of Melam during Thermal Condensation of Melamine. 13, 4956-4968.

Lotsch, B.V.S., W. , 2005. Thermal Conversion of Guanylurea Dicyanamide into Graphitic Carbon Nitride via Prototype CNx Precursors. Chem. Mater. 17, 3976−3982.

Ma, S.-Q., Du, X.-D., Zhao, C., Fu, H., Wang, P., 2019. The facile fabrication of 2D/3D Z-scheme g-C_3N_4/UiO-66 heterojunction with enhanced photocatalytic Cr(VI) reduction performance under white light. Chemical Engineering Journal 375, 121944.

Maeda, K., Wang, X., Nishihara, Y., Lu, D., Antonietti, M., Domen, K., 2009. Photocatalytic Activities of Graphitic Carbon Nitride Powder for Water Reduction and Oxidation under Visible Light. The Journal of Physical Chemistry C 113, 4940-4947.

Mafa, P.J., Malefane, M.E., Idris, A.O., Liu, D., Gui, J., Mamba, B.B., Kuvarega, A.T., 2022. Multi-elemental doped g-C_3N_4 with enhanced visible light photocatalytic Activity: Insight into naproxen Degradation, Kinetics, effect of Electrolytes, and mechanism. Separation and Purification Technology 282, 120089

Mann, P.B., McGregor, I.J., Bourke, S., Burkitt-Gray, M., Fairclough, S., Ma, M.T., Hogarth, G., Thanou, M., Long, N., Green, M., 2019. An atom efficient, single-source precursor route to plasmonic CuS nanocrystals. Nanoscale Advances 1, 522-526.

Martin, D.J., Reardon, P.J.T., Moniz, S.J.A., Tang, J., 2014. Visible Light-Driven Pure Water Splitting by a Nature-Inspired Organic Semiconductor-Based System. Journal of the American Chemical Society 136, 12568-12571.

Masih D, M.Y., Rohani S., 2017. Graphitic C3N4 based noble-metal-free photocatalyst systems: A review. 2017; Applied Catalysis B: Environmental. 206, 556-588.

Maya, L., Cole, D.R., Hagaman, E.W., 1991. Carbon–Nitrogen Pyrolyzates: Attempted Preparation of Carbon Nitride. J. Am. Ceram. Soc. 74, 1686.

Miller, N.C., Bernechea, M., 2018. Research Update: Bismuth based materials for photovoltaics. APL Materials 6.

Mishra, A., Mehta, A., Basu, S., Shetti, N.P., Reddy, K.R., Aminabhavi, T.M., 2019. Graphitic carbon nitride (g–C_3N_4)–based metal-free photocatalysts for water splitting: A review. Carbon 149, 693-721.

Mlowe, S., Lewis, D.J., Malik, M.A., Raftery, J., Mubofu, E.B., O'Brien, P., Revaprasadu, N., 2016. Heterocyclic dithiocarbamato-iron(iii) complexes: single-source precursors for aerosol-assisted chemical vapour deposition (AACVD) of iron sulfide thin films. Dalton Transactions 45, 2647-2655.

Mourdikoudis, S., Liz-Marzán, L.M., 2013. Oleylamine in Nanoparticle Synthesis. Chemistry of Materials 25, 1465-1476.

Mousavi, M., Habibi-Yangjeh, A., Pouran, S.R., 2018. Review on magnetically separable graphitic carbon nitride-based nanocomposites as promising visible-light-driven photocatalysts. Journal of Materials Science: Materials in Electronics 29, 1719-1747.

Murtaza, G., Venkateswaran, S.P., Thomas, A.G., O'Brien, P., Lewis, D.J., 2018. Chemical vapour deposition of chromium-doped tungsten disulphide thin films on glass and steel substrates from molecular precursors. Journal of Materials Chemistry C 6, 9537-9544.

Nakamura, M., Nakamura, H., Ohsawa, T., Imura, M., Shimamura, K., Ohashi, N., 2015. $AgBiS_2$ single crystal grown using slow cooling method and its characterization. Journal of Crystal Growth 411, 1-3.

Nakhal, S., Wiedemann, D., Stanje, B., Dolotko, O., Wilkening, M., Lerch, M., 2016. $LiBi_3S_5$—A lithium bismuth sulfide with strong cation disorder. Journal of Solid State Chemistry 238, 60-67.

Nanomaterials, J., 2019. Corrigendum to "Study of Modern Nano Enhanced Techniques for Removal of Dyes and Metals". Journal of Nanomaterials 2019, 1-2.

Nemiwal, M., Zhang, T.C., Kumar, D., 2021. Recent progress in g-C_3N_4, TiO_2 and ZnO based photocatalysts for dye degradation: Strategies to improve photocatalytic activity. Science of The Total Environment 767, 144896

Niu, P., Zhang, L., Liu, G., Cheng, H.-M., 2012. Graphene-Like Carbon Nitride Nanosheets for Improved Photocatalytic Activities. 22, 4763-4770.

Olatunde, O.C., Onwudiwe, D.C., 2021a. Temperature Controlled Evolution of Pure Phase Cu_9S_5 Nanoparticles by Solvothermal Process. Frontiers in Materials 8.

Ong, W.-J.T., L.-L.; Chai, S.-P.; Yong, S.-T. , 2015. Graphene Oxide as a Structure-Directing Agent for the Two-Dimensional Interface Engineering of Sandwich-Like Graphene-g-C_3N_4 Hybrid Nanostructures with Enhanced Visible-Light Photoreduction of CO_2 to Methane. . Chem. Commun 51, 858-861.

Ong, W.J., Tan, L.L., Ng, Y.H., Yong, S.T., Chai, S.P., 2016. Graphitic Carbon Nitride (g-C_3N_4)-Based Photocatalysts for Artificial Photosynthesis and Environmental Remediation: Are We a Step Closer To Achieving Sustainability? Chem Rev 116, 7159-7329.

Ou, H., Lin, L., Zheng, Y., Yang, P., Fang, Y., Wang, X., 2017. Tri-s-triazine-based crystalline carbon nitride nanosheets for an improved hydrogen evolution. Advanced Materials 29, 1700008.

Paca, A.M., Ajibade, P.A., 2021. Bis-(N-ethylphenyldithiocarbamato)palladium(II) as molecular precursor for palladium sulfide nanoparticles. Journal of Molecular Structure 1243, 130777.

Pai et al., 2018. "Spray deposition of $AgBiS_2$ and Cu_3BiS_3 thin films for photovoltaic applications,". J. Mater. Chem. C6, 2483-2494.

Patra, B.K., Khilari, S., Bera, A., Mehetor, S.K., Pradhan, D., Pradhan, N., 2017. Chemically Filled and Au-Coupled $BiSbS_3$ Nanorod Heterostructures for Photoelectrocatalysis. Chemistry of Materials 29, 1116-1126.

Pauling, L., Sturdivant, J.H., 1937. The Structure of Cyameluric Acid, Hydromelonic Acid and Related Substances. Proc Natl Acad Sci U S A 23, 615-620.

Peng, L., Shen, S., Zhang, Y., Xu, H., Wang, Q., 2012. Controllable synthesis of MnS nanocrystals from a single-source precursor. Journal of Colloid and Interface Science 377, 13-17.

Prasad, C., Tang, H., Bahadur, I., 2019. Graphitic carbon nitride based ternary nanocomposites: From synthesis to their applications in photocatalysis: A recent review. Journal of Molecular Liquids 281, 634-654.

Qamar, M.A., Shahid, S., Javed, M., Sher, M., Iqbal, S., Bahadur, A., Li, D., 2021. Fabricated novel g-C_3N_4/Mn doped ZnO nanocomposite as highly active photocatalyst for the disinfection of pathogens and degradation of the organic pollutants from wastewater under sunlight radiations. Colloids and Surfaces A: Physicochemical and Engineering Aspects 611, 125863.

Qiu, R., Zhang, D., Diao, Z., Huang, X., He, C., Morel, J.-L., Xiong, Y., 2012. Visible light induced photocatalytic reduction of Cr(VI) over polymer-sensitized TiO_2 and its synergism with phenol oxidation. Water Research 46, 2299-2306.

Redemann, C.E., Lucas, H.J., 1940. Some Derivatives of Cyameluric Acid and Probable Structures of Melam, Melem and Melon. Journal of the American Chemical Society 62, 842-846.

S. C. Yan , Z. G. Zou , 2009. Langmuir 25, 10397.

Sarker, J.C., Hogarth, G., 2021. Dithiocarbamate Complexes as Single Source Precursors to Nanoscale Binary, Ternary and Quaternary Metal Sulfides. Chemical Reviews 121, 6057-6123.

Schrank, S.G., José, H.J., Moreira, R.F.P.M., 2002. Simultaneous photocatalytic Cr(VI) reduction and dye oxidation in a TiO_2 slurry reactor. Journal of Photochemistry and Photobiology A: Chemistry 147, 71-76.

Shahbazi, M.A., Faghfouri, L., Ferreira, M.P.A., Figueiredo, P., Maleki, H., Sefat, F., Hirvonen, J., Santos, H.A., 2020. The versatile biomedical applications of bismuth-based nanoparticles and composites: therapeutic, diagnostic, biosensing, and regenerative properties. Chemical Society reviews 49, 1253-1321.

Shi, L.L., L.; Wang, F.; Ma, J.; Sun, . 2014, 4, , 2014. Polycondensation of Guanidine Hydrochloride into a Graphitic Carbon Nitride Semiconductor with a Large Surface Area as a Visible Light Photocatalyst. J. Catal. Sci. Technol 4, 3235−3243.

Shinde, S.D., Sakla, A.P., Shankaraiah, N., 2020. An insight into medicinal attributes of dithiocarbamates: Bird's eye view. Bioorganic Chemistry 105, 104346.

Singh, P., Shandilya, P., Raizada, P., Sudhaik, A., Rahmani-Sani, A., Hosseini-Bandegharaei, A., 2020. Review on various strategies for enhancing photocatalytic activity of graphene based nanocomposites for water purification. Arabian Journal of Chemistry 13, 3498-3520.

Song, W., Ge, P., Ke, Q., Sun, Y., Chen, F., Wang, H., Shi, Y., Wu, X.-L., Lin, H., Chen, J., Shen, C., 2019. Insight into the mechanisms for hexavalent chromium reduction and sulfisoxazole degradation catalyzed by graphitic carbon nitride: The Yin and Yang in the photo-assisted processes. Chemosphere 221, 166-174.

Srinivasan, N., 2019. Fabrication and photocatalytic properties of Multi–Morphological CdS NSs prepared by the thermolysis of heterocyclic dithiocarbamate cadmium(II) complexes as precursors. Dyes and Pigments 162, 786-796.

Su, X., Zhang, G., Liu, T., Liu, Y., Qin, J., Chen, C., 2006. A facile and clean synthesis of pure bismuth sulfide iodide crystals. Russian Journal of Inorganic Chemistry - Russ J Inorg Chem 51, 1864-1868.

Tan, Y.S., Yeo, C.I., Tiekink, E.R.T., Heard, P.J., 2021. Dithiocarbamate Complexes of Platinum Group Metals: Structural Aspects and Applications. Inorganics 9, 60.

Tanabe, T., Osaki, J., Miyajima, M., Kitamura, K., Oyama, Y., 2021. Raman and TEM characterization of 2D layered MoS_2 crystals grown on non-metal surfaces by friction-induced synthesis. Applied Surface Science 561, 150016.

Tanveer, M., Guyer, G.T., Abbas, G., 2019. Photocatalytic degradation of ibuprofen in water using TiO_2 and ZnO under artificial UV and solar irradiation. Water environment research : a research publication of the Water Environment Federation 91, 822-829.

Teter, D., Hemley, R., 1996. Low-Compressibility Carbon Nitrides. Science 271, 53-55.

Thongtem, T., Jaroenchaichana, J., Thongtem, S., 2009. Cyclic microwave-assisted synthesis of flower-like and hexapod silver bismuth sulfide. Materials Letters 63, 2163-2166.

Todor Serafimovski, Goran Tasev, Stefanova, V., 2015. mineral assemblages group of major and associated mineral phases in the kadiica porphyry copper deposit, eastern macedonia Geologica Macedonica 29, 183-196.

Topare, N. and Patil, D.K., 2013. A review on parameters affecting the photocatalytic degradation of dyes using photocatalysts. 66th Annual Session of Indian Institute of Chemical Engineers Hosted at Institute of Chemical Technology, Mumbai.

Van Embden, J., Della Gaspera, E., 2019. Ultrathin Solar Absorber Layers of Silver Bismuth Sulfide from Molecular Precursors. ACS Applied Materials & Interfaces 11, 16674-16682.

Viet, N.M., Trung, D.Q., Giang, B.L., Tri, N.L.M., Thao, P., Pham, T.H., Kamand, F.Z., Al Tahtamouni, T.M., 2019. Noble metal -doped graphitic carbon nitride photocatalyst for enhancement photocatalytic decomposition of antibiotic pollutant in wastewater under visible light. Journal of Water Process Engineering 32, 100954.

Visa, M., Andronic, L., Enesca, A., 2016. Behavior of the new composites obtained from fly ash and titanium dioxide in removing of the pollutants from wastewater. Applied Surface Science 388, 359-369.

Wang, A., Wang, C., Fu, L., Wong-Ng, W., Lan, Y., 2017. Recent Advances of Graphitic Carbon Nitride-Based Structures and Applications in Catalyst, Sensing, Imaging, and LEDs. Nanomicro Lett 9, 47.

Wang, H., Xie, Z., Wang, X., Jia, Y., 2020a. $NaBiS_2$ as a Novel Indirect Bandgap Full Spectrum Photocatalyst: Synthesis and Application. Catalysts 10, 413.

Wang, J., Yang, X., Hu, W., Li, B., Yan, J., Hu, J., 2007. Synthesis of $AgBiS_2$ microspheres by a templating method and their catalytic polymerization of alkylsilanes. Chemical Communications, 4931-4933.

Wang, P., Lo, I.M.C., 2009. Synthesis of mesoporous magnetic γ-Fe_2O_3 and its application to Cr(VI) removal from contaminated water. Water Research 43, 3727-3734.

Wang, S., Li, J., Li, Q., Bai, X., Wang, J., 2020b. Metal single-atom coordinated graphitic carbon nitride as an efficient catalyst for CO oxidation. Nanoscale 12, 364-371.

Wang, X., Blechert, S., Antonietti, M., 2012a. Polymeric Graphitic Carbon Nitride for Heterogeneous Photocatalysis. ACS Catalysis 2, 1596-1606.

Wang, X.M., K.; Thomas, A.; Takanabe, K.; Xin, G.; Carlsson, J. M.; Domen, K.; Antonietti, M. , 2009. A Metal-Free Polymeric Photocatalyst for Hydrogen Production from Water under Visible Light. Nat. Mater. 8, 76-80.

Wang, Y., Bao, S., Liu, Y., Yang, W., Yu, Y., Feng, M., Li, K., 2020c. Efficient photocatalytic reduction of Cr(VI) in aqueous solution over CoS_2/g-C_3N_4-rGO nanocomposites under visible light. Applied Surface Science 510, 145495.

Wang, Y., Wang, X., Antonietti, M., 2012b. Polymeric graphitic carbon nitride as a heterogeneous organocatalyst: from photochemistry to multipurpose catalysis to sustainable chemistry. Angew Chem Int Ed Engl 51, 68-89.

Wang, Z., Murugananthan, M., Zhang, Y., 2019. Graphitic carbon nitride based photocatalysis for redox conversion of arsenic(III) and chromium(VI) in acid aqueous solution. Applied Catalysis B: Environmental 248, 349-356.

William W. Anku, Samuel O.B. Oppong, Govender, P.P., 2018. Bismuth-Based Nanoparticles as Photocatalytic Materials. intechopen.

Wu, M.-h., Li, L., Xue, Y.-c., Xu, G., Tang, L., Liu, N., Huang, W.-y., 2018. Fabrication of ternary GO/g-C_3N_4/MoS_2 flower-like heterojunctions with enhanced photocatalytic activity for water remediation. Applied Catalysis B: Environmental 228, 103-112.

Wu, Y., Zhou, B., Yang, C., Zhou, X., Zhang, W.-H., 2017. A bismuth-based ternary nanowires as an efficient electrocatalyst for dye sensitized solar cells. Chem. Commun. 53.

Xu, C., Ravi Anusuyadevi, P., Aymonier, C., Luque, R., Marre, S., 2019. Nanostructured materials for photocatalysis. Chemical Society reviews 48, 3868-3902.

Xu, J., Wang, Z., Zhu, Y., 2020. Highly efficient visible photocatalytic disinfection and degradation performances of microtubular nanoporous g-C_3N_4 via hierarchical construction and defects engineering. Journal of Materials Science & Technology 49, 133-143.

Xu, J., Zhang, L., Shi, R., Zhu, Y., 2013. Chemical exfoliation of graphitic carbon nitride for efficient heterogeneous photocatalysis. Journal of Materials Chemistry A 1, 14766-14772.

Yan, F., Wu, Y., Jiang, L., Xue, X., Lv, J., Lin, L., Yu, Y., Zhang, J., Yang, F., Qiu, Y., 2020. Design of C_3N_4-Based Hybrid Heterojunctions for Enhanced Photocatalytic Hydrogen Production Activity. 13, 876-881.

Yan, H., 2012. Soft-templating synthesis of mesoporous graphitic carbon nitride with enhanced photocatalytic H_2 evolution under visible light. Chemical Communications 48, 3430-3432.

Yang, Y., Xiong, X., Yin, H., Zhao, M., Han, J., 2019. Study of copper bismuth sulfide thin films for the photovoltaic application. Journal of Materials Science: Materials in Electronics 30, 1832-1837

Yang, J.-K., Lee, S.-M., 2006. Removal of Cr(VI) and humic acid by using TiO_2 photocatalysis. Chemosphere 63, 1677-1684.

Yang, S., Gong, Y., Zhang, J., Zhan, L., Ma, L., Fang, Z., Vajtai, R., Wang, X., Ajayan, P.M., 2013. Exfoliated graphitic carbon nitride nanosheets as efficient catalysts for hydrogen evolution under visible light. Adv Mater 25, 2452-2456.

Ye, M., Wei, W., Zheng, L., Liu, Y., Wu, D., Gu, X., Wei, A., 2019. Enhanced visible light photoreduction of aqueous Cr(VI) by Ag/Bi_4O_7/g-C_3N_4 nanosheets ternary metal/non-metal Z-scheme heterojunction. Journal of Hazardous Materials 365, 674-683.

Yu, T., Lv, L., Wang, H., Tan, X., 2018. Enhanced photocatalytic treatment of Cr(VI) and phenol by monoclinic $BiVO_4$ with {010}-orientation growth. Materials Research Bulletin 107, 248-254.

Zeng, N., Hopkinson, D.G., Spencer, B.F., McAdams, S.G., Tedstone, A.A., Haigh, S.J., Lewis, D.J., 2019. Direct synthesis of MoS_2 or MoO_3via thermolysis of a dialkyl dithiocarbamato molybdenum(iv) complex. Chemical Communications 55, 99-102.

Zhang, C., Li, Y., Shuai, D., Shen, Y., Xiong, W., Wang, L., 2019. Graphitic carbon nitride (g-C_3N_4)-based photocatalysts for water disinfection and microbial control: A review. Chemosphere 214, 462-479.

Zhang, G., Zhang, J., Zhang, M., Wang, X., 2012. Polycondensation of thiourea into carbon nitride semiconductors as visible light photocatalysts. Journal of Materials Chemistry 22, 8083-8091.

Zheng, Y., Lin, L., Wang, B., Wang, X., 2015. Graphitic Carbon Nitride Polymers toward Sustainable Photoredox Catalysis. Angew. Chem., Int. Ed. 54, 12868−12884.

Zhong, J., Xiang, W., Xie, C., Liang, X., Xu, X., 2013. Synthesis of spheroidal $AgBiS_2$ microcrystals by l-cysteine assisted method. Materials Chemistry and Physics 138, 773-779.

CHAPTER THREE

Synthesis and characterization of Ag_2S nanoparticles made by using silver(I) complex of *N*-methyl-*N*-phenyl-dithiocarbamate as single-source precursor

3.0 Introduction

Silver sulphide nanoparticles have low toxicity, good chemical stability, and exist in three phases: γ-Ag_2S, β-Ag_2S (argentite) and monoclinic α-Ag_2S (acanthite) (Ismail et al., 2020). The monoclinic crystal phase is the most common, and has been applied in areas such as electrochemical cells, photovoltaic cells, IR detectors and photocatalysis (Jadhav et al., 2013). Due to the numerous applications of silver sulphide, several routes have been used for its synthesis including techniques such as gamma irradiation, sol-gel, thermal evaporation, molecular beam epitaxy, successive ionic layer adsorption and reaction, spray pyrolysis deposition, chemical bath deposition and solvothermal processes (Sadovnikov et al., 2016). Solvothermal approach is advantageous because it is simple and affords products with high surface area and homogenous structure (Yang et al., 2012).

One of the factors that determine the quality of products obtained through solvothemal technique is the type of solvent used for the synthesis (Stock, 2010). Oleylamine is a common solvent and capping agents used in solvothermal synthesis. It is often used because of its ability to form complex with metals and subsequent decomposition under controlled condition to produce the nanoparticles. In addition to its cheapness, it is a liquid at room temperature with high boiling point, which implies that complexes with high decomposition temperature could be accommodated. It is able to modulate the important particles parameters such as shape, size and the composition, thereby ultimately influence the properties of the nanoparticles (Mourdikoudis and Liz-Marzán, 2013). The type and amount of precursor used for the synthesis is also very important in determining the shape and size of the final product in solvothermal synthesis (Jen-La Plante et al., 2010).

The use of single source precursors is particularly important in the synthesis of nanoparticles due to the generation of a pure product, ease of handling and the fact that pre-reaction is prevented unlike when other types of precursors are used in synthesis (Bochmann, 1996). Some of the common single source precursors are xanthate (Bishop et al., 2019), oxalate (Chenakin and Kruse, 2021), dithiophosphates (Kato et al., 2021) and dithiocarbamate (Shinde et al., 2020) complexes. Among these complexes, dithiocarbamate precursors have been the most

utilized because they are easy to prepare, and their decomposition properties could be altered by changing the type of substituents on the nitrogen. Their ligands can form complexes with all the transition metals and the physical properties of these complexes can be altered (Roffey et al., 2019; Ajiboye et al., 2021; Ajiboye et al., 2022).

Ehsan et al., (2013) previously reported the synthesis of thin film acanthite (Ag_2S) from silver diethyldithiocarbamate cluster precursor. The synthesis was carried out between 350 and 400 °C through aerosol assisted chemical vapor deposition. However, the size of the particles obtained was relatively large (>100 nm) and there was the presence of SnO_2 impurities. Acanthite (Ag_2S) has also been synthesized from bis(dibenzyl dithiocarbamato) Ag(I) complex but the thermolysis was carried out at 220 ^oC (Ajibade et al., 2020). It was also prepared at a temperature of 200 ^oC in air by using silver diethyldithiocarbamate as precursor without using any capping agent (Wang et al., 2008). Ag_2S is not stable at a temperature above 186 ^oC since it experiences phase transition at this temperature (Cava et al., 1980; Wen et al., 2005). The synthesis at a temperature below 186 ^oC is therefore desirable. Hence, the aim of the present study is to synthesize pure acanthite using solvothermal method at a relatively lower temperature (180 °C). Silver(I) complex of *N*-methyl-*N*-phenyl- dithiocarbamate was used as single-source precursor for the synthesis of acanthite (Ag_2S), while oleylamine was used as the capping agent. Finally, the antioxidant activities of the as-prepared nanoparticles were investigated and compared to the antioxidant activities of the metallic silver.

3.1 Experimental

3.1.1 Materials and physical measurements

Ammonium hydroxide solution, *N*-methyl aniline, toluene, methanol, ethanol, oleylamine, silver nanoparticles, carbon disulphide and silver nitrate were procured from Merck, SA. All solvents and materials used were analytical grade and no additional purification was required. The FTIR spectrum was recorded on a Bruker IFS 66v/S between 4000–400 cm^{-1} frequency range. NMR analysis of both the ^1H and ^{13}C environment of the complex was conducted using 600 MHz Bruker Avance III NMR spectrometers (dimethylsulfoxide was used as the solvent). Thermogravimetric analysis/ differential scanning calorimetry was carried out on a Mettler-Toledo GmbH, Gieβen, Germany machine. The optical and crystalline phase of the nanoparticles were studied using Spectroquant Prove 300 UV-vis spectrophotometer and Bruker D8 Advance X-ray diffractometer with CuKa radiation (λ = 1.5418 Å), while the

morphology of the particles was analysed using TECNAI G2 (ACI) transmission electron microscope. The EDX analysis was carried out by using LYRA 3, TESCAN.

3.1.2 *Synthesis of ammonium N-methyl-N-phenyl dithiocarbamate ligand*

Ammonium *N*-methyl-*N*-phenyl dithiocarbamate ligand was prepared following the procedure described previously, with slight modifications (Onwudiwe and Ajibade, 2010). Briefly, concentrated aqueous ammonia (61.60 mL,1.60 mol) was mixed with N-methyl aniline (22.00 mL, 0.20 mol) in ice and stirred for about 10 min. To this solution was added ice-cold carbon disulphide (12.00 ml, 0.20 mol) dropwise, followed by steady stirring for about 7 h, while the low temperature (less than 4 °C) was maintained throughout the reaction process. The resulting yellow solid was filtered via suction and washed with methanol that had been kept under ice. The obtained ammonium *N*-methyl-*N*-phenyl dithiocarbamate ligand was kept in the refrigerator to prevent decomposition.

3.1.3 Synthesis of Ag(I) complex of *N*-methyl-*N*-phenyl dithiocarbamate

An ethanol solution of the ammonium *N*-methyl-*N*–phenyl dithiocarbamate ligand (1.2 g, 6 mmol) was reacted with an aqueous solution of silver nitrate (1.02 g, 6 mmol) in a round bottom flask charged with magnetic stirrer. The solution was stirred for 1 h, producing a deep brown precipitate, which was filtered and rinsed with ethanol. Finally, the product was recrystallized by using chloroform.

3.1.4 *Synthesis of silver sulphide nanoparticles*

About 0.10 g of the prepared silver dithiocarbamate complex was introduced into a 100 mL three-necked flask containing 15 mL oleylamine. The mixture was degassed for 20 min by allowing the flow of nitrogen through the reaction system, while the temperature was maintained at 30 °C. The temperature of the reaction was gradually increased to 180 °C and maintained for 70 min. Afterwards, the temperature was cooled to about 60 °C, and a large volume of methanol was added to the solution to afford the immediate precipitation of the nanoparticles. The nanoparticles were isolated by centrifuging and rinsing with a solution of ethanol and toluene several times to obtain pure nanoparticles. The obtained product was air-dried in the fume hood and stored for further characterization.

3.1.5 *Thermal studies of Ag(I) complex of N-methyl-N-phenyl dithiocarbamate*

To obtain the thermogravimetry analysis/ differential scanning calorimetry (TGA/DSC) profile of the complex, 2.466 mg of the sample was heated in the temperature ranging from 0 to 600 °C under argon atmosphere running at a flow rate of 75 mL/min.

3.2 Results and Discussion

3.2.1 *NMR studies of Ag(I) complex of N-methyl-N-phenyl dithiocarbamate*

The proton NMR spectrum of the complex showed a singlet peak at 1.48 ppm, which was attributed to the methyl group (-CH_3) attached to nitrogen of the dithiocarbamate, and a multiplet between 6.51-7.38 ppm due to the phenyl group. A pronounced singlet peak at 2.50 ppm emanated from the solvent (dimethylsulfoxide) used for the analysis (Bitterling et al., 2022).

In the carbon-13 NMR spectrum, the signal at 204.85 ppm was the resonant frequency of the quaternary carbon. The presence of the heteroatoms around this characteristic signal was responsible for greater deshielding, thereby resulting in the appearance of the peak significantly downfield (Onajole et al., 2010). The resonant signals of the phenyl group were identified at 126.92, 128.72, 129.42, 130.09 and 146.31 ppm (Onwudiwe and Nkwe, 2020). The presence of the nitrogen of tertiary amine was confirmed by signal at 46.13 ppm, while the signal at 79.45 ppm showed the presence of methyl group that is attached to nitrogen. The dimethylsulfoxide peak was a pronounced peak at 39.50 ppm on the spectrum (Bitterling et al., 2022).

3.2.2 *Thermal studies of Ag(I) complex of N-methyl-N-phenyl dithiocarbamate*

The thermogravimetric analysis (TGA), presented in Fig. 3.1, showed that there was no loss in weight up to 100 °C, indicating that there was no entrapped water molecule in the structure of the complex or any solvent (Singh et al., 2019). The curve showed a pronounced loss in weight around 162 °C in a single step. This stage was due to the decomposition of the organic part of the complex. A gradual loss in weight observed after 200 °C could be ascribed to a loss of sulphur and formation of metal sulphides due to higher residual weight. The residual weight at 600 °C was 61.23%, indicating a large residual weight and this could be due to the percentage

of silver in the complex. High residual weight of silver sulphide (Ag_2S) after decomposition of the complex is also an indication that the synthesized nanoparticle is stable to heat (Abbasi et al., 2018) and it is in agreement with previous report (Ehsan et al., 2013; Abbasi et al., 2018).

In the differential scanning calorimetry (DSC) thermogram, the first step of decomposition around 164 °C was an endothermic peak associated with the decomposition of the complex and the formation of the respective silver sulphide. There was no peak after 350 °C, indicating that the final product (silver sulphide) is stable to thermal decomposition at a temperature that is less or equal to 600 °C, which was the maximum temperature used for the analysis.

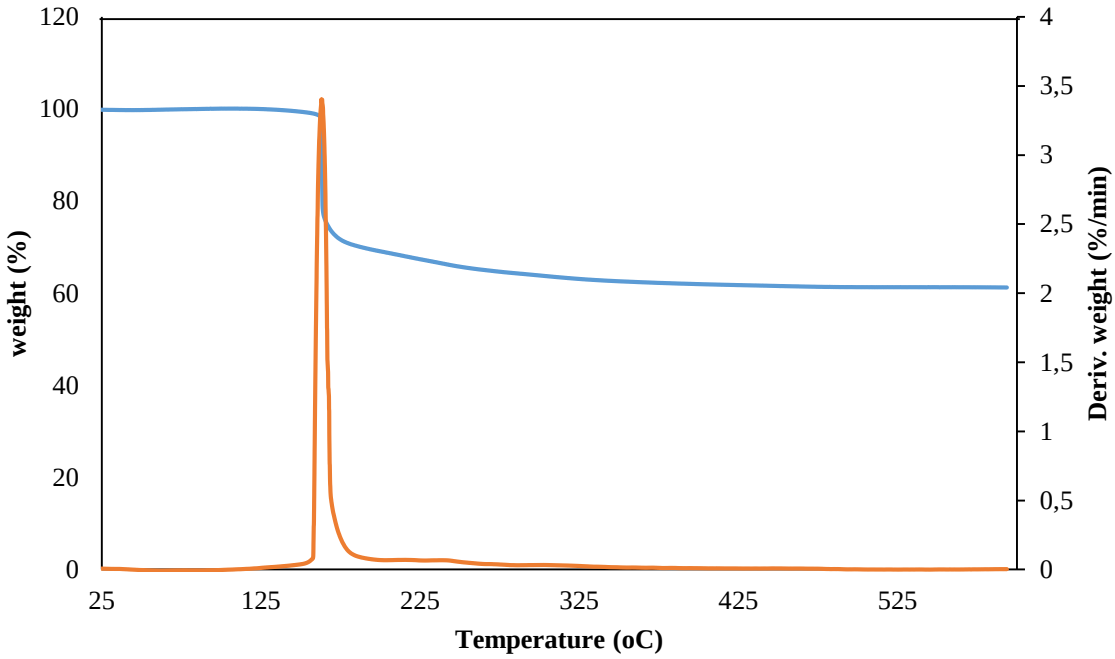

Figure 3.1: TGA/DSC plot of Ag(I) complex of (*N*-methyl-*N*-phenyl dithiocarbamate). TGA is shown in blue, while DSC is shown in orange color.

3.2.3 *FTIR spectroscopic studies of Ag(I) complex of N-methyl-N-phenyl dithiocarbamate and Ag_2S nanoparticles*

The FTIR spectrum of the complex (Fig. 3.2a) showed the characteristic stretching vibration of the C-N and –CSS groups as two sharp peaks at 1116 cm^{-1} and 1057 cm^{-1} respectively, while the stretching vibration of C-N bond appeared as an intense peak around 1400 cm^{-1} (Ahmad et al., 2020). The observed shift to higher wavelength of –CN stretching vibration was due to enhanced double bond character of –CN, caused by the delocalization of electron toward

the silver metal in the complex (Faraglia et al., 2005). The bands identified at 2647 cm^{-1} and 765 cm^{-1} were attributed to the aromatic ring stretching and bending vibrations of C-H bond respectively (Ghaedi et al., 2017). The silver-sulphur characteristic peaks (Ag-S) appeared at 556 cm^{-1} and 2293 cm^{-1} and the peak slightly above 1500 cm^{-1} is the characteristic peak for aromatic C=C (Elbayomi et al., 2021). The peaks at 1487 cm^{-1} and 1413 cm^{-1} were due to the C-C symmetric and asymmetric stretching vibration. All these values are consistent with the values obtained from previously reported studies (Onwudiwe and Ajibade, 2011; Andrew and Ajibade, 2019).

The FTIR analysis of the Ag_2S nanoparticles (Fig. 3.2b) was carried out in order to explore the functional groups present on the surface of the nanoparticle and therefore ascertain the capping of the nanoparticles. The FTIR, measured in the range of 500–4000 cm^{-1}, shows peaks at 522, 622, 2114 and 2317 cm^{-1} which were due to the vibration of the oleylamine capped Ag-S bond (Ismail et al., 2020). The characteristic peak for the stretching vibration of the sulphide group in the Ag_2S structure appeared at 1738 cm^{-1}. This was consistent with the results reported for silver sulphide obtained through laser ablation (Ismail et al., 2020). There was a disappearance of the two characteristic peaks for -C-N and -CSS of dithiocarbamate around 1100 cm^{-1} and this showed that the dithiocarbamate complex has been decomposed into the metal sulphide. It was noted, however, that the peaks due to the capping agent are more pronounced. The peaks at 3616 cm^{-1} were assigned to the symmetric stretching vibration of NH_2, and peaks at 2908, 2830 and 2670 cm^{-1} were due to the C-H bending vibration, asymmetric and symmetric stretching vibration of $–CH_2$ in oleylamine. The peaks around 1400 cm^{-1} and 716 cm^{-1} were attributed to the stretching and bending vibrations of C-C bonds. The presence of the functional groups attributed to oleylamine confirmed that oleylamine served as both solvent and capping agents during the synthesis since it has the ability to bind to the nanoparticles (Mourdikoudis and Liz-Marzán, 2013).

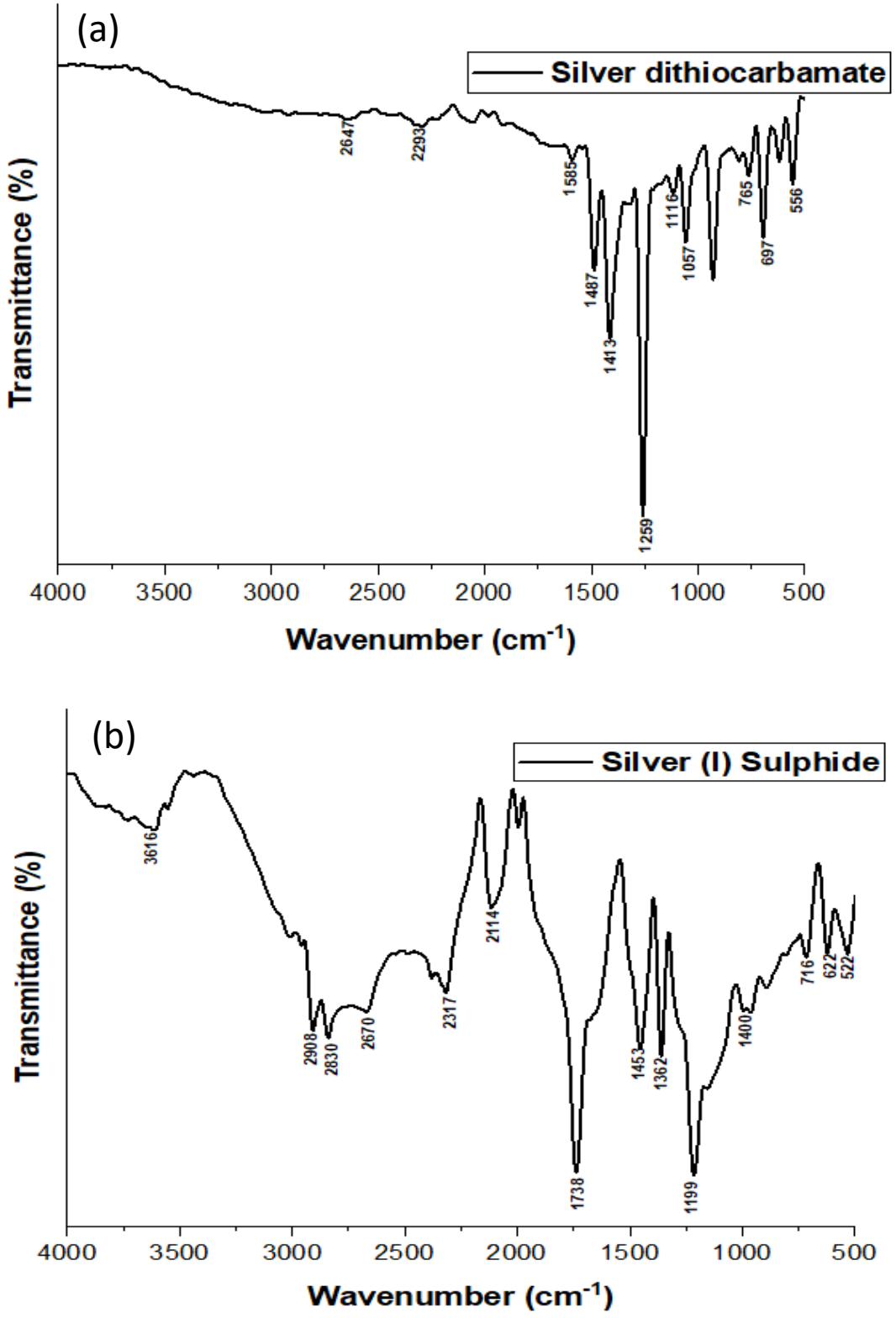

Figure 3.2: FTIR spectra of (a) silver(I) complex of *N*-methyl-*N*-phenyl dithiocarbamate and (b) oleylamine-capped Ag_2S.

3.2.4 *X-ray diffraction (XRD) analysis of Ag_2S nanoparticles*

The X-ray diffraction pattern of the silver sulphide nanoparticles is shown in Fig. 3.3. The peaks at 2θ of 22.43º, 25,90º, 28.97º, 31.52º, 33.61º, 34.39º, 36.56º, 37.72º, 40.74º,43.41º, 46.21º, 47.76º, 48.76º, 53.28º, 61.21º and 63.74º could be indexed to the (-101), (-111), (111), (-112), (120), (-121), (112), (-103), (031), (200), (-123), (-212), (014), (-213), (015) and (-134) respectively. This perfectly conformed to the pattern of the monoclinic phase of acanthite silver(I) sulphide (Ag_2S) (JCPDS card No.14-0072; with the lattice constant a=4.22900 Å, b = 6.93100 Å, c = 7.86200 Å; space group P21/n (14) (Wang et al., 2012; Chen et al., 2021). The most prominent peak was at 2θ value of 34.39 º, which was indexed to the (-121) plane. The absence of characteristic peaks for silver and silver oxide showed that all the silver in the complex was converted to silver (I) sulphide (Chen et al., 2021) and pure phase of acanthite silver(I) sulphide was successfully prepared (Wang et al., 2008). The thermal energy at 180 °C was enough to cause the C-S bond in the dithiocarbamate complex to cleave, leading to the generation of silver(I) sulphide fragment which joined together to form the pure crystallites. The sulphide of silver was formed instead of the oxide of silver due to the inert environment maintained in the reaction system and the greater stability of silver(I) sulphide compared to that of silver(I) oxide (Wang et al., 2008; Wells, 2012). The unindexed peaks may be attributed to the presence of negligible amount of metallic silver impurities in the as-synthesized Ag_2S.Visible between 2θ = 45 and 50 are the (200) and (111) peaks of silver nanoparticles (Temgire et. al.,2004).

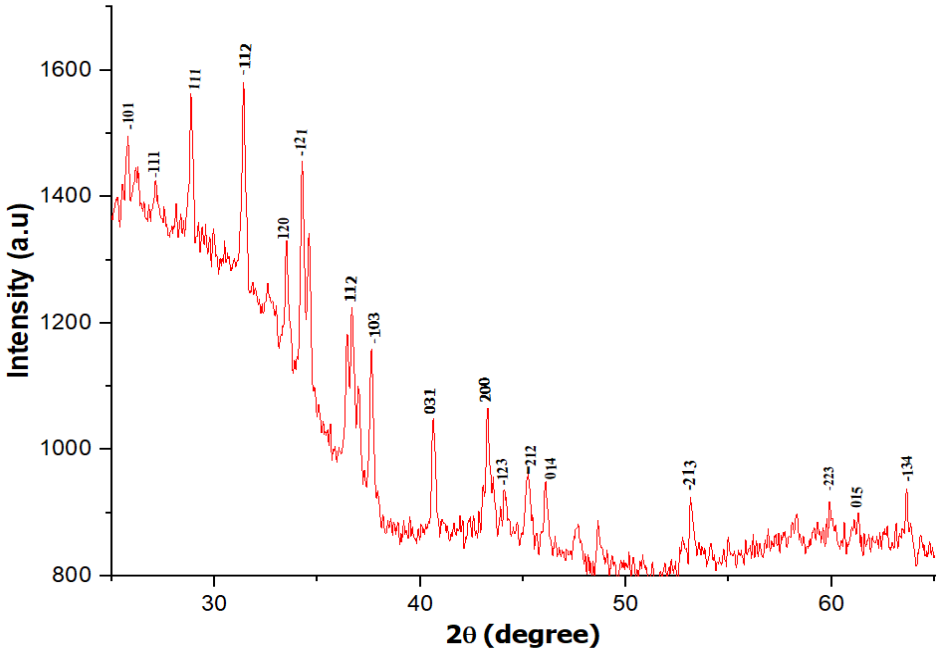

Figure 3.3: XRD pattern of Ag_2S prepared from Ag(I) complex of *N*-methyl-*N*-phenyl dithiocarbamate.

The crystallite size of the nanoparticles was estimated by using Debye–Scherrer's equation (Eq. 2) (Norouzzadeh et al., 2020):

$$D = \frac{k\lambda}{\beta cos\theta} \qquad 2$$

where *D* is the crystallite size; β is the full width at half maximum (FWHM); K is a constant and it is close to unity (1); λ is X-ray's wavelength (1.5406 Å); θ is the Bragg angle in degrees which usually agrees with the maxima value of the diffraction peak. The crystallite size was found to be 48.61 nm when (-121) peak was used for the estimation. This value of the particle size was in the range of the similar size obtained when silver sulphide was prepared from sodium sulphide and silver nitrate (Hamed et al., 2020).

3.2.5 *UV-vis spectroscopic studies of the Ag_2S nanoparticles*

Figure 3 presents the UV-vis absorption spectrum of the Ag_2S nanoparticles, which showed the wavelength of maximum absorption at 220 nm (Fig. 3.4 (a). The optical bandgap energy was estimated from Tauc plot by plotting $(\alpha h\upsilon)^{1/n}$ against hυ. Here, hυ is the energy of the incident photon, while n is the transition value and its value could be 3, 2, 3/2 or ½ if the electron transition is indirect-forbidden, indirect, direct-forbidden or direct respectively (Heiba et al., 2022). The direct bandgap energy obtained from the Tauc plot was 4.9 eV (Fig.3. 4 (b)).

This value was very much higher than the values previously reported for the bulk Ag_2S (1.0 eV). This may be due to significant size reduction occasioned by the use of capping agent, which reduced the particle size of Ag_2S. The band gap energy of nanoparticles has an indirect relationship with the size (Javed et al., 2016). Hence, as the particle size decreases, the band gap energy of the nanoparticle increases.

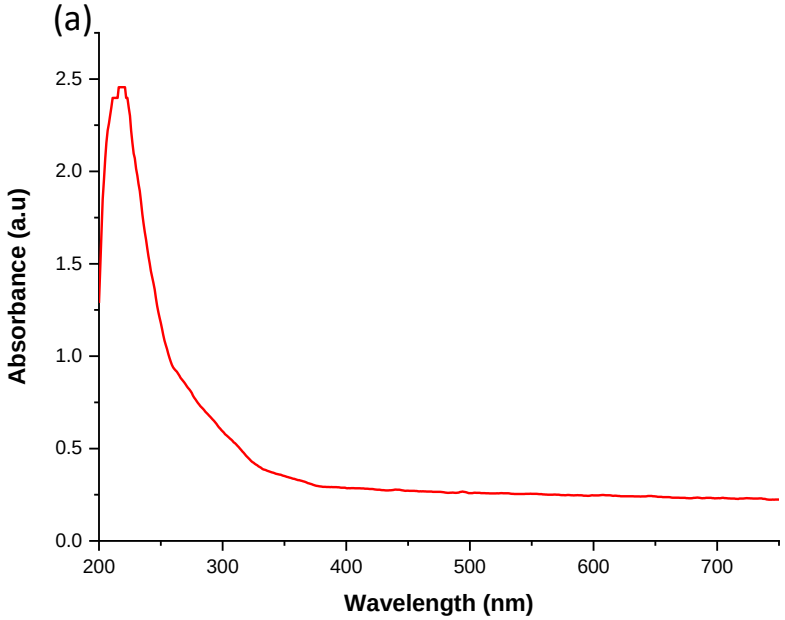

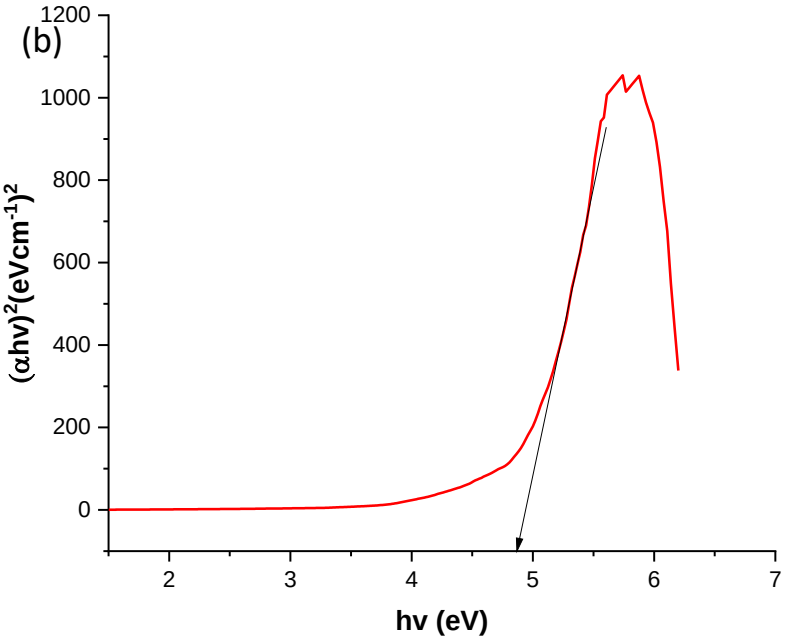

Figure 3.4: (a) UV spectrum of the synthesized Ag_2S, and (b) Tauc plot for obtaining direct bandgap energy.

3.2.6 *Morphological and EDX analysis of Ag_2S*

Fig. 3.5 (a) shows the TEM image of the Ag_2S nanoparticles and the respective particle size distribution histogram. The particles are of spherical morphology with observable degree of agglomeration and the average particle size was 40.50 nm with a wide size distribution as shown in histogram in Fig. 3.5 (b). The value of particle size obtained from the TEM analysis was very close to the value obtained from the XRD data. Also, it was in the range of values of the particle size obtained by Vijayan et al., (Vijayan and Vijayachamundeeswari, 2022) when silver(I) sulphide was prepared via co-precipitation method. Fig. 3.5 (c) presents the EDX, showing two main peaks of sulphur and silver. The percentage of silver and sulphur were 87.27 and 12.73% respectively. There were no impurities in the prepared sample as shown in the EDX analysis. The ratio of silver-to-sulphur was estimated to be 2.03:1.00, which further confirmed the formation of Ag_2S.

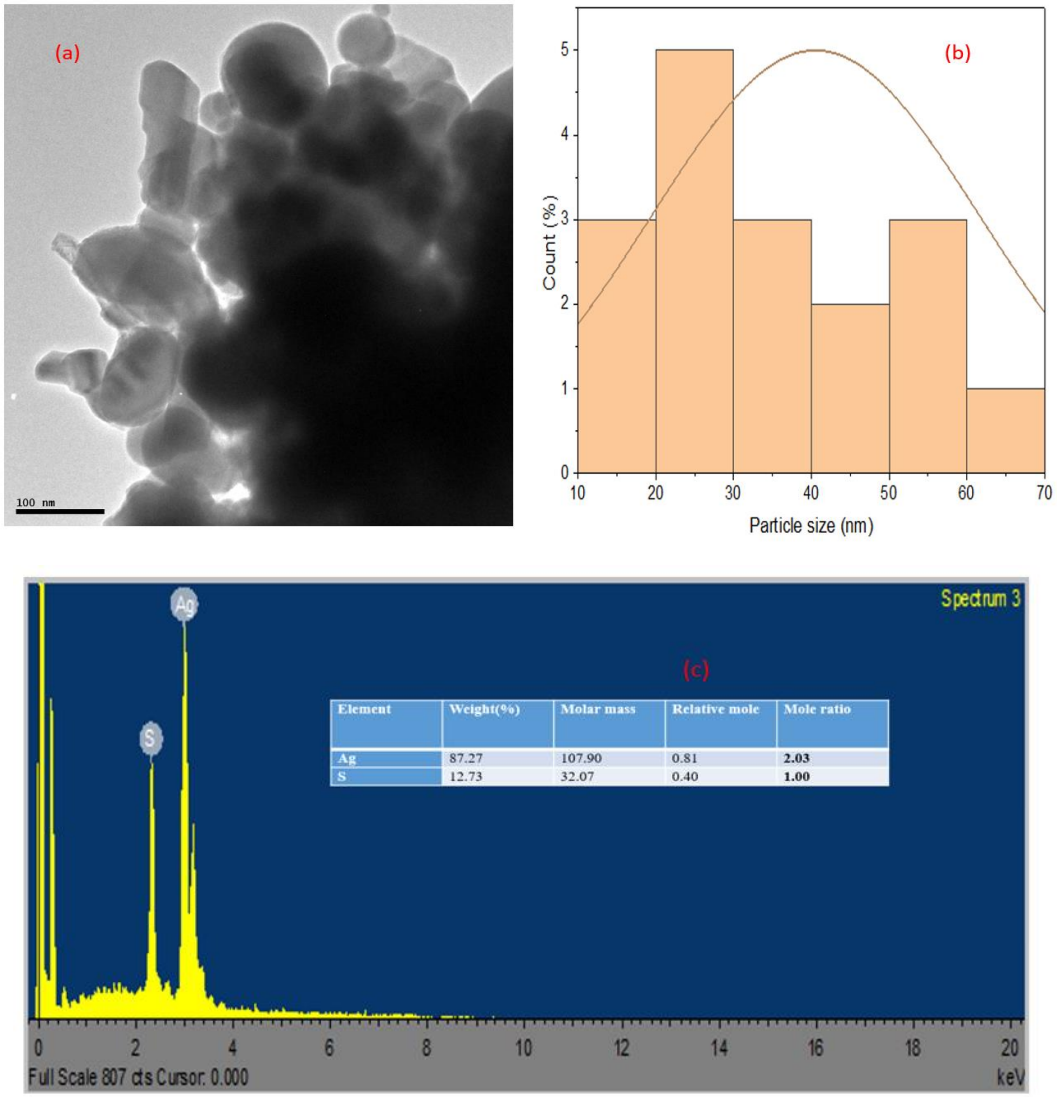

Figure 3.5: (a) TEM image of the synthesized Ag_2S nanoparticles (b) Particle size distribution obtained from the TEM image of Ag_2S and (c) EDS spectrum of Ag_2S.

CONCLUSION

Acanthite phase of Ag_2S was successfully prepared from Silver(I) complex of *N*-methyl-*N* – phenyl dithiocarbamate at a relatively low temperature of 180 ^oC. The characterization techniques (UV-vis spectrometry, EDS, FTIR and XRD) confirmed the formation of silver sulphide. The particle size obtained from XRD and TEM results was estimated to be in the range of 40-48 nm. The EDS analysis confirmed that the pure form of the nanoparticle was synthesized. The technique devised for the synthesis is easy and cost effective, and shows simple approach for the formation for Ag_2S nanoparticles, which may find usefulness in different applications.

REFERENCES

Abbasi, M., Rafique, U., Murtaza, G., Ashraf, M.A., 2018. Synthesis, characterisation and photocatalytic performance of ZnS coupled Ag_2S nanoparticles: A remediation model for environmental pollutants. Arabian Journal of Chemistry 11, 827-837.

Ahmad, K.S., Zafar, A., Jaffri, S.B., Alamgir, M.K., Sohail, M., Mehmood, R.F., Rehman, M.u., Ali, D., 2020. Chemosynthesis and physical vapor deposition of acanthite thin films: Characterization and electrochemistry explorationwe. Results in Physics 19, 103647.

Ajibade, P.A., Sikakane, B.M., Botha, N.L., Oluwalana, A.E., Omondi, B., 2020. Synthesis and crystal structures of bis(dibenzyl dithiocarbamato)Cu(II) and Ag(I) complexes: Precursors for Cu1.8S and Ag2S nano-photocatalysts. Journal of Molecular Structure 1221, 128791.

Ajiboye, T.O., Ajiboye, T.T., Marzouki, R., Onwudiwe, D.C., 2022. The Versatility in the Applications of Dithiocarbamates. 23, 1317.

Ajiboye, T.O., Oluwarinde, B.O., Montso, P.K., Ateba, C.N., Onwudiwe, D.C., 2021. Antimicrobial activities of Cu(II), In(III), and Sb(III) complexes of N-methyl-N–phenyl dithiocarbamate complexes. Results in Chemistry 3, 100241.

Andrew, F.P., Ajibade, P.A., 2019. Synthesis, characterization, and electrochemical studies of Co(II, III) dithiocarbamate complexes. Journal of Coordination Chemistry 72, 1171-1186.

Bishop, M.T., Zhang, L., Dolganov, A., Chen, G.Z., Peng, C., Hu, D., 2019. Synthesis and performance optimisation of spray coated Cu_2ZnSnS_4 absorbing layers from single-source xanthate precursors. Thin Solid Films 690, 137530.

Bitterling, H., Lorenz, P., Vetter, W., Kammerer, D.R., Stintzing, F.C., 2022. Photo-protective effects of selected furocoumarins on β-pinene, R-(+)-limonene and γ-terpinene upon UV-A irradiation. Journal of Photochemistry and Photobiology A: Chemistry 424, 113623.

Bochmann, M., 1996. Metal Chalcogenide Materials: Chalcogenolato complexes as “single-source” precursors. Chemical Vapor Deposition 2, 85-96.

Cava, R.J., Reidinger, F., Wuensch, B.J., 1980. Single-crystal neutron diffraction study of the fast-ion conductor β-Ag_2S between 186 and 325°C. Journal of Solid State Chemistry 31, 69-80.

Chen, Y.-C., Bai, Y.-M., Hsu, Y.-K., 2021. Biomarker detection for disease diagnosis via versatile Ag_2S nanowires as electrochemical sensor and SERS substrate. Journal of Alloys and Compounds 881, 160647.

Chenakin, S., Kruse, N., 2021. X-ray induced ion desorption from transition metal oxalates. Applied Surface Science 570, 151112.

Ehsan, M.A., Khaledi, H., Tahir, A.A., Ming, H.N., Wijayantha, K.G.U., Mazhar, M., 2013. Synthesis and characterization of silver diethyldithiocarbamate cluster for the deposition of acanthite (Ag_2S) thin films for photoelectrochemical applications. Thin Solid Films 536, 124-129.

Elbayomi, S.M., Wang, H., Tamer, T.M., You, Y., 2021. Enhancement of Antioxidant and Hydrophobic Properties of Alginate via Aromatic Derivatization: Preparation, Characterization, and Evaluation. Polymers 13, 2575.

Faraglia, G., Sitran, S., Montagner, D., 2005. Pyrrolidine dithiocarbamates of Pd(II). Inorganica Chimica Acta 358, 971-980.

Ghaedi, H., Ayoub, M., Sufian, S., Lal, B., Uemura, Y., 2017. Thermal stability and FT-IR analysis of Phosphonium-based deep eutectic solvents with different hydrogen bond donors. Journal of Molecular Liquids 242, 395-403.

Hamed, M.S.G., Adedeji, M.A., Zhang, Y., Mola, G.T., 2020. Silver sulphide nano-particles enhanced photo-current in polymer solar cells. Applied Physics A 126, 207.

Heiba, Z.K., Bakr Mohamed, M., Ahmed, S.I., 2022. Exploring the physical properties of PVA/PEG polymeric material upon doping with nano gadolinium oxide. Alexandria Engineering Journal 61, 3375-3383.

Ismail, R.A., Rawdhan, H.A., Ahmed, D.S., 2020. High-responsivity hybrid α-Ag_2S/Si photodetector prepared by pulsed laser ablation in liquid. Beilstein Journal of Nanotechnology 11, 1596-1607.

Jadhav, U., Patel, S., Patil, R., 2013. Synthesis of silver sulphide nanoparticles by modified chemical route for solar cell applications. Research Journal of Chemical Sciences 2231, 606X.

Javed, R., Usman, M., Tabassum, S., Zia, M., 2016. Effect of capping agents: Structural, optical and biological properties of ZnO nanoparticles. Applied Surface Science 386, 319-326.

Jen-La Plante, I., Zeid, T.W., Yang, P., Mokari, T., 2010. Synthesis of metal sulfide nanomaterials via thermal decomposition of single-source precursors. Journal of Materials Chemistry 20, 6612-6617.

Kato, S., Onoda, A., Grimm, A.R., Schwaneberg, U., Hayashi, T., 2021. Construction of a whole-cell biohybrid catalyst using a Cp*Rh(III)-dithiophosphate complex as a precursor of a metal cofactor. Journal of Inorganic Biochemistry 216, 111352.

Mourdikoudis, S., Liz-Marzán, L., 2013. Oleylamine in Nanoparticle Synthesis. Chemistry of Materials 25.

Norouzzadeh, P., Golzan, M.M., Mabhouti, K., Naderali, R., 2020. Effect of Mn-substitution on impedance spectroscopy and magnetic properties of Al-doped ZnO nanoparticles. Nanotechnology 31, 325704.

Onajole, O.K., Makatini, M.M., Govender, P., Govender, T., Maguire, G.E.M., Kruger, H.G., 2010. Synthesis and NMR assignment of pentacycloundecane precursors of potential pharmaceutical agents. 48, 249-255.

Onwudiwe, D.C., Ajibade, P.A., 2010. Synthesis and characterization of metal complexes of *N*-alkyl-*N*-phenyl dithiocarbamates. Polyhedron 29, 1431-1436.

Onwudiwe, D.C., Ajibade, P.A., 2011. Synthesis, Characterization and Thermal Studies of Zn(II), Cd(II) and Hg(II) Complexes of *N*-Methyl-*N*-Phenyldithiocarbamate: The Single Crystal Structure of $[(C_6H_5)(CH_3)NCS_2]_4Hg_2$. International Journal of Molecular Sciences 12, 1964-1978.

Onwudiwe, D.C., Nkwe, V.M., 2020. Morphological variations in Bi_2S_3 nanoparticles synthesized by using a single source precursor. Heliyon 6, e04505.

Roffey, A., Hollingsworth, N., Hogarth, G., 2019. Synthesis of ternary sulfide nanomaterials using dithiocarbamate complexes as single source precursors. Nanoscale Advances 1, 3056-3066.

Sadovnikov, S.I., Kuznetsova, Y.V., Rempel, A.A., 2016. Ag_2S silver sulfide nanoparticles and colloidal solutions: Synthesis and properties. Nano-Structures & Nano-Objects 7, 81-91.

Shinde, S.D., Sakla, A.P., Shankaraiah, N., 2020. An insight into medicinal attributes of dithiocarbamates: Bird's eye view. Bioorganic Chemistry 105, 104346.

Singh, R.P., Maurya, V.K., Maiti, B., Siddiqui, K.A., Prasad, L.B., 2019. Synthesis, structure and thermogravimetric analysis of novel dithiocarbamate based Zn(II), Cd(II) and Hg(II) complexes. Journal of Molecular Structure 1198, 126912.

Stock, N., 2010. High-throughput investigations employing solvothermal syntheses. Microporous and Mesoporous Materials 129, 287-295.

Temgire M.K., Joshi S.S., 2004. Optical and structural studies of silver nanoparticles, Radiation Physics and Chemistry 71 1039-1044.

Vijayan, K., Vijayachamundeeswari, S.P., 2022. Enhancement on the structural, functional, optical and morphological properties of temperature treated silver sulfide nanostructures. Journal of the Indian Chemical Society 99, 100420.

Wang, M., Wang, Y., Tang, A., Li, X., Hou, Y., Teng, F., 2012. Optical properties and self-assembly of Ag_2S nanoparticles synthesized by a one-pot method. Materials Letters 88, 108-111.

Wang, T.X., Xiao, H., Zhang, Y.C., 2008. Simple solid state synthesis of Ag_2S crystallites using a single-source molecular precursor. Materials Letters 62, 3736-3738.

Wells, A.F., 2012. Structural inorganic chemistry. Oxford university press.

Wen, X., Wang, S., Xie, Y., Li, X.-Y., Yang, S., 2005. Low-Temperature Synthesis of Single Crystalline Ag_2S Nanowires on Silver Substrates. The Journal of Physical Chemistry B 109, 10100-10106.

Yang, J., Akbarzadeh, J., Maurer, C., Peterlik, H., Schubert, U., 2012. Sol–gel synthesis of $ZnTiO_3$ using a single-source precursor based on p-carboxybenzaldehyde oxime as a linker. Journal of Materials Chemistry 22, 24034-24041.

CHAPTER FOUR

Photocatalytic reduction of hexavalent chromium using $Cu_{3.21}Bi_{4.79}S_9$/g-C_3N_4 composite

4.0 INTRODUCTION

Chromium is used in catalysis, leather tanning, electroplating, metal finishing, and also in the manufacturing of electronic devices, pigments, and magnetic tapes (Türkmen et al., 2022). The vast applications of chromium have raised concerns about their fate and impacts on the environment (Zhao et al., 2019). It has the ability to accumulate in the food chain and enter into the systems of humans and animals where it causes damage to vital organs (Ajiboye et al., 2021a). Chromium exists in different oxidation states, and out these are the poisonous hexavalent chromium and the trivalent chromium that is useful as micro-nutrients for the plants (Viti and Giovannetti, 2007). The hexavalent chromium is stable and does not easily precipitate out of environmental samples, while trivalent chromium easily precipitates out under alkaline conditions (Dhal et al., 2013). Hence, the reduction of toxic hexavalent chromium to useful trivalent chromium is a tenable approach for the removal of hexavalent chromium (Koutavarapu et al., 2022). The reduction reaction could be inspired by different processes and photocatalysis has emerged as a sustainable approach because it relies on the utilization of naturally available light absorbed by the photocatalyst.

The efficiency of the photocatalytic process depends on the effectiveness of the photocatalyst used (Kumar and Pandey, 2017; Ajiboye et al., 2020; Ajiboye et al., 2021b). Consequently, several photocatalysts have been investigated for the process. For instance, metallic (Qiu et al., 2019), binary or ternary metal chalcogenides (Rahman and Khan, 2021), doped materials (such as Mn^{2+} doped CuS (Sun et al., 2022) and Ag doped CoO (Okla et al., 2022)) nanoparticles, and heterojunction systems including $BaFe_2O_4/SnO_2$ (Kenfoud et al., 2022); In_2S_3-$ZnIn_2S_4$(Chen et al., 2022); TiO_2/MoS_2 (Shawky et al., 2022) and WO_3/In_2S_3(Hua et al., 2022) have been used for the photocatalytic Cr(VI) reduction. The incorporation of nanoparticles into polymeric materials such as graphitic carbon nitride has also been explored. Graphitic carbon nitride is a non-metallic photocatalyst, which has attracted attention due to its inertness, stability, and its ability to absorb light in the visible region of the solar spectrum (Ajiboye et al., 2020; Li et al., 2020). The performance of graphitic carbon nitride has been functionalized with different materials in order to form composite photocatalysts. Examples of functionalized

graphitic carbon nitride reported for the photocatalytic reduction of hexavalent chromium are $ZnIn_2S_4$/g-C_3N_4 (Wang et al., 2022a) and g-C_3N_4/Bi_3NbO_7(Ren et al., 2022).

Dithiocarbamate complexes are precursors for synthesizing chalcogenides because parameters such as the time of reaction, temperature of reaction and solvent used could be tuned to obtain different morphological phases of the nanoparticles (Sarker and Hogarth, 2021). The compounds have been used for the synthesis of binary (Ajiboye et al., 2022a) and ternary sulphides. Copper bismuth sulphide is one of the numerous ternary sulphides that have been synthesized via the thermal decomposition of dithiocarbamate complexes (Deng et al., 2014; Olatunde and Onwudiwe, 2022).

Several non-fractional phases of copper bismuth sulphide (Cu_3BiS_3, $Cu_{24}Bi_{26}S_{51}$, $Cu_4Bi_7S_{12}$, $Cu_6Bi_4S_9$, $CuBiS_2$ and $CuBi_5S_8$ have been reported (Sugaki and Shima, 1972; Yan et al., 2013; Balasubramanian et al., 2017; Ajiboye et al., 2021b). The non-common fractional stoichiometric phase ($Cu_{3.21}Bi_{4.79}S_9$) also exists, and Barma et al. has reported its synthesis via mechanical alloying (Barma et al., 2016). The synthesis of the non-fractional stoichiometric phases has been reported by the solvothermal route (Ajiboye et al., 2021b; Olatunde and Onwudiwe, 2022). However, to the authors best of knowledge, no report exists on the synthesis of the fractional phase via solvothermal route. Hence, the present study reports the synthesis of the fractional phase of copper bismuth sulphide ($Cu_{3.21}Bi_{4.79}S_9$) through a solvothermal method. The *N*-methyl-*N*-phenyl dithiocarbamate complexes of copper and bismuth were used as the precursor compounds. The as-synthesized ternary nanoparticles was used to functionalize graphitic carbon nitride to produce a novel composite photocatalyst ($Cu_{3.21}Bi_{4.79}S_9$ /gC_3N_4). The nanocomposite was utilized for the photocatalytic reduction of hexavalent chromium under visible light.

4.1 Experimental

4.1.1 *Materials*

Melamine ($C_3H_6N_6$), oleylamine ($C_{18}H_{37}N$), hydrated bismuth(III) nitrate ($Bi(NO_3)_3$•$5H_2O$)), copper(II) nitrate pentahydrate ($Cu(NO_3)_2$·$5H_2O$**),** absolute ethanol (CH_3CH_2OH), 2,4,6-trichlorophenol and chloroform ($CHCl_3$), used in this study were all procured from Merck chemicals company, were of analytical grade reagents. Phillips X'pert diffractometer (fixed with single-wavelength Cu Kα radiation (λ = 1.546060 Å and operated at 40 kV/50 mA) was used for obtaining the X-ray diffraction (XRD) results. Perkin Elmer λ20 UV–vis–NIR

spectrophotometer and PerkinElmer LS 45 fluorimeter were used to obtain the absorption and emission properties respectively. Also, LYRA 3, TESCAN and JEM—2100 JEOL equipment were used to obtain the scanning electron microscopy (SEM) and transmission electron microscopy (TEM) respectively. Thermogravimetry analysis was conducted using SDTQ 600 V20.9 Build 20 Thermal analyser. Malvern Zetasizer Nanoseries was used for the Zeta potential determination.

4.1.2 *Synthesis of graphitic carbon nitride (gC_3N_4)*

About 8.0 g of melamine was measured and transferred into an alumina crucible with a lid. The covered crucible was placed in the muffle furnace and heated at 550 °C for 4 h. The white melamine powder was observed to change to a yellow solid. The obtained solid was cooled to room temperature and crushed with mortar and pestle

4.1.3 *Synthesis of N-methyl-N-phenyl dithiocarbamate ligand and complexes*

The *N*-methyl-*N*-phenyl dithiocarbamate ligand was prepared by following an already reported procedure with slight modification (Onwudiwe and Ajibade, 2011). Briefly, N-methyl aniline (0.05 mol) was introduced into a round-bottom flask and carbon disulphide (0.05 mol) was added. The solution was placed inside ice to maintain a very low temperature and stirred for about 15 min. This was followed by the addition of 15 mL of concentrated aqueous ammonia and was further stirred for 5 h. Light yellow solid precipitate was obtained at the end of the reaction and the obtained precipitate was filtered under suction and rinsed with 100 mL of ice-cold absolute ethanol.

The copper(II)-*N*-methyl-*N*-phenyl dithiocarbamate complex was prepared by reacting 20 mL aqueous solution of the dithiocarbamate ligand (8.0 mmol) with 30 mL ethanol solution of copper(II) nitrate hemipentahydrate (4.0 mmol) in a round-bottomed flask. The reaction was continued for 1 h at room temperature, forming deep brown precipitates. The obtained product was filtered, rinsed with absolute ethanol and recrystallized in a solution of chloroform. Similar procedure was used for the synthesis of the bismuth(III)- tris(*N*-methyl-*N*-phenyl dithiocarbamate) complex but 12.0 mmol of the *N*-methyl-*N*-phenyl dithiocarbamate ligand was used against the 4.0 mmol of the bismuth salt.

4.1.4 Synthesis of $Cu_{3.21}Bi_{4.79}S_9$

The $Cu_{3.21}Bi_{4.79}S_9$ nanoparticles were synthesized under nitrogen to prevent oxidation. 0.1069 g (0.25 mmol) of copper (II) bis(*N*-methyl-*N*-phenyl dithiocarbamate) complex, 0.5663 g (0.75 mmol) of bismuth(III)- bis(*N*-methyl-*N*-phenyl dithiocarbamate) and 30 mL of oleylamine (capping agent) were introduced into three-necked round bottom flask. The mixture was heated to 200 °C at a constant heating rate of 10 °C/min and stirred for 1 h. After the reaction, the flask was allowed to cool to 40 °C and the addition of excess ethanol resulted into the precipitation of the nanoparticles. The products were separated from the solution by centrifuging at 4500 rpm for 5 min followed by decantation of the supernatant. The as-synthesized nanoparticles were washed four times with absolute ethanol and dried. The entire process is summarized in **Scheme 1**.

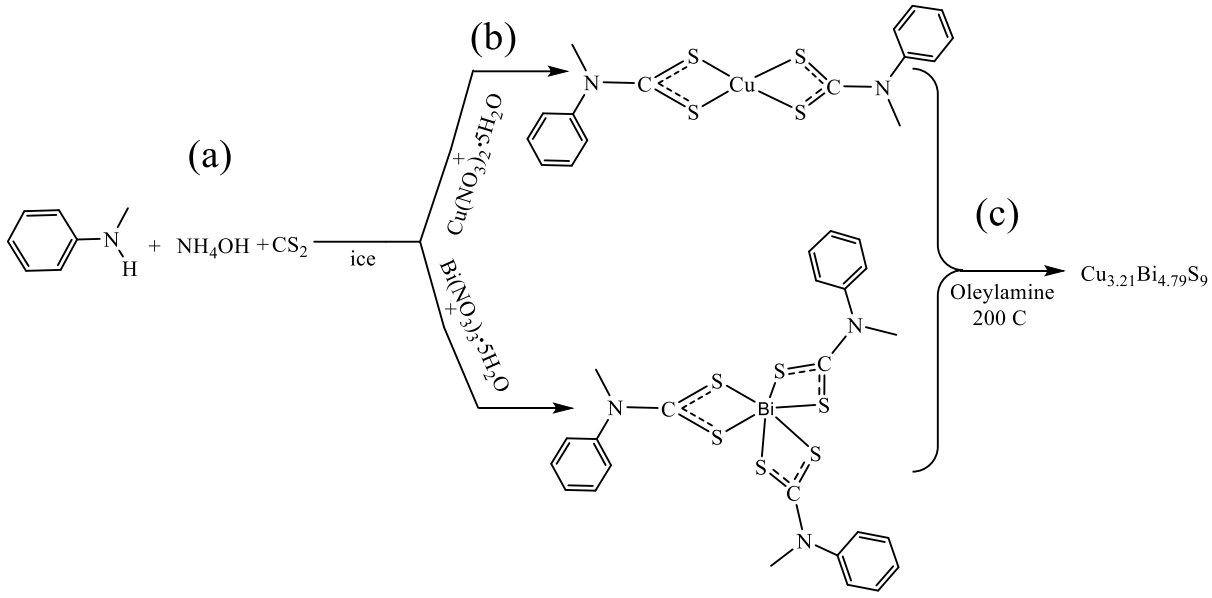

Scheme 1: Reaction process for the synthesis of (a) ligand, (b) complexes and (c) copper bismuth sulphide ($Cu_{3.21}Bi_{4.79}S_9$) nanoparticles.

4.1.5 *Synthesis of $Cu_{3.21}Bi_{4.79}S_9$/ gC_3N_4*

The graphitic carbon nitride and the as-prepared copper bismuth sulphide were homogenised in the ratio of 3:1 w/w respectively. The homogenized sample was ground and calcined at 300 ^oC for 2 h in a muffle furnace to obtain $Cu_{3.21}Bi_{4.79}S_9$/ gC_3N_4.

4.1.6 *Photocatalytic investigations*

Reduction of aqueous solution of hexavalent chromium was evaluated by using $Cu_{3.21}Bi_{4.79}S_9$/ gC_3N_4 photocatalyst. In a typical investigation, 40 mL of 10 mg/L $K_2Cr_2O_7$ solution was introduced into a 100 mL beaker. Dilute hydrochloric acid was used to adjust the pH of the solution to 2. Afterwards, 10 mg of the photocatalyst was measured into the content in the beaker and stirred for 20 min in the dark to attain the adsorption-desorption equilibrium. This was immediately followed by the irradiation with 48 W visible LED light. During the reaction, aliquots were taken at 15 min regular intervals. The concentration of each aliquot was determined by using UV-visible spectrophotometer. The percentage of Cr(VI) that was photocatalytically reduced was estimated by using **Equation** (i), while the rate of photocatalytic reduction was obtained via pseudo- first order kinetics given in **Equation (ii**).

$$\boldsymbol{Percentage\ photocatalytic\ reduction} = \frac{C_o - C_t}{C_o} \times \mathbf{100\%} \text{.....(i)}$$

$$-\boldsymbol{Kt} = \mathbf{ln}(\frac{C_t}{C_o}) \text{..... (ii)}$$

$$\boldsymbol{Half - life} = {}^{\mathbf{ln\,2}}/_{\boldsymbol{k}} = {}^{\mathbf{0.693}}/_{\boldsymbol{k}} \text{..... (iii)}$$

Where C_o and C_t represent the initial and concentration at time t of aqueous Cr(VI), t is the reaction time and k is the pseudo- first order reaction rate constant.

4.2 Results and Discussion

4.2.1 *X-ray diffraction (XRD) studies*

The XRD pattern (Fig. 4.1) showed the formation of graphitic carbon nitride functionalized with $Cu_{3.21}Bi_{4.79}S_9$ without the appearance of peaks corresponding to metallic bismuth, copper sulphides and bismuth sulphides. The two peaks at 2 theta values of 13.2° and 27.5°, which are indexed as the (100) and (002) respectively, emanated from the graphitic carbon nitride. The (100) peak is ascribed to the in-planar structural packing of tris-s-triazine, while the (002) peak is because of the interlayer stacking of the aromatic conjugated systems (Ajiboye et al., 2020; Ajiboye et al., 2022b; Hasanvandian et al., 2022; Zhong et al., 2022). Apart from the peaks indexed for the graphitic carbon nitride, other major peaks in the pattern indexed to (202), (-204), (-112), (-403), (-312), (311), (-514) and (-316) planes corresponded to the base-centered

monoclinic structure (JCPDS card No_01-073-1202, space group C2/m (12). The existence of these peaks confirmed the formation of graphitic carbon nitride functionalized with $Cu_{3.21}Bi_{4.79}S_9$.

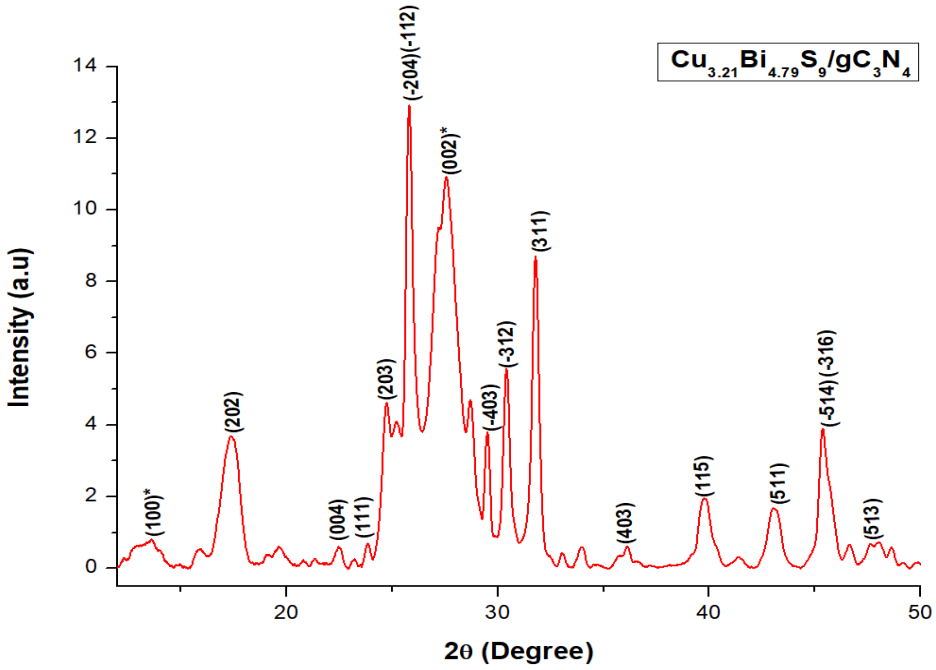

Figure 4.1: XRD pattern of $Cu_{3.21}Bi_{4.79}S_9/gC_3N_4$. The peaks of graphitic carbon nitride are asterisked (*).

4.2.2 *FTIR studies*

Fig. S1 is the FTIR spectrum of pristine copper bismuth sulphide, the peaks due the NH_2 bending mode (873 cm^{-1}), NH_2 scissor mode (1429 cm^{-1}), C-N stretch (1009 cm^{-1}), C-H bending mode (1569 cm^{-1}) and C-H stretching mode (2920-2669 cm^{-1}) were all from the oleylamine (used as the surfactant) (Salavati-Niasari et al., 2009). The FTIR of pristine graphitic carbon nitride and $Cu_{3.21}Bi_{4.79}S_9/gC_3N_4$-are presented in Fig. 4.2. Both spectra showed characteristic broad peak at 3128 cm^{-1} due to the presence of N-H bonds. Also, the peaks between 1225-1629 cm^{-1} appeared in both spectra due to the presence of –CN bonds for the heterocyclic ring. The last peak that is common to them appeared at 799 cm^{-1}, and this is attributed to the heptazine rings in the structure of graphitic carbon nitride and the nanocomposite (Xu et al., 2013; Zhong et al., 2022). In addition to these peaks, the peaks at 603 and 1104 cm^{-1} were visible in the spectra of the nanocomposite but they were absent in the

pristine graphitic carbon nitride. The peak at 603 cm^{-1} can be attributed to the Cu-S bond (Riyaz et al., 2016), while the peak at 1104 cm^{-1} can be attributed to the Bi-S stretching vibration (Veerakumar et al., 2022). This further showed that the ternary copper bismuth sulphide was incorporated into the graphitic carbon nitride.

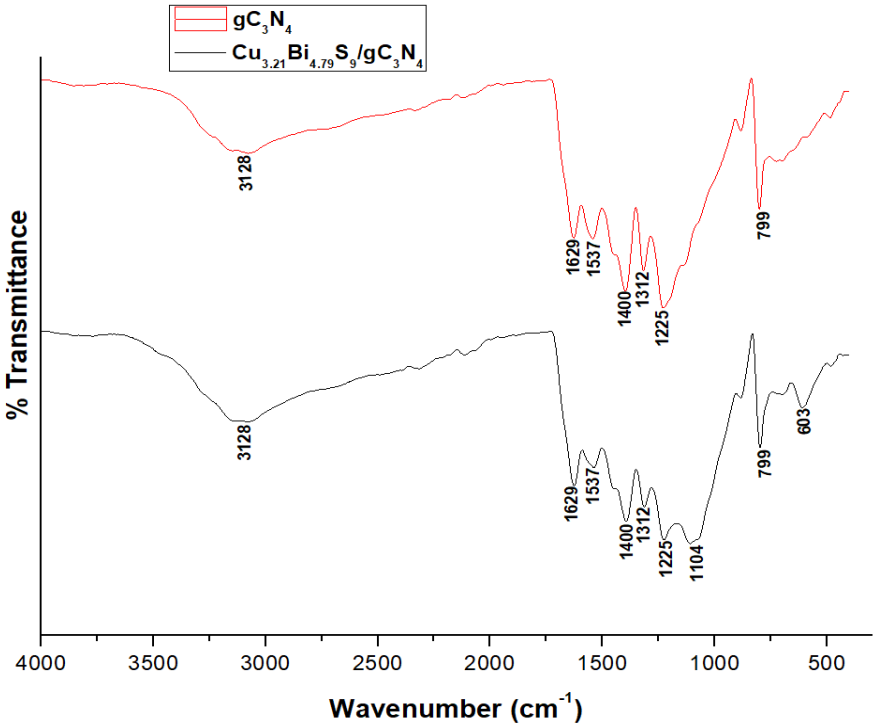

Figure 4. 2: FTIR spectra of gC_3N_4 and $Cu_{3.21}Bi_{4.79}S_9/gC_3N_4$ nanocomposite.

4.2.3 *Morphological properties of the $Cu_{3.21}Bi_{4.79}S_9$ and $Cu_{3.21}Bi_{4.79}S_9/gC_3N_4$*

The SEM images of $Cu_{3.21}Bi_{4.79}S_9$ and $Cu_{3.21}Bi_{4.79}S_9/gC_3N_4$ shown in Fig. 4.3(a-b) showed some agglomeration in their surface morphology. The level of agglomeration is higher in the pristine $Cu_{3.21}Bi_{4.79}S_9$ compared to that of $Cu_{3.21}Bi_{4.79}S_9/gC_3N_4$. Similarly, there is more uniformity in the particles obtained from the pristine copper bismuth sulphide compared to that of the nanocomposite. Hence, there is noticeable change in the surface morphology after the incorporation of graphitic carbon nitride to the pristine $Cu_{3.21}Bi_{4.79}S_9$. The EDX analysis (Fig. 4.3(c-d)) confirmed the presence of copper, bismuth and sulphur in the $Cu_{3.21}Bi_{4.79}S_9$. Also, the EDX analysis showed the presence of carbon, nitrogen, copper, bismuth and sulphur in

$Cu_{3.21}Bi_{4.79}S_9/gC_3N_4$. The oxygen and carbon impurities were visible in the EDX spectra of $Cu_{3.21}Bi_{4.79}S_9$ and while oxygen impurity was detected in the nanocomposite.

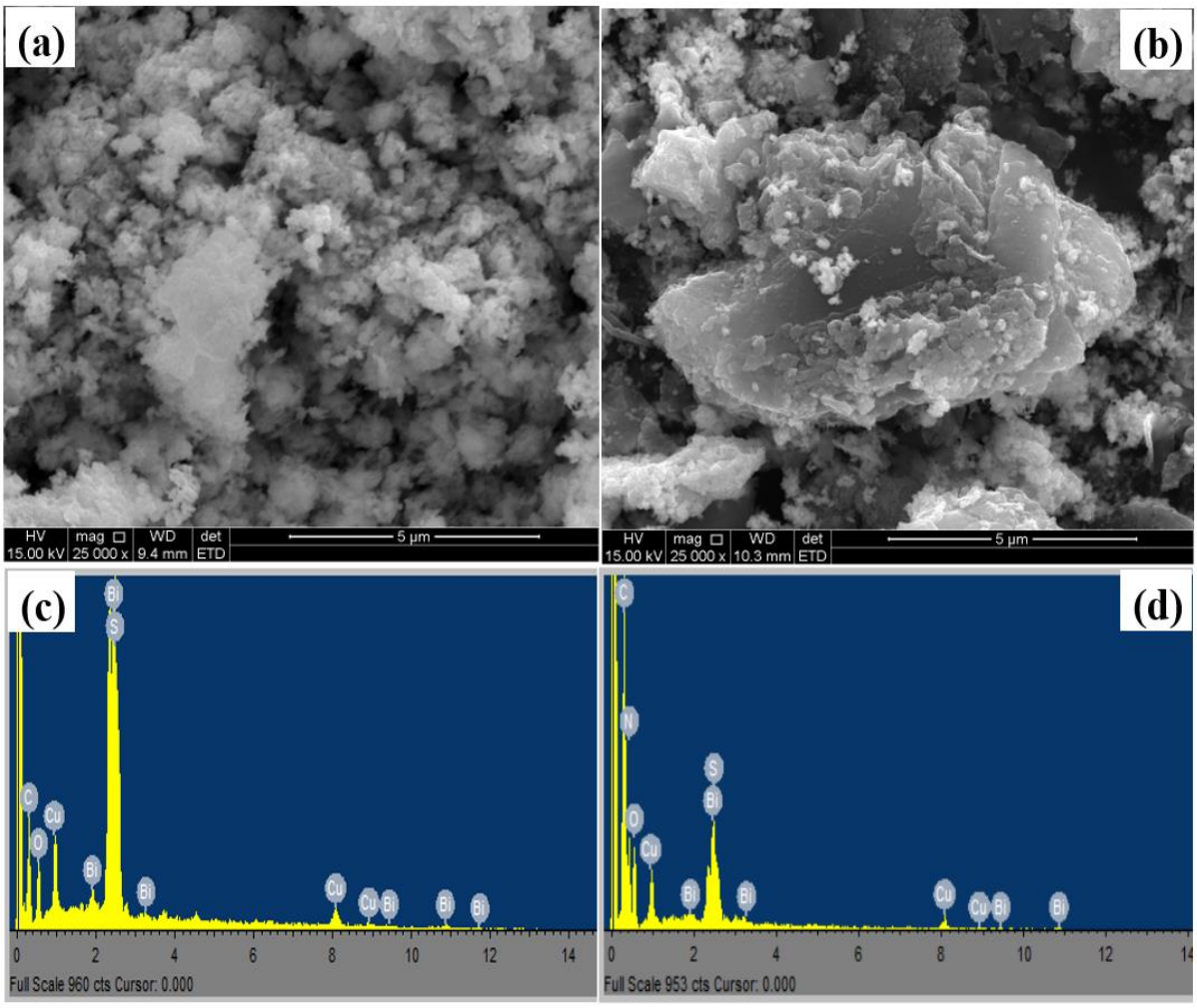

Figure 4.3: SEM images of (a) $Cu_{3.21}Bi_{4.79}S_9$, (b) $Cu_{3.21}Bi_{4.79}S_9/gC_3N_4$; and their respective EDX spectra (c and d).

The TEM images of the $Cu_{3.21}Bi_{4.79}S_9$ nanoparticles and the $Cu_{3.21}Bi_{4.79}S_9/gC_3N_4$ nanocomposite is shown in Fig. 4.4. The internal morphology and microstructure of the nanocomposite showed a rod-like structure embedded within a sheet-like aggregate. The sheet-like structure is due to the presence of graphitic carbon nitride in the nanocomposites (Esmati et al., 2021). The rods have a length of 190.0 nm and breadth of 14.4 nm as presented in the particle-size distribution histograms (Fig. 4.4(e-f)). As shown in the TEM image of pristine $Cu_{3.21}Bi_{4.79}S_9$ (Fig. S1), the rod-like structures are the pristine $Cu_{3.21}Bi_{4.79}S_9$. The HRTEM

image revealed that the d-spacing of the nanocomposite is 0.5206 nm along the (311) plane of the $Cu_{3.21}Bi_{4.79}S_9$ in the nanocomposite. In the pristine $Cu_{3.21}Bi_{4.79}S_9$, the d-spacing was 0.3822 nm along the (311) plane (Fig. S2). These d-spacings were obtained from Bragg's equation and there was noticeable increase in the d-spacing of the nanocomposite compared with that of the pristine $Cu_{3.21}Bi_{4.79}S_9$. The elemental mapping (Figure S3 and S4) further revealed that the copper bismuth sulphide was well dispersed across the matrices of the graphitic carbon nitride in the nanocomposite.

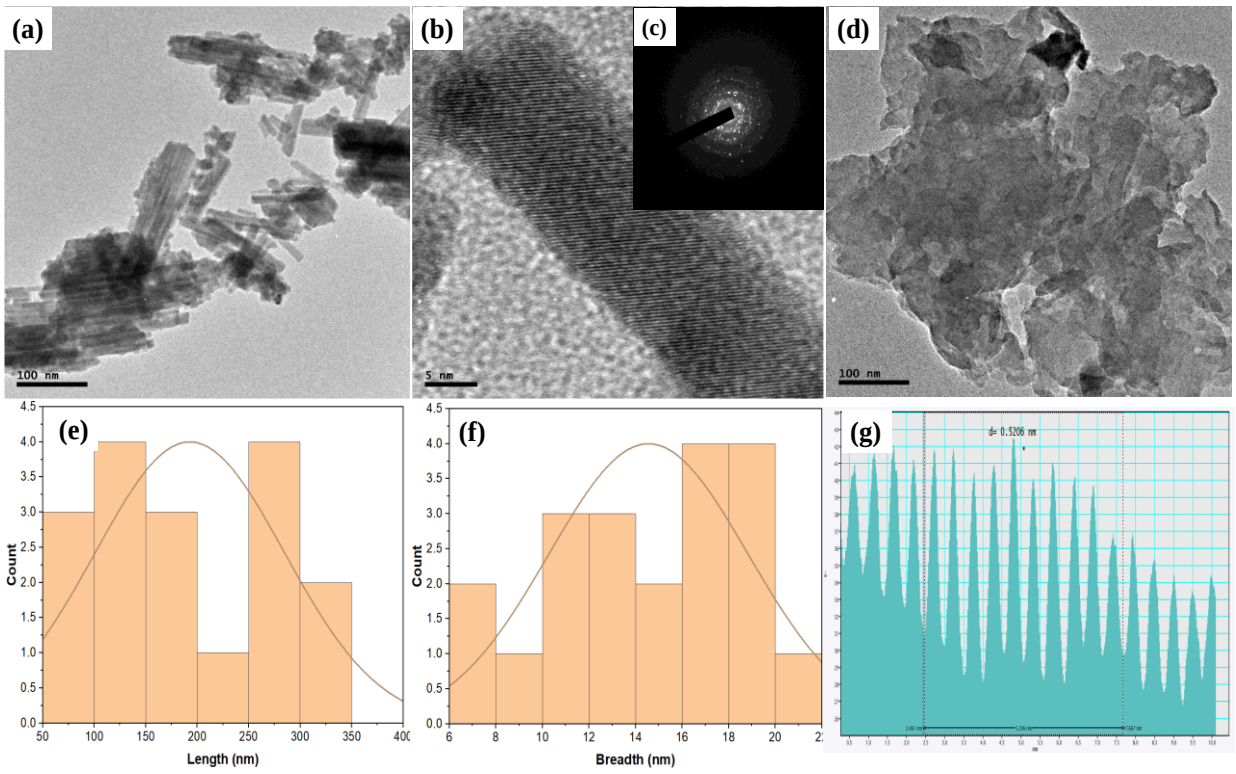

Figure 4.4: (a)TEM, (b) HRTEM and (c)SAED images of $Cu_{3.21}Bi_{4.79}S_9$; (d) TEM image of $Cu_{3.21}Bi_{4.79}S_9/gC_3N_4$; particle size distribution histogram of $Cu_{3.21}Bi_{4.79}S_9$; showing (e) length and (f) breadth. (g) of the encapsulated nanoparticles showing no change in d spacing.

4.2.4 *Optical properties*

Fig. 4.5 presents the overlaid absorption spectra of the gC_3N_4, $Cu_{3.21}Bi_{4.79}S_9$ and $Cu_{3.21}Bi_{4.79}S_9/gC_3N_4$.The spectrum of the gC_3N_4 showed its characteristic absorption maximum at 337 nm due to unsaturated n-π^* transitions arising from the nitrogen atoms of the terminal $–NH_2$, polyheptazine and polytriazine structural units. Another characteristic

absorption maximum appeared at 394 nm and it is attributed to the $\pi - \pi^*$ transition of conjugated heterocyclic aromatic components of graphitic carbon nitride (Fig. 4.5a). This transition also accounts for the pale-yellow colouration of graphitic carbon nitride (Miller et al., 2017; Ajiboye et al., 2022b). The maximum absorption for $Cu_{3.21}Bi_{4.79}S_9$ was found at 218 nm, unlike in the non-fractional phase (Cu_3BiS_3) whose absorption maximum was reported to be at 468 nm (Yan et al., 2013). The absorption maximum of $Cu_{3.21}Bi_{4.79}S_9$ shifted to 225 nm after compositing with graphitic carbon nitride. The absorption peak of the graphitic carbon nitrides also appeared in the nanocomposites, but with a reduction in the intensities of these peaks. The indirect band gap energy of gC_3N_4, $Cu_{3.21}Bi_{4.79}S_9$ and $Cu_{3.21}Bi_{4.79}S_9/gC_3N_4$ were estimated by plotting $(ahv)^{1/2}$ against the energy of the photon (hv), and were obtained as 2.88, 0.55, and 1.25 eV respectively (Fig. 4.5b).

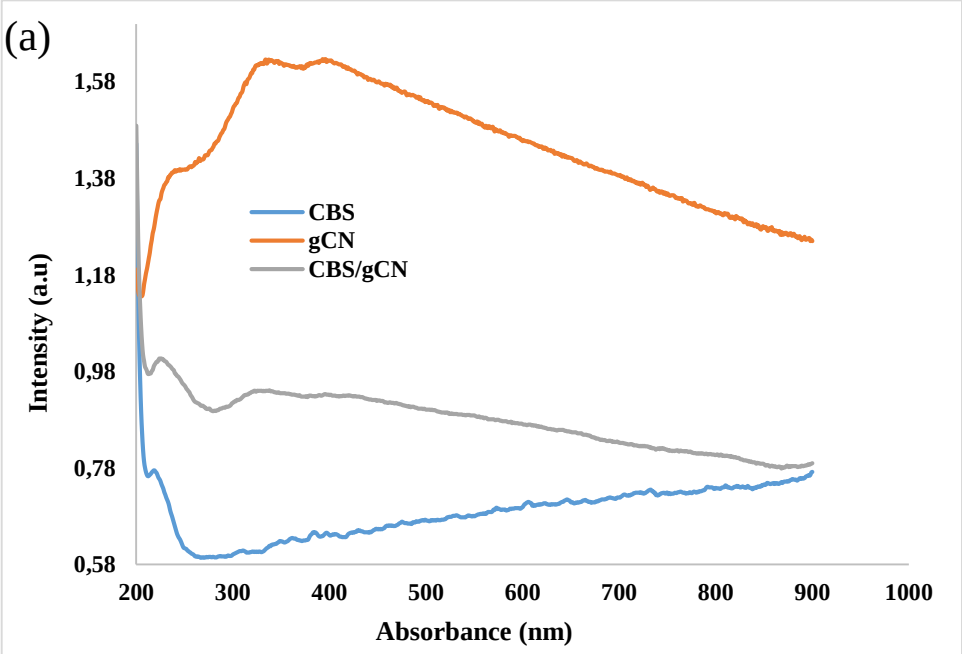

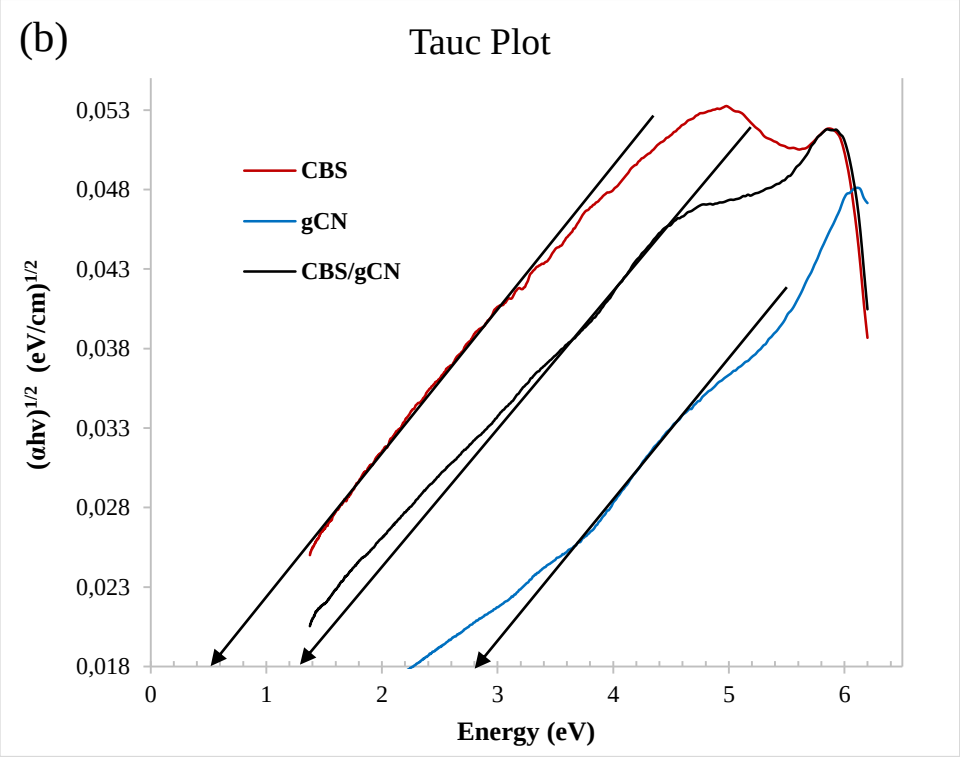

Figure 4.5: (a) Overlaid UV spectra of $Cu_{3.21}Bi_{4.79}S_9$, gC_3N_4 and $Cu_{3.21}Bi_{4.79}S_9/gC_3N_4$; (b) Tauc plot of $Cu_{3.21}Bi_{4.79}S_9$, gC_3N_4 and $Cu_{3.21}Bi_{4.79}S_9/gC_3N_4$

4.2.5 *Thermal studies of $Cu_{3.21}Bi_{4.79}S_9/gC_3N_4$ composite*

The TGA graph (Fig. 4.6a) of the nanocomposite showed a slight weight loss at 72 °C due to the elimination of low-molecular weight molecules (such as water and methanol) (Wang et al., 2015). A pronounced weight loss occurred between 439 °C to 507 °C, which indicated the decomposition of graphitic carbon nitride. Complete volatilization of graphitic carbon nitride was observed at 677 °C. The decomposition profile was in agreement with the results obtained from the DSC graph (Fig. 4.6b), which showed endothermic peaks at 71.97 °C and 676.65 °C respectively. The high melting point of graphitic carbon nitride could be attributed to the presence of hydrogen bonding that exists between the strands of the polymeric melon units containing NH and NH_2 groups (Guan et al., 2016). Even after the heating temperature reached 1000 °C, the complete decomposition of the nanocomposite was not achieved because approximately 20% of the sample remained as residue and may be ascribed to the $Cu_{3.21}Bi_{4.79}S_9$ nanoparticles. This shows that the total volatilization of the nanocomposite is not feasible at 1000 °C due to the prsecence of the nanoparticles, which enhances the thermal stability of the nanocomposite

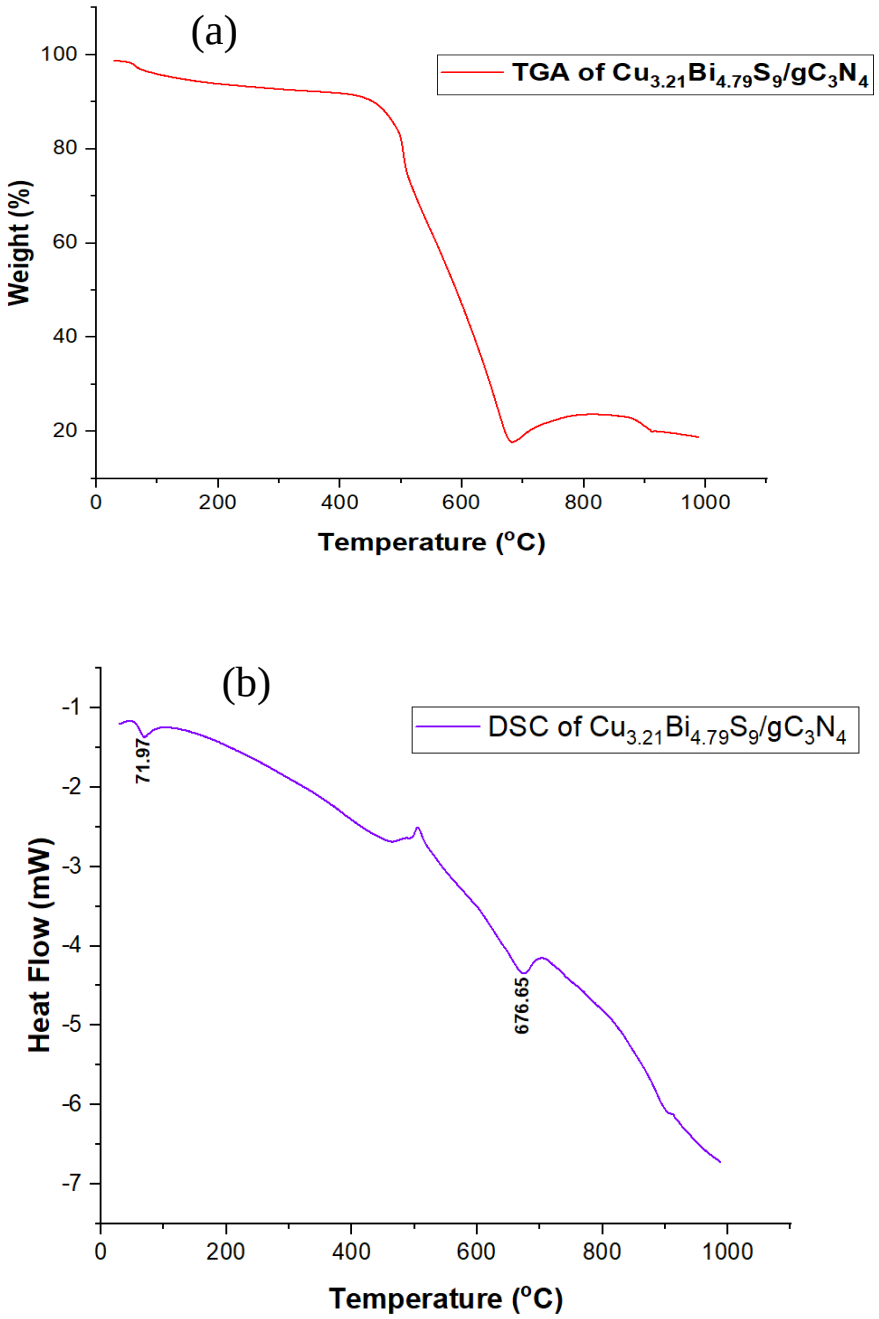

Figure 4.6: TGA and DSC of $Cu_{3.21}Bi_{4.79}S_9/gC_3N_4$ under nitrogen gas

4.3 Optimum conditions for the photocatalytic investigations

The zeta potential of the nanocomposite was found to be highly negative in the alkaline pH (-33.73 mV) and under neutral pH (-18.70 mV) while it is positive under acidic condition (+12.95 mV) (Fig. 4.7). It has earlier been reported that hexavalent chromium exists as negatively-charged CrO_4^{2-} under acidic condition. Since the surface of the photocatalyst has positive zeta

potential, there will be better hexavalent chromium adsorption under acidic condition. This is because of the electrostatic force of attraction between the species and the surface of the photocatalyst. Consequently, the pH used for the photocatalytic reduction of chromium was pH of 2. Based on previous reports, the concentration of Cr(VI) and the dosage of the photocatalyst chosen for the investigations are 10 mg/L and 10 mg respectively (Yang and Lee, 2006; Abinaya et al., 2020; Gan et al., 2020).

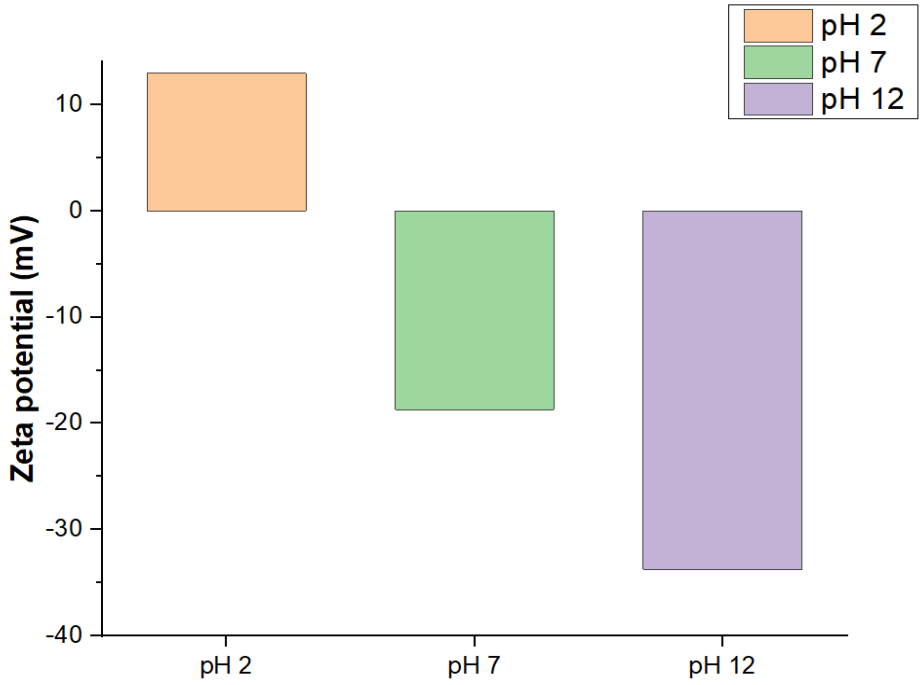

Figure 4.7: Zeta potential of $Cu_{3.21}Bi_{4.79}S_9/gC_3N_4$ at pH 2, 7 and 12.

4.4 Photocatalytic investigations

The rate of photocatalytic reduction of Cr(VI) was investigated by using the pristine $Cu_{3.21}Bi_{4.79}S_9$ nanoparticles, graphitic carbon nitride and their nanocomposite as the photocatalyst under visible light irradiation. As shown in (Fig. 4.8(a and b)), the rate and percentage of photocatalytic reduction of Cr(VI) was found to be 0.0076 min^{-1} and 41.98% respectively when the pristine $Cu_{3.21}Bi_{4.79}S_9$ were used as the photocatalyst, while it was 0.0286 min^{-1} and 78.57% respectively when the graphitic carbon nitride and the $Cu_{3.21}Bi_{4.79}S_9$ nanocomposites were used as the photocatalysts. The over three folds' increase could be due to the polymeric nature of graphitic carbon nitride and its ability to adsorb the Cr(VI) better

than the $Cu_{3.21}Bi_{4.79}S_9$photocatalyst (Ajiboye et al., 2020; Hasija et al., 2021; Ajiboye et al., 2022b). Due to better adsorption property, the photocatalytic performance was higher when graphitic carbon nitride was used as the photocatalyst (Qi et al., 2020; Saha et al., 2020). There was a synergistic effect when the composite made from the two photocatalysts was used under visible light. The pseudo first order rate constant and percentage photocatalytic reduction increased to 0.0393 min^{-1} and 92.77% respectively. This shows that there was improvement in the photocatalytic rate of reduction of Cr(VI) by a factor of 1.37 and 5.17 compared to pristine graphitic carbon nitride and $Cu_{3.21}Bi_{4.79}S_9$respectively. Similar synergistic photocatalytic effect was reported when graphitic carbon nitride was functionalized with other chalcogenides (Niu et al.; Wang et al., 2020; Wu et al., 2022).

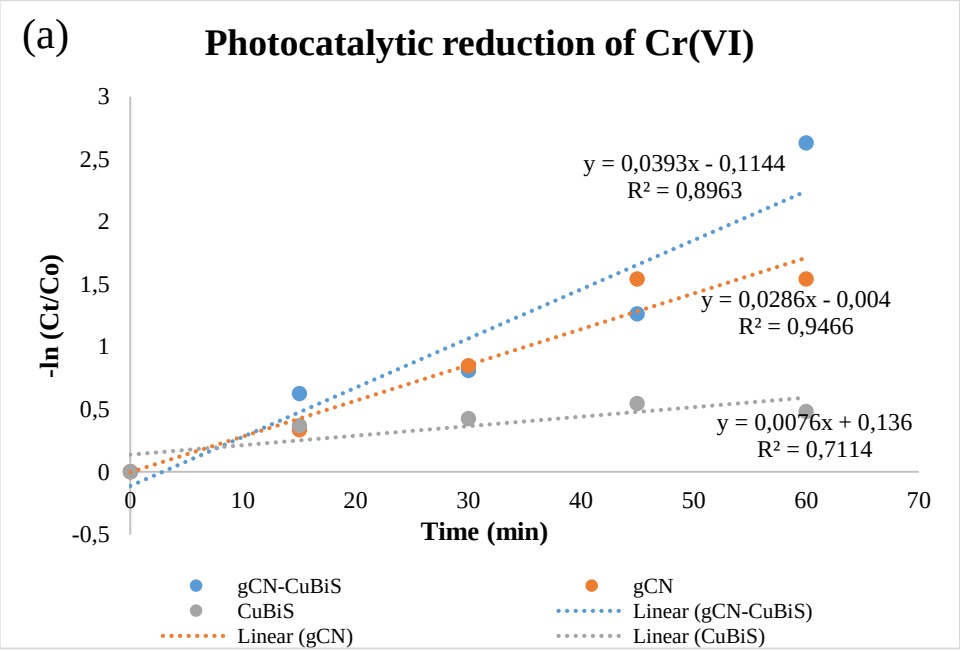

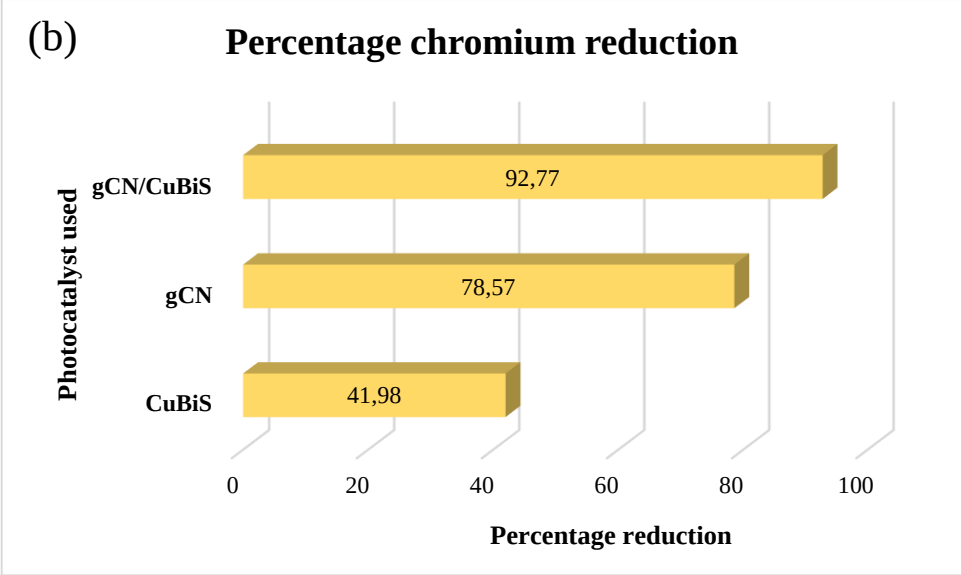

Figure 4.8: The (a) Pseudo-first order rate and (b) percentage of photocatalytic reduction of Cr(VI) using pristine $Cu_{3.21}Bi_{4.79}S_9$, graphitic carbon nitride and their composite.

4.4.1 Effect of initial temperature

The rate of photocatalytic reduction of Cr(VI) was investigated at very low temperature in ice (8 ^oC), at 25 and 50 ^oC, and the obtained results were compared. The rate was 0.0393 min^{-1} under room temperature conditions, while it dropped to 0.0077 and 0.0041 min^{-1} respectively in ice and at elevated temperature. The results showed that the rate of photocatalytic reduction was comparatively higher under room temp. conditions than at higher and lower temperature (Fig. 4.9). Based on the kinetic postulates and the fact that the excitation process could make the change in Gibb's free energy (ΔG) to be lower than zero; the increase in temperature is expected to lead to increasing rate of photocatalytic process. However, higher temperature also leads to a drop in photocurrent and higher rate of recombination of the photogenerated holes and electrons (Meng et al., 2018). Furthermore, Gibb's free energy ΔG of the photocatalysts has been reported not to be affected by heat change (Liu et al., 2014). The decrease in the rate of photocatalytic reduction of Cr(VI) at high temperature may be attributed to these reasons highlighted. Temperature increase can lead to the rate of photocatalytic reduction of Cr(VI) if there is enough thermodynamic driving force for electron transfer in the photocatalytic interface (Meng et al., 2018) as shown in **Equation (iv)**. Obviously, this cannot be attained at a temperature that is as low as 8 ^oC, which also accounts for low photocatalytic reduction of Cr(VI).

$$K_{IT} = V_o e^{\frac{-Q}{KT}} \text{.....(iv)}$$

Where T is the thermal temperature, k is Boltzmann constant, V_o is a pre-exponential factor, Q is apparent activation energy of the interfacial transfer and k_{IT} is the rate constant of interfacial transfer.

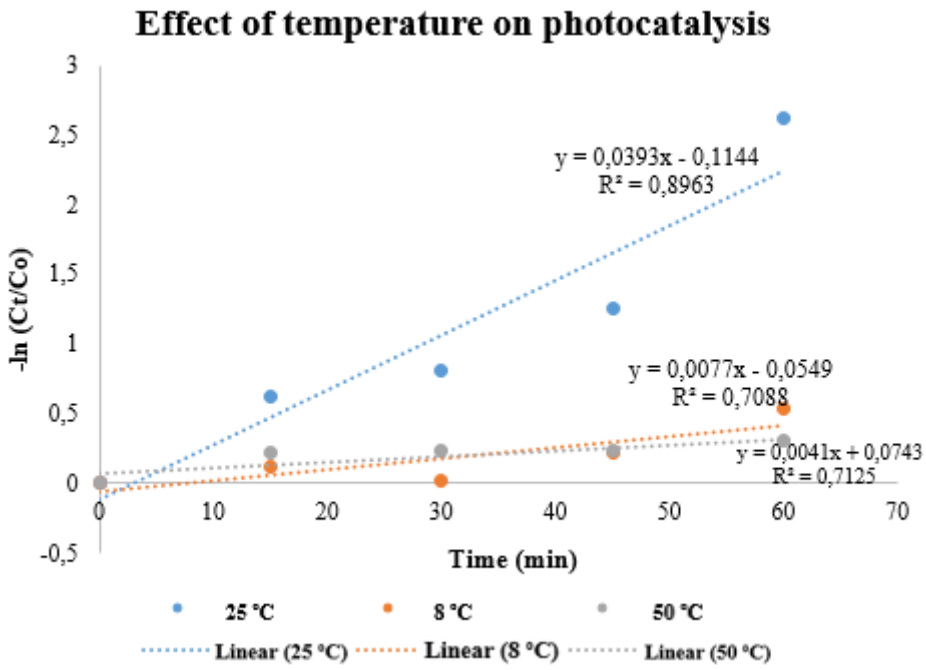

Figure 4.9: Photocatalytic reduction of Cr(VI) at varied temperature.

4.4.2 Effect of the presence of bisphenol A

The effects of the presence of bisphenol A on the photocatalytic reduction of Cr(VI) was investigated. It was observed that the presence of bisphenol A reduced the rate of photocatalytic reduction of Cr(VI) by more than 20 folds (from 0.0393 min^{-1} to 0.0019 min^{-1}) (Fig. 4.10). The bisphenol A in the photocatalytic system degraded with the pseudo-first order rate constant of 0.0164 min^{-1}. The simultaneous degradation of bisphenol A with the photocatalytic reduction of Cr(VI) is in agreement with the report of the studies by Kim et al.,(Kim et al., 2015). It shows that the Cr(VI) could be the electron scavenger of $Cu_{3.21}Bi_{4.79}S_9/gC_3N_4$-mediated photocatalytic bisphenol A degradation (Xie et al., 2006). However, there was retarded performance in the reduction of Cr(VI) in the presence of bisphenol A contrary to the synergistic performance reported by Kim et al.,(Kim et al., 2015). The observation could be

because bisphenol A is an aromatic compound and could resists photocatalytic degradation unlike the easily-oxidizable organics such as oxalic acid, which enhances the rate of photocatalytic process (Peller et al., 2003; Wang et al., 2008). Due to the resistance to degradation, the possibility of electron capture by Cr(VI) is reduced since the positively-charged holes are not scavenged by the added organics (Yang et al., 2012).

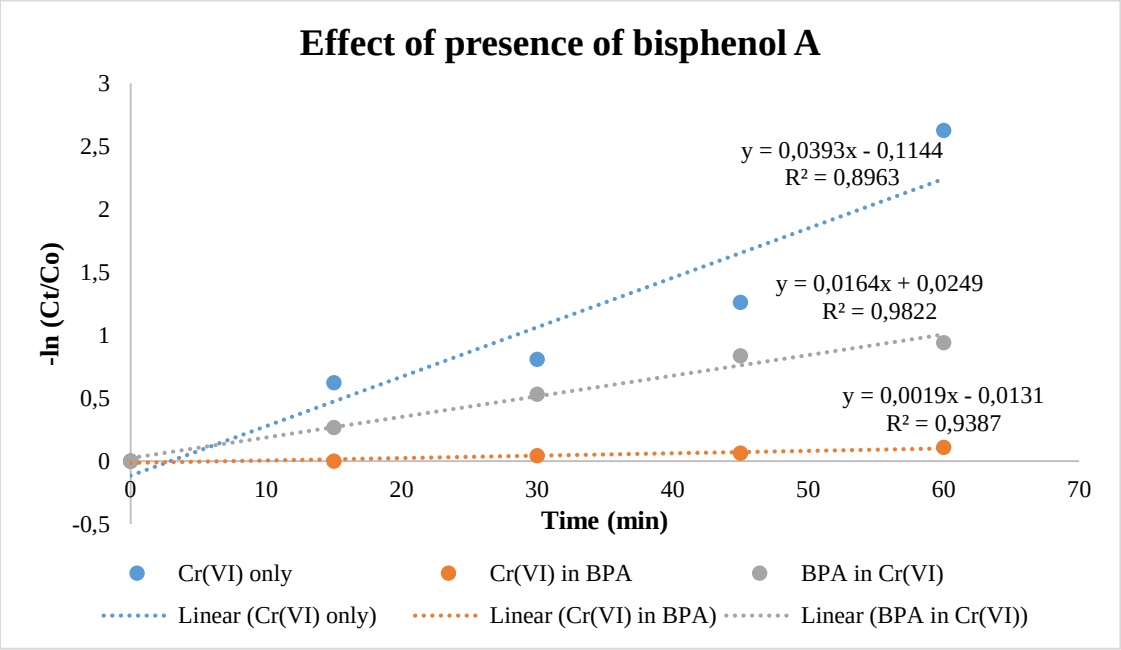

Figure 4.10: The photocatalytic reduction of Cr(VI) in the presence and absence of bisphenol A.

4.4.3 Effects of the presence of other heavy metal ions

The photocatalytic reduction of Pb(II) and Ag(I) was also investigated under similar photocatalytic conditions used for the reduction of Cr(VI) to Cr(III). This was for the purpose of studying how the presence of other ions affects the photoreduction process. The rate of photocatalytic reduction of these heavy metal ions was found to be low compared to that of Cr(VI). This could be because the surface of the photocatalyst is positively charged as well as Pb(II) and Ag(I), unlike Cr(VI) that exists as negatively-charged CrO_4^{2-} under the operating conditions. There was an electrostatic repulsion between the positively charged ions and the positively charged surface of the photocatalyst, while electrostatic attraction exists between the negatively charged CrO_4^{2-} and the positively-charged photocatalyst surface. Therefore, the adsorption of CrO_4^{2-} to the surface of the photocatalyst is better than that of Pb(II) and Ag(I). So, the rate of photocatalytic reduction is 0.0393, 0.0032 and 0.0004 min^{-1} for Cr(VI), Ag(I)

and Pb(II) respectively (Fig. 4.11a). The rate of photocatalytic reduction of Ag(I) is higher than that of Pb(II) and this could be ascribed to the reduction of monovalent silver, which requires one electron while the reduction of divalent lead requires two electrons. Also, the standard reduction potential of Ag^{+}/Ag is positive, while the standard reduction potential of Pb^{2+}/Pb is negative (as shown in **Equations (v-vii)**). The more positive the standard electrode potential, the more feasible the reaction (Song et al., 2014). The high rate of photocatalytic reduction of Cr(VI) can also be attributed to the high positive potential of Cr^{6+}/Cr^{3+}.

$Cr_2O_7^{2-} + 14H^{+} + 6e^{-} \rightarrow 2Cr^{3+} + 7H_2O$ $E^{o} = +1.36$ V……(v)

$Ag^{+} + e^{-} \rightarrow Ag_{(S)}$ $E^{o} = +0.80$ V……(vi)

$Pb^{2+} + 2e^{-} \rightarrow Pb_{(S)}$ $E^{o} = -0.13$ V……(vii)

The rate of photocatalytic reduction of Cr(VI) dropped from 0.0393 to 0.0039 min^{-1} (half-life of 17.64 mins to 177.73 min) when the mixture of Ag(I) and Pb(II) was introduced into the photocatalytic system as shown in Fig. 4.11b. This clearly shows that the presence of other heavy metal ions in the system containing Cr(VI) has antagonistic effects on the rate of photocatalytic reduction of Cr(VI). It has been reported that cations such as Mg(II), Ca(II), K(I) and Na(I) have little effects on the photocatalytic reduction of Cr(VI) due to the high oxidation state and stability of Cr(VI) (Wang et al., 2022b). On the contrary, the present results showed that the presence of heavy metal ions such as Pb(II) and Ag(I) has a significant impact.

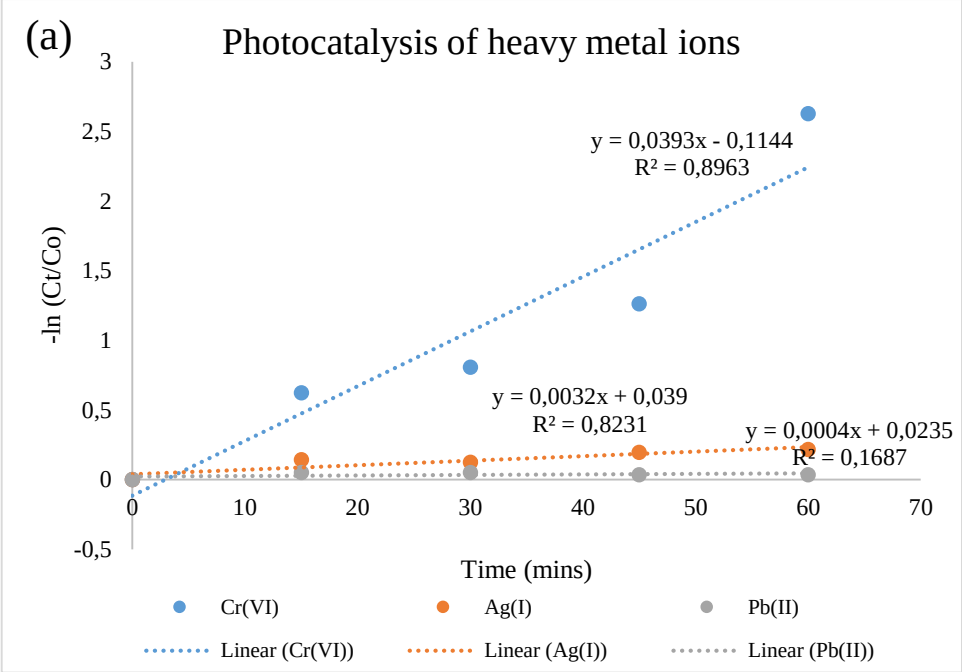

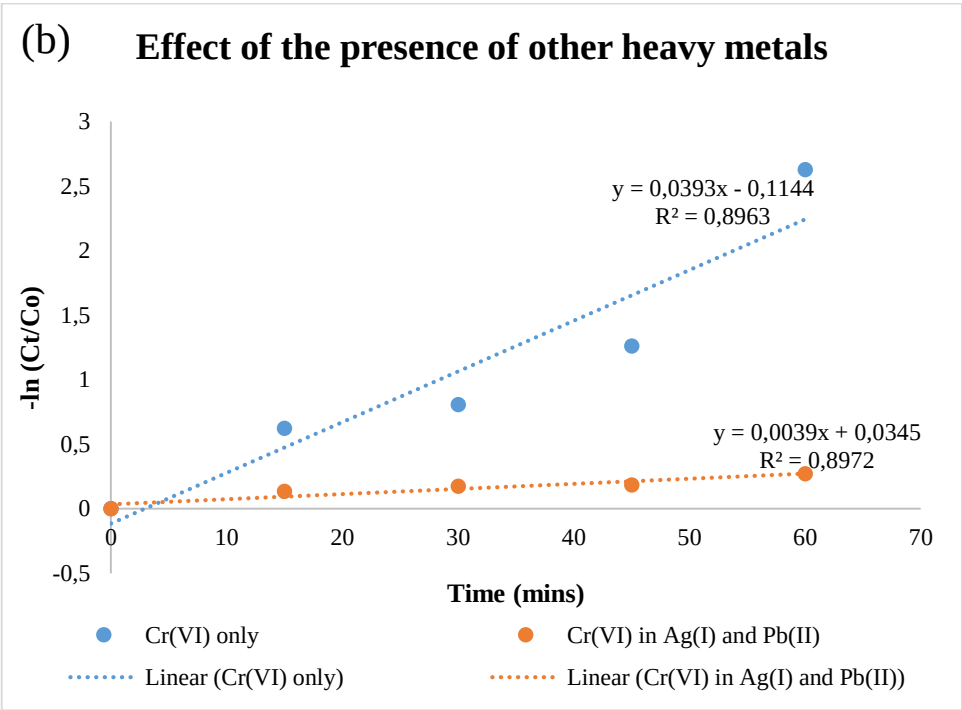

Figure 4.11: (a) Comparative studies of the photocatalytic reduction of Ag(I), Pb(II) and Cr(VI), (b) The photocatalytic reduction of Cr(VI) in the presence and absence of Ag(I) and Pb(II).

4.4.4 Radical scavenging experiment

The active species that participated in the photocatalytic reduction process were investigated using sodium nitrate, ascorbic acid (ASC), tert-butanol (TBA) and triethanol amine (TEA) as the scavenger for electrons (e^-), hydroxyl radicals ($\cdot OH^-$), superoxide ($\cdot O_2^-$) and holes (h^+) respectively. Without adding these scavengers, 92.77% of Cr(VI) was photocatalytically reduced over the $Cu_{3.21}Bi_{4.79}S_9/gC_3N_4$ under visible light. With the addition of ASC and TBA into the photocatalytic system, the percentage of Cr(VI) that was photocatalytically reduced decreased from 92.77% to 8.2% and 11.04% respectively (Fig. 4.12). This shows that both hydroxyl radicals and holes were captured during the photocatalytic reduction process. This was in agreement with the report that capturing of $\cdot O_2^-$ and $\cdot OH^-$ could improve the photocatalytic activities of e^- in reducing Cr(VI) (Shen et al., 2020). The introduction of sodium nitrate into the solution led to the drop in percentage photocatalytic reduction from 92.77% to 16.5%, which shows that e^- plays a prominent role in the photocatalytic reduction of Cr(VI). Compared to other scavengers, the contribution of TEA is the lowest. Although, there was also a significant decrease in the percentage reduction because once the h^+ has been captured, the rate of photocatalytic recombination reduces which allows the free e^- to effect the reduction of Cr(VI) to Cr(III).

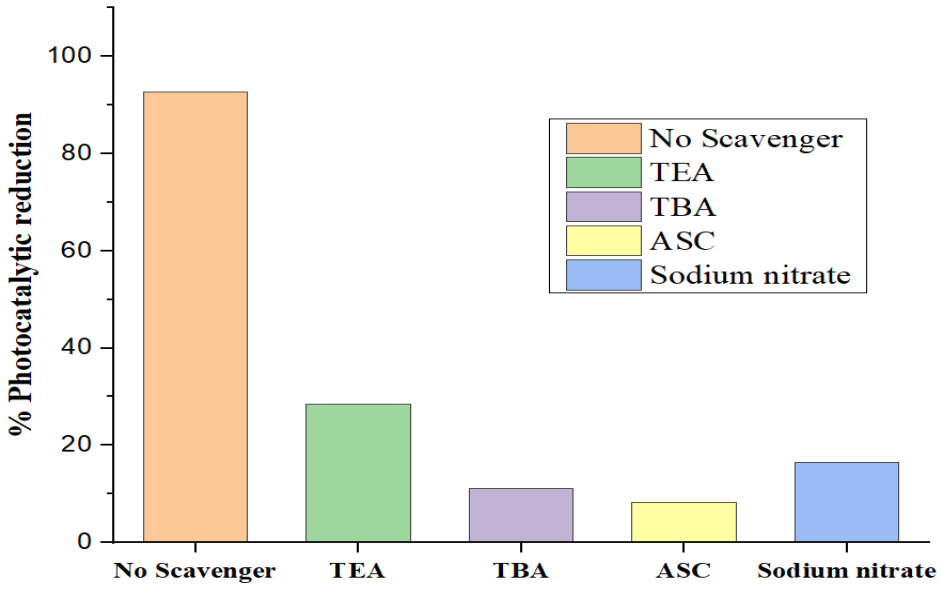

Figure 4.12: The results of the radical scavenging experiment.

CONCLUSION

In general, the graphitic carbon nitride functionalized with rod-like $Cu_{3.21}Bi_{4.79}S_9$ photocatalyst displayed a good photocatalytic reduction efficiency for Cr(VI) under visible light irradiation. The results revealed that over 90% of Cr(VI) was photocatalytically reduced within 1 h at a pH of 2, photocatalyst dosage of 10 mg and Cr(VI) concentration of 10 mg/L. The presence of bisphenol A, Ag(I) and Pb(II) in the photocatalytic system had inhibitory effects on the photocatalytic reduction of Cr(VI). The radical scavenging experiments revealed that electrons (e^-), hydroxyl radicals ($\cdot OH^-$) and superoxide ($\cdot O_2^-$) played significant roles in the photocatalytic reduction of Cr(VI) in the presence of as-prepared photocatalyst under visible light. A pseudo-first order kinetic study indicated 0.0076 min^{-1},0.0286 min^{-1} and 0.0393 min^{-1} rate constant for the nanoparticles, pristine gC_3N_4 and the nanocomposite respectively. This indicated an enhancement in rate of reduction by the functionalized graphitic carbon nitride by 1.37 and 5.17 folds than the pristine gC_3N_4 and $Cu_{3.21}Bi_{4.79}S_9$ respectively.

REFERENCES

Abinaya, M., Govindan, K., Kalpana, M., Saravanakumar, K., Prabavathi, S.L., Muthuraj, V., Jang, A., 2020. Reduction of hexavalent chromium and degradation of tetracycline using a novel indium-doped Mn_2O_3 nanorod photocatalyst. Journal of Hazardous Materials 397, 122885.

Ajiboye, T.O., Ajiboye, T.T., Marzouki, R., Onwudiwe, D.C., 2022a. The Versatility in the Applications of Dithiocarbamates. International Journal of Molecular Sciences 23, 1317.

Ajiboye, T.O., Imade, E.E., Oyewo, O.A., Onwudiwe, D.C., 2022b. Silver functionalized gC3N4: Photocatalytic potency for chromium(VI) reduction, and evaluation of the antioxidant and antimicrobial properties. Journal of Photochemistry and Photobiology A: Chemistry 432, 114107.

Ajiboye, T.O., Kuvarega, A.T., Onwudiwe, D.C., 2020. Graphitic carbon nitride-based catalysts and their applications: A review. Nano-Structures & Nano-Objects 24, 100577.

Ajiboye, T.O., Oyewo, O.A., Onwudiwe, D.C., 2021a. Conventional and Current Methods of Toxic Metals Removal from Water Using g-C_3N_4-Based Materials. Journal of Inorganic and Organometallic Polymers and Materials 31, 1419-1442.

Ajiboye, T.O., Oyewo, O.A., Onwudiwe, D.C., 2021b. The performance of bismuth-based compounds in photocatalytic applications. Surfaces and Interfaces 23, 100927.

Balasubramanian, V., Kumar, P.N., Sengottaiyan, D., 2017. Effect of deposition temperature on structural, optical and electrical properties of copper bismuth sulphide ($CuBiS_2$) thin films deposited by chemical bath deposition. Materials Science-Poland 35, 329-334.

Barma, M.C., Long, B.D., Sabri, M.F.M., Ramesh, S., Saidur, R., Said, S.M., Kimura, K., Hai, N.H., Huy, T.D., Trung, T.B., 2016. Synthesis of $Cu_{3.21}Bi_{4.79}S_9$ bismuth chalcogenide by mechanical alloying. Powder Technology 294, 348-352.

Chen, Q., Wang, X., Liu, W., Luo, T., Jin, Z., Zhang, Y., Huang, J., Zhang, H., Wang, J., Peng, F., 2022. Rapid photocatalytic reduction of Cr(VI) with high concentration in wastewater by In_2S_3-$ZnIn_2S_4$ heterostructure hierarchical microtubes under visible light. Journal of Solid State Chemistry 306, 122721.

Deng, M., Shen, S., Zhang, Y., Xu, H., Wang, Q., 2014. A generalized strategy for controlled synthesis of ternary metal sulfide nanocrystals. New Journal of Chemistry 38, 77-83.

Dhal, B., Thatoi, H.N., Das, N.N., Pandey, B.D., 2013. Chemical and microbial remediation of hexavalent chromium from contaminated soil and mining/metallurgical solid waste: A review. Journal of Hazardous Materials 250-251, 272-291.

Esmati, M., Allahresani, A., Naghizadeh, A., 2021. Synthesis and characterization of Graphitic Carbon Nitride/Mesoporous Nano-Silica (g-C_3N_4/KCC-1) nanocomposite as a novel highly efficient and recyclable photocatalyst for degradation of antibiotic in aqueous solution. Research on Chemical Intermediates 47, 1447-1469.

Gan, L., Geng, A., Song, C., Xu, L., Wang, L., Fang, X., Han, S., Cui, J., Mei, C., 2020. Simultaneous removal of rhodamine B and Cr(VI) from water using cellulose carbon nanofiber

incorporated with bismuth oxybromide: The effect of cellulose pyrolysis temperature on photocatalytic performance. Environmental Research 185, 109414.

Guan, B., Shan, Q.Y., Chen, H., Xue, D., Chen, K., Zhang, Y.X., 2016. Morphology Dependent Supercapacitance of Nanostructured $NiCo_2O_4$ on Graphitic Carbon Nitride. Electrochimica Acta 200, 239-246.

Hasanvandian, F., Shokri, A., Moradi, M., Kakavandi, B., Rahman Setayesh, S., 2022. Encapsulation of spinel $CuCo_2O_4$ hollow sphere in V_2O_5-decorated graphitic carbon nitride as high-efficiency double Z-type nanocomposite for levofloxacin photodegradation. Journal of Hazardous Materials 423, 127090.

Hasija, V., Raizada, P., Singh, P., Verma, N., Khan, A.A.P., Singh, A., Selvasembian, R., Kim, S.Y., Hussain, C.M., Nguyen, V.-H., Le, Q.V., 2021. Progress on the photocatalytic reduction of hexavalent Cr (VI) using engineered graphitic carbon nitride. Process Safety and Environmental Protection 152, 663-678.

Hua, Y., Hu, C., Arif, M., Chen, S.-m., Zhang, M., Liu, X., 2022. Direct Z-scheme WO_3/In_2S_3 heterostructures for enhanced photocatalytic reduction Cr(VI). Journal of Alloys and Compounds 908, 164488.

Kenfoud, H., Nasrallah, N., Baaloudj, O., Derridj, F., Trari, M., 2022. Enhanced photocatalytic reduction of Cr(VI) by the novel hetero-system $BaFe_2O_4/SnO_2$. Journal of Physics and Chemistry of Solids 160, 110315.

Kim, Y., Joo, H., Her, N., Yoon, Y., Sohn, J., Kim, S., Yoon, J., 2015. Simultaneously photocatalytic treatment of hexavalent chromium (Cr(VI)) and endocrine disrupting compounds (EDCs) using rotating reactor under solar irradiation. Journal of Hazardous Materials 288, 124-133.

Koutavarapu, R., Reddy, C.V., Syed, K., Reddy, K.R., Saleh, T.A., Lee, D.-Y., Shim, J., Aminabhavi, T.M., 2022. Novel Z-scheme binary zinc tungsten oxide/nickel ferrite nanohybrids for photocatalytic reduction of chromium (Cr (VI)), photoelectrochemical water

splitting and degradation of toxic organic pollutants. Journal of Hazardous Materials 423, 127044.

Kumar, A., Pandey, G., 2017. A review on the factors affecting the photocatalytic degradation of hazardous materials. Mater. Sci. Eng. Int. J 1, 1-10.

Li, Y., Li, X., Zhang, H., Xiang, Q., 2020. Porous graphitic carbon nitride for solar photocatalytic applications. Nanoscale Horizons 5, 765-786.

Liu, B., Zhao, X., Terashima, C., Fujishima, A., Nakata, K., 2014. Thermodynamic and kinetic analysis of heterogeneous photocatalysis for semiconductor systems. Physical Chemistry Chemical Physics 16, 8751-8760.

Meng, F., Liu, Y., Wang, J., Tan, X., Sun, H., Liu, S., Wang, S., 2018. Temperature dependent photocatalysis of g-C_3N_4, TiO_2 and ZnO: Differences in photoactive mechanism. Journal of Colloid and Interface Science 532, 321-330.

Miller, T.S., Jorge, A.B., Suter, T.M., Sella, A., Corà, F., McMillan, P.F., 2017. Carbon nitrides: synthesis and characterization of a new class of functional materials. Physical Chemistry Chemical Physics 19, 15613-15638.

Niu, B., Xiao, J. and Xu, Z., 2022. Recycling Spent LiCoO2 Battery as a High-efficient Lithium-doped Graphitic Carbon Nitride/Co3O4 Composite Photocatalyst and Its Synergistic Photocatalytic Mechanism. *Energy & Environmental Materials*.

Okla, M.K., Kokilavani, S., Mohebaldin, A., Thomas, A.M., Soufan, W., Abdel-Maksoud, M.A., AbdElgawad, H., Raju, L.L., Khan, S.S., 2022. Ag decorated CoO NPs supported on chitosan matrix for colorimetric detection of L-cysteine, antibacterial application and photocatalytic reduction of hexavalent chromium ions. Colloids and Surfaces A: Physicochemical and Engineering Aspects 640, 128318.

Olatunde, O.C., Onwudiwe, D.C., 2022. UV-light assisted activation of persulfate by rGO-Cu_3BiS_3 for the degradation of diclofenac. Results in Chemistry 4, 100273.

Onwudiwe, D.C., Ajibade, P.A., 2011. Synthesis, Characterization and Thermal Studies of Zn(II), Cd(II) and Hg(II) Complexes of N-Methyl-N-Phenyldithiocarbamate: The Single Crystal Structure of $[(C_6H_5)(CH_3)NCS_2]_4Hg_2$. International Journal of Molecular Sciences 12, 1964-1978.

Peller, J., Wiest, O., Kamat, P.V., 2003. Synergy of Combining Sonolysis and Photocatalysis in the Degradation and Mineralization of Chlorinated Aromatic Compounds. Environmental Science & Technology 37, 1926-1932.

Qi, K., Liu, S.-y., Zada, A., 2020. Graphitic carbon nitride, a polymer photocatalyst. Journal of the Taiwan Institute of Chemical Engineers 109, 111-123.

Qiu, J., Zhang, X., Xie, K., Zhang, X.-F., Feng, Y., Jia, M., Yao, J., 2019. Noble metal nanoparticle-functionalized Zr-metal organic frameworks with excellent photocatalytic performance. Journal of Colloid and Interface Science 538, 569-577.

Rahman, A., Khan, M.M., 2021. Chalcogenides as photocatalysts. New Journal of Chemistry 45, 19622-19635.

Ren, Y., Gong, T., Tan, S., Chen, M., Zhou, F., Lin, Y., Yang, L., Peng, Q., 2022. Photocatalytic activities of g-C_3N_4, Bi_3NbO_7 and g-C_3N_4/Bi_3NbO_7 in photocatalytic reduction of Cr(VI). Journal of Alloys and Compounds 902, 163752.

Riyaz, S., Parveen, A., Azam, A., 2016. Microstructural and Optical Properties of CuS Nanoparticles prepared by Sol Gel route. Perspectives in Science 8.

Saha, D., Hoinkis, T.J., Van Bramer, S.E., 2020. Electrospun, flexible and reusable nanofiber mat of graphitic carbon nitride: Photocatalytic reduction of hexavalent chromium. Journal of Colloid and Interface Science 575, 433-442.

Salavati-Niasari, M.; Fereshteh, Z.; Davar, F., 2009. Synthesis of oleylamine capped copper nanocrystals via thermal reduction of a new precursor. Polyhedron 28, 126-130

Sarker, J.C., Hogarth, G., 2021. Dithiocarbamate Complexes as Single Source Precursors to Nanoscale Binary, Ternary and Quaternary Metal Sulfides. Chemical Reviews 121, 6057-6123.

Shawky, A., Mohamed, R.M., Alahmadi, N., Zaki, Z.I., 2022. Enhanced photocatalytic reduction of hexavalent chromium ions over S-Scheme based 2D MoS_2-supported TiO_2 heterojunctions under visible light. Colloids and Surfaces A: Physicochemical and Engineering Aspects 641, 128564.

Shen, X., Zheng, T., Yang, J., Shi, Z., Xue, Q., Liu, W., Shan, S., Wong, M.H., 2020. Removal of Cr(VI) from Acid Wastewater by BC/$ZnFe_2O_4$ Magnetic Nanocomposite via the Synergy of Absorption-Photocatalysis. ChemCatChem 12, 4121-4131.

Song, J., Klein, E.L., Neese, F., Ye, S., 2014. The Mechanism of Homogeneous CO_2 Reduction by Ni(cyclam): Product Selectivity, Concerted Proton–Electron Transfer and C–O Bond Cleavage. Inorganic Chemistry 53, 7500-7507.

Sugaki, A., Shima, H., 1972. Phase relations of the Cu_2S-Bi_2S_3 system. Yamaguchi University for Technical Report 1, 45-70.

Sun, Y., Tan, R., Jin, Z., Zhang, Y., Li, X., Cai, Q., Nan, J., Liu, D., Yu, H., Gui, J., 2022. Template-free synthesis of Mn^{2+} doped hierarchical CuS yolk–shell microspheres for photocatalytic reduction of Cr(vi). CrystEngComm 24, 2171-2178.

Türkmen, D., Bakhshpour, M., Akgönüllü, S., Aşır, S., Denizli, A., 2022. Heavy Metal Ions Removal From Wastewater Using Cryogels: A Review. Frontiers in Sustainability 3, 765592.

Veerakumar, P., Jaysiva, G., Chen, S.-M., Lin, K.-C., 2022. Development of Palladium on Bismuth Sulfide Nanorods as a Bifunctional Nanomaterial for Efficient Electrochemical Detection and Photoreduction of Hg(II) Ions. ACS Applied Materials & Interfaces 14, 5908-5920.

Viti, C., Giovannetti, L., 2007. Bioremediation of soils polluted with hexavalent chromium using bacteria: a challenge. Environmental bioremediation technologies. Springer, pp. 57-76.

Wang, D., Cao, M., Feng, Y., Yao, J., 2022a. Self-assembly of $ZnIn_2S_4$ nanosheets on g-C_3N_4 nanotubes for efficient photocatalytic reduction of Cr(VI). Microporous and Mesoporous Materials 330, 111598.

Wang, H., Yuan, X., Wu, Y., Zeng, G., Chen, X., Leng, L., Li, H., 2015. Synthesis and applications of novel graphitic carbon nitride/metal-organic frameworks mesoporous photocatalyst for dyes removal. Applied Catalysis B: Environmental 174-175, 445-454.

Wang, H., Zhang, J., Wang, P., Yin, L., Tian, Y., Li, J., 2020. Bifunctional copper modified graphitic carbon nitride catalysts for efficient tetracycline removal: Synergy of adsorption and photocatalytic degradation. Chinese Chemical Letters 31, 2789-2794.

Wang, L., Wang, N., Zhu, L., Yu, H., Tang, H., 2008. Photocatalytic reduction of Cr(VI) over different TiO_2 photocatalysts and the effects of dissolved organic species. Journal of Hazardous Materials 152, 93-99.

Wang, Y., Liu, Y., Tian, F., Bao, S., Sun, C., Yang, W., Yu, Y., 2022b. $MnIn_2S_4$ nanosheets growing on rods-like β-MnO_2 via covalent bonds as high-performance photocatalyst for boosting Cr(VI) photocatalytic reduction under visible light irradiation: Behavior and mechanism study. Journal of Colloid and Interface Science 625, 264-277.

Wu, Q., Lu, D., Zhang, B., Kondamareddy, K.K., Zeng, Y., Zhang, Y., Wang, J., Zhou, M., D, N., Hao, H., Fan, H., 2022. Interfacial optimization of CeO_2 nanoparticles loaded two-dimensional graphite carbon nitride toward synergistic enhancement of visible-light-driven photoelectric and photocatalytic hydrogen evolution. International Journal of Hydrogen Energy 47, 2313-2326.

Xie, B., Zhang, H., Cai, P., Qiu, R., Xiong, Y., 2006. Simultaneous photocatalytic reduction of Cr(VI) and oxidation of phenol over monoclinic $BiVO_4$ under visible light irradiation. Chemosphere 63, 956-963.

Xu, J., Zhang, L., Shi, R., Zhu, Y., 2013. Chemical exfoliation of graphitic carbon nitride for efficient heterogeneous photocatalysis. Journal of Materials Chemistry A 1, 14766-14772.

Yan, C., Gu, E., Liu, F., Lai, Y., Li, J., Liu, Y., 2013. Colloidal synthesis and characterizations of wittichenite copper bismuth sulphide nanocrystals. Nanoscale 5, 1789-1792.

Yang, J.-K., Lee, S.-M., 2006. Removal of Cr(VI) and humic acid by using TiO_2 photocatalysis. Chemosphere 63, 1677-1684.

Yang, J.K., Lee, S.M., Siboni, M.S., 2012. Effect of different types of organic compounds on the photocatalytic reduction of Cr(VI). Environmental Technology 33, 2027-2032.

Zhao, Z., An, H., Lin, J., Feng, M., Murugadoss, V., Ding, T., Liu, H., Shao, Q., Mai, X., Wang, N., Gu, H., Angaiah, S., Guo, Z., 2019. Progress on the Photocatalytic Reduction Removal of Chromium Contamination. 19, 873-882.

Zhong, J., Ni, T., Huang, J., Li, D., Tan, C., Liu, Y., Chen, P., Wen, C., Liu, H., Wang, Z., Lv, W., Liu, G., 2022. Directional utilization disorder charge via In-plane driving force of functionalized graphite carbon nitride for the robust photocatalytic degradation of fluoroquinolone. Chemical Engineering Journal 442, 135943.

CHAPTER FIVE

Visible light-driven photocatalytic reduction of monovalent silver using a composite of $Ni_3Bi_2S_2$ incorporated into O-doped gC_3N_4

5.0 Introduction

Silver(I) ions are highly toxic to living organisms and they are able to persist in the environment since they are not removable by natural phenomenon (Zhang et al., 2018). One of the toxic effects of Ag(I) is noticeable in its actions against beneficial (and non-beneficial) bacteria. The membranes of bacteria are negatively charged which enhances their affinity for positively charged silver, but has no affinity for uncharged silver nanoparticles (Hsiao et al., 2015). Therefore, Ag(I) causes undesirable toxicological responses. It specifically slows down the signal transduction within the cell, thereby binding with DNA and/or protein that are present in the body of living organisms. Their abundance in the environment can be likened to natural mechanisms such as Trojan-horse mechanism that contributes to the conversion of zero-valent Ag to Ag(I) (Hsiao et al., 2015). In fact, the observed toxicities associated with the metallic silver nanoparticles have been linked to the formation of Ag(I) (Hou et al., 2013; Tan et al., 2019).

Due to the toxicity of Ag(I), several strategies have been employed for their elimination. One of these strategies is the reaction of Ag(I) with sulphide to form a more stable Ag_2S. However, this process is often hampered by the presence of dissolved oxygen (Liu et al., 2011). Hence, a strategy involving the reduction of Ag(I) into metallic Ag (which is more useful) is being considered as a good alternative. Although, direct reduction to metallic silver is not thermodynamically spontaneous, and this is because the redox potential of Ag^+/Ag is highly negative ($Ag^+ + e^- \rightarrow Ag^0$, $E^0 = -1.80$ V) (Peng et al., 2021). Consequently. substances such as fulvic acid (Sal'nikov et al., 2009), sodium citrate (Šileikaitė et al., 2009), sodium formaldehydesulfoxylate (Khanna and Subbarao, 2003), natural organic matter with sunlight (Hou et al., 2013), have been employed for the reduction of Ag(I) to metallic Ag. Photocatalytic reduction has also been employed and photocatalysts such as TiO_2 (Chen and K. Ray, 2001; López-Muñoz et al., 2009), carbon dots-photosensitized polyoxometalates (Madonia et al., 2022) and graphitic carbon nitride (Abdel Moneim et al., 2016) have been reported for the removal of Ag^+. As far as we know, this current study is the first report on the use of nanocomposite composed of nickel bismuth sulphide and O-doped graphitic carbon nitride

($Ni_3Bi_2S_2$/O-gC_3N_4) for the reduction of Ag(I) to metallic Ag in the presence of LED visible light. The effect of the presence of hexavalent chromium, persulfate and mixed organic pollutants (comprising of pharmaceuticals and dyes) on the rate of photocatalytic reduction of Ag(I) were also studied.

Nickel bismuth sulphide has some metallic behavior and Pauli paramagnetic properties which makes them to have wide applications in several fields. Despite their usefulness, they are not widely explored due to the difficulties in synthesis (Qian et al., 2005). High temperature and other harsh conditions are usually required for their synthesis. For example, Baranov et al., (Baranov et al., 2001) synthesized nickel bismuth sulphide by reacting Bi, S and Ni inside an evacuated quartz tube which was maintained for 168 h at 600 °C. As far as we know, this will be the first time that nickel bismuth sulphide will be prepared at a temperature that is lower than 180 °C in less than 21 h. EDTA (a chelating agent) was included in the synthesis of the sulphide in order to improve the morphological properties of the nanomaterials (Qiu et al., 2011).

Graphitic carbon nitride (gC_3N_4) was employed for the formation of composite because of its semiconducting property with band gap energy of 2.7 eV (Ajiboye et al., 2020), hence also possess photocatalytic property. It is also a base carrier for the ternary photocatalyst and has been reported to enhance the removal of the photocatalyst from the aqueous solution after usage, by reducing the aggregation of the ternary sulphide photocatalyst (Xu et al., 2018; Ajiboye et al., 2020). The graphitic carbon nitride used was doped with oxygen prior to the incorporation of the ternary sulphide because oxygen has been reported to be an effective dopant that enhances the effectiveness of carbon-based materials for photocatalytic applications since it initiates change in textural and electronic properties of graphitic carbon nitride (Putri et al., 2020; Zhang et al., 2021).

5.1 Experimental

5.1.1 *Materials*

Dicyanamide, hydrated nickel chloride ($NiCl_2.6H_2O$), hydrated bismuth nitrate ($Bi(NO_3)_3.5H_2O$)), ethylene glycol, ethylene diaminetetraacetic acid (EDTA), thioacetamide and thiourea used in this study were all of analytical grade reagent sourced from Merck chemicals company. The XRD analysis was carried out on a Phillips X'pert diffractometer with

a Cu anticathode (CuKα radiation λ = 1.54056 Å). The emission property was obtained by using PerkinElmer LS 45 fluorimeter while the absorption spectroscopy was obtained on a PerkinElmer Lambda 365 double-beam UV–visible spectrophotometer. Transmission electron microscopy (TEM) was obtained on a JEM—2100 JEOL equipment while LYRA 3, TESCAN was used for obtaining scanning electron microscopy (SEM).

5.1.2 *Synthesis of oxygen-doped graphitic carbon nitride (O-gC_3N_4)*

The graphitic carbon nitride was prepared following the widely reported procedures (Ajiboye et al., 2020; Ajiboye et al., 2021b; Rehman et al., 2021; Shaheen et al., 2022). Briefly, about 10g of dicyandiamide was placed inside a crucible, which was not completely covered in order to allow air penetration. The partly-covered crucible was placed inside a muffle furnace operated at 10 °C/min for 4 h at the temperature of 550 ^{o}C. After the reaction, yellow lump was obtained and was allowed to cool to room temperature, after which it was ground into powder.

5.1.3 *Synthesis of nickel bismuth sulphide ($Ni_3Bi_2S_2$)*

2.0 g of Nickel chloride ($NiCl_2.6H_2O$) and 2.0 g of bismuth nitrate ($Bi(NO_3)_3.5H_2O$) were ground separately in a mortar so as to increase their surface area. From the ground stock, 0.7131 g of hydrated nickel chloride (3 mmol) and 0.9700 g of hydrated bismuth nitrate (2 mmol) were introduced into a 100 mL beaker containing 60 mL of ethylene glycol. To this mixture, were added 0.152 g of thiourea (2 mmol) and 0.1503 g of thioacetamide (2 mmol). Finally,0.3723 g of ethylene diaminetetraacetic acid (EDTA) (1 mmol) was added and the entire mixture was stirred for 30 minutes under room conditions. The content in the beaker was transferred into the autoclave which was maintained at 175 °C for 20 h. The product was washed by centrifugation at 5000 rpm for 5 minutes with ethanol and water sequentially. Finally, it was dried in the muffle furnace at a temperature of 80 °C for 6 h.

5.1.4 *Synthesis of $Ni_3Bi_2S_2$ /O-gC_3N_4 nanocomposite*

The as-prepared oxygen-doped graphitic carbon nitride and nickel bismuth sulphide were mixed in the ratio of 3:1 w/w respectively. The mixed reagents were ground together and calcinated at 300 ^oC for 2 h using a muffle furnace to afford $Ni_3Bi_2S_2$/O-gC_3N_4 nanocomposite.

5.2. Photocatalytic investigations

The photoreduction property of the nanocomposite ($Ni_3Bi_2S_2$/O-gC_3N_4) was evaluated on an aqueous solution of monovalent silver. Typically, 50 mL of 10 mg/L $AgNO_3$ solution was measured into a 100 mL beaker. The pH of the solution was adjusted to 4 by using dilute hydrochloric acid. Then, 10 mg of $Ni_3Bi_2S_2$/O-gC_3N_4 was accurately measured into the solution in the beaker and stirred for 20 min in the absence of light to achieve the adsorption-desorption equilibrium. After the equilibrium had been attained, the solution was irradiated by a 28 W visible LED light. During the reaction, aliquots of the $AgNO_3$ solution were taken at a regular 15 min interval. The concentration of the aqueous Ag(I) at a particular time was measured using a UV-visible spectrophotometer. The percentage of Ag(I) reduction was estimated by using **Equation (i),** while the data obtained was fitted into linearized form of the pseudo first order kinetics (**Equation (ii))**. The half-life for the photocatalytic reduction process was calculated by using **Equation (iii).**

$$Percentage\ photocatalytic\ reduction = \frac{C_o - C_t}{C_o} \times 100\% \quad \text{.....(i)}$$

$$-Kt = \ln(\frac{C_t}{C_o}) \quad \text{.....(ii)}$$

$$Half - life = {}^{\ln 2}/_{k} = {}^{0.693}/_{k} \quad \text{.....(iii)}$$

Where C_o and C_t represent the initial and final concentration of aqueous Ag(I), t is the reaction time and k is the pseudo- first order reaction rate constant.

5.3 Results and Discussion

5.3.1 *X-ray diffraction (XRD) studies of $Ni_3Bi_2S_2$/O-gC_3N_4 nanocomposite*

The PXRD of the studied compounds are presented in Fig. 5.1. A search in the PCPDF database by using the X'pert High score software (Degen and van den Oever, 2009), showed that the $Ni_3Bi_2S_2$ crystallizes in the monoclinic system space group C2/m that matches with the PCPDF number 01-080-2191 (Fig.5.1a). There are no peaks from the binary oxides, binary sulphides or other impurities, indicating the purity of the sample.

The diffraction pattern of the oxygen-doped graphitic carbon nitride is shown (Fig.5.1b). The oxygen-doped gC_3N_4 crystallizes in the hexagonal system, space group P-6m2 (PCPDF number 01-087-1526). The PXRD displayed a very prominent peak at 27.50^o, which was indexed to the (002) and it is the characteristic peak for graphitic carbon nitride. The peak arises from the aromatic conjugation system of the interlayer stacking (Chidhambaram and Ravichandran, 2017; Ajiboye et al., 2020). Fig.5.1c shows the PXRD of the nanocomposite of the oxygen-doped gC_3N_4 and $Ni_2Bi_2S_3$. Appearance of the prominent (002) peak at 27.60° confirmed the presence of graphitic carbon nitride. All other peaks were indexed to the $Ni_2Bi_3S_3$ crystal system.

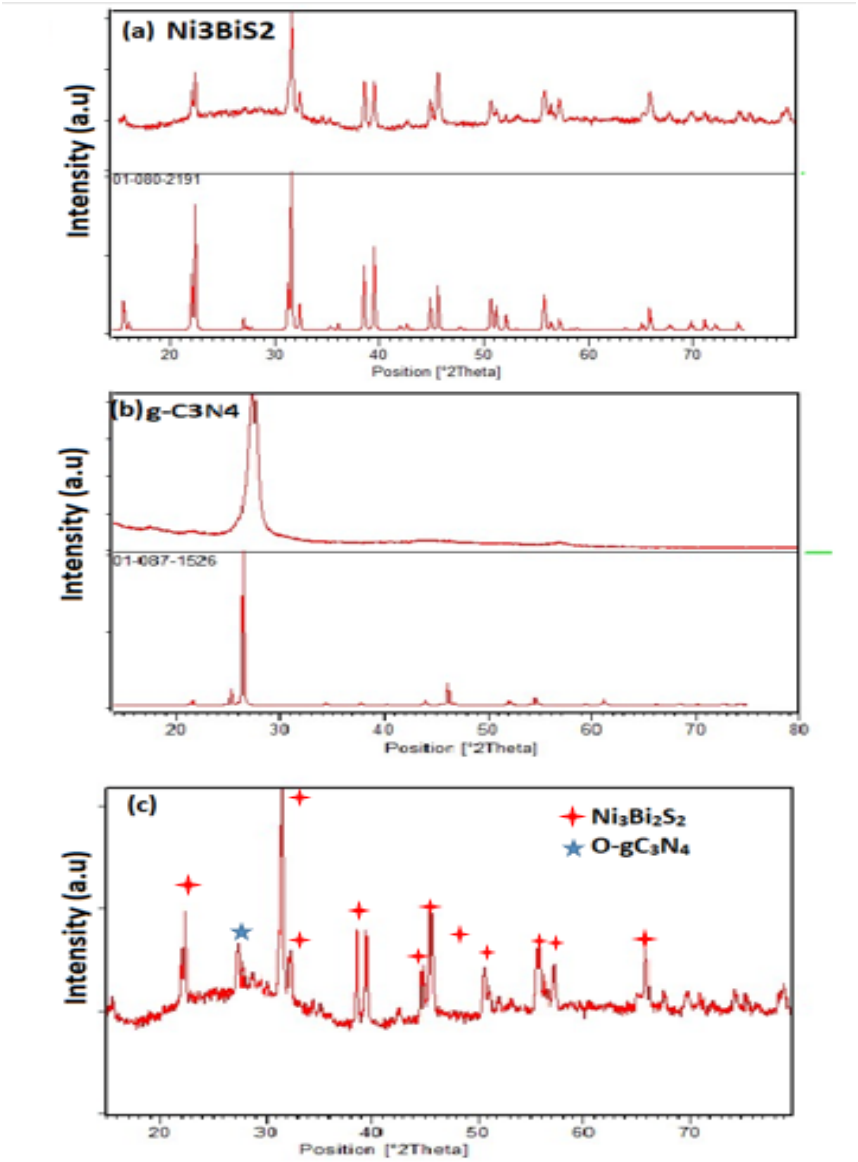

Figure 5.1: XRD plot of the (a) Nickel bismuth sulphide ($Ni_2Bi_2S_3$) (b) oxygen-doped graphitic carbon nitride, and (c) $Ni_3Bi_2S_2$/O-gC_3N_4 nanocomposites.

5.3.2 FTIR studies of $Ni_3Bi_2S_2$/O-gC_3N_4 nanocomposite

The FTIR spectrum of the oxygen-doped graphitic carbon nitride and the nanocomposite are presented in Fig 5.2 (a and b) which show a broadband at 3075 cm^{-1} that could be attributed to the stretching vibration of N-H. The peak at 2308 cm^{-1} due to the N═C═C or C≡N group present in the structure of the graphitic carbon nitride. The characteristic sharp peak of melon appears at 1228 cm^{-1} and this peak appears due to the vibration of the nitrogen atom that is

present in the aromatic ring (Pandey et al., 2020). Also, the band at 883 cm^{-1} appeared as a result of the deformation mode of the N-H present in amino groups (Dong et al., 2013), while the peak at 800 cm^{-1} is attributed to the characteristic breathing mode of the tri-s-triazine cycles has a (Zhang et al., 2012; Lan et al., 2016). The peak at 626 cm^{-1} indicated the presence of S-S bond, while the peak at 723 cm^{-1} was due to the presence of metal-sulphur bond (Devamani et al., 2018). The sharp peaks at 1128 cm^{-1} was as a result of the vibration from the non-symmetric S-H bonds formed through the interaction of the ternary sulphide with the solvent (Koh et al., 2003; Dashairya et al., 2020). The characteristic peaks of both the nickel bismuth sulphide and oxygen-doped graphitic carbon nitride appeared in the nanocomposite. The peak around 1540 cm^{-1} is due to the bending vibration of the N-H, while the 1627 cm^{-1} could be attributed O-H bending vibration as a result of the physically adsorbed water molecules (Zhang et al., 2019).

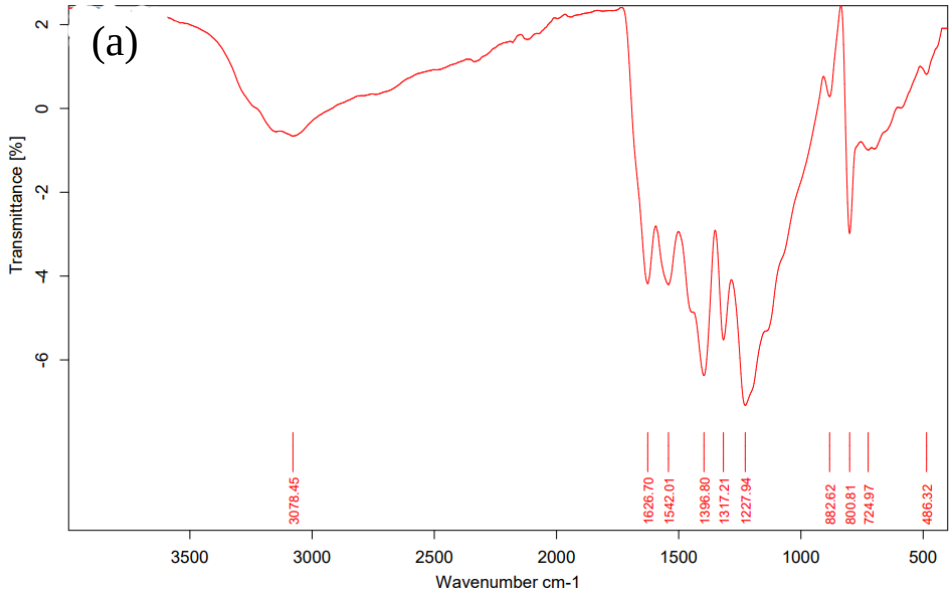

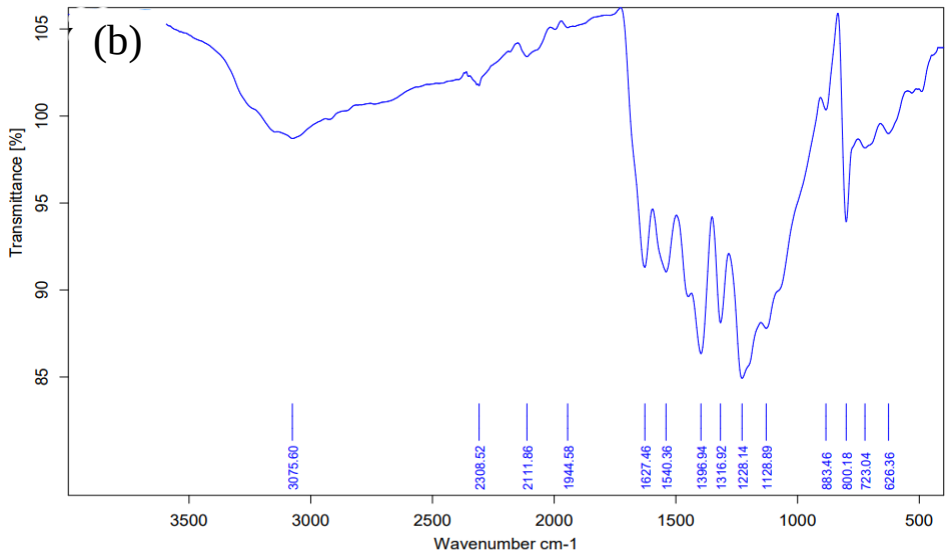

Figure 5.2: FTIR spectra of (a) O-gC_3N_4 and (b)$Ni_2Bi_2S_3$/O-gC_3N_4 nanocomposite.

5.3.3 *Morphological Properties studies of the $Ni_2Bi_2S_3$/O-gC_3N_4 nanocomposite*

The surface morphology of the nanocomposite explored using scanning electron microscopy (SEM) image and presented in Figure 5.3a**,** revealed that the synthesized composite is aggregated with particles of irregular shape. The TEM image in Figure 3b shows nanorods with dissimilar orientations. As shown in the HRTEM image in the inset, the nanorods contains distinct fringes characteristic of crystalline materials and the lattice spacing was approximately 0.296 nm that corresponds to the (022) planes of the nickel bismuth sulphide. This value of the lattice spacing is in good agreement with previously reported value for the nickel bismuth sulphide deposited on nickel foam (Yao et al., 2022). The EDS (Figure 5.3c) shows the presence of carbon, nitrogen, oxygen, nickel, bismuth and sulphur with weight percentage of 45.13, 29.45, 9.81, 3.78, 9.94 and 1.89% respectively. The length and width of the nanorods are presented in the size distribution histogram presented in Figures 5.3(d and e), which showed 132 and 29 nm as the average length and width respectively.

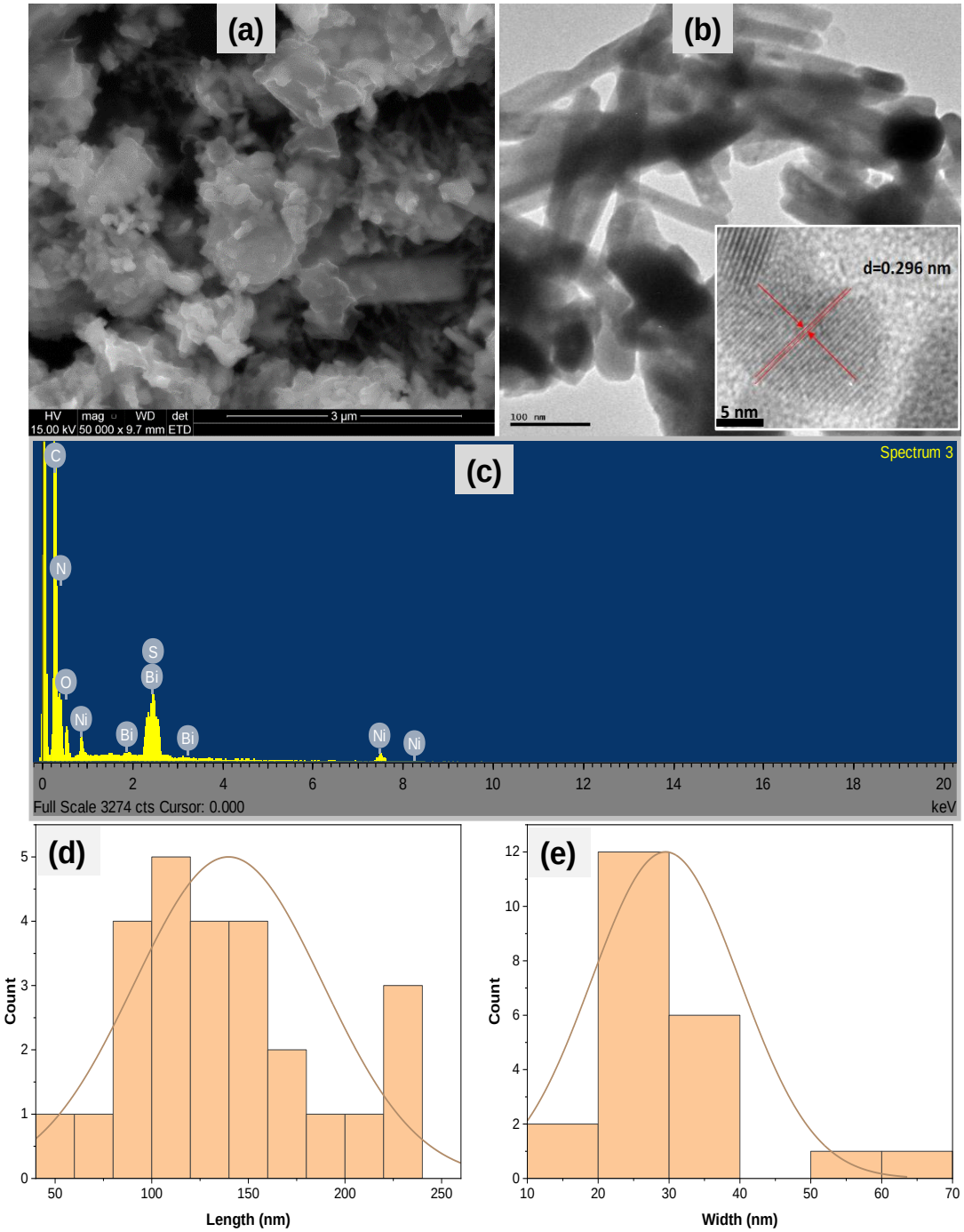

Figure 5.3: (a) SEM image, (b) TEM image (inset is the HRTEM image), and (c) EDS of $Ni_2Bi_2S_3$/O-gC_3N_4. (d) and (e) Particle size distribution for the length and width of the nanorods respectively.

The elemental mapping images (Fig. 5.4(a-g)) confirmed that the $Ni_2Bi_2S_3$ particles were well dispersed on the graphitic carbon nitride. It also confirmed that the elemental compositions C, N, O, Ni, Bi and S were evenly distributed homogeneously and co-existed in the sample. This further showed the formation of the nanocomposite.

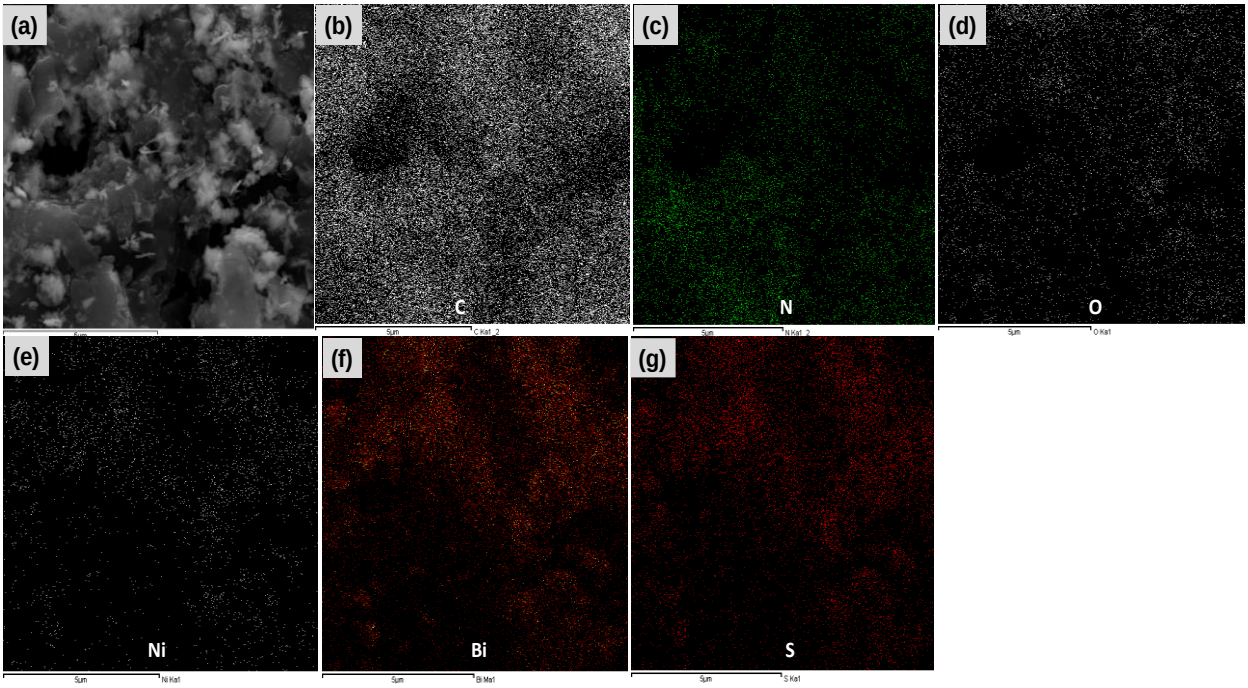

Figure 5.4: (a) Elemental mapping of $Ni_2Bi_2S_3$/O-gC_3N_4 (b) C, (c) N, (d) O, (e) Ni, (f) Bi, and (g) S $Ni_2Bi_2S_3$/O-gC_3N_4.

5.3.4 *Optical properties of the $Ni_2Bi_2S_3$/O-gC_3N_4 nanocomposite*

UV-visible absorption of the $Ni_2Bi_2S_3$/O-gC_3N_4 nanocomposite is shown in Fig.5. 5a. There are three absorption maxima in the UV spectrum. The two close intensities around 350 nm were from the graphitic carbon nitride and were the results of unsaturated n-$\pi*$ transitions involving the nitrogen atoms and the poly conjugated heteroaromatic $\pi-\ \pi*$ transition (Mohanraj et al., 2021). The strong intensity around 220 nm could be attributed to absorption due to the nickel bismuth sulphide nanoparticles present within the nanocomposite (as shown in Figure 5c). Similar results were reported with the incorporation of ternary Cu_3SnS_4 into graphitic carbon nitride (Olatunde and Onwudiwe, 2022). The optical indirect bandgap energy of the nanocomposite was estimated by using the Tauc plot, obtained from Equation (iv) by plotting $(\alpha hv)^{1/2}$ against the energy (hν) and extrapolating the linear portion of the curve to the energy axis. The value obtained was 3.0 eV, which is significantly higher than 2.7 eV which is the value that has been widely reported in several literature as the bandgap energy for pristine graphitic carbon nitride (Oh et al., 2017; Ismael et al., 2019; Ajiboye et al., 2021b; Olatunde and Onwudiwe, 2022).

$$\propto hv = \left(hv - E_g\right)^n \quad \text{(iv)}$$

where E_g is the optical band gap, v is the photon frequency, h is the Planck constant and α is the absorbance. The type of electronic transitions(n) and the value of electronic transitions: n= 3, 3/2, 2 or ½ for indirect-forbidden, direct-forbidden, indirect-allowed and direct-allowed transitions respectively (López and Gómez, 2012).

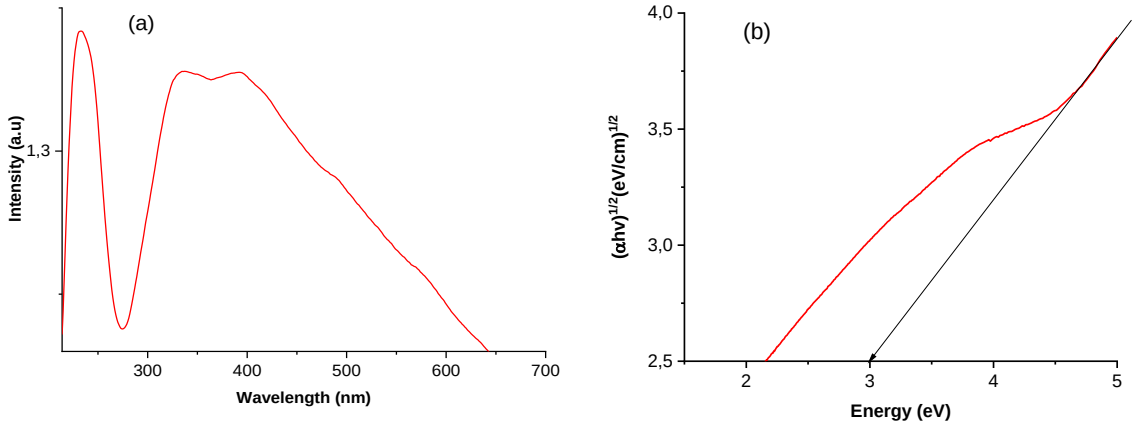

Figure 5.5: (a) UV plot of $Ni_2Bi_2S_3$/O-gC_3N_4 (b) Tauc plot of $Ni_2Bi_2S_3$/O-gC_3N_4.

5.4 Photocatalytic investigations

The wavelength of maximum absorption for aqueous silver(I) was found at 215 nm and the absorption maxima decreased with the increase in the irradiation time (Fig. 5.6a). Firstly, the chemical reduction of Ag(I) was investigated without irradiation or addition of photocatalyst to the system and the percentage degraded were found to be negligible. After a 60 min irradiation, only about 0.5% of reduction was achieved for Ag(I) without any photocatalyst. Also, the treatment of the solution with the nanocomposite photocatalyst in the absence of light led to the Ag(I) reduction of less than 1.0%. Thereafter, the process was carried out with the addition of oxygen-doped graphitic carbon nitride, nickel bismuth sulphide, and their composite ($Ni_2Bi_2S_3$/O-gC_3N_4) as the photocatalyst under visible LED light. The results showed that the photocatalytic reduction of Ag(I) was higher when oxygen-doped graphitic carbon nitride was used as photocatalyst compared to the photocatalytic reduction when nickel bismuth sulphide was used as the photocatalyst. This may be due to the polymeric nature of oxygen-doped graphitic carbon nitride as a result of the layered structure, which contributed to better adsorption of Ag(I) unlike in the pristine nickel bismuth sulphide (Cao et al., 2015; Ajiboye et al., 2020).

The pseudo-first order rate constant changed from 0.0035 min^{-1} when pure nickel bismuth sulphide was used as the photocatalyst to 0.0061 min^{-1} when graphitic carbon nitride was introduced into it to form a composite (as shown in Fig. 5.6 (b and c). This may be attributed to better separation of holes/electrons, and a reduction in the rate of recombination of holes and electrons due to the formation of heterojunction systems (Wang et al., 2014; Ajiboye et al., 2021b).The enhanced photocatalytic performance has been reported for other graphitic carbon nitride nanocomposite including gC_3N_4/carbon dots (Li et al., 2022), g-C_3N_4/Bi_2WO_6 (Zhou et al., 2022), silver-functionalized graphitic carbon nitride (Ajiboye et al., 2022) and BiOxCly/BiOmBrn/BiOpIq/g-C_3N_4 (Lin et al., 2022).

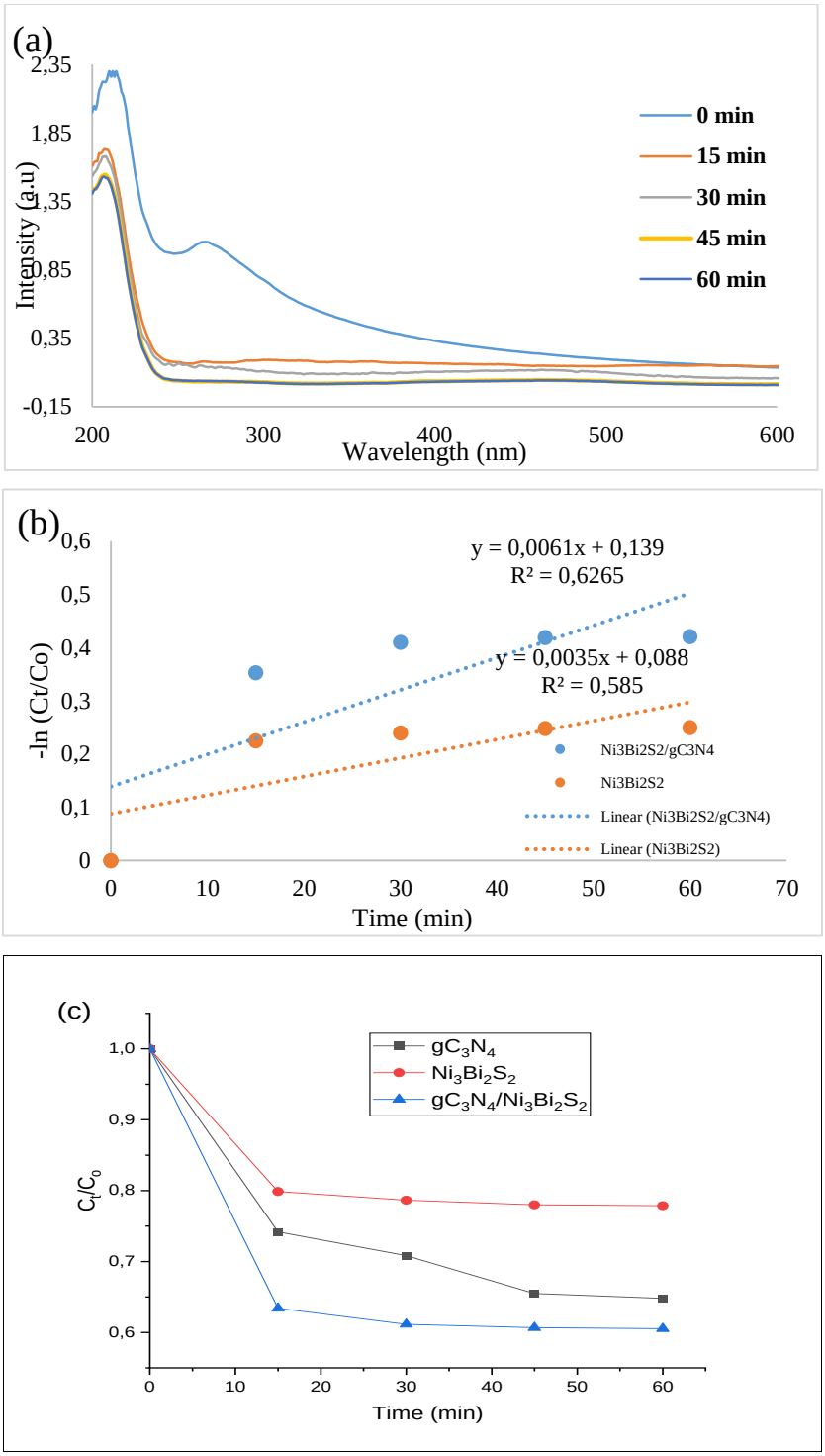

Figure 5.6: (a) The UV plot for the photocatalytic reduction of Ag^{+} using $Ni_2Bi_2S_3$/O-gC_3N_4 as the photocatalyst at varied time of irradiation (b) The pseudo first order plot for pristine $Ni_3Bi_2S_2$ and $Ni_2Bi_2S_3$/O-gC_3N_4 (c) The performance of oxygen-doped gC_3N_4, $Ni_3Bi_2S_2$ and $Ni_2Bi_2S_3$/O-gC_3N_4. carried out at pH 6 with 25 mg of photocatalyst and 10 mg/L of silver(I) ions.

5.4.1 *Effect of pH*

The pseudo-first order rate constant of Ag(I) photocatalytic reduction was 0.0053 min^{-1} at pH 4 which decreased to 0.0047 min^{-1} at pH 12 under the same conditions. This shows that the presence of hydrogen ions favours the rate of reduction of Ag^{+} ions in the presence of light. When the concentration of hydrogen ion was adjusted by changing the pH to 6, the pseudo-first order rate constant increased from 0.0047 min^{-1} to 0.0070 min^{-1} (Fig. 5.7). This indicated that there is an optimum value for the hydrogen ions that is required to obtain a maximum photocatalytic reduction rate of Ag(I). The observed change in photocatalytic reduction rate with change in pH could be linked to the modification of the surface charge of the photocatalyst in the presence of hydrogen ions (Zhou et al., 2016). Although, the presence of hydrogen ions is beneficial, but at a low pH, the concentration of hydrogen ions was too high and the hydrogen ion began to influence the equilibrium between the photocatalyst and Ag(I) which reduced the rate of photocatalytic Ag(I) reduction (Song et al., 2018).

The observed increase in the rate of photocatalytic reduction of Ag(I) from a more acidic pH to a less acidic pH is consistent with earlier reported by Ohtani et al., (Ohtani et al., 1987). Similar variation has also been reported for other heavy metal ions. For instance, the enhanced photocatalytic oxidation of trivalent arsenic to pentavalent arsenic prior to adsorption of pentavalent arsenic has also been reported to occur maximally at near neutral pH (Sun et al., 2017). Contrarily, the photocatalytic reduction of hexavalent chromium has been reported to be higher at a pH of 4 compared to the pH of 6, which is the opposite of the observed trend in the current study for the photocatalytic reduction of Ag(I) (Nanda et al., 2017).

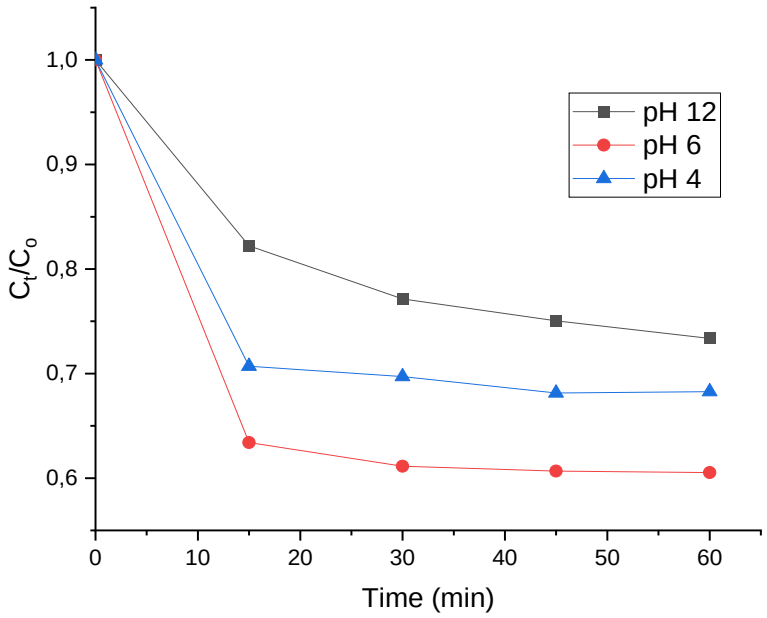

Figure 5.7: Effect of pH on the photocatalytic reduction of silver(I) ions using $Ni_2Bi_2S_3$/O-gC_3N_4 as the photocatalyst. (experimental conditions: 10 mg/L Ag(I) concentration, 25 mg Photocatalyst dosage and 28 W LED light)

5.4.2 *Effect of initial Ag(I) ion concentration*

The optimum photocatalytic reduction of Ag(I) was obtained when the initial concentration of Ag(I) was 10 mg/L. As shown in Fig. 5.8, there was significant decrease in photocatalytic reduction of Ag(I) when the initial concentration of Ag(I)was increased by a factor of 2 and 3 under the same conditions. At 10 mg/L, the pseudo-first order rate constant was 0.0045 min^{-1} and this value dropped to 0.0041 min^{-1} and 0.0029 min^{-1} when the concentration was increased to 20 mg/L and 30 mg/L respectively. This might be due to the fast re-oxidation of the reduced silver in the presence of excess Ag(I) (Troupis et al., 2003). In addition, the increase in the silver ion photo-reduction with decrease in initial Ag(I) concentration could also be as a result of insufficient photons reaching the surface of the photocatalyst (Sane et al., 2018).

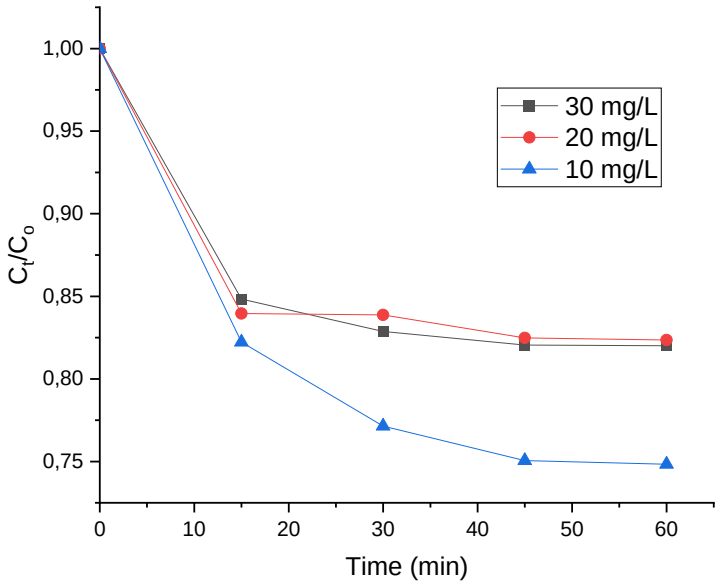

Figure 5.8: Influence of initial Ag(I) ion concentration on photocatalytic reduction of silver(I) ions. (experimental conditions: pH 6, 25 mg Photocatalyst dosage and 28 W LED light).

5.4.3 *Effect of photocatalyst dosage*

An increase in the value of the pseudo-first order rate constant from 0.0066 min^{-1} to 0.0070 min^{-1} occurred when the quantity of the photocatalyst used was increased from 10 to 25 mg (Fig.5. 9). The observed increase in the rate of photocatalytic reduction might be due to the increase in the site of reaction, leading to the increase in the adsorption of Ag(I) to the photocatalyst (Ajiboye et al., 2021a; Li et al., 2021). However, when the photocatalyst dosage was further increased from 25 to 50 mg, the pseudo-first order rate constant dropped from 0.0070 to 0.0047 min^{-1}. The observed decrease in the photocatalytic reduction rate could be as a result of the increased turbidity caused by excessive photocatalyst, thereby resulting in a decrease in light transmittance and light intensity reaching the surface of the photocatalyst (Abdel Moneim et al., 2016). Also, agglomeration of the photocatalyst as a result of particle-particle interaction, which results in the loss in surface area must have contributed to the decrease in the rate of photocatalytic reduction with high quantity of the photocatalyst (Kaneco et al., 2004).

Hence, the photocatalyst dosage of 25 mg (500 mg/L) resulted into an enhanced photocatalytic reduction of Ag(I) compared with the result obtained when 10 mg (200 mg/L) and 50 mg (1000

mg/L) were used under similar conditions. This optimum value was clearly lower than the optimum value of 2000 mg/L and 3000 mg/L that were previously reported when TiO_2 and $SrWO_4$ were respectively used for the photocatalytic reduction of Ag^+ (Chen and Ray, 2001; Sharma et al., 2008).

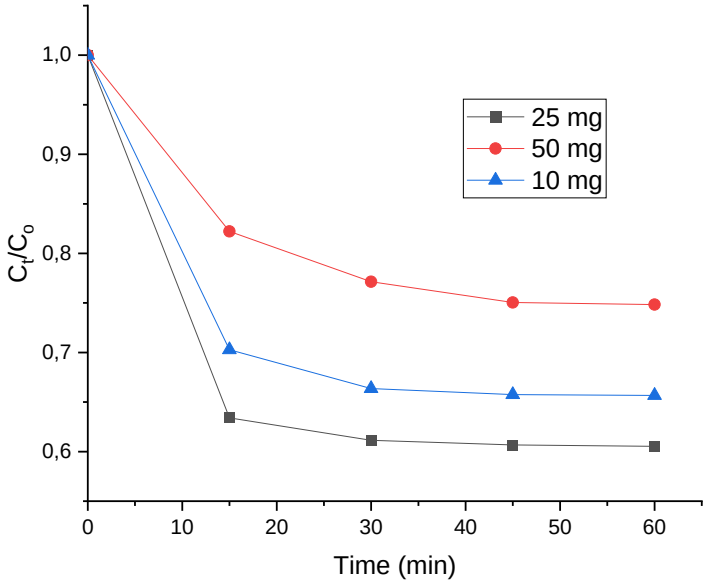

Figure 5.9: Effect of catalyst ($Ni_2Bi_2S_3$/O-gC_3N_4) dosage on the photocatalytic reduction of silver(I) ions. (experimental conditions: 10 mg/L Ag(I) concentration, 25 mg Photocatalyst dosage and 28 W LED light).

5.4.4 *Influence of Persulfate activation*

Persulfate has been considered as an important additive used to enhance the photocatalytic process because of its high oxidizing power due to high positive values of its electrode potential (E^0 = +2.01 V). It produces a stronger oxidizing sulphate radical (Zhang et al., 2015) upon activation. The generated sulphate radical is more stable than the hydroxyl radicals at room temperature (Zhang et al., 2015). We investigated the effect of persulfate addition on the photocatalytic reduction of Ag(I) by adding 10 mg/L of potassium persulfate into the system and it was observed that it has inhibitory effects on the rate of photocatalytic Ag(I) reduction (Fig. 5.10). The reason could be that the addition of persulfate into the system had significantly increased the oxidant species in the system which result into re-oxidation of the zero-valent Ag back to Ag(I) (Diao et al., 2016; Wang et al., 2022).

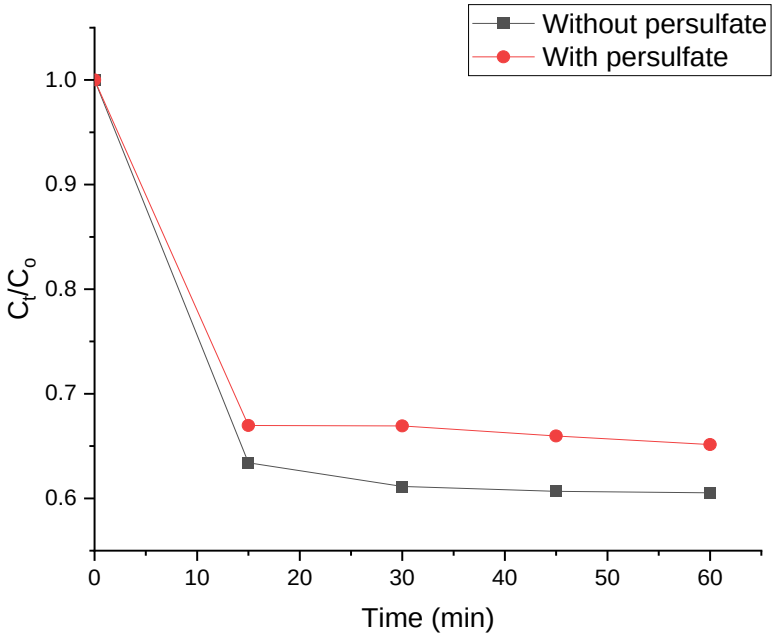

Figure 5.10: Effect of the presence of persulfate on the photocatalytic reduction of silver(I) ions using $Ni_2Bi_2S_3$/O-gC_3N_4 as $Ni_2Bi_2S_3$/O-gC_3N_4. (experimental conditions: 10 mg/L Ag(I) concentration, pH 6, 25 mg Photocatalyst dosage and 28 W LED light).

5.4.5 *Effect of mixed organic pollutants on the photocatalytic efficiency of gC_3N_4/O-$Ni_3Bi_2S_2$*

The effects of the presence of different organic pollutants on the rate of photocatalytic reduction of different metal ions have been previously investigated (Tan et al., 2003). The photocatalytic reduction of metal ions had been earlier reported to be enhanced by the presence of organics due to synergistic effects (Wang et al., 2008). However, when the mixture of 10 mg/L acyclovir and 10 mg/L methyl orange were introduced into the catalytic system containing 10 mg/L of Ag(I) solution, a pronounced reduction in the photocatalytic reduction rate was observed. The pseudo-first order rate constant changed from 0.0070 min^{-1} to 0.0021 min^{-1} corresponding to the change in half-life from 99 min to 330 min. This accounts for over three-fold decrease in photototocatalytic silver(I) reduction. When the single organic pollutant was used (acyclovir only), there was slight improvement in the rate of photocatalytic reduction at the end of 60-min LED irradiation as shown in Fig.5.11. The overall reduction in the rate of photocatalytic reduction could be due to the poor oxidizability of the two organic pollutants.

In previous reports, the presence of easily oxidizable organics such as oxalic acid boosted the rate of photocatalytic reduction of metal ions, since the easily oxidizable organic scavenged the positive holes in the photocatalysts (Yang et al., 2012).

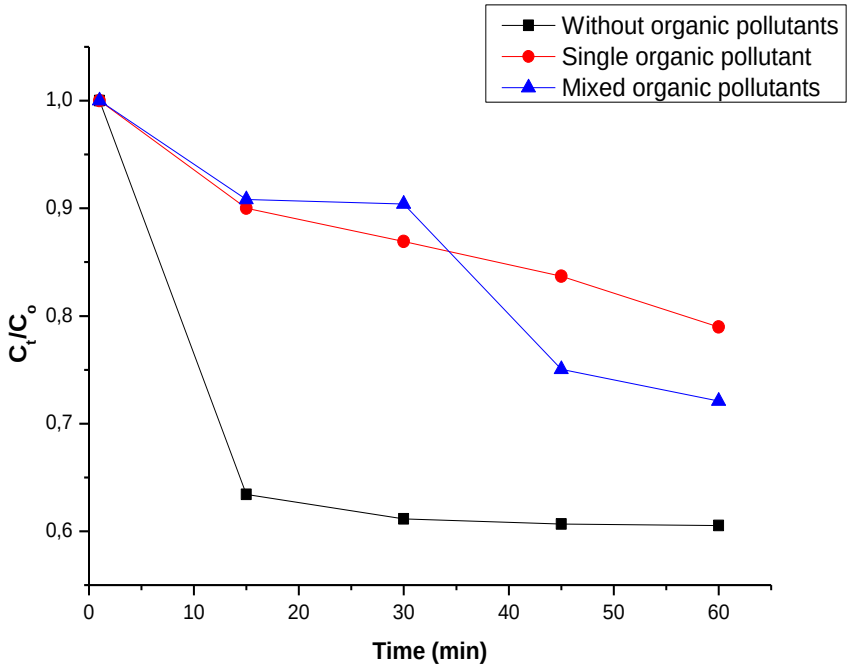

Figure 5.11: effect of the presence of mixed organic pollutants on the photocatalytic reduction of silver(I) ions using $Ni_2Bi_2S_3$/O-gC_3N_4. (experimental conditions: 10 mg/L Ag(I) concentration, pH 6, 25 mg photocatalyst dosage and 28 W LED light).

5.4.6 *Effect of the presence of Cr(VI) ions on the photocatalytic efficiency of $Ni_2Bi_2S_3$/O-gC_3N_4*

The effect of other metal ions on the rate of photocatalytic reduction of Ag(I) has not been properly studied. Chen et al., (Chen and K. Ray, 2001) demonstrated that the rate of photocatalytic reduction of monovalent silver is higher than the rate at which hexavalent chromium was reduced under similar conditions. Since the two ions are reduced in the presence of light, it is necessary to study the effect of their joint existence in the photocatalytic system. The effect of the presence of Cr(VI) on the photocatalytic reduction of silver(I) was studied, and the rate of Ag(I) reduction was found to be suppressed with the addition of equal mole of hexavalent chromium (Figure 5. 12).

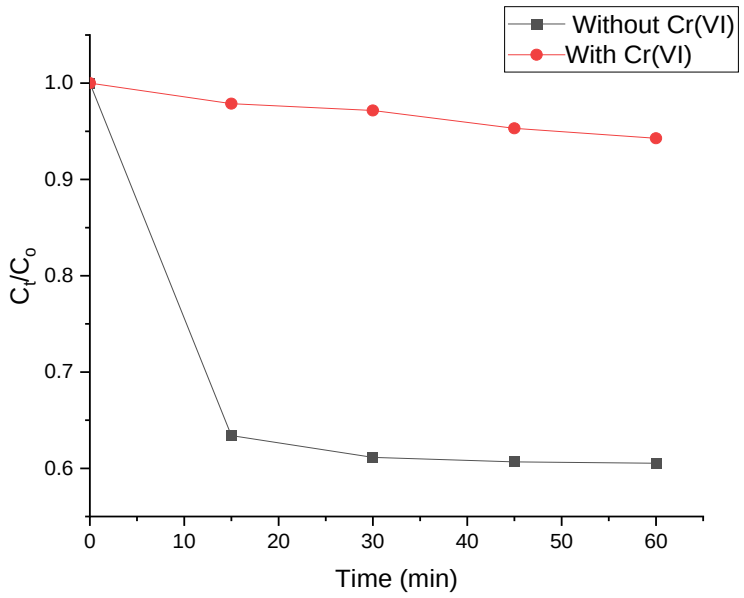

Figure 5.12: Effect of the presence of hexavalent chromium on photocatalytic reduction of silver(I) ions using $Ni_2Bi_2S_3$/O-gC_3N_4 as photocatalyst. (experimental conditions: 10 mg/L Ag(I) concentration, pH 6, 25 mg photocatalyst dosage and 28 W LED light).

The pseudo first order rate constant of the photocatalytic reduction of silver was 0.0070 min^{-1} in the absence of Cr(VI), but the rate constant was reduced to 0.0058 min^{-1} when Cr(VI) was introduced into the system. This accounts for the reduction in photocatalytic performance by a factor of 1.2. The reason for the inhibitory role played by Cr(VI) could be ascribed to the competition between Ag^+, $Cr_2O_7^{2-}$ and $HCrO_4^-$ (Wahyuni et al., 2015). The effect of the presence of Cu(II) on the photocatalytic reduction of ions of silver has been previously studied. The studies showed that the presence of Cu(II) has no effect on the rate of Ag(I) reduction in the presence of light (Herrmann et al., 1988) unlike what was obtained when Cr(VI) was introduced into the system. The inhibition observed was more pronounced than what was observed when the mixture of organic pollutants was introduced into the system as shown in Table 5.1.

Table 5.1: The pseudo-first order rate constant data and half-life values obtained at varied conditions but constant light intensity (28 W)

Initial Ag(I) Concentration+ pH	Photocatalyst + dosage	Additives	Equation	Pseudo first order rate constant (min^{-1})	R^2	Half-life (min)
10 mg/L + pH 6	$Ni_2Bi_2S_3$/O-gC_3N_4+ 25 mg	-	0.0061x + 0.139	0.0061	0.6265	113.63
10 mg/L + pH 6	$Ni_3Bi_2S_2$ +25 mg	-	0.0035x + 0.088	0.0035	0.5850	198.04
30 mg/L + pH 4	$Ni_2Bi_2S_3$/O-gC_3N_4+50 mg	-	0.0029x + 0.0637	0.0029	0.6431	239.02
20 mg/L + pH 4	$Ni_2Bi_2S_3$/O-gC_3N_4+ 50 mg	-	0.0041x + 0.7370	0.0041	0.7370	169.06
10 mg/L + pH 4	$Ni_2Bi_2S_3$/O-gC_3N_4+ 50 mg	-	0.0045x + 0.0722	0.0045	0.7633	154.00
10 mg/L + pH 4	$Ni_2Bi_2S_3$/O-gC_3N_4+ 25 mg	-	0.0053x +0.1346	0.0053	0.5855	130.75
10 mg/L + pH 12	$Ni_2Bi_2S_3$/O-gC_3N_4+ 25 mg	-	0.0047x + 0.0682	0.0047	0.8068	147.45
10 mg/L + pH 6	$Ni_2Bi_2S_3$/O-gC_3N_4+ 25 mg	-	0.0070x + 0.1802	0.0070	0.5739	099.00
10 mg/L + pH 6	$Ni_2Bi_2S_3$/O-gC_3N_4+ 10 mg	-	0.0066x + 0.1018	0.0066	0.7866	105.00
10 mg/L + pH 6	$Ni_2Bi_2S_3$/O-gC_3N_4 + 25 mg	10mg/L persulfate	0.0058x + 0.1550	0.0058	0.5586	119.48
10 mg/L + pH 6	$Ni_2Bi_2S_3$/O-gC_3N_4 + 25 mg	10 mg/L diclofenac + 10 mg/L methyl orange	0.0021x-0.0143	0.0021	0.9260	330.00
10 mg/L + pH 6	$Ni_2Bi_2S_3$/O-gC_3N_4 + 25 mg	10 mg/L dichromate solution	0.0010x + 0.0026	0.0010	0.9808	693.00

The optimum conditions obtained for the photocatalytic reduction of monovalent silver using Ni_3Bi_2/O- $gC_3N_4S_2$ was pH 6, 10 mg/L Ag(I) concentration and 25 mg of photo-catalyst's dosage with 28 W LED light. However, when the source of light was changed to 48 W LED light, there was a significant increase in the rate of photocatalytic reduction. The pseudo-first order rate constant changed from 0.0070 min^{-1} to 0.0460 min^{-1} (Fig.5.13), which was equivalent to a change from 39.50 to 93.08%. This clearly shows that the intensity of light plays a significant role in the photocatalytic reduction of Ag(I) ions. The excitation rate of holes and electrons increased with the increase in light intensity and the rate of photocatalytic process was enhanced (Ani et al., 2018).

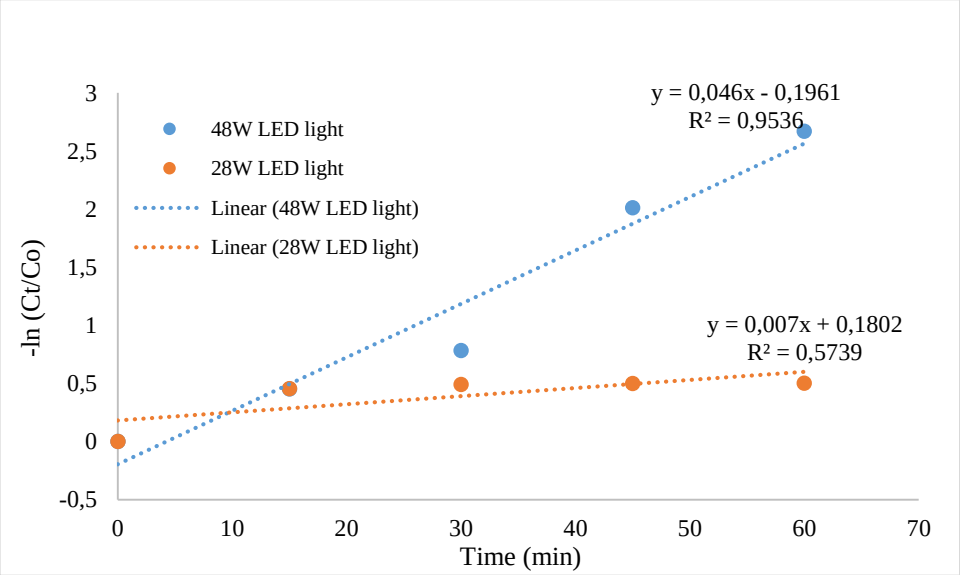

Figure 5.13: Pseudo-first order rate constant plot for 48 W LED light compared to 28 W LED light under the same conditions.

5.4.7 *Radical scavenging experiment*

The mechanism of photocatalytic reduction of Ag(I) were studied via radical scavenging experiments. Sodium nitrate was used as the electron scavengers while triethanol amine (TEA), tert-butanol (TBA) and ascorbic acids (ASC) were used as the scavengers for hole, hydroxyl and superoxide radicals respectively. The influence of these scavengers on the photocatalytic reduction process was compared with the photocatalytic reduction without the presence of these scavengers. The introduction of 0.01 M TBA into the photocatalytic system had lower effect on the percentage of Ag(I) ions reduced compared to the other scavengers used for the investigations. There was 63.9% photocatalytic reduction in the presence of TBA, which was

a reduction of 22.7%. There were less than 3% photocatalytic silver(I) reduction when 0.01 M TEA, 0.01 M ASC and 0.01 M $NaNO_3$ were separately used as the scavengers under similar conditions (Fig.5.14). The observations show that the contribution of hydroxyl radical is low compared to the contribution of electrons, holes and superoxide, although, they all contributed to the photocatalytic reduction process.

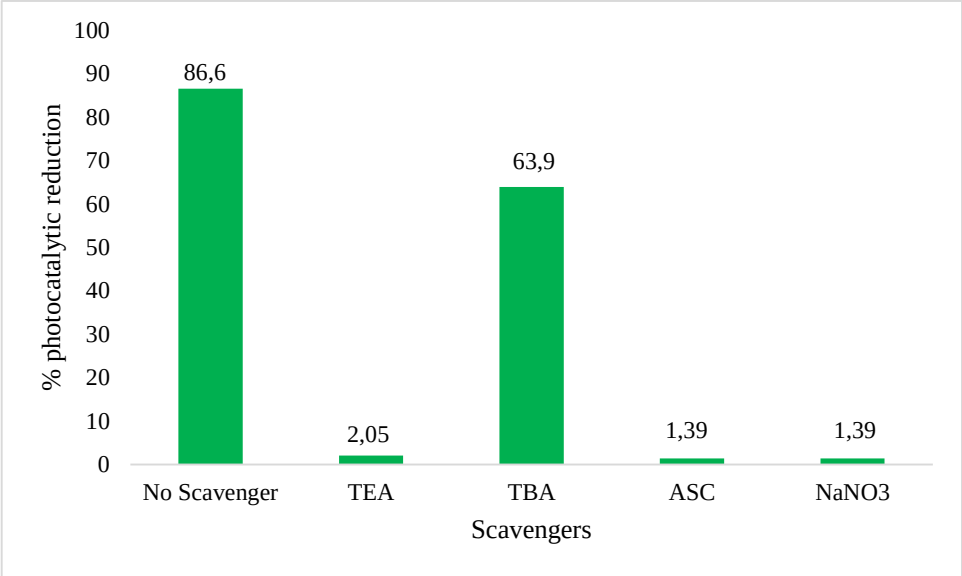

Figure 5.14: The result of the radical scavenging experiment for the photocatalytic reduction of Ag(I) ion using $Ni_2Bi_2S_3$/o-gC_3N_4 photocatalyst.

5.4.8 *Reusability study of the photocatalytic reduction of Ag^+ using $Ni_2Bi_2S_3$/O-gC_3N_4*

The three consecutive recycling of the same photocatalyst for the photocatalytic reduction of Ag(I) was carried out to understand the reusability of the photocatalyst. After each complete cycle, the used photocatalyst was washed with distilled water, centrifuged at 6000 rpm for 5 min and dried at 50 ^oC for 2 h. As shown in Fig. 5.15, $Ni_2Bi_2S_3$/O-gC_3N_4 retained its photocatalytic activities even after three consecutive cycles with an efficiency still above 85%. This shows that the photocatalytic activity of the photocatalyst was sustainable and it is stable as well as reusable under visible light.

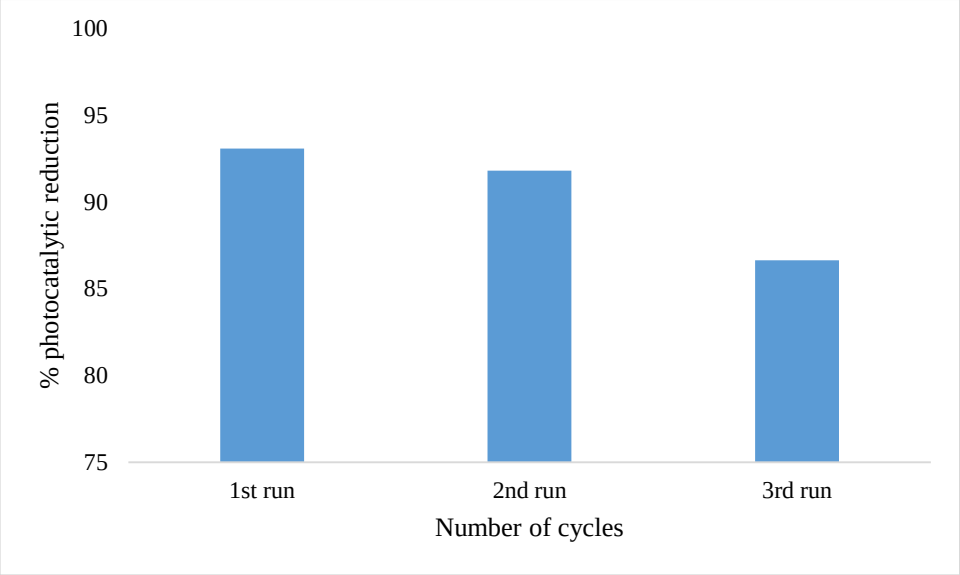

Figure 5.15: The reusability study of $Ni_2Bi_2S_3$/O-gC_3N_4 photocatalyst for the photocatalytic reduction of Ag(I) ion.

CONCLUSION

A nanocomposite of nickel bismuth sulphide and oxygen doped graphitic carbon nitride was successfully synthesized. The performance of this nanocomposite on the visible light enhanced reduction of Ag(I) was investigated. The addition of persulfate, Cr(VI) solution and mixture of organic pollutants (pharmaceutical and dyes) significantly reduced the rate of photocatalytic reduction of silver(I). The optimum conditions obtained for the photocatalytic reduction process was pH 6, using 10 mg/L Ag(I) concentration, 25 mg of photo-catalyst's dosage, and 28 W LED lamp. There was an increase in the pseudo-first order rate constant by a factor of 6.5 when 48 W LED lamp was used under similar conditions. The photocatalyst was stable even after it has been used for three consecutive runs. The results obtained showed that the use of $Ni_2Bi_2S_3$/O-gC_3N_4 for the reduction of silver(I) is very promising.

REFERENCES

Abdel Moneim, S.M., Gad-Allah, T.A., El-Shahat, M.F., Ashmawy, A.M., Ibrahim, H.S., 2016. Novel application of metal-free graphitic carbon nitride (g-C_3N_4) in photocatalytic reduction—Recovery of silver ions. Journal of Environmental Chemical Engineering 4, 4165-4172.

Ajiboye, T.O., Imade, E.E., Oyewo, O.A., Onwudiwe, D.C., 2022. Silver functionalized gC_3N_4: Photocatalytic potency for chromium(VI) reduction, and evaluation of the antioxidant and antimicrobial properties. Journal of Photochemistry and Photobiology A: Chemistry 432, 114107.

Ajiboye, T.O., Kuvarega, A.T., Onwudiwe, D.C., 2020. Graphitic carbon nitride-based catalysts and their applications: A review. Nano-Structures & Nano-Objects 24, 100577.

Ajiboye, T.O., Oyewo, O.A., Onwudiwe, D.C., 2021a. Adsorption and photocatalytic removal of Rhodamine B from wastewater using carbon-based materials. FlatChem 29, 100277.

Ajiboye, T.O., Oyewo, O.A., Onwudiwe, D.C., 2021b. Conventional and Current Methods of Toxic Metals Removal from Water Using g-C_3N_4-Based Materials. Journal of Inorganic and Organometallic Polymers and Materials 31, 1419-1442.

Ani, I.J., Akpan, U.G., Olutoye, M.A., Hameed, B.H., 2018. Photocatalytic degradation of pollutants in petroleum refinery wastewater by TiO_2- and ZnO-based photocatalysts: Recent development. Journal of Cleaner Production 205, 930-954.

Baranov, A.I., Olenev, A.V., Popovkin, B.A., 2001. Crystal and electronic structure of $Ni_3Bi_2S_2$ (parkerite). Russian Chemical Bulletin 50, 353-358.

Cao, S., Low, J., Yu, J., Jaroniec, M., 2015. Polymeric photocatalysts based on graphitic carbon nitride. Advanced Materials 27, 2150-2176.

Chen, D., K. Ray, A., 2001. Removal of toxic metal ions from wastewater by semiconductor photocatalysis. Chemical Engineering Science 56, 1561-1570.

Chidhambaram, N., Ravichandran, K., 2017. Single step transformation of urea into metal-free g-C_3N_4 nanoflakes for visible light photocatalytic applications. Materials Letters 207, 44-48.

Dashairya, L., Mehta, A., Saha, P., Basu, S., 2020. Visible-light-induced enhanced photocatalytic degradation of Rhodamine-B dye using $BixSb_2$-xS_3 solid-solution photocatalysts. Journal of Colloid and Interface Science 561, 71-82.

Degen, T., van den Oever, J., 2009. D-16 A Major Update of X'pert Highscore Plus. Powder Diffraction 24, 163-163.

Devamani, R.H.P., Archana, M., Maheshwari, K., Susmitha, D., 2018. Synthesis and characterization of lead II sulphide nanoparticles. Intl J Eng Sci Invent 7, 58-65.

Diao, Z.-H., Xu, X.-R., Jiang, D., Kong, L.-J., Sun, Y.-X., Hu, Y.-X., Hao, Q.-W., Chen, H., 2016. Bentonite-supported nanoscale zero-valent iron/persulfate system for the simultaneous removal of Cr(VI) and phenol from aqueous solutions. Chemical Engineering Journal 302, 213-222.

Dong, F., Wang, Z., Sun, Y., Ho, W.-K., Zhang, H., 2013. Engineering the nanoarchitecture and texture of polymeric carbon nitride semiconductor for enhanced visible light photocatalytic activity. Journal of Colloid and Interface Science 401, 70-79.

Herrmann, J.-M., Disdier, J., Pichat, P., 1988. Photocatalytic deposition of silver on powder titania: Consequences for the recovery of silver. Journal of Catalysis 113, 72-81.

Hou, W.-C., Stuart, B., Howes, R., Zepp, R.G., 2013. Sunlight-Driven Reduction of Silver Ions by Natural Organic Matter: Formation and Transformation of Silver Nanoparticles. Environmental Science & Technology 47, 7713-7721.

Hsiao, I.L., Hsieh, Y.-K., Wang, C.-F., Chen, I.C., Huang, Y.-J., 2015. Trojan-Horse Mechanism in the Cellular Uptake of Silver Nanoparticles Verified by Direct Intra- and Extracellular Silver Speciation Analysis. Environmental Science & Technology 49, 3813-3821.

Ismael, M., Wu, Y., Taffa, D.H., Bottke, P., Wark, M., 2019. Graphitic carbon nitride synthesized by simple pyrolysis: role of precursor in photocatalytic hydrogen production. New Journal of Chemistry 43, 6909-6920.

Kaneco, S., Rahman, M.A., Suzuki, T., Katsumata, H., Ohta, K., 2004. Optimization of solar photocatalytic degradation conditions of bisphenol A in water using titanium dioxide. Journal of Photochemistry and Photobiology A: Chemistry 163, 419-424.

Khanna, P., Subbarao, V., 2003. Nanosized silver powder via reduction of silver nitrate by sodium formaldehydesulfoxylate in acidic pH medium. Materials Letters 57, 2242-2245.

Koh, Y.W., Lai, C.S., Du, A.Y., Tiekink, E.R.T., Loh, K.P., 2003. Growth of Bismuth Sulfide Nanowire Using Bismuth Trisxanthate Single Source Precursors. Chemistry of Materials 15, 4544-4554.

Lan, Z.-A., Zhang, G., Wang, X., 2016. A facile synthesis of Br-modified g-C_3N_4 semiconductors for photoredox water splitting. Applied Catalysis B: Environmental 192, 116-125.

Li, H., Qing, Q., Zheng, L., Xie, L., Gan, Z., Huang, L., Liu, S., Wang, Z., Lu, Y., Chen, J., 2022. Carbon dots and carbon nitride composite for photocatalytic removal of uranium under air atmosphere. Chinese Chemical Letters.

Li, Z., Wang, L., Qin, L., Lai, C., Wang, Z., Zhou, M., Xiao, L., Liu, S., Zhang, M., 2021. Recent advances in the application of water-stable metal-organic frameworks: Adsorption and photocatalytic reduction of heavy metal in water. Chemosphere 285, 131432.

Lin, Y.-Y., Hung, J.-T., Chou, Y.-C., Shen, S.-J., Wu, W.-T., Liu, F.-Y., Lin, J.-H., Chen, C.-C., 2022. Synthesis of bismuth oxybromochloroiodide/graphitic carbon nitride quaternary composites ($BiO_xCl_y/BiO_mBr_n/BiO_pI_q$/g-$C_3N_4$) enhances visible-light-driven photocatalytic activity. Catalysis Communications 163, 106418.

Liu, J., Pennell, K.G., Hurt, R.H., 2011. Kinetics and Mechanisms of Nanosilver Oxysulfidation. Environmental Science & Technology 45, 7345-7353.

López-Muñoz, M.-J., Aguado, J., van Grieken, R., Marugán, J., 2009. Simultaneous photocatalytic reduction of silver and oxidation of cyanide from dicyanoargentate solutions. Applied Catalysis B: Environmental 86, 53-62.

López, R., Gómez, R., 2012. Band-gap energy estimation from diffuse reflectance measurements on sol–gel and commercial TiO_2: a comparative study. Journal of Sol-Gel Science and Technology 61, 1-7.

Madonia, A., Martin-Sabi, M., Sadaoui, A., Ruhlmann, L., Ammar, S., Schaming, D., 2022. Dawson-type polyoxometalates photosensitized with carbon dots for photocatalytic reduction of silver ions. Materials Research Bulletin 149, 111721.

Mohanraj, J., Durgalakshmi, D., Saravanan, R., 2021. Water-soluble graphitic carbon nitride for clean environmental applications. Environmental Pollution 269, 116172.

Nanda, B., Pradhan, A.C., Parida, K.M., 2017. Fabrication of mesoporous CuO/ZrO_2-MCM-41 nanocomposites for photocatalytic reduction of Cr(VI). Chemical Engineering Journal 316, 1122-1135.

Oh, J., Lee, J.M., Yoo, Y., Kim, J., Hwang, S.-J., Park, S., 2017. New insight of the photocatalytic behaviors of graphitic carbon nitrides for hydrogen evolution and their associations with grain size, porosity, and photophysical properties. Applied Catalysis B: Environmental 218, 349-358.

Ohtani, B., Okugawa, Y., Nishimoto, S., Kagiya, T., 1987. Photocatalytic activity of titania powders suspended in aqueous silver nitrate solution: correlation with pH-dependent surface structures. The Journal of Physical Chemistry 91, 3550-3555.

Olatunde, O.C., Onwudiwe, D.C., 2022. A Comparative Study of the Effect of Graphene Oxide, Graphitic Carbon Nitride, and Their Composite on the Photocatalytic Activity of Cu_3SnS_4. Catalysts 12, 14.

Pandey, B., Rani, S., Roy, S.C., 2020. A scalable approach for functionalization of TiO_2 nanotube arrays with g-C_3N_4 for enhanced photo-electrochemical performance. Journal of Alloys and Compounds 846, 155881.

Peng, H., Guo, H., Gao, P., Zhou, Y., Pan, B., Xing, B., 2021. Reduction of silver ions to silver nanoparticles by biomass and biochar: Mechanisms and critical factors. Science of The Total Environment 779, 146326.

Putri, L.K., Ng, B.-J., Er, C.-C., Ong, W.-J., Chang, W.S., Mohamed, A.R., Chai, S.-P., 2020. Insights on the impact of doping levels in oxygen-doped gC_3N_4 and its effects on photocatalytic activity. Applied Surface Science 504, 144427.

Qian, G., Shao, M., Tong, Y., Ni, Y., 2005. Self-template route to $Ni_3Bi_2S_2$ (parkerite) nanoribbons at mild condition. Journal of Crystal Growth 284, 412-416.

Qiu, H., Chen, G., Sun, L., Hao, S., Han, G., Yang, C., 2011. Ethylenediaminetetraacetic acid (EDTA)-controlled synthesis of multicolor lanthanide doped $BaYF_5$ upconversion nanocrystals. Journal of Materials Chemistry 21, 17202-17208.

Rehman, Z.U., Butt, F.K., Balayeva, N.O., Idrees, F., Hou, J., Tariq, Z., Rehman, S.U., Haq, B.U., Alfaify, S., Ali, S., Zaman, S., 2021. Two dimensional graphitic carbon nitride Nanosheets as prospective material for photocatalytic degradation of nitrogen oxides. Diamond and Related Materials 120, 108650.

Sal'nikov, D., Pogorelova, A., Makarov, S., Vashurina, I.Y., 2009. Silver ion reduction with peat fulvic acids. Russian Journal of Applied Chemistry 82, 545-548.

Sane, P., Chaudhari, S., Nemade, P., Sontakke, S., 2018. Photocatalytic reduction of chromium (VI) using combustion synthesized TiO_2. Journal of Environmental Chemical Engineering 6, 68-73.

Shaheen, A., Taj, A., Jameel, F., Tahir, M.A., Mujahid, A., Butt, F.K., Khan, W.S., Bajwa, S.Z., 2022. Synthesis of graphitic carbon nitride nanosheets-layered imprinted polymer system as a nanointerface for detection of chloramphenicol. Applied Nanoscience 12, 139-150.

Sharma, J.C., Gandhi, J., Sharma, A., Gupta, N., Bhardwaj, S., 2008. Photocatalytic Reduction of Silver (I) to Metallic Silver over SrWO4. Int. J. Chem. Sci. 6, 509-518.

Šileikaitė, A., Puišo, J., Prosyčevas, I., Tamulevičius, S., 2009. Investigation of silver nanoparticles formation kinetics during reduction of silver nitrate with sodium citrate. Materials Science (Medžiagotyra) 15, 21-27.

Song, W., Salvador, P.A., Rohrer, G.S., 2018. The effect of pH on the photochemical reactivity of $BaTiO_3$. Surface Science 675, 83-90.

Sun, T., Zhao, Z., Liang, Z., Liu, J., Shi, W., Cui, F., 2017. Efficient As(III) removal by magnetic CuO-Fe_3O_4 nanoparticles through photo-oxidation and adsorption under light irradiation. Journal of Colloid and Interface Science 495, 168-177.

Tan, T., Beydoun, D., Amal, R., 2003. Effects of organic hole scavengers on the photocatalytic reduction of selenium anions. Journal of Photochemistry and Photobiology A: Chemistry 159, 273-280.

Tan, Z., Guo, X., Yin, Y., Wang, B., Bai, Q., Li, X., Liu, J., Jiang, G., 2019. Freezing Facilitates Formation of Silver Nanoparticles under Natural and Simulated Sunlight Conditions. Environmental Science & Technology 53, 13802-13811.

Troupis, A., Hiskia, A., Papaconstantinou, E., 2003. Photocatalytic reduction—recovery of silver using polyoxometalates. Applied Catalysis B: Environmental 42, 305-315.

Wahyuni, E., Aprilita, N., Hatimah, H., Wulandari, A., Mudasir, M., 2015. Removal of toxic metal ions in water by photocatalytic method. American Chemical Science Journal 5, 194-201.

Wang, H., Zhang, L., Chen, Z., Hu, J., Li, S., Wang, Z., Liu, J., Wang, X., 2014. Semiconductor heterojunction photocatalysts: design, construction, and photocatalytic performances. Chemical Society Reviews 43, 5234-5244.

Wang, L., Wang, N., Zhu, L., Yu, H., Tang, H., 2008. Photocatalytic reduction of Cr(VI) over different TiO_2 photocatalysts and the effects of dissolved organic species. Journal of Hazardous Materials 152, 93-99.

Wang, Q., Zhang, Y., Li, Y., Ren, J., Qu, G., Wang, T., Jia, H., 2022. Simultaneous Cu-EDTA oxidation decomplexation and Cr(VI) reduction in water by persulfate/formate system: Reaction process and mechanisms. Chemical Engineering Journal 427, 131584.

Xu, D., Cheng, B., Wang, W., Jiang, C., Yu, J., 2018. Ag_2CrO_4/g-C_3N_4/graphene oxide ternary nanocomposite Z-scheme photocatalyst with enhanced CO_2 reduction activity. Applied Catalysis B: Environmental 231, 368-380.

Yang, J.K., Lee, S.M., Siboni, M.S., 2012. Effect of different types of organic compounds on the photocatalytic reduction of Cr(VI). Environmental Technology 33, 2027-2032.

Yao, D., Hao, W., Weng, S., Hou, M., Cen, W., Li, G., Chen, Z., Li, Y., 2022. Local Photothermal Effect Enabling $Ni_3Bi_2S_2$ Nanoarray Efficient Water Electrolysis at Large Current Density. Small 18, 2106868.

Zhang, J., Zhang, M., Zhang, G., Wang, X., 2012. Synthesis of Carbon Nitride Semiconductors in Sulfur Flux for Water Photoredox Catalysis. ACS Catalysis 2, 940-948.

Zhang, M., Chen, X., Zhou, H., Murugananthan, M., Zhang, Y., 2015. Degradation of p-nitrophenol by heat and metal ions co-activated persulfate. Chemical Engineering Journal 264, 39-47.

Zhang, W., Xiao, B., Fang, T., 2018. Chemical transformation of silver nanoparticles in aquatic environments: Mechanism, morphology and toxicity. Chemosphere 191, 324-334.

Zhang, X.Y., Liu, S.G., Zhang, W.J., Wang, X.H., Han, L., Ling, Y., Li, N.B., Luo, H.Q., 2019. Photoelectrochemical platform for glucose sensing based on g-C_3N_4/$ZnIn_2S_4$ composites coupled with bi-enzyme cascade catalytic in-situ precipitation. Sensors and Actuators B: Chemical 297, 126818.

Zhang, Y., Chen, Z., Li, J., Lu, Z., Wang, X., 2021. Self-assembled synthesis of oxygen-doped g-C_3N_4 nanotubes in enhancement of visible-light photocatalytic hydrogen. Journal of Energy Chemistry 54, 36-44.

Zhou, W., Liu, Y.-L., Stallworth, A.M., Ye, C., Lenhart, J.J., 2016. Effects of pH, Electrolyte, Humic Acid, and Light Exposure on the Long-Term Fate of Silver Nanoparticles. Environmental Science & Technology 50, 12214-12224.

Zhou, W., Yang, B., Liu, G., Xu, C., Ji, Q., Xiang, W., Sun, D., Zhong, Q., He, H., Yazi, L., Xu, Z., Qi, C., Li, S., Yang, S., 2022. Perylene diimide supermolecule (PDI) as a novel and highly efficient cocatalyst for photocatalytic degradation of tetracycline in water: A case study of PDI decorated graphitic carbon nitride/bismuth tungstate composite. Journal of Colloid and Interface Science 615, 849-864.

CHAPTER 6

Synthesis of $AgBiS_2/gC_3N_4$ and its application in the photocatalytic reduction of Pb(II) in the matrix of methyl orange, crystal violet and methylene blue dyes

6.0 Introduction

Lead pollution occurs through the release of lead-containing waste that is generated during chemical manufacturing, mining and from municipal waste. It is common in the environment because of its presence in water pipes, batteries, gasoline additive, paint, ammunitions (as slugs in bullets or lead shots) and insecticides (Clausen et al., 2011). Lead is also found in natural form in the ground water (Murruni et al., 2007), and it has been reported to be toxic to internal organs such as livers and kidneys (Ajiboye et al., 2021a). Also, it is carcinogenic (Leroyer et al., 2022). Hence, their removal from water is a necessity.

Removal of lead from water is usually achieved through hydroxide or carbonate precipitation (Li et al., 2019). The use of precipitating agents such as nitriloacetic acid and ethylenediaminetetraacetic acid, followed by recovery via chemical oxidation, electrolysis or precipitation has also been reported (Koehler et al., 2009; Li et al., 2019). However, these methods are not cost effective as they also require the use of other methods in order to recover the lead from water (Li et al., 2019; Zhu et al., 2019; Ajiboye et al., 2021a). The fact that lead(II) usually co-exists with other organic pollutants such as pharmaceuticals and dyes makes their removal from polluted water more difficult (Ajiboye et al., 2021b). Therefore, photocatalysis is considered as a viable alternative to its removal since it could simultaneously oxidize the organic pollutants and deposit the lead via reduction reaction. Photocatalysts such as metal chalcogenides (oxides and sulphides), and light are required for the photocatalytic process. The synthesis of oxides is relatively easier compared to the synthesis of sulphides which might not be possible without a good sulphur source and favourable reaction conditions.

Maltide ($AgBiS_2$) has two known crystal phases: hexagonal β-$AgBiS_2$ and cubic α-$AgBiS_2$. The cubic phase exists at a low temperature, while the hexagonal phase exists at a high temperature. At 195 °C, inter-conversion of one crystal phase to another takes place. Its crystal structure in the trigonal stable state is shown in Fig. 6.1, in which BiS_6 octahedra are alternated with AgS_6 tetrahedra in their unit cell (Zhong et al., 2013; Ganguly et al., 2019).

A few studies have reported the removal of Pb ions within the matrix of dye pollutants. For example, Wang et al., (Wang et al., 2019) simultaneously reduced Pb(II) and oxidized new coccine dyes by using a nanocomposite of TiO_2 and graphene oxide. Pt-doped TiO_2 has also been utilized as a photocatalyst for the reduction of Pb(II) (Murruni et al., 2007). Several metal sulphide photocatalysts have also been used for the degradation of dyes (Li et al., 2012; Yang and Hao, 2022) and removal of heavy metals (Ajiboye et al., 2021b; Cherifi et al., 2021). $AgIn_5S_8/SnS_2$ heterojunction system has also been used to photocatalytically reduce Pb(II) to metallic lead(Lin et al., 2021). However, an extensive search of the literatures showed that the removal of divalent lead from the matrix of dyes using a nanocomposite of graphitic carbon nitride and silver bismuth sulphide has not been studied. Hence, the current study focussed on the photocatalytic reduction of Pb(II) using $AgBiS_2/gC_3N_4$ composites as the photocatalysts. Three different dyes chosen for the investigations are methyl orange, methylene blue and crystal violet. This was due to their numerous application and their abundance in the wastewater (Dhanalakshmi et al., 2020; R et al., 2021). Graphitic carbon nitride was incorporated because the nitrogen atoms in its structure can form a coordinate bond with the lead metal ions. In addition, it is highly stable and insoluble in water (Ajiboye et al., 2020; Zheng et al., 2021).

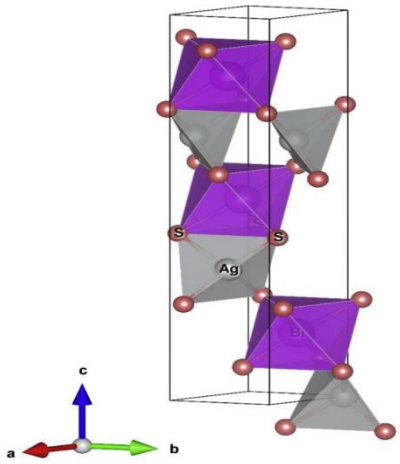

Figure 6.1: Crystal structure of $AgBiS_2$. Colour code: light pink = Bi, red = S grey = Ag (Ganguly et al., 2019).

6.1 Experimental

6.1.1 *Materials and instruments*

Melamine, silver nitrate ($AgNO_3$), bismuth nitrate pentahydrate ($Bi(NO_3)_3{\cdot}5H_2O$)), thioacetamide (CH_3CSNH_2), sodium sulphide (Na_2S), dyes (methylene blue, crystal violet and methyl orange) and lead nitrate ($Pb(NO_3)_2$) used in this study were all of analytical grade supplied by Merck chemicals. The XRD analysis was carried out on a Bruker D8 Advance X-ray diffractometer (Karlsruhe, Germany). The diffractometer has single-wavelength Cu Kα radiation (λ = 1.546060 Å). JEOL 6400F field-emission SEM (Zeiss, Oberkochen Germany) was used for obtaining scanning electron microscopy (SEM) while Transmission electron microscopy (TEM) was obtained on a JEM—2100 JEOL equipment. Bruker alpha-P FTIR spectrophotometer was used for FTIR measurement. SDTQ 600 V20.9 Build 20 Thermal analyser was used for the Thermogravimetric (TG) analysis. Perkin Elmer λ20 UV–vis spectrophotometer was used to obtain the absorption properties.

6.1.2 *Synthesis of graphitic carbon nitride (gC_3N_4)*

10.00 g of melamine was measured into a clean alumina crucible with a lid. It was heated in a muffle furnace for 4 h at 550 °C (constant heating rate of 4 °C min^{-1}) to obtain yellow solid via thermal polymerization (Fig. 6.2). The yellow solid obtained was crushed with mortar and pestle, after cooling, to obtain a yellow powder. The obtained yellow powder was kept in the desiccator to prevent moisture.

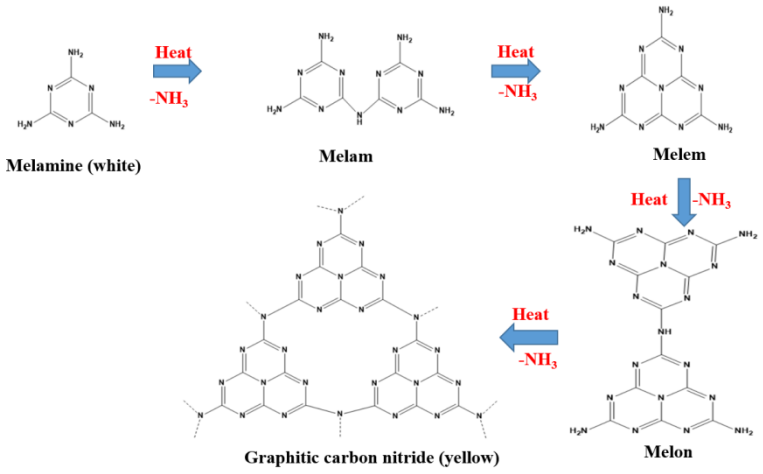

Figure 6.2**:** Thermal condensation of melamine for the formation of graphitic carbon nitride. *Adapted with permission from* (Liu et al., 2016b). *Copyright (2016), The Royal Society of Chemistry.*

6.1.3 *Synthesis of silver bismuth sulphide ($AgBiS_2$)*

1.00 g of bismuth nitrate pentahydrate ($Bi(NO_3)_3{\cdot}5H_2O$) and 1.00 g of silver nitrate ($AgNO_3$) were separately ground with mortar and pestle to increase their surface area. From the ground portion, 0.243 g of bismuth nitrate pentahydrate (0.5 mmol) and 0.085 g of silver nitrate (0.5 mmol) were measured into a 100 mL beaker. A solution of 0.240 g of sodium sulphide (1.0 mmol) and 0.076 g of thioacetamide (1.0 mmol) in 50 mL of distilled water was added to the mixture of bismuth nitrate and silver nitrate. The mixture was stirred at 40 ℃ for 1 h to form a homogenous solution and was transferred into a mini autoclave operated at 180 ℃ for 40 h. After the reaction, deep grey solids were collected from the autoclave. Then, the solid formed was washed by centrifugation several times with absolute ethanol at 6000 rpm. Finally, the pure sample was dried in a muffle furnace at 75 °C for 8 h.

6.1.4 *Synthesis of $AgBiS_2/gC_3N_4$ composite*

The as-prepared silver bismuth sulphide and graphitic carbon nitride were homogenised together in the ratio of 3:1 w/w respectively. The mixture was ground together and calcined at 350 ^oC for 2 h using a muffle furnace to obtain $AgBiS_2/gC_3N_4$ nanocomposite.

6.2 Photocatalytic investigations

About 50 mL solution containing specific concentration of Pb(II) and known mass of as-prepared $AgBiS_2/gC_3N_4$ nanocomposite were introduced into 100 mL glass beaker. The pH was adjusted with NaOH and HCl to pH 12 and 2 respectively. The mixture was allowed to equilibrate in the dark for 20 min. Thereafter, a 28 W visible LED light was switched on to initiate the reaction. The solution was constantly stirred to ensure homogeneity in the system while irradiated with visible light. As the reaction progressed, about 5 mL aliquot of Pb(II) solution was sampled at 15-min regular intervals. The concentration of Pb(II) in each irradiated sample was obtained by using UV-visible spectrophotometer after filtration with 0.45 μm cellulose acetate filters. The percentage of Pb(II) reduced, the pseudo-first order rate constant and the half-life of the reaction were obtained by using **Equations (iv), (v) and (vi)** respectively.

$$\textbf{Percentage photocatalytic reduction} = \frac{C_o - C_t}{C_o} \times 100\% \quad \text{(iv)}$$

$$-Kt = \ln\left(\frac{C_t}{C_o}\right) \quad \text{(v)}$$

$$\textbf{Half} - \textbf{life} = {}^{\ln 2}/_{k} = {}^{0.693}/_{k} \quad \text{(vi)}$$

Where C_o and C_t represent the initial concentration and concentration at time t of aqueous Pb(II) respectively, t is the reaction time and k is the pseudo- first order reaction rate constant.

6.3 Theoretical Background

6.3.1 *Estimation of crystallite size, lattice strain and dislocation density*

The crystallite size of the ternary nanoparticles and the nanocomposites were estimated by using Williamson-Hall plot (the deformation model). This model expresses the full width at half maximum (FWHM) in terms of the lattice strain and crystallite size. The total broadening of a peak is the summation of the effect of the micro strain (β_ε) and crystallite size (β_D), which can be expressed mathematically by **Equation (vii)**.

$$\beta = \beta_D + \beta\varepsilon \quad \text{(vii)}$$

The Scherrer equation (**Equation (viii)**) relates the crystallite size (D), the broadening effect of the crystallite size (β_D), shape factor (k =0.9) and the wavelength of the X-ray source (λ = 0.15406 nm). The value of the shape factor changes with the morphology of the material and the wavelength of the source (Cu Kα radiation). Also, the strain (ε), peak position in radian and the broadening effect due to strain ($\beta\varepsilon$) are connected by **Equation (ix).**

$$\beta_D = \frac{K\lambda}{D\cos\theta} \quad \text{(viii)}$$

$$\beta_\varepsilon = 4\varepsilon\left(\frac{\sin\theta}{\cos\theta}\right) \quad \text{(ix)}$$

Incorporating **Equations (viii) and (ix)** into **Equation (vii)** with re-arrangement gives **Equation (x)**. To obtain Williamson-Hall plot from **Equation (x)**, $\beta \cos\theta$ is plotted against $4 \sin\theta$. The gradient of the plot is the strain (**ε**), while the crystallite size is estimated from the intercept (**Equation (xi)).**

$$\boldsymbol{\beta \cos\theta = \varepsilon\,(4 \sin\theta) + \frac{K\lambda}{D}} \quad \text{(x)}$$

$$\textbf{Intercept} = \frac{K\lambda}{D} \quad \text{(xi)}$$

The amount of dislocation that is present in a unit volume of the prepared material (dislocation density) was determined by using **Equation (xii)**.

$$\textbf{Dislocation Density} = \frac{1}{(\textbf{Crystallite size})^2} \quad \text{(xii)}$$

6.3.2 *Determination of valence band and conduction band edge*

The conduction band potential (E_{CB}) and valence band potential (E_{VB}) of the nanoparticles were determined by using **Equations (xiii) and (xiv)** respectively.

$$\mathbf{E_{CB} = \chi - E_e - 0.5E_g} \quad \text{(xiii)}$$

$$\mathbf{E_{VB} = E_{CB} + E_g} \quad \text{(xiv)}$$

Where E_e is the energy of free electrons measured on the hydrogen scale (4.5 eV) (Mousavi et al., 2016), and χ is the electronegativity of the semiconductor nanoparticles. It is estimated from the geometric mean of all the elements in the semiconductor nanoparticles. For instance, for a semiconductor nanoparticle containing elements D, E, F and G with the number of atoms of d, e, f and g respectively. The formula for obtaining the electronegativity for that semiconductor nanoparticle is represented in **Equation (xv)**.

$$\boldsymbol{\chi_{dDeEfFgG} = (\chi\,(D)^d + \chi(E)^e + \chi(F)^f + \chi(G)^g)^{(d+e+f+g)^{-1}}} \quad \text{(xv)}$$

The Mulliken electronegativity of each atom in the semiconductor nanoparticles $(\boldsymbol{\chi(D), \chi(E), \chi(F) and\ \chi(G)})$ are estimated from the first ionization energy and the electron affinity of the atoms via **Equation (xvi)**.

$$\chi_{element} = \frac{(\textbf{First ionization energy (eV)} + \textbf{Electron affinity (eV)})}{2} \quad \text{..... (xvi)}$$

Where $\chi_{element}$ is the Mulliken's electronegativity of element in eV.

6.4 Results and Discussion

6.4.1 *Synthesis of the nanoparticles*

Both sodium sulphide and thioacetamide are good sulphur sources for preparing metal sulphide nanoparticles. In the synthesis reaction involving sodium sulphide, it reacts directly with bismuth nitrate pentahydrate and silver nitrate to give the ternary silver bismuth sulphide under favourable reaction conditions. On the contrary, thioacetamide hydrolyses into acetamide and hydrogen sulphide (Wang et al., 2014). The hydrogen sulphide formed, then reacts with bismuth nitrate pentahydrate and silver nitrate to give the ternary silver bismuth sulphide. The proposed equations of reactions are shown in **Equations (i-iii).** Other sulphur sources have been utilized in the synthesis of $AgBiS_2$ under different conditions to obtain different morphological structures and they have been utilized for several applications as shown in Table 6.1**.**

$$Bi(NO_3)_3{\bullet}5H_2O_{(aq)} + AgNO_{3\,(aq)} + 2Na_2S(aq) \rightarrow AgBiS_{2(s)} + 4NaNO_{3(aq)} + 5H_2O_{(l)} \quad \text{..... (i)}$$

$$CH_3CSNH_{2(aq)} + H_2O_{(l)} \rightarrow CH_3CONH_{2(aq)} + H_2S_{(g)} \quad \text{.....(ii)}$$

$$2H_2S(g) + Bi(NO_3)_3{\bullet}5H_2O(aq) + AgNO_{3(aq)} \rightarrow AgBiS_{2(s)} + 4HNO_{3(aq)} + 5H_2O(l) \quad \text{..... (iii)}$$

Table 6.1: Synthesis and applications of $AgBiS_2$

Sulphur source	Morphology	Conditions	Applications	Ref.
Sodium sulphide	Roughly round	150 °C; air; 1 h	Sensitized solar cell	(Huang et al., 2013)
Thiourea	-	180 °C; 24 h	Hydrogen generation	(Ganguly et al., 2019)
l-cysteine	Spheroidal	150–230 °C; 12 h	-	(Zhong et al., 2013)

Oleic acid	Microspheres	180 °C; 20 h; 20 kHz agitation	Catalytic polymerization of alkylsilanes	(Wang et al., 2007)
Sulphur powder	Cubic structure	1020 °C; 15 min; Ar/H_2; pressure of 25 mbar	Infrared detector	(Mak et al., 2018)
Hexamethyldisilathiane	Spherical	100 °C; 2 h;	Solar cell	(Wang et al.)
Thiourea	Hollow Nanospheres	130 °C; 1 h	Tumor Therapy	(Chen et al., 2020)
Hexamethyldisilathiane	Quantum dots	100 °C; argon; 6 h	Solar cells	(Ming et al., 2020)
1-octanethiol	Nanosphere	-	Photovoltaic applications	(Pai et al., 2018)
Thioacetamide	Fingerprint-like	180 °C; 30 min; Tween-20; Degassing	Phototherapy	(Cheng et al., 2020)
Thiosemicarbazide	Nanostructured flowers	140–200 °C; 24–72 h	-	(Thongtem et al., 2010)

6.4.2 *X-ray diffraction (XRD) studies*

The peaks obtained in the XRD pattern (Fig.63a) correspond to the cubic phase of the $AgBiS_2$. The (111), (200), (220), (311), (222), (400), (331) and (420) peaks appeared at 27.5°, 31.8°, 45.5°, 53.7°, 56.5°, 66.0°, 72.9° and 75.2° respectively, in good agreement with the JCPDS card no. 89-3672. There were no peaks emanating from silver, bismuth, silver sulphide, silver oxide, bismuth sulphide and bismuth oxide in the pattern. And this was an indication of the high purity of the synthesized ternary nanoparticles (Zhong et al., 2013). The sharpness and intensity of the peaks further showed that the material is highly crystalline in nature (Liu et al., 2011).

The characteristic peak of graphitic carbon nitride is a pronounced peak at $2\theta = 27.5°$, which is indexed to (002) pattern (Fig.6 3a). This peak corresponds to the stacking of the aromatics in the structure of graphitic carbon nitride (Ben-Refael et al., 2020). All the ternary silver bismuth sulphide peaks and those of graphitic carbon nitrides were evident in the as-synthesized nanocomposites. The results obtained are in agreement with other previous reports (Zhong et

al., 2013; Manimozhi et al., 2019; Shi et al., 2020). The lattice parameter (a) was obtained by using **Equation (xvii)**.

$$\boldsymbol{a = d\ (h^2 + k^2 + l^2)} \quad \text{(xvii)}$$

where d is the spacing between the planes for miller indices (hkl). The miller indices used for the calculation was the (200) plane. The obtained lattice parameter (a) was 5.610 Å, which agrees well with the JCPDS card no: 89-3672 (5.648 Å) (Manimozhi et al., 2019). The peaks obtained for the composites were the combination of peaks from the silver bismuth sulphide and graphitic carbon nitride (Fig.6 3b). There was a 0.10 °C shift in the position of (002) peak of graphitic carbon nitride after the formation of composite. The position of the peak changed from 27.5° in the pristine graphitic carbon nitride to 27.4° in the composite. This shift in position after incorporation also affected the (111) peak of the ternary silver bismuth sulphide. The increase in the broadness of the peak at 27.4° of the composite showed the overlap of the peak indexed as (111) of the ternary silver bismuth sulphide and the peak indexed as (002) of the pristine graphitic carbon nitride (Sun et al., 2017).

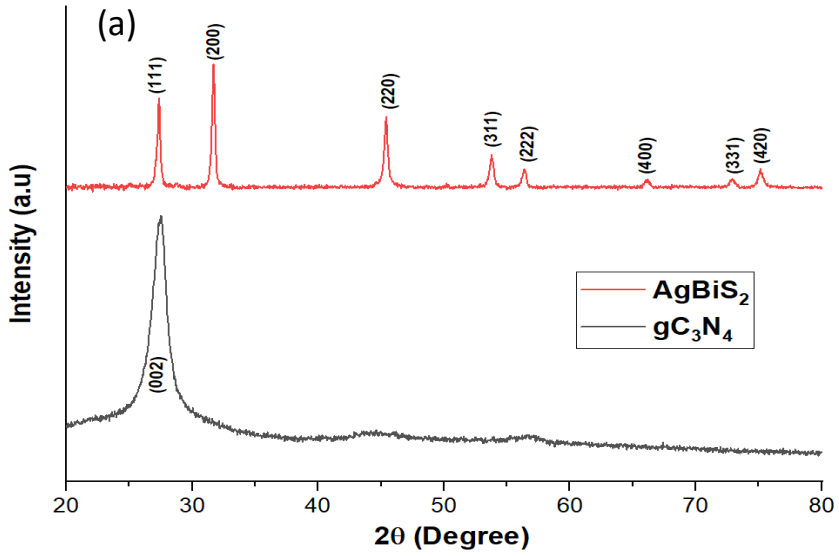

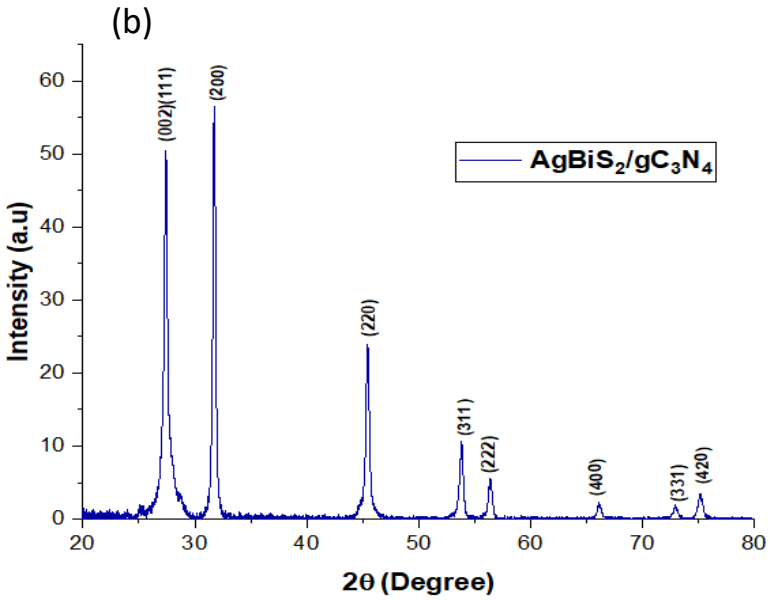

Figure 6.3: The XRD spectra of (a) graphitic carbon nitride, (b) silver bismuth sulphide and (c) composite of graphitic carbon nitride and ternary silver bismuth sulphide.

Williamson-Hall plot was used to obtain the lattice strain of the graphitic carbon nitride (Fig.6 4), the ternary nanoparticles and the nanocomposite. The lattice strain of the graphitic carbon nitride was obtained as 0.466, which was more than the lattice strain of the ternary silver bismuth sulphide (0.0044) and their composite (0.2091). The particle size derived from Scherrer's equations are 32.86, 70.94, and 54.55 nm for $AgBiS_2$, gC_3N_4 and $AgBiS_2/gC_3N_4$ composites respectively. From their sizes, the respective dislocation densities were obtained as 9.26×10^{-4}, 1.99×10^{-4} and 3.36×10^{-4} nm^{-2} respectively. The high dislocation density of the composite compared to that of the graphitic carbon nitride was an indication that the ternary silver bismuth functionalized graphitic carbon nitride was stronger than the pristine graphitic carbon nitride (Morito et al., 2003; Niu et al., 2019).

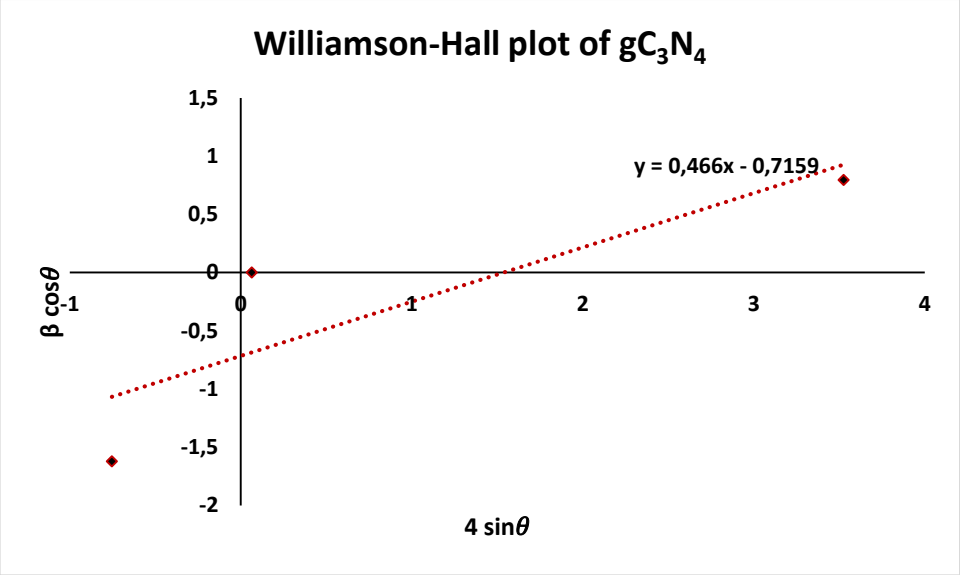

Figure 6.4: Williamson-Hall plot of graphitic carbon nitride.

6.4.3 *FTIR studies*

The FTIR spectrum of $AgBiS_2$ (Fig.6.5) showed the characteristic Ag-S peak around 492 cm^{-1} and the peak at 597 cm^{-1} showed that the Bi-S bond was present in the ternary material (Sugarthi et al., 2020). The S-H stretching vibrational peak appeared at 2107 cm^{-1} which may be as a result of the interaction of sulphur atoms in the ternary sulphide with the hydrogen of acetamide that was used as the sulphur source. The pattern obtained was consistent with the report of Nakazawa et al., (Nakazawa et al., 2021). The FTIR spectrum of graphitic carbon nitride (Fig.6. 5) shows several peaks within 1200-1750 cm^{-1} and could be attributed to the presence of aromatic heterocycles in the structure of graphitic carbon nitride. Specifically, the vibration of s-triazine rings and the C=N group (Ben-Refael et al., 2020). A sharp peak at 799 cm^{-1} was as a result of the breathing mode of the s-triazine unit (Nabi et al., 2020). At 3123 cm^{-1}, the broad peak was as a result of the uncondensed amino group (N-H), which might have overlapped with the hydrogen-bonded –OH from the adsorbed water (Xu et al., 2013; Ben-Refael et al., 2020). The result obtained is in tandem with previous reports on graphitic carbon nitride (Xu et al., 2013; Ajiboye et al., 2020; Chamorro-Posada et al., 2022; Rahmati et al., 2022). All the peaks in the graphitic carbon nitrides and silver bismuth sulphide appeared in the FTIR peaks of the composite $AgBiS_2/gC_3N_4$ (Figure 6.5**)**.

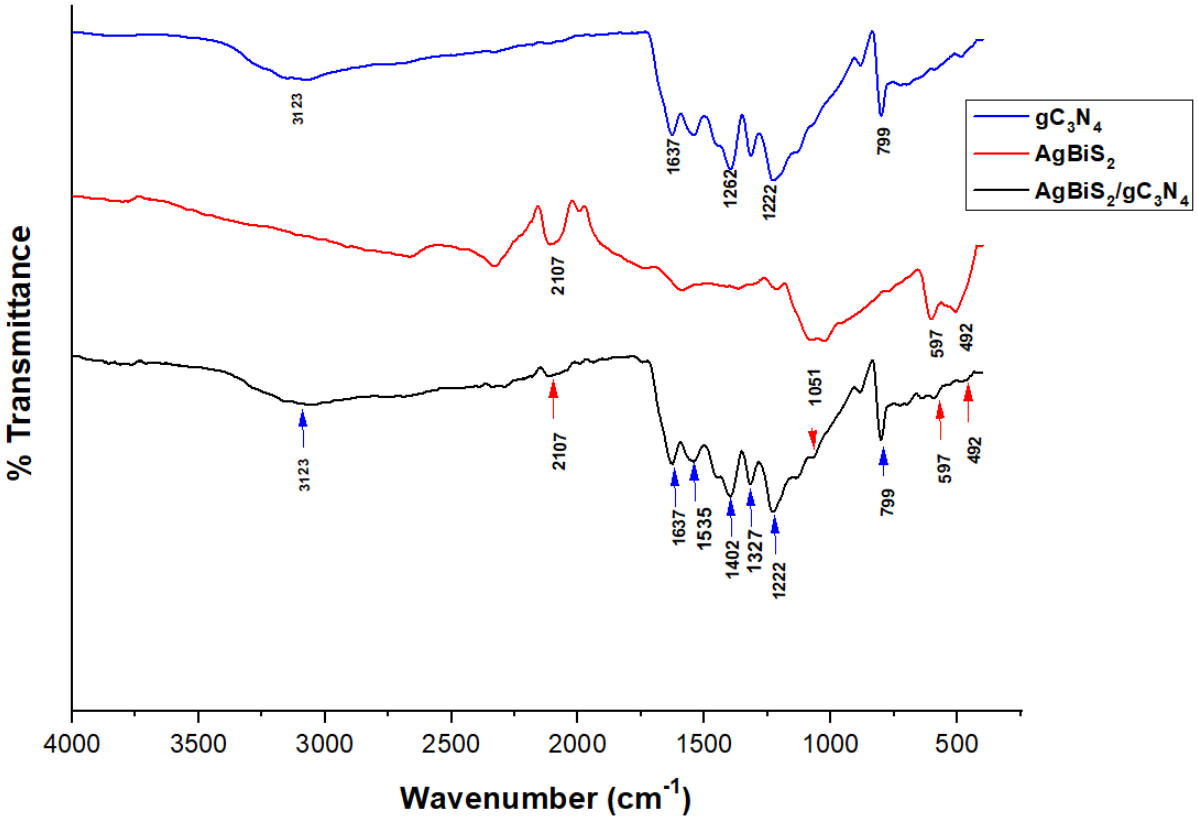

Figure 6.5: The FTIR spectra of graphitic carbon nitride (blue), silver bismuth sulphide (red) and their nanocomposite. The peaks arising from silver bismuth sulphides are indicated with red-arrows, while the peaks arising from graphitic carbon nitrides are shown with blue arrows.

6.4.4 *Morphological properties of $AgBiS_2$ and $AgBiS_2/gC_3N_4$ composite*

The SEM image (Fig. 6.6a) showed that the ternary nanoparticles have spherical external morphology, while the TEM image (Fig. 6.6b) revealed that the internal morphology of the material is pseudo-spherical. The average diameter of the sphere obtained from the TEM result of $AgBiS_2$ is shown in the particle size distribution histogram and it shows that the diameter of the nanosphere was about 25.0 nm (Inset of Fig.6.6d**)** which was close to the value obtained from the XRD pattern (32.9 nm). HRTEM image (Inset of Fig. 6.6b) showed the lattice spacing of the ternary sulphide, which was found to be 0.140 nm and corresponded to the (200) plane of $AgBiS_2$. The EDX spectrum of $AgBiS_2$ (Fig. 6.6c) shows the presence of silver, bismuth and sulphur atoms. From the mean percentage composition by weight, the mole ratio of Ag: Bi: S was estimated to be 1.00: 1.02: 2.12. This ratio confirms the formation of ternary silver bismuth sulphide. The carbon and oxygen are impurities in the synthesized nanoparticles as shown in

the EDX spectrum. The elemental mapping images (Fig. 6(e-h)) shows the uniform distribution of silver, bismuth and sulphide in the ternary silver bismuth sulphide.

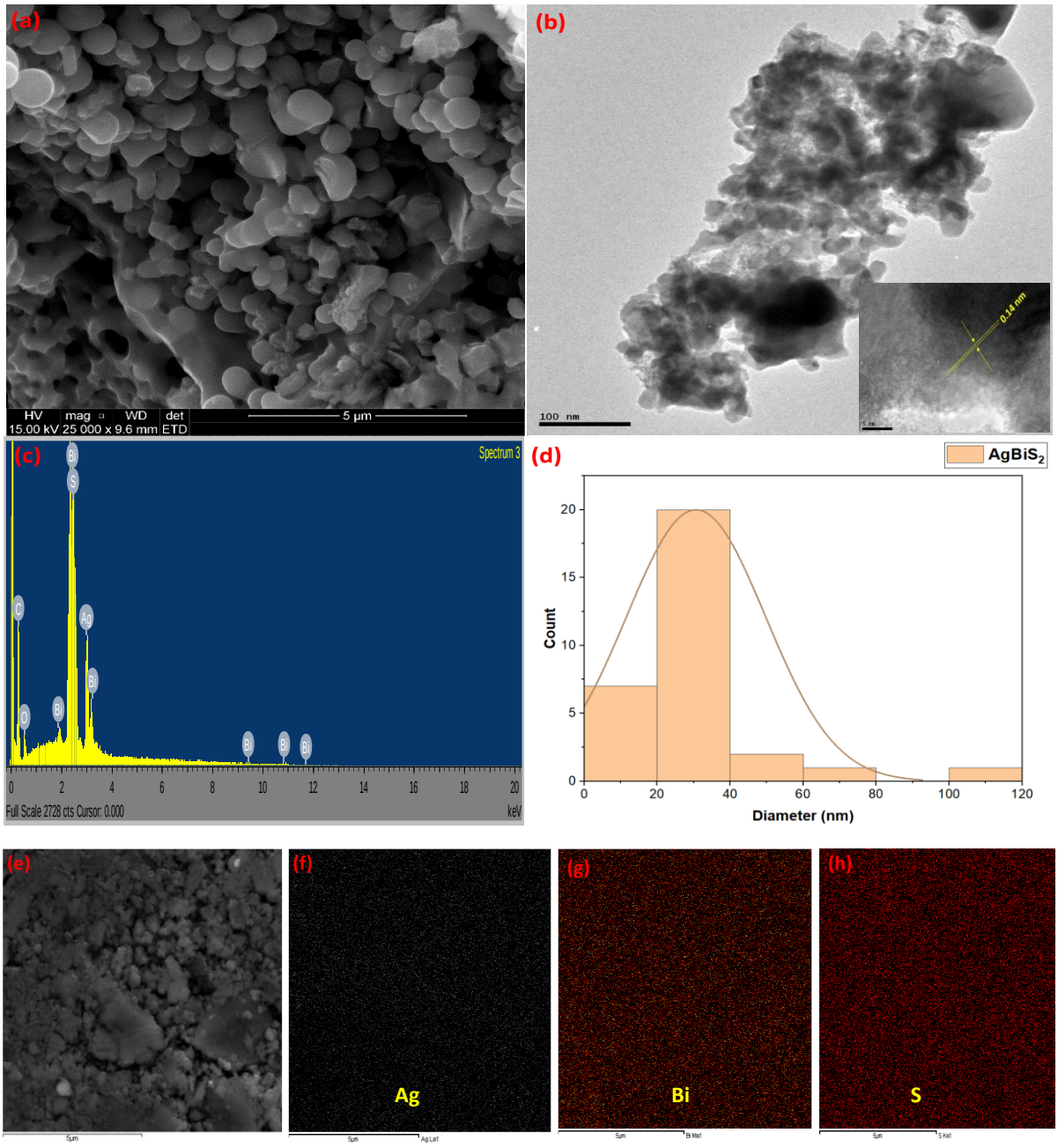

Figure 6.6: (a) SEM image of silver bismuth sulphide (b) TEM image (insets are the particle size distribution histogram and the high resolution TEM image showing the lattice spacing of silver bismuth sulphide and (e-h) the elemental mapping of silver, bismuth and sulphur in silver bismuth sulphide (c) The EDX spectrum of silver bismuth sulphide.

The SEM result showed that graphitic carbon nitride has an aggregated nanospherical morphology (Fig. 6.7a), while the TEM result showed that its internal morphology has an irregular folded sheet (Fig.6 7b). The EDX spectrum of graphitic carbon nitride confirmed the presence of carbon and nitrogen (Fig. 6.7c). The mean percentage composition by weight showed that the mole ratio of carbon: nitrogen was 3.30: 4.06 (0.72). This further confirmed the formation of gC_3N_4. The value of the carbon-to-nitrogen ratio which was lower than 0.75, showed that the graphitic carbon nitride produced was a disordered phase and there were uncondensed $–NH_2$ in its structures (Liu et al., 2016a; Wang et al., 2022). The elemental mapping images (Fig.6 7(d-f)**)** confirmed the uniform distribution of carbon and nitrogen across the sheet.

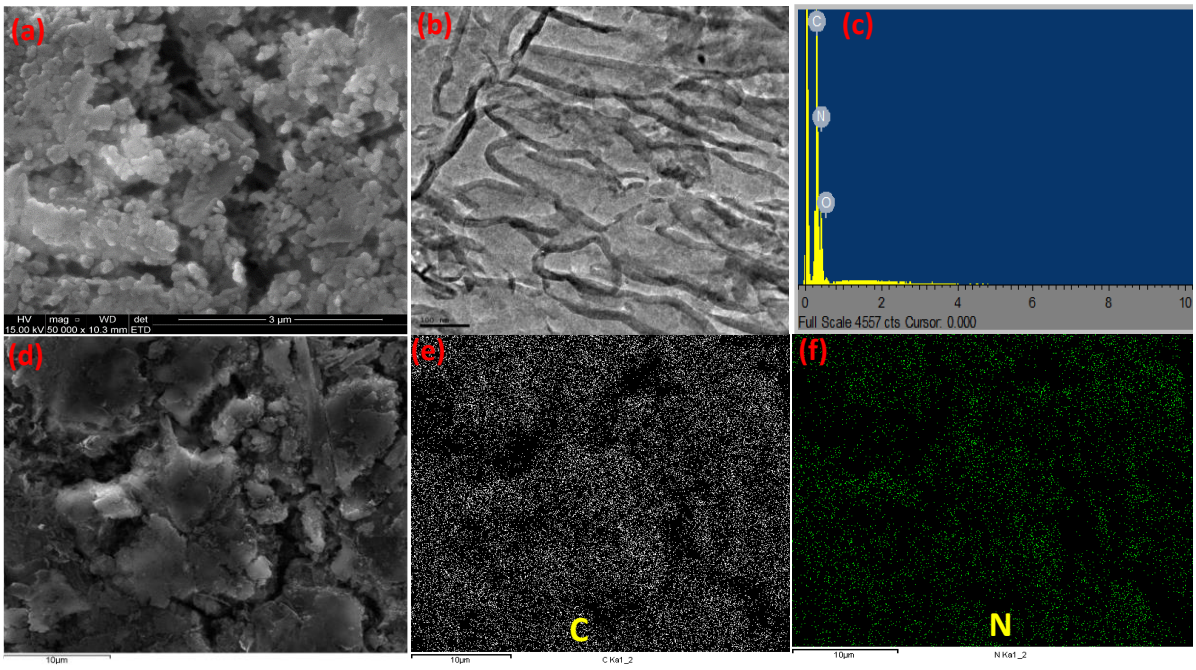

Figure 6.7: (a)The SEM image of graphitic carbon nitride (b) TEM image of graphitic carbon nitride (c) EDX spectrum of graphitic carbon nitride and (d-f) the distribution of carbon and nitrogen in graphitic carbon nitride.

The SEM image of the $AgBiS_2/gC_3N_4$ (Fig.6.8a) revealed a change in the surface morphology of the material from spherical to irregular shape after the incorporation of the silver bismuth sulphide into the graphitic carbon nitride. The EDS spectrum showed the presence of silver, bismuth, sulphur, carbon and nitrogen with weight percentage of 6.97, 11.10, 1.92, 36.03 and 39.55% respectively. Oxygen has been reported to be a natural impurity in graphitic carbon

nitride and is located at the defect of termination site, (Chen et al., 2019; Irfan et al., 2019; Praus, 2021). The TEM micrograph showed a highly agglomerated image with lack of distinct edges (Fig.6. 8b). The HRTEM image (Fig. 8c-d) showed an increase in the lattice spacing from 0.14 nm in the pristine silver bismuth sulphide to 0.34 nm along (200) plane after incorporation into graphitic carbon nitride to form composite $AgBiS_2/gC_3N_4$ nanocomposites.

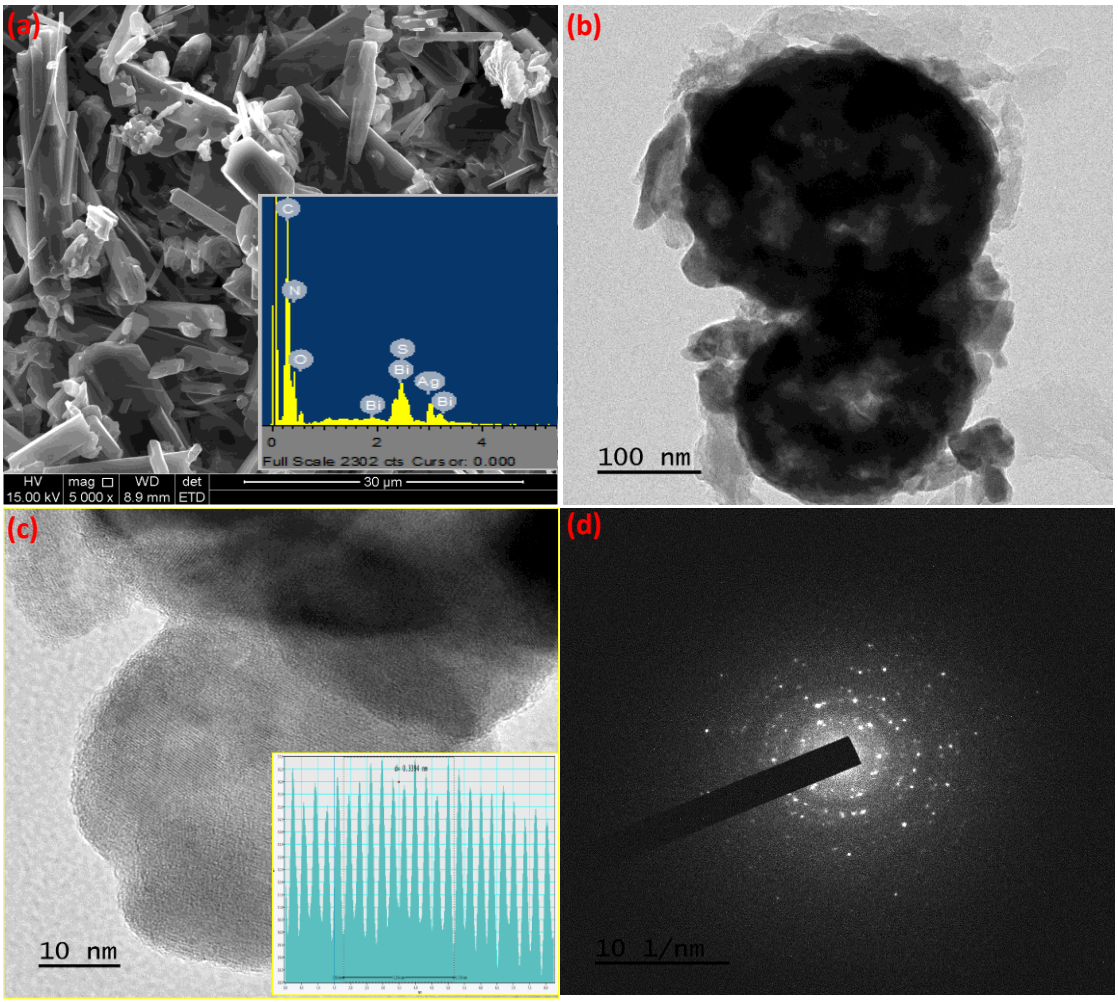

Figure 6.8: (a) The SEM image (inset is the EDS) of $AgBiS_2/gC_3N_4$ (b) the TEM image of $AgBiS_2/gC_3N_4$ and (c) the HRTEM image of $AgBiS_2/gC_3N_4$. (d) SAED of $AgBiS_2/gC_3N_4$.

6.4.5 *Thermal studies of $AgBiS_2/gC_3N_4$*

Fig. 6.9 presents the thermogravimetric and differential scanning calorimetry of the $AgBiS_2/gC_3N_4$. The first loss in mass observed in the TGA plot (Fig.6. 9a) of the composite $AgBiS_2/gC_3N_4$ below 200 ºC is attributed to the loss of the adsorbed water through

volatilization (Antony et al., 2022). As the heating temperature increased, the graphitic carbon nitride decomposed into gases containing nitrogen and carbon around 600 ^{o}C and a collapse of the heterocyclic ring and complete decomposition occurred around 700 ^{o}C (Han et al., 2017; Antony et al., 2022). This process was accompanied by an endothermic process with peaks observed at 616 ^{o}C and 718 ^{o}C on the DSC thermogram (Fig.6 9b). The pronounced weight loss around 800 ^{o}C could be due to the melting of the ternary bismuth sulphide (Nakamura et al., 2015). An increase in the decomposition temperature of the graphitic carbon nitride composite was noticeable compared to the values earlier reported in different studies (Fronczak et al., 2022; Shcherban et al., 2022) for pristine graphitic carbon nitride. This observation showed that the graphitic carbon nitride was functionalized with the silver bismuth sulphide (Fronczak et al., 2022; taghi Bagherian Jamnani et al., 2022). As shown in the TGA and DSC thermograms of pristine silver bismuth sulphide (Fig. S5 and S6), there was no pronounced loss in weight until the temperature increased to 468 ^{o}C. The fact that approximately 20.0% by weight residue was found in the TGA thermogram of both pristine ternary silver bismuth sulphide and the composite after 1000 ^{o}C showed that total volatilization of $AgBiS_2$ is not possible at 1000 ^{o}C.

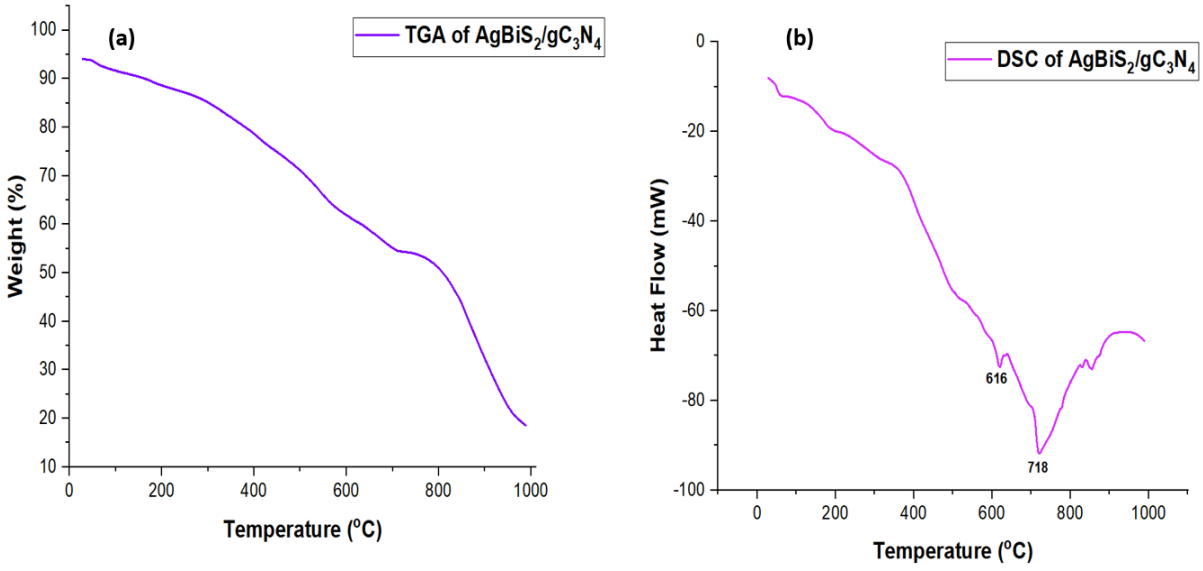

Figure 6.9: (a) Thermo gravimetric (TG) and (b) Differential scanning calometry (DSC) graphs of $AgBiS_2/gC_3N_4$.

The Muliken's electronegativity of graphitic carbon nitride was obtained as 6.91 eV when the electronegativity of carbon and nitrogen were 6.43 and 7.30 eV respectively. This value agrees

well with the values reported by Praus (Praus, 2021) after the values obtained by several authors for the Mulliken's electronegativity of graphitic carbon nitride were corrected (Lu et al., 2011; Fang et al., 2015). However, Praus estimated the average of all the values reported by all the authors and considered factors such as presence of oxygen as natural impurities, defects, layers' distortions, degree of exfoliation and polymerization, synthesis atmosphere, temperature and precursors. The electronegativity value of graphitic carbon nitride was hence considered to be 4.22 eV since 6.91 eV has not been experimentally proven. From this value, the conduction band of -1.63 eV and valence band potentials of +1.07 eV were obtained instead of +1.06 eV and +3.76 eV for conduction band and valence band respectively, which were obtained when the Mulliken's electronegativity values of 6.91 eV was used for graphitic carbon nitride. The band gap energy of 2.70 eV used for the graphitic carbon nitride has been widely reported (Praus, 2021; Fronczak et al., 2022; Kumar et al., 2022; Xing et al., 2022; Lin et al., 2023). Also, the Mulliken's electronegativity values for the elements, $AgBiS_2$ and $AgBiS_2/gC_3N_4$ composites are shown in the Tables 6.2 (a and b**)**.

Table 6.2a: Electron affinity, first ionization energy and Mulliken's electronegativity value for the elements in the composite.

Element	Electron Affinity (eV)	First Ionization Energy (eV)	$\chi_{element}$
Sulphur	2.07	10.36	6.215
Bismuth	0.95	7.29	4.120
Silver	1.30	7.58	4.440
Carbon	1.59	11.26	6.425
Nitrogen	0.07	14.53	7.300

Table 6.2b: Mulliken's electronegativity, conduction band, valence band and the band gap energy for the pristine nanoparticles and the nanocomposite.

Semiconductors	Mulliken's electronegativity (eV)	Bandgap energy (eV)	Conduction band potential (eV)	Valence band potential (eV)
gC_3N_4	4.22	2.70	-1.63	+1.07
$AgBiS_2$	5.15	3.00	-0.85	+2.15
$AgBiS_2/gC_3N_4$	6.22	1.65	+0.90	+2.54

6.4.6 *Photocatalytic investigations*

The wavelength of maximum absorption for Pb(II) was found at 212 nm. As shown in Fig.6 10a, a sequential decrease in the intensity of absorption occurred as the time of irradiation increased in the presence of $AgBiS_2/gC_3N_4$ under visible light irradiation**.** This shows that the composite is a good photocatalyst. The performance of the composite photocatalyst was compared to that of pristine graphitic carbon nitride (Fig.6. 10b). About 58.2% of the Pb(II) was observed to be photocatalytically reduced when pristine graphitic carbon nitride alone was utilized under visible light irradiation, but the performance was better when the as-synthesized nanocomposite was used as photocatalyst under visible light irradiation. A photocatalytic efficiency of 64.3% of Pb(II) reduction was achieved with the nanocomposite. A control experiment, conducted without the photocatalyst and under light irradiation, showed that there was about 19.1% self-reduction of Pb(II) ions when there was no catalyst. The observation was in line with the previous reports for other functionalized graphitic carbon nitrides (Ajiboye et al., 2020; Zhao et al., 2021). The enhanced photocatalytic performance of the composite could be attributed to better charge separation and reduction in the rate of recombination (Sarkar et al., 2021).

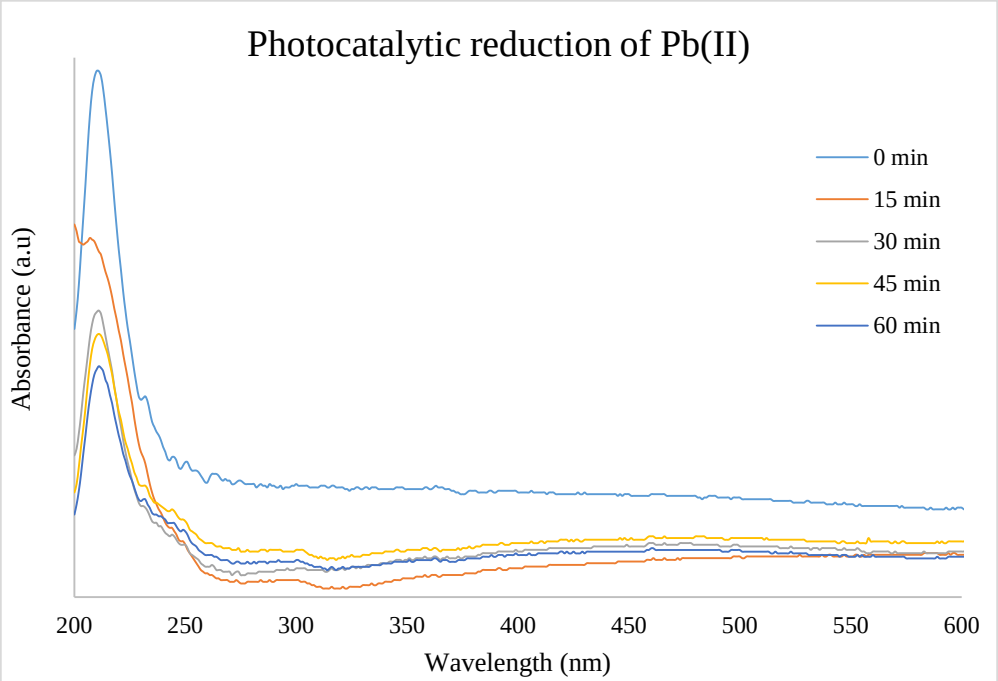

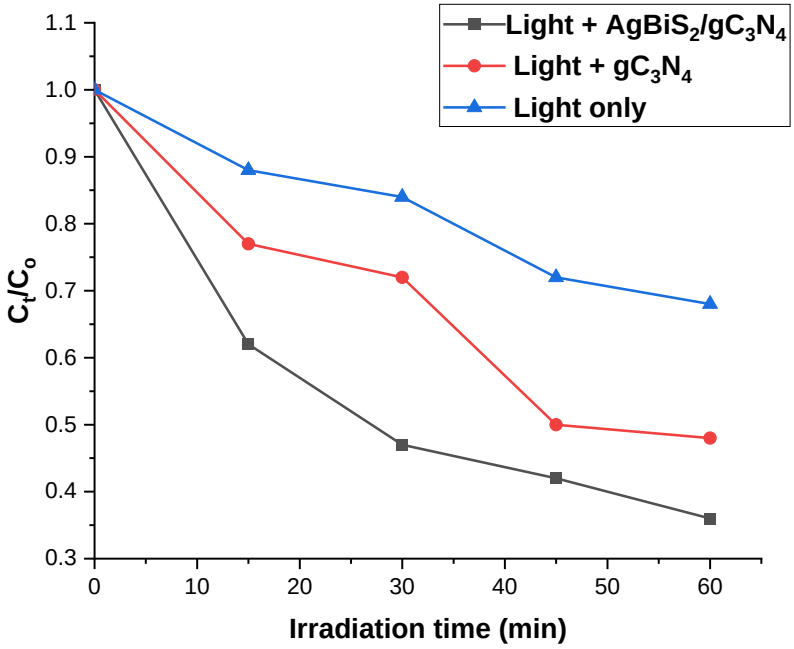

Figure 6.10: (a) Photocatalytic reduction of Pb(II) ions in aqueous system using $AgBiS_2/gC_3N_4$ as photocatalyst. (b) Comparative studies of the photocatalytic reduction of Pb(II) ions using only light, graphitic carbon nitride and functionalized graphitic carbon nitride.

6.4.7 *Conditions for the photocatalytic reduction of Pb(II) in dyes using $AgBiS_2/gC_3N_4$ photocatalyst*

The optimum pH for the photocatalytic reduction of Pb(II) was found to be the neutral pH. The pseudo-first order rate constant for the photocatalytic reduction were 0.0045, 0.0193 and 0.0019 min^{-1} for pH 3, pH 7 and pH 12 respectively, while the half-life were 154, 36 and 365 min respectively (Fig. 6.11). It shows that highly alkaline pH is not effective for the photocatalytic reduction process. The result is consistent with the results obtained by Majidnia and Idris (Majidnia and Idris, 2016). Acidic pH has been reported as the optimum pH for the degradation of methylene blue and methyl orange (Dai et al., 2007; Nguyen et al., 2018; Isai and Shrivastava, 2019), while the optimum pH could range from acidic to alkaline for crystal violet (Senthilkumaar and Porkodi, 2005; Fahoul et al., 2022). Since the photocatalytic reduction was carried out in the matrix of dyes, the acidic pH was used for the investigation to favour both photodegradation of Pb(II) and photodegradation of dyes. Based on the observed trend in previous reports on the photocatalytic reduction of Pb(II) (Murruni et al., 2007;

Majidnia and Idris, 2016), the dosage of the photocatalyst and the initial concentration of the dyes used throughout the investigations were 30 mg and 20 mg/L respectively at room temperature.

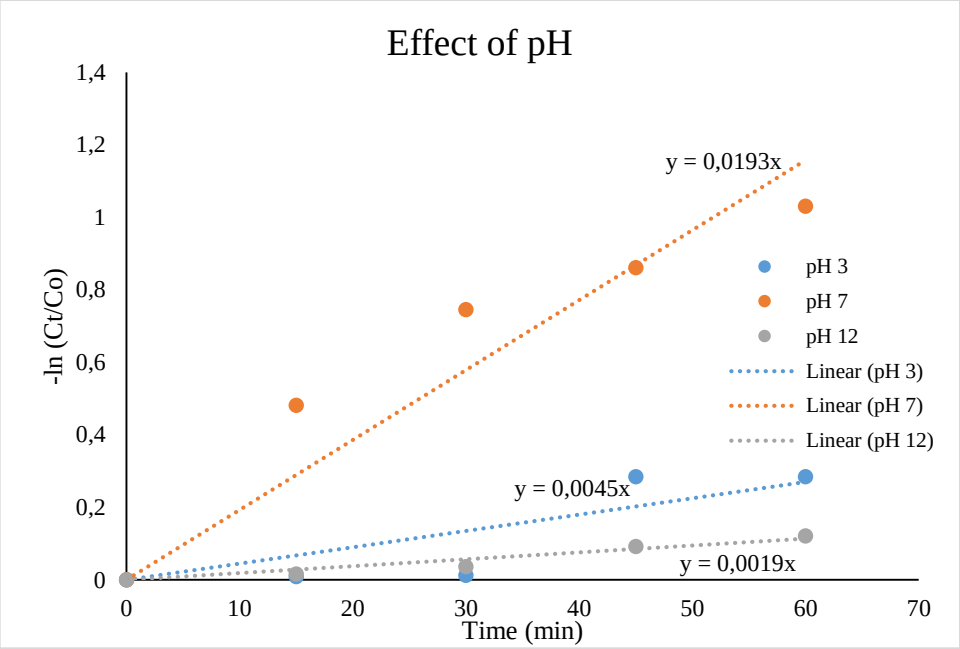

Figure 6.11: Influence of pH on the photocatalytic reduction of Pb(II) ions by using $AgBiS_2/gC_3N_4$ photocatalyst under visible light.

6.4.8 *Effect of sacrificial easily-oxidizable organics and persulfate on the photocatalytic reduction of Pb(II) using $AgBiS_2/gC_3N_4$ photocatalyst*

Easily-oxidizable organics such as oxalic acid, formic acid, lactic acid, glucose, acetaldehyde, methanol and ethanol are commonly used for photocatalytic investigations. Studies have shown that ethanol has least effect on the rate of photocatalysis among these common easily-oxidizable organics (Kmetykó et al., 2016). This implies that the performance of others in photocatalytic applications is believed to be better than that of ethanol. Against this background, the effect of the presence of ethanol in the photocatalytic reduction of Pb(II) was investigated. The study revealed that the pseudo-first order rate constant increased by more than two folds with the addition of 10 mL of absolute ethanol compared to the results obtained in the absence of ethanol. The rate of photocatalytic reduction changed from 0.0045 to 0.0096 min^{-1} (the half-life changed from 154 to 72.2 min) (Fig. 6.12a). The observed difference in performance could be ascribed to the action of photo-generated holes, electrons and peroxyl radicals.

The oxidation of the organic is initiated by the holes and peroxyl radicals, which reduce the rate of holes and electrons recombination (Zou et al., 2020). The rate at which electrons cause the reduction of Pb(II) becomes faster as the easily oxidizable organic (ethanol) consumes the electrons in the system. According to Muggli et al., (Muggli et al., 1998), ethanol is oxidized into acetaldehyde on more than one site in the presence of the photocatalyst and light. In one of the sites, it is difficult to desorb acetaldehyde while it could easily be desorbed in the other sites. The adsorbed acetic acid can either form formaldehyde/formic acid mixture or acetic acid. The α-carbon of acetic acid is oxidized into carbon dioxide, while its *β*-carbon is oxidized into formaldehyde/formic acid mixture intermediates before the final oxidation into carbon dioxide. The oxidation processes lead to better reduction of the metal ions in the solution.

The effect of the presence of persulfate on the photocatalytic reduction of Pb(II) was also investigated. The presence of persulfate was found to exhibit some inhibitory effects on the rate of photocatalytic reduction of Pb(II). The rate of photocatalytic reduction of Pb(II) dropped from 0.0045 min^{-1} (half-life 154 min) to 0.001 min^{-1} (half-life of 693 min) when 10 mL of 300 mg/L potassium persulfate was introduced into the system (Fig. 6.12a). The low photocatalytic reduction could be due to the re-oxidation of the lead in the oxidation state of zero back to the divalent state by the persulfate ions and sulfate radicals as shown in **Equations (xviii-xxi)**. The standard potential of sulfate radicals and persulfate ions are +2.60 V and +2.10 V respectively vs. normal hydrogen electrode (Tsitonaki et al., 2010), while the standard potential of Pb^{2+}/Pb is -0.13 V vs. normal hydrogen electrode. Based on the requirement of the thermodynamics, the high positive electrode potential values of the sulfate radicals and persulfate ions make them a good oxidizing agents for lead that has a negative electrode potential. Also, persulfate has been reported to be an electron scavenger (Zhao et al., 2021), which shows that electron play crucial roles in the photocatalytic reduction of metal ions.

$Pb^{2+} + 2e^{-} \rightarrow Pb^{o}$…….…….. (xviii)

$K_2S_2O_8 \rightarrow 2K^{+} + S_2O_8^{2-}$ ……..….. (xix)

$S_2O_8^{2-} + Pb^{o} \rightarrow SO_4^{2.-} + SO_4^{2-} + Pb^{2+}$……... (xx)

$SO_4^{2.-} + Pb^{o} \rightarrow SO_4^{2-} + Pb^{2+}$…… (xxi)

This observation of persulfate with Pb(II) reduction was a direct opposite of what was reported for different organic pollutants when functionalized graphitic carbon nitrides were used as the photocatalyst. For instance, the presence of persulfate has led to the fast degradation of antibiotics (Zhao et al., 2019), bisphenol A (Zhang et al., 2019), amaranth and benzoquinone dye (Yang et al., 2019b), methylene blue, acetaminophen, phenol and caffeine (Yang et al.,

2019a). Infact, persulfate has enhancement effects on the photocatalytic oxidation of organic pollutants, although it has inhibitory effects on the photocatalytic reduction of toxic metals.

The effect of the combination of persulfate and easily oxidizable organics were also investigated (Fig. 6. 12b). It was observed that the percentage of the Pb(II) that was photocatalytically reduced dropped from 48.4% to 47.8% within 1 h of visible light irradiation when potassium persulfate was introduced into the system. This shows that the inhibitory effect of the persulfate was countered by the presence of easily oxidizable organics. In fact, the introduction of easily oxidizable organics (ethanol) to the system containing persulfate alone boosted the percentage of Pb(II) that was photocatalytically reduced from a very low value (0.072%) to 47.8% within 1 h of visible light irradiation.

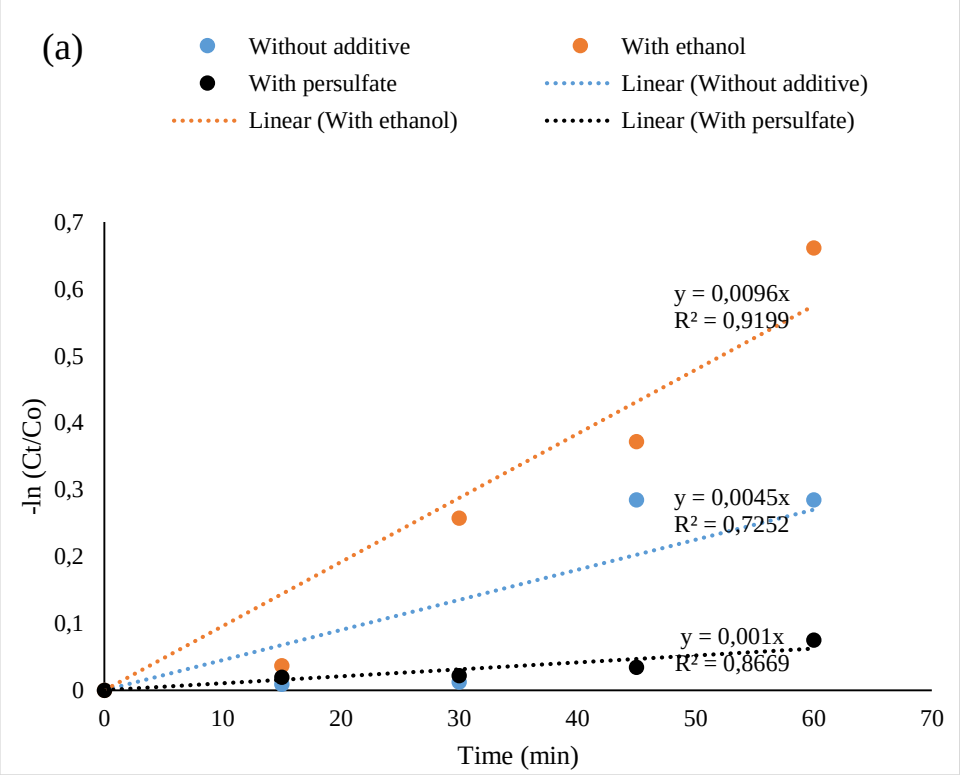

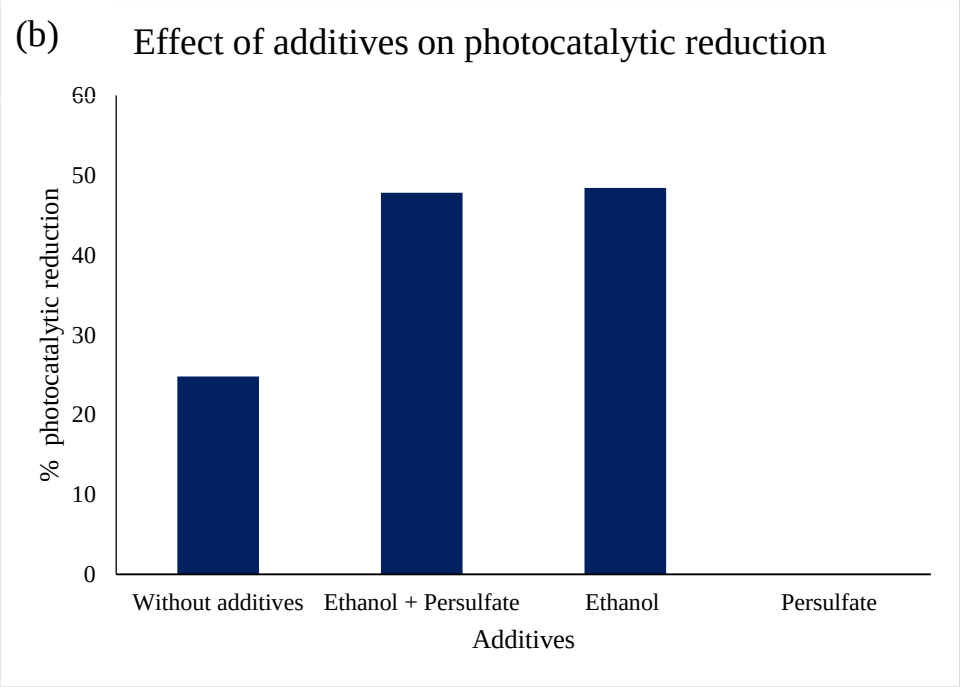

Figure 6.12: (a) Pseudo-first order kinetics (b) the bar chart showing the effect of easily-oxidizable organics and persulphate on the photocatalytic reduction of lead(II)**.**

6.4.9 *Photocatalytic reduction of Pb(II) in the matrix of methyl orange using $AgBiS_2/gC_3N_4$ photocatalyst*

Methyl orange is used in leather, paper, pulp and textile industries. It has both quinoid and azo functional groups (Nguyen et al., 2018). The wavelength of maximum absorption for methyl orange is the characteristic flat peak around 479 nm as shown in the UV plot (Fig.6. 13a). When Pb(II) was photocatalytically reduced in the matrix of methyl orange, it was observed that the rate of photocatalytic reduction reduced from 0.0045 min^{-1} to 0.0036 min^{-1} (half-life of 154 min to 192.5 min) (Fig.6. 13b). This showed that the presence of methyl orange in the lead-contaminated water had significant impact on the rate of photocatalytic reduction of Pb(II) unlike when ethanol, which is an easily-oxidizable organic, was in the photocatalytic system. The observed impacts may also be related to higher molecular weight of methyl orange. The molecular weight of methyl orange is 327.33 $gmol^{-1}$ while ethanol has a molecular weight of just 46.00 $gmol^{-1}$. Another factor could be due to the higher stability of methyl orange, that is associated with the presence of two benzene rings in its structure (Inset of Fig.6. 13a) which are involved in canonical isomeric structures that are more than two (Dominikowska and Palusiak, 2011; Zhang and Guo, 2022). Their resistance to oxidation reduces the rate at which

holes are consumed. Hence, an increase in the rate of recombination of holes and electrons, thereby leading to a decrease in the rate of photocatalysis (Devi et al., 2010).

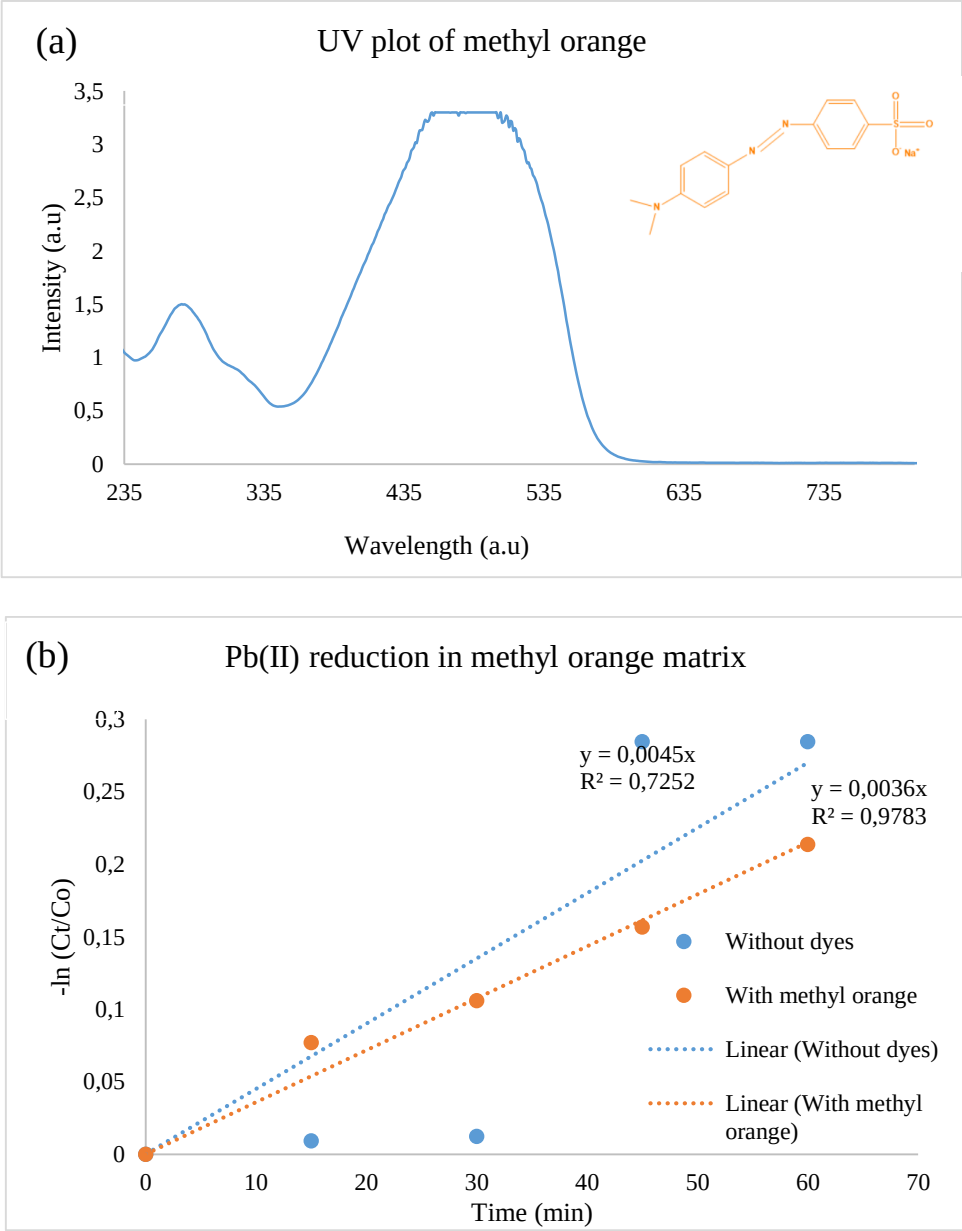

Figure 6.13: (a) The absorption spectrum of methyl orange (b) the pseudo-first order fittings for the reduction of Pb(II) in the matrix of methyl orange. Inset (a) is the structure of methyl orange.

6.4.10 *Photocatalytic reduction of Pb(II) using $AgBiS_2/gC_3N_4$ in the matrix of methylene blue*

Methylene blue is an aromatic cationic dye that is well known for dyeing silk, wool and cotton. It is harmful in the wastewater because it causes diarrhoea, vomiting, nausea and eyes irritation. In addition, it is poisonous to the skin and when inhaled (Isai and Shrivastava, 2019). Pb(II) is often found in the matrix of methylene blue dyes (Li et al., 2018; Zare et al., 2018). The wavelength of maximum absorption of methylene blue is around 667 nm, with another smaller sharp peak at 294 nm (Fig. 6. 14a). Methylene blue absorbs strongly at a longer wavelength because the ground state electrons of methylene blue are excited to a stable state with the emission of light and with minimal losses (Vardevanyan et al., 2013). In the matrix of methylene blue, the rate of photocatalytic reduction of Pb(II) reduced from 0.0045 to 0.0016 min^{-1} (half-life of 154 to 433.2 min respectively) (Fig. 6.14b**).** The pseudo-first order rate constant for the photocatalytic reduction of Pb(II) in methylene blue is lower than its value in the matrix of methyl orange even though the molecular weight of methylene blue (319.85 $gmol^{-1}$) is lower than that of methyl orange (327.33 $gmol^{-1}$). This may be due to the is the presence of tricyclic phenothiazine group in methylene blue dye (inset of Fig. 14a), while methyl orange contains two benzene rings which may cause a difference in their ease of oxidation by holes and hydroxyl radicals.

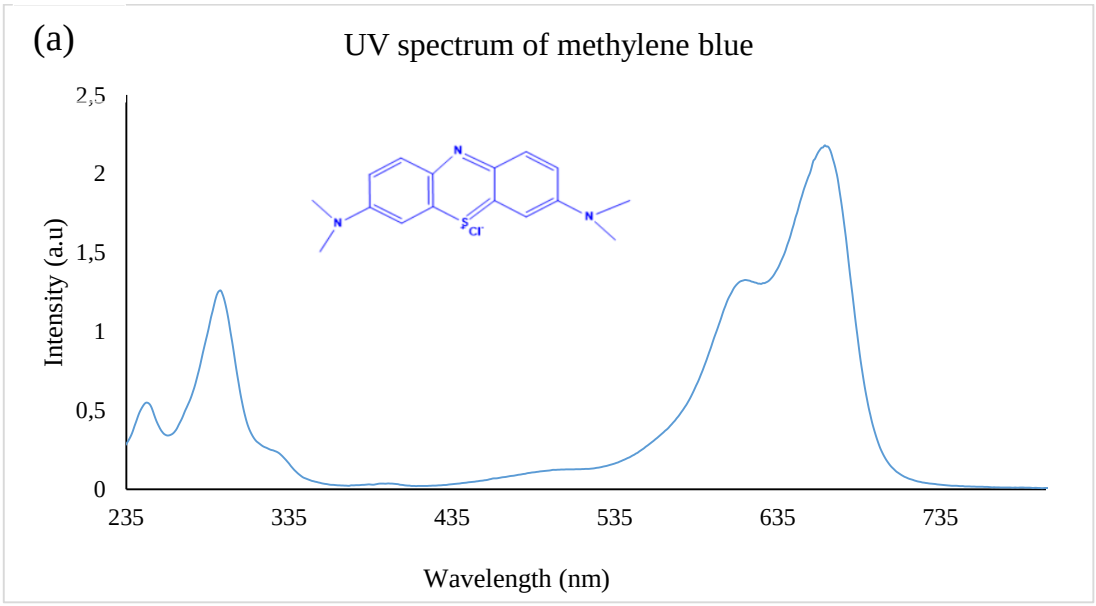

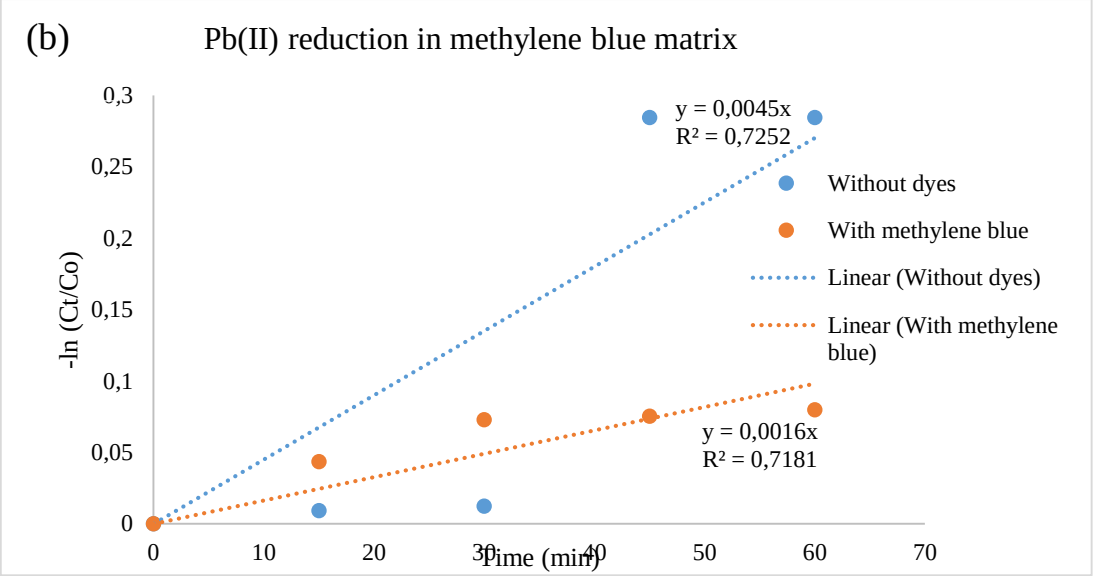

Figure 6.14: (a) The UV spectrum of methylene blue (b) the pseudo-first order fittings for the reduction of Pb(II) in the matrix of methylene blue. Insert of (a) is the structure of methylene blue

6.4.11 *Photocatalytic reduction of Pb(II) using $AgBiS_2/gC_3N_4$ in the matrix of crystal violet*

Hexamethyl-*p*-rosaniline chloride also known as Crystal violet is another common dye that is used in analytical chemistry, cosmetics, foodstuffs, additives, leather, paper and textiles. They often co-exist in wastewater with toxic metals such as Pb(II) (Senthilkumaar and Porkodi, 2005). The wavelength of maximum absorption is around 589 nm as shown in Fig.6. 15a. The wavelength of maximum absorption is at a longer wavelength than that of methyl orange and the methylene blue. The rate of photocatalytic reduction of Pb(II) increased from 0.0045 to 0.0096 min^{-1} (half-life of 154 min to 72.2 min) **(**Fig.6. 15b). This is contrary to the reduction in the rate of photocatalytic reduction of lead observed in the presence of methyl orange and methylene blue dyes. The observed increase in the rate of photocatalytic reduction of Pb(II) in the matrix of crystal violet might be attributed to strength of light absorption of crystal violet, which absorbs light more strongly than methyl orange and methylene blue. From the structure of crystal violet (Inset of Fig.6. 15a), there are ten conjugated pie-system while in the structures of methyl orange and methylene blue there are seven and nine conjugated pie-system respectively. Previous reports have shown that the number of pie-conjugated systems have direct relationships with photon absorption (Ahn et al., 2006; Yamaguchi et al., 2008). Better

light absorption enhances the rate of excitation of the photo-generated electrons, which leads to improved photocatalytic reduction of the Pb(II).

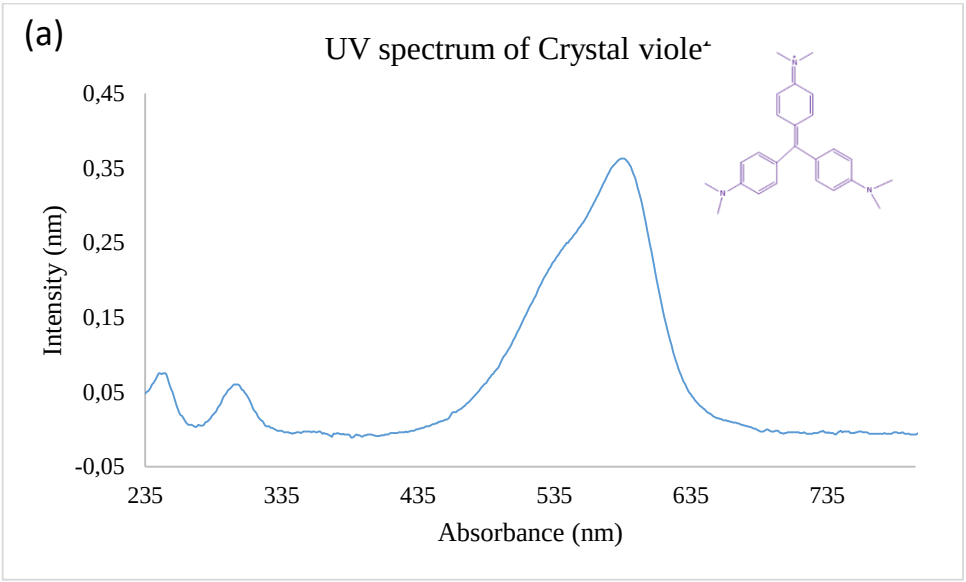

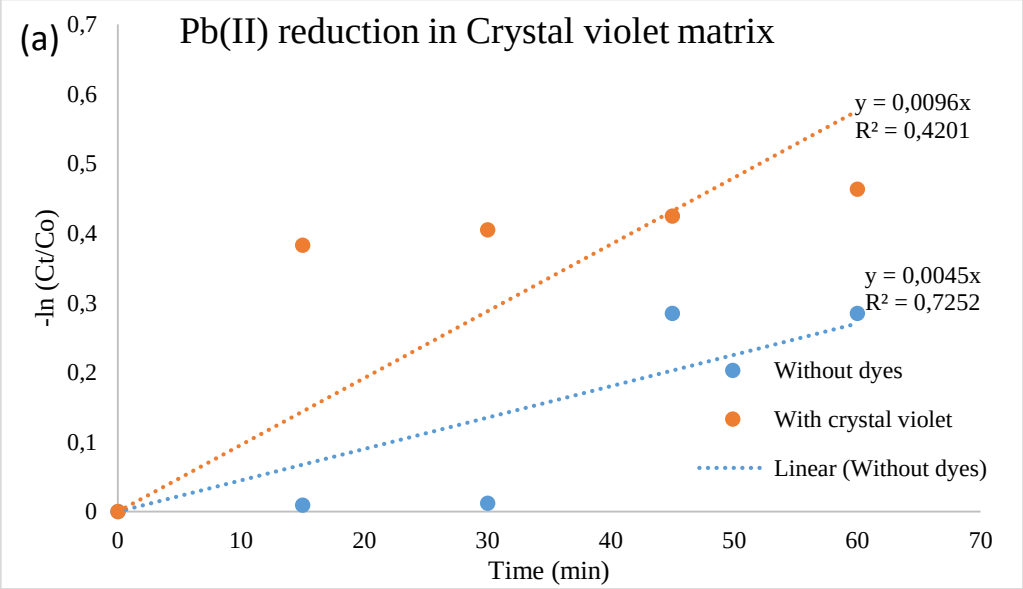

Figure 6.15: (a) The Absorption spectrum of crystal violet (b) the pseudo-first order fittings for the reduction of Pb(II) in the matrix of crystal violet. Inset of (a) is the structure of crystal violet.

6.4.12 Comparative studies of the dyes degradation in the presence of Lead(II)

The degradation of methyl orange, methylene blue and crystal violet in the presence of Pb(II) was also investigated. It was observed that the percentage degradation of methyl orange, crystal violet and methylene blue were 94.85, 71.81 and 39.64% respectively (corresponding to pseudo-first order rate constant of 0.0443, 0.0233 and 0.0104 min^{-1} respectively) (Figures 6.16 a and b). The pattern in the rate of degradation might be related to their structure. Both methylene blue and crystal violet are tricyclic aromatic compounds, while methyl orange is bicyclic aromatic compound. The aromatic rings are resistant to degradation and compounds with high number of aromatic rings are likely to resist degradation than compounds with lower number of aromatic rings (Demanèche et al., 2004; Haritash and Kaushik, 2009). The complete degradation of cyclic aromatic compounds involves ring opening which requires high activation energy (Fuchs, 2008). The degradation rate of crystal violet was higher than the methylene blue despite the higher molecular weight of crystal violet than methylene blue. This might be linked to the high photon absorption of crystal violet as a result of the higher number of pie-conjugated system compared to that of methylene blue.

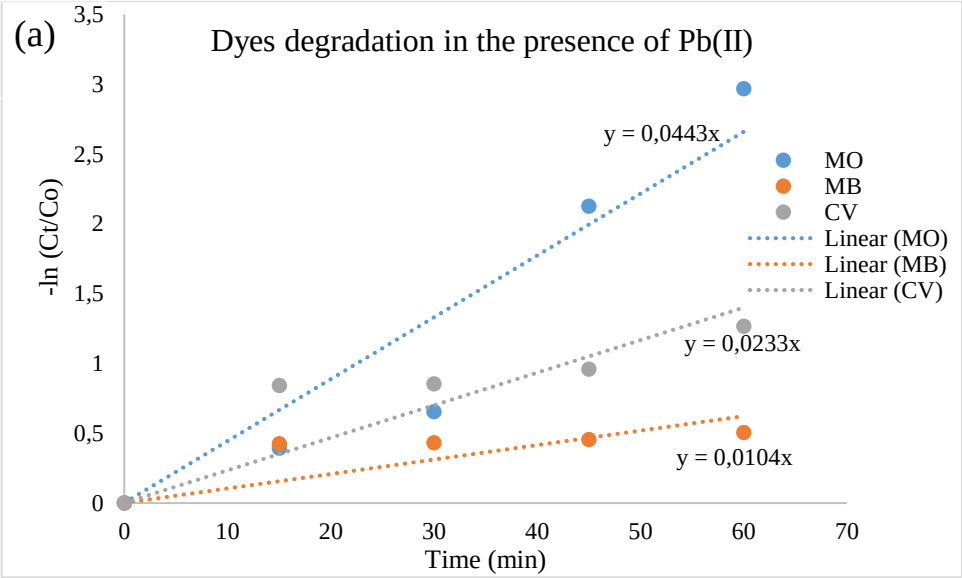

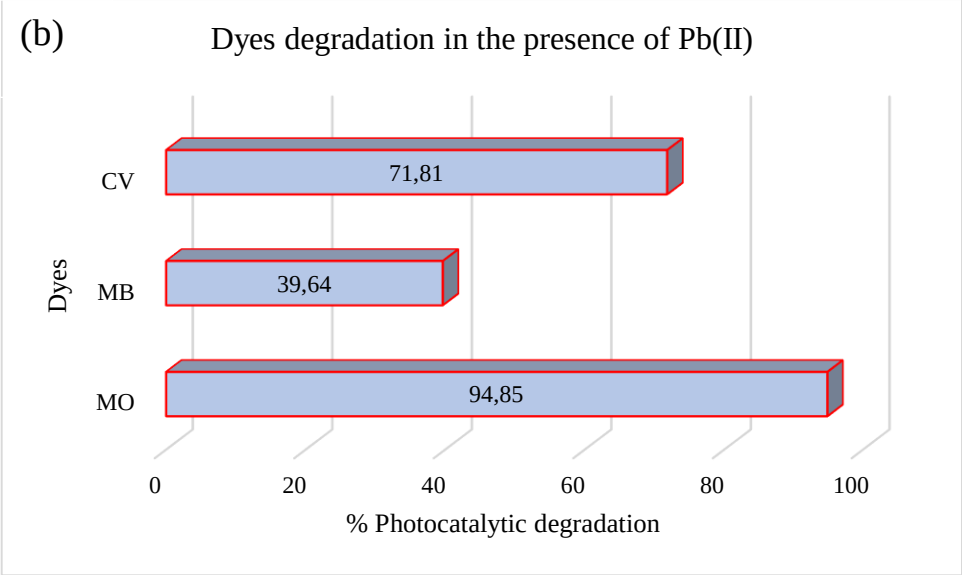

Figure 6.16: (a) pseudo first order kinetics plot, and (b) histogram for the photodegradation of dyes in the system containing Pb(II) ions.

6.4.13 Radical Scavenging experiment

The photocatalytic Pb(II) reduction was studied by carrying out radical trapping experiments. Ascorbic acids (ASC), tert-butanol (TBA), triethanol amine (TEA) were used as scavengers for superoxide radicals, hydroxyl radicals and holes respectively while sodium nitrate was used as the scavenger of electrons. The effects of these scavengers for the reduction of divalent lead were investigated in the presence of $AgBiS_2/gC_3N_4$ photocatalyst under visible light. The results were compared with the photocatalytic reduction obtained without the scavengers as shown in Figure 6.17. Without scavenger, the rate of photocatalytic reduction was 0.0163 min^{-1}. However, the rate of photocatalytic reduction dropped to 0.0057, 0.0047, 0.0016 and 0.000093 min^{-1} in the presence of $NaNO_3$, TEA, TBA and ASC respectively. This result revealed that superoxide radicals, hydroxyl radicals, electrons and holes contributed to the photocatalytic reduction of Pb(II) in the presence of dyes. Since the contribution of superoxide is more than other scavengers, the reduction of divalent lead is effected by superoxide radicals. The results obtained is in tandem with what was reported by Murunni et al.,(2007). It is also possible that there is oxidation of water to oxygen and protons by holes. Based on these results, the proposed mechanism is as shown in Equations (xxii-xxvii).

$AgBiS_2/gC_3N_4 \rightarrow AgBiS_2/gC_3N_4 (e^- + h^+)$ (xxii)

$h^+ + 2H_2O \rightarrow O_2 + 4\,H^+$ (xxiii)

$O_2 + e^- \rightarrow {}^{\bullet}O_2^-$ (xxiv)

${}^{\bullet}O_2^- + Pb(II) \rightarrow Pb(0) + O_2$ (xxv)

$e^- + Pb(II) \rightarrow Pb(0)$ (xxvi)

${}^{\bullet}OH + dyes \rightarrow$ Degradation products (xxvii)

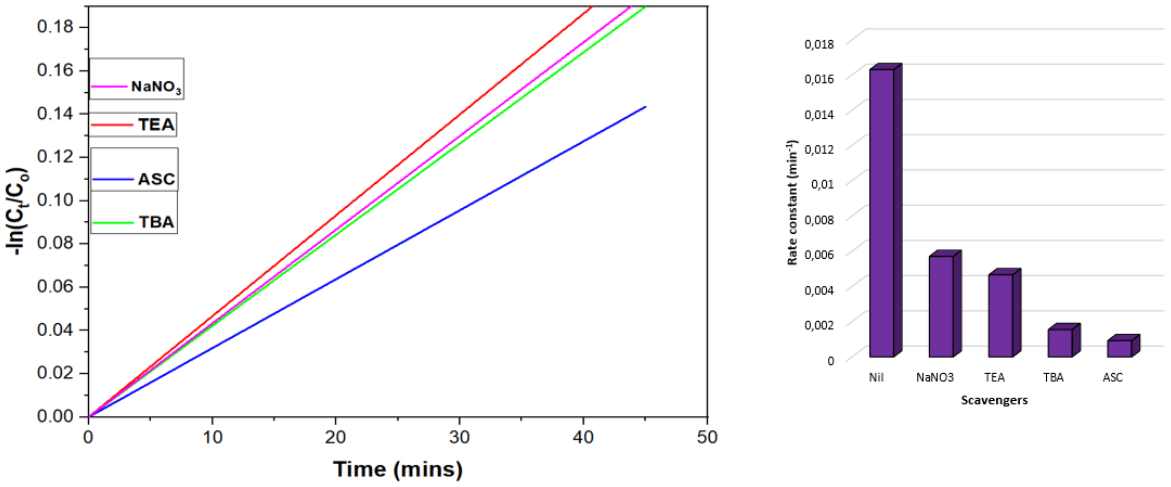

Figure 6.17: The radical scavenging experiment conducted in the presence of TEA, $NaNO_3$, ASC and TBA.

6.4.14 Investigation of divalent lead conversion to metallic lead

To investigate the deposition of lead on the photocatalyst , the solution containing photocatalyst was filtered after the photocatalytic reduction experiments. The residue was left to dry under room conditions and the XRD spectrum of the dried used photocatalyst was obtained. This spectrum was compared with that of the unused photocatalyst. As shown in Figure 6.18, there

were other peaks apart from the peaks emanating from the unused photocatalyst. These extra peaks matched the peaks obtained for metallic lead nanoparticles that was synthesized by Elango et al.,(2015). This shows that the divalent lead was converted into metallic lead and the metallic lead was deposited on the photocatalyst during the photocatalytic investigations.

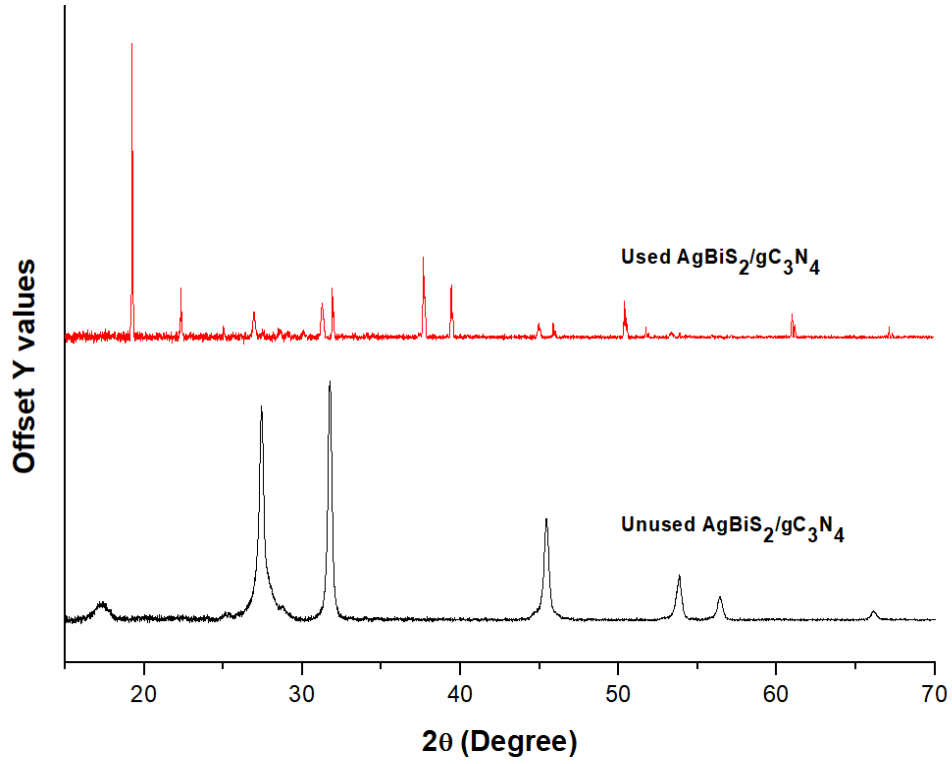

Figure 6.18 : The XRD spectra of $AgBiS_2/gC_3N_4$ photocatalyst before and after photocatalysis.

CONCLUSION

In this study, divalent lead ions were photocatalytically removed from water containing different matrix of dyes- methylene blue, methyl orange and crystal violet, using silver bismuth sulphide incorporated into graphitic carbon nitride and under visible light irradiation. The removal rate of Pb(II) was 0.0045 min^{-1} when studied in the absence of other dye contaminants, but changed to 0.0016, 0.0036 and 0.0096 min^{-1} in the presence of methylene blue, methyl orange and crystal violet. This showed that the existence of methylene blue and methyl orange negatively impacted on the rate of photocatalytic Pb(II) removal, while crystal violet exhibited synergistic effects on the rate of photocatalytic Pb(II) removal. A simultaneous degradation of the dyes occurred with the removal of the Pb(II), and the highest efficiency of dyes degradation

was observed in the matrix containing methyl orange. A study of the effect of the combination of persulfate and ethanol (used as easily oxidizable organics) showed a slight reduction in the percentage of the Pb(II) from 48.4 to 47.8% within 1 h of visible light irradiation. There was 94.85, 71.81 and 39.64% degradation of methyl orange, crystal violet and methylene blue respectively in the matrix containing Pb(II) ions. The results of this study revealed that functionalized graphitic carbon nitride is an effective photocatalyst for the collective removal of Pb(II) ions and dyes in aqueous solution compared to the pristine graphitic carbon nitride.

REFERENCES

Ahn, T.K., Kim, K.S., Kim, D.Y., Noh, S.B., Aratani, N., Ikeda, C., Osuka, A., Kim, D., 2006. Relationship between Two-Photon Absorption and the π-Conjugation Pathway in Porphyrin Arrays through Dihedral Angle Control. Journal of the American Chemical Society 128, 1700-1704.

Ajiboye, T.O., Kuvarega, A.T., Onwudiwe, D.C., 2020. Graphitic carbon nitride-based catalysts and their applications: A review. Nano-Structures & Nano-Objects 24, 100577.

Ajiboye, T.O., Oyewo, O.A., Onwudiwe, D.C., 2021a. Conventional and Current Methods of Toxic Metals Removal from Water Using g-C_3N_4-Based Materials. Journal of Inorganic and Organometallic Polymers and Materials 31, 1419-1442.

Ajiboye, T.O., Oyewo, O.A., Onwudiwe, D.C., 2021b. Simultaneous removal of organics and heavy metals from industrial wastewater: A review. Chemosphere 262, 128379.

Antony, A.M., Kandathil, V., Kempasiddaiah, M., Shwetharani, R., Balakrishna, R.G., El-Bahy, S.M., Hessien, M.M., Mersal, G.A.M., Ibrahim, M.M., Patil, S.A., 2022. Graphitic carbon nitride supported palladium nanocatalyst as an efficient and sustainable catalyst for treating environmental contaminants and hydrogen evolution reaction. Colloids and Surfaces A: Physicochemical and Engineering Aspects 647, 129116.

Ben-Refael, A., Benisti, I., Paz, Y., 2020. Transient photoinduced phenomena in graphitic carbon nitride as measured at nanoseconds resolution by step-scan FTIR. Catalysis Today 340, 97-105.

Chamorro-Posada, P., Dante, R.C., Vázquez-Cabo, J., Dante, D.G., Martín-Ramos, P., Rubiños-López, Ó., Sánchez-Arévalo, F.M., 2022. From urea to melamine cyanurate: Study of a class of thermal condensation routes for the preparation of graphitic carbon nitride. Journal of Solid State Chemistry 310, 123071.

Chen, B., Zhang, C., Wang, W., Chu, Z., Zha, Z., He, X., Zhou, W., Liu, T., Wang, H., Qian, H., 2020. Ultrastable $AgBiS_2$ Hollow Nanospheres with Cancer Cell-Specific Cytotoxicity for Multimodal Tumor Therapy. ACS Nano 14, 14919-14928.

Chen, H.-R., Cai, C., Zhang, Z.-W., Zhang, L., Lu, H.-P., Xu, X., Van Bui, H., Qiu, K.-H., Yin, L.-J., 2019. Enhancing the luminescent efficiency of $Y_3Al_5O_{12}:Ce^{3+}$ by coating graphitic carbon nitride: Toward white light-emitting diodes. Journal of Alloys and Compounds 801, 10-18.

Cheng, J., Wang, W., Xu, X., Lin, Z., Xie, C., Zhang, Y., Zhang, T., Li, L., Lu, Y., Li, Q., 2020. $AgBiS_2$ nanoparticles with synergistic photodynamic and bioimaging properties for enhanced malignant tumor phototherapy. Materials Science and Engineering: C 107, 110324.

Cherifi, Y., Barras, A., Addad, A., Ouddane, B., Roussel, P., Chaouchi, A., Szunerits, S., Boukherroub, R., 2021. Simultaneous photocatalytic Cr(VI) reduction and phenol degradation over copper sulphide-reduced graphene oxide nanocomposite under visible light irradiation: Performance and reaction mechanism. Chemosphere 268, 128798.

Clausen, J.L., Bostick, B., Korte, N., 2011. Migration of Lead in Surface Water, Pore Water, and Groundwater With a Focus on Firing Ranges. Critical Reviews in Environmental Science and Technology 41, 1397-1448.

Dai, K., Chen, H., Peng, T., Ke, D., Yi, H., 2007. Photocatalytic degradation of methyl orange in aqueous suspension of mesoporous titania nanoparticles. Chemosphere 69, 1361-1367.

Demanèche, S., Meyer, C., Micoud, J., Louwagie, M., Willison, J.C., Jouanneau, Y., 2004. Identification and functional analysis of two aromatic-ring-hydroxylating dioxygenases from a

Sphingomonas strain that degrades various polycyclic aromatic hydrocarbons. Applied Environmental Microbiology 70, 6714-6725.

Devi, L.G., Kottam, N., Kumar, S.G., Rajashekhar, K.E., 2010. Preparation, characterization and enhanced photocatalytic activity of Ni^{2+} doped titania under solar light. Open Chemistry 8, 142-148.

Dhanalakshmi, M., Lakshmi Prabavathi, S., Saravanakumar, K., Filip Jones, B., Muthuraj, V., 2020. Iridium nanoparticles anchored WO_3 nanocubes as an efficient photocatalyst for removal of refractory contaminants (crystal violet and methylene blue). Chemical Physics Letters 745, 137285.

Dominikowska, J., Palusiak, M., 2011. Does the concept of Clar's aromatic sextet work for dicationic forms of polycyclic aromatic hydrocarbons?—testing the model against charged systems in singlet and triplet states. Physical Chemistry Chemical Physics 13, 11976-11984.

Elango, G., Roopan, S.M., 2015. Green synthesis, spectroscopic investigation and photocatalytic activity of lead nanoparticles. Spectrochimica Acta Part A: Molecular and Biomolecular Spectroscopy 139, 367-373.

Fahoul, Y., Tanji, K., Zouheir, M., Mrabet, I.E., Naciri, Y., Hsini, A., Nahali, L., Kherbeche, A., 2022. Novel River Sediment@ZnOCo nanocomposite for photocatalytic degradation and COD reduction of crystal violet under visible light. Journal of Molecular Structure 1253, 132298.

Fang, J., Fan, H., Li, M., Long, C., 2015. Nitrogen self-doped graphitic carbon nitride as efficient visible light photocatalyst for hydrogen evolution. Journal of Materials Chemistry A 3, 13819-13826.

Fronczak, M., Tálas, E., Pászti, Z., Szijjártó, G.P., Mihály, J., Tompos, A., Baranowski, P., Tiwari, S.K., Bystrzejewski, M., 2022. Photocatalytic performance of alkali metal doped graphitic carbon nitrides and Pd-alkali metal doped graphitic carbon nitride composites. Diamond and Related Materials 125, 109006.

Fuchs, G., 2008. Anaerobic Metabolism of Aromatic Compounds. 1125, 82-99.

Ganguly, P., Mathew, S., Clarizia, L., Kumar R, S., Akande, A., Hinder, S., Breen, A., Pillai, S.C., 2019. Theoretical and experimental investigation of visible light responsive $AgBiS_2$-TiO_2 heterojunctions for enhanced photocatalytic applications. Applied Catalysis B: Environmental 253, 401-418.

Han, Z., Wang, N., Fan, H., Ai, S., 2017. Ag nanoparticles loaded on porous graphitic carbon nitride with enhanced photocatalytic activity for degradation of phenol. Solid State Sciences 65.

Haritash, A.K., Kaushik, C.P., 2009. Biodegradation aspects of Polycyclic Aromatic Hydrocarbons (PAHs): A review. Journal of Hazardous Materials 169, 1-15.

Huang, P.-C., Yang, W.-C., Lee, M.-W., 2013. $AgBiS_2$ Semiconductor-Sensitized Solar Cells. The Journal of Physical Chemistry C 117, 18308-18314.

Irfan, M., Sevim, M., Koçak, Y., Balci, M., Metin, Ö., Ozensoy, E., 2019. Enhanced photocatalytic NO_x oxidation and storage under visible-light irradiation by anchoring Fe_3O_4 nanoparticles on mesoporous graphitic carbon nitride (mpg-C_3N_4). Applied Catalysis B: Environmental 249, 126-137.

Isai, K.A., Shrivastava, V.S., 2019. Photocatalytic degradation of methylene blue using ZnO and 2%Fe–ZnO semiconductor nanomaterials synthesized by sol–gel method: a comparative study. SN Applied Sciences 1, 1247.

Kmetykó, Á., Szániel, Á., Tsakiroglou, C., Dombi, A., Hernádi, K., 2016. Enhanced photocatalytic H_2 generation on noble metal modified TiO_2 catalysts excited with visible light irradiation. Reaction Kinetics, Mechanisms and Catalysis 117, 379-390.

Koehler, F.M., Rossier, M., Waelle, M., Athanassiou, E.K., Limbach, L.K., Grass, R.N., Günther, D., Stark, W.J., 2009. Magnetic EDTA: coupling heavy metal chelators to metal nanomagnets for rapid removal of cadmium, lead and copper from contaminated water. Chemical Communications, 4862-4864.

Kumar, A., Kashyap, S., Sharma, M., Krishnan, V., 2022. Tuning the surface and optical properties of graphitic carbon nitride by incorporation of alkali metals (Na, K, Cs and Rb): Effect on photocatalytic removal of organic pollutants. Chemosphere 287, 131988.

Leroyer, A., Gomajee, H., Leroy, R., Mazzuca, M., Leleu, B., Nisse, C., 2022. Cancer mortality and chemical exposure in a retrospective zinc and lead smelter cohort: A 48-year follow-up. International Journal of Hygiene and Environmental Health 242, 113955.

Li, R., Liang, W., Wang, J.J., Gaston, L.A., Huang, D., Huang, H., Lei, S., Awasthi, M.K., Zhou, B., Xiao, R., Zhang, Z., 2018. Facilitative capture of As(V), Pb(II) and methylene blue from aqueous solutions with MgO hybrid sponge-like carbonaceous composite derived from sugarcane leafy trash. Journal of Environmental Management 212, 77-87.

Li, X., Zhu, J., Li, H., 2012. Comparative study on the mechanism in photocatalytic degradation of different-type organic dyes on SnS_2 and CdS. Applied Catalysis B: Environmental 123-124, 174-181.

Li, Y., He, J., Zhang, K., Liu, T., Hu, Y., Chen, X., Wang, C., Huang, X., Kong, L., Liu, J., 2019. Super rapid removal of copper, cadmium and lead ions from water by NTA-silica gel. RSC Advances 9, 397-407.

Lin, H., Wu, J., Zhou, F., Zhao, X., Lu, P., Sun, G., Song, Y., Li, Y., Liu, X., Dai, H., 2023. Graphitic carbon nitride-based photocatalysts in the applications of environmental catalysis. Journal of Environmental Sciences 124, 570-590.

Lin, Z., Zheng, Y., Deng, F., Luo, X., Zou, J., Shao, P., Zhang, S., Tang, H., 2021. Target-directed design of dual-functional Z-scheme $AgIn_5S_8/SnS_2$ heterojunction for Pb(II) capture and photocatalytic reduction of Cr(VI): Performance and mechanism insight. Separation and Purification Technology 277, 119430.

Liu, H., Zhong, J., Liang, X., Zhang, J., Xiang, W., 2011. A mild biomolecule-assisted route for preparation of flower-like $AgBiS_2$ crystals. Journal of Alloys and Compounds 509, L267-L272.

Liu, J., Wang, H., Antonietti, M., 2016a. Graphitic carbon nitride “reloaded”: emerging applications beyond (photo)catalysis. Chemical Society Reviews 45, 2308-2326.

Liu, X., Hao, J.-W., Gaan, S., 2016b. Recent studies of decomposition and strategies of smoke and toxicity suppression for polyurethane based materials. RSC Adv. 6.

Lu, J., Jin, H., Dai, Y., Yang, K., Huang, B., 2011. Effect of electronegativity and charge balance on the visible-light-responsive photocatalytic activity of nonmetal doped anatase TiO_2. International Journal of Photoenergy 2012.

Majidnia, Z., Idris, A., 2016. Synergistic Effect of Maghemite and Titania Nanoparticles in PVA-Alginate Encapsulated Beads for Photocatalytic Reduction of Pb(II). Chemical Engineering Communications 203, 425-434.

Mak, C.H., Qian, J., Rogée, L., Lai, W.K., Lau, S.P., 2018. Facile synthesis of $AgBiS_2$ nanocrystals for high responsivity infrared detectors. RSC Advances 8, 39203-39207.

Manimozhi, T., Archana, J., Navaneethan, M., Ramamurthi, K., 2019. Shape-controlled synthesis of $AgBiS_2$ nano-/microstructures using PEG-assisted facile solvothermal method and their functional properties. Applied Surface Science 487, 664-673.

Ming, S., Liu, X., Zhang, W., Xie, Q., Wu, Y., Chen, L., Wang, H.-Q., 2020. Eco-friendly and stable silver bismuth disulphide quantum dot solar cells via methyl acetate purification and modified ligand exchange. Journal of Cleaner Production 246, 118966.

Morito, S., Nishikawa, J., Maki, T., 2003. Dislocation density within lath martensite in Fe-C and Fe-Ni alloys. ISIJ international 43, 1475-1477.

Mousavi, M., Habibi-Yangjeh, A., Abitorabi, M., 2016. Fabrication of novel magnetically separable nanocomposites using graphitic carbon nitride, silver phosphate and silver chloride and their applications in photocatalytic removal of different pollutants using visible-light irradiation. Journal of Colloid and Interface Science 480, 218-231.

Muggli, D.S., McCue, J.T., Falconer, J.L., 1998. Mechanism of the Photocatalytic Oxidation of Ethanol on TiO_2. Journal of Catalysis 173, 470-483.

Murruni, L., Leyva, G., Litter, M.I., 2007. Photocatalytic removal of Pb(II) over TiO_2 and Pt–TiO_2 powders. Catalysis Today 129, 127-135.

Nabi, G., Malik, N., Raza, W., 2020. Degradation effect of temperature variation and dye loading g-C3N4 towards organic dyes. Inorganic Chemistry Communications 119, 108050.

Nakamura, M., Nakamura, H., Ohsawa, T., Imura, M., Shimamura, K., Ohashi, N., 2015. $AgBiS_2$ single crystal grown using slow cooling method and its characterization. Journal of Crystal Growth 411, 1-3.

Nakazawa, T., Kim, D., Oshima, Y., Sato, H., Park, J., Kim, H., 2021. Synthesis and Application of $AgBiS_2$ and Ag_2S Nanoinks for the Production of IR Photodetectors. ACS Omega 6, 20710-20718.

Nguyen, V.N., Tran, D.T., Nguyen, M.T., Le, T.T.T., Ha, M.N., Nguyen, M.V., Pham, T.D., 2018. Enhanced photocatalytic degradation of methyl orange using ZnO/graphene oxide nanocomposites. Research on Chemical Intermediates 44, 3081-3095.

Niu, G., Tang, Q., Zurob, H.S., Wu, H., Xu, L., Gong, N., 2019. Strong and ductile steel via high dislocation density and heterogeneous nano/ultrafine grains. Materials Science and Engineering: A 759, 1-10.

Pai, N., Lu, J., Senevirathna, D.C., Chesman, A.S.R., Gengenbach, T., Chatti, M., Bach, U., Andrews, P.C., Spiccia, L., Cheng, Y.-B., Simonov, A.N., 2018. Spray deposition of $AgBiS_2$ and Cu_3BiS_3 thin films for photovoltaic applications. Journal of Materials Chemistry C 6, 2483-2494.

Praus, P., 2021. On electronegativity of graphitic carbon nitride. Carbon 172, 729-732.

R, S., Jebasingh, J.A., S, M.V., Stanley, P.K., Ponmani, P., Shekinah, M.E., Vasanthi, J., 2021. Excellent Photocatalytic degradation of Methylene Blue, Rhodamine B and Methyl Orange dyes by Ag-ZnO nanocomposite under natural sunlight irradiation. Optik 231, 166518.

Rahmati, M., Ghafuri, H., Ghanbari, N., Tajik, Z., 2020. 1,4 Butanesultone Functionalized Graphitic Carbon Nitride: Efficient Catalysts for the One-Pot Synthesis of 1,4-Dihydropyridine and Polyhydroquinoline Derivative through Hantzsch Reaction. Polycyclic Aromatic Compounds, 1-17.

Sarkar, R., Kar, M., Habib, M., Zhou, G., Frauenheim, T., Sarkar, P., Pal, S., Prezhdo, O.V., 2021. Common Defects Accelerate Charge Separation and Reduce Recombination in CNT/Molecule Composites: Atomistic Quantum Dynamics. Journal of the American Chemical Society 143, 6649-6656.

Senthilkumaar, S., Porkodi, K., 2005. Heterogeneous photocatalytic decomposition of Crystal Violet in UV-illuminated sol–gel derived nanocrystalline TiO_2 suspensions. Journal of Colloid and Interface Science 288, 184-189.

Shcherban, N.D., Shvalagin, V.V., Korzhak, G.V., Yaremov, P.S., Skoryk, M.A., Sergiienko, S.A., Ya. Kuchmiy, S., 2022. Hard template synthesis and photocatalytic activity of graphitic carbon nitride in the hydrogen evolution reaction using organic acids as electron donors. Journal of Molecular Structure 1250, 131741.

Shi, X.-X., Li, X.-Q., Wei, X.-P., Li, J.-P., 2020. Molecularly Imprinted Photoelectrochemical Sensor Based on $AgBiS_2/Bi_2S_3$ for Determination of Propoxur. Chinese Journal of Analytical Chemistry 48, 396-404.

Sugarthi, S., Bakiyaraj, G., Abinaya, R., Navaneethan, M., Archana, J., Shimomura, M., 2020. Effect of different growth temperature on the formation of ternary metal chalcogenides $AgBiS_2$. Materials Science in Semiconductor Processing 107, 104781.

Sun, B.-w., Yu, H.-y., Yang, Y.-j., Li, H.-j., Zhai, C.-y., Qian, D.-J., Chen, M., 2017. New complete assignment of X-ray powder diffraction patterns in graphitic carbon nitride using

discrete Fourier transform and direct experimental evidence. Physical Chemistry Chemical Physics 19, 26072-26084.

taghi Bagherian Jamnani, M., Hajinasiri, R., Ghafuri, H., Hossaini, Z., 2022. Synthesis and characterization of graphitic carbon nitride supported Tris(hydroxymethyl)aminomethanes) g-C3N4/THAM) as a novel catalyst for the synthesis of poly hydroquinoline and pyranopyrazole derivatives. Polyhedron 221, 115878.

Thongtem, T., Tipcompor, N., Thongtem, S., 2010. Characterization of $AgBiS_2$ nanostructured flowers produced by solvothermal reaction. Materials Letters 64, 755-758.

Tsitonaki, A., Petri, B., Crimi, M., MosbÆK, H., Siegrist, R.L., Bjerg, P.L., 2010. In Situ Chemical Oxidation of Contaminated Soil and Groundwater Using Persulfate: A Review. Critical Reviews in Environmental Science and Technology 40, 55-91.

Vardevanyan, P.O., Antonyan, A.P., Parsadanyan, M.A., Shahinyan, M.A., Hambardzumyan, L.A., 2013. Mechanisms for Binding between Methylene Blue and DNA. Journal of Applied Spectroscopy 80, 595-599.

Wang, C.-Y., Maeda, K., Chang, L.-L., Tung, K.-L., Hu, C., 2022. Synthesis and applications of carbon nitride (CN_x) family with different carbon to nitrogen ratio. Carbon 188, 482-491.

Wang, G., Fan, W., Li, Q., Deng, N., 2019. Enhanced photocatalytic New Coccine degradation and Pb(II) reduction over graphene oxide-TiO_2 composite in the presence of aspartic acid-β-cyclodextrin. Chemosphere 216, 707-714.

Wang, J., Yang, X., Hu, W., Li, B., Yan, J., Hu, J., 2007. Synthesis of $AgBiS_2$ microspheres by a templating method and their catalytic polymerization of alkylsilanes. Chemical Communications, 4931-4933.

Wang, W., Shen, H., He, X., Li, J., 2014. Effects of sulfur sources on properties of Cu_2ZnSnS_4 nanoparticles. Journal of Nanoparticle Research 16, 2437.

Wang, Y., Peng, L., Wang, Z., Konstantatos, G., Environmentally Friendly $AgBiS_2$ Nanocrystal Inks for Efficient Solar Cells Employing Green Solvent Processing. Advanced Energy Materials n/a, 2200700.

Xing, W., Liu, C., Zhong, H., Zhang, Y., Zhang, T., Cheng, C., Han, J., Wu, G., Chen, G., 2022. Phosphate group-mediated carriers transfer and energy band over carbon nitride for efficient photocatalytic H_2 production and removal of rhodamine B. Journal of Alloys and Compounds 895, 162772.

Xu, M., Han, L., Dong, S., 2013. Facile Fabrication of Highly Efficient g-C_3N_4/Ag_2O Heterostructured Photocatalysts with Enhanced Visible-Light Photocatalytic Activity. ACS Applied Materials & Interfaces 5, 12533-12540.

Yamaguchi, Y., Matsubara, Y., Ochi, T., Wakamiya, T., Yoshida, Z.-i., 2008. How the π Conjugation Length Affects the Fluorescence Emission Efficiency. Journal of the American Chemical Society 130, 13867-13869.

Yang, L., Bai, X., Shi, J., Du, X., Xu, L., Jin, P., 2019a. Quasi-full-visible-light absorption by D35-TiO_2/g-C_3N_4 for synergistic persulfate activation towards efficient photodegradation of micropollutants. Applied Catalysis B: Environmental 256, 117759.

Yang, M.-T., Zhang, Z.-Y., Lin, K.-Y.A., 2019b. One-step fabrication of cobalt-embedded carbon nitride as a magnetic and efficient heterogeneous catalyst for activating oxone to degrade pollutants in water. Separation and Purification Technology 210, 1-9.

Yang, Q., Hao, J., 2022. Synthesis of metal sulfides via ionic liquid-mediated assembly strategy and their photocatalytic degradation of dyes in water. Colloids and Surfaces A: Physicochemical and Engineering Aspects 633, 127848.

Zare, E.N., Lakouraj, M.M., Kasirian, N., 2018. Development of effective nano-biosorbent based on poly m-phenylenediamine grafted dextrin for removal of Pb (II) and methylene blue from water. Carbohydrate Polymers 201, 539-548.

Zhang, S., Song, S., Gu, P., Ma, R., Wei, D., Zhao, G., Wen, T., Jehan, R., Hu, B., Wang, X., 2019. Visible-light-driven activation of persulfate over cyano and hydroxyl group co-modified mesoporous g-C_3N_4 for boosting bisphenol A degradation. Journal of Materials Chemistry A 7, 5552-5560

Zhang, X., Guo, J., 2022. Adsorption, stability and evolution path of benzene on graphene surface: Size and edge effects. Applied Surface Science 571, 151376.

Zhao, G.-Q., Zou, J., Hu, J., Long, X., Jiao, F.-P., 2021. A critical review on graphitic carbon nitride (g-C_3N_4)-based composites for environmental remediation. Separation and Purification Technology 279, 119769.

Zhao, J., Liu, P., Ma, J., Li, D., Yang, H., Chen, W., Jiang, Y., 2019. Enhancement of radiosensitization by silver nanoparticles functionalized with polyethylene glycol and aptamer As1411 for glioma irradiation therapy. International Journal of Nanomedicine 14, 9483.

Zheng, C.-W., Niu, H.-Y., Liang, C., Niu, C.-G., Zhao, X.-F., Zhang, L., Li, J.-S., Guo, H., Liu, H.-Y., Liang, S., 2021. A study on advanced oxidation mechanism of $MnCo_2O_4$/g-C_3N_4 degradation of nitrobenzene: Sacrificial oxidation and radical oxidation. Chemical Engineering Journal 403, 126400.

Zhong, J., Xiang, W., Xie, C., Liang, X., Xu, X., 2013. Synthesis of spheroidal $AgBiS_2$ microcrystals by l-cysteine assisted method. Materials Chemistry and Physics 138, 773-779.

Zhu, Y., Fan, W., Zhou, T., Li, X., 2019. Removal of chelated heavy metals from aqueous solution: A review of current methods and mechanisms. Science of The Total Environment 678, 253-266.

Zou, Q., Zhang, Z., Li, H., Pei, W., Ding, M., Xie, Z., Huo, Y., Li, H., 2020. Synergistic removal of organic pollutant and metal ions in photocatalysis-membrane distillation system. Applied Catalysis B: Environmental 264, 118463.

CHAPTER SEVEN

Silver functionalized g-C_3N_4: photocatalytic potency for chromium(VI) reduction

7.0 Introduction

Graphitic carbon nitride (g-C_3N_4) is a semiconductor material with a bandgap energy of 2.7 eV (Ajiboye et al., 2020; Ismael, 2020). It has recently been widely utilized as a photocatalyst in water splitting, CO_2 reduction, oxygen reduction, and degradation of organic pollutants due to its low cost, non-toxicity, photo-activity, and stability (Ajiboye et al., 2020; Ajiboye et al., 2021). Despite the desirable properties, a few limitations are associated with g-C_3N_4, such as fast carrier charge recombination, low conductivity, and small surface area. One of the strategies that have been employed to overcome these limitations is the formation of functionalized nanocomposites of g-C_3N_4. Several semiconductors have been used to functionalize g-C_3N_4 (Ismael, 2020; Kadi et al., 2020). The choice of nanomaterial used to form nanocomposite with g-C_3N_4 is determined by the desired application, such as removing toxic materials from water.

The carcinogenicity, toxicity, and high mobility of heavy metals make them pollutants of great concern, especially when they find their way into surface or underground water (Aggarwal et al., 2022). Chromium is prominent in the environment among these heavy metal pollutants because of its numerous applications. It is used in paint production, leather tanning, and electroplating (Barnhart, 1997; Emadian et al., 2020). In all these various applications, toxic hexavalent chromium is used as the main ingredient. However, the trivalent form of chromium is beneficial to the plants as micronutrients (Emadian et al., 2020). The World Health Organization (WHO) gave the permissible concentration of 0.05 mg/L for Cr(VI) in drinking water (Wang et al., 2020). Hence, to ensure that humans and the environment are protected, reducing the toxic hexavalent chromium in wastewater to environmentally friendly trivalent chromium before its discharge is beneficial. Numerous photocatalysts have been investigated for the photocatalytic reduction of hexavalent chromium, such as zero-valent iron (Samadi et al., 2021), and silver nanoparticles (Lakra et al., 2021), titanium oxide, and its nanocomposite (Zafar et al., 2021).

Silver nanoparticles are common among noble metals due to their numerous applications. They are used in environmental pollution control, water purification, textile industries, food

industries, and therapeutic/biomedical industries (Abass Sofi et al., 2022). In material synthesis, it has been used to functionalize materials such as graphene oxide, polyhexamethylene biguanide, 4-mercaptopyridine, glucosamine, fatty acids, cyclodextrins, and synthetic polymers (Li et al., 2012b; Patel et al., 2015; Zhai et al., 2017; Anwar et al., 2019; Zhao et al., 2019; Abass Sofi et al., 2022). The present studies involve the functionalization of gC_3N_4 with silver nanoparticles. The photocatalytic performance of this nanocomposite was investigated for the reduction of hexavalent chromium to trivalent chromium.

7.1 Chemicals and instruments

Melamines, silver nitrate, sodium chromate and 2,2- diphenyl-1picrythydrazyl hydrate, and ethanol were supplied by Sigma-Aldrich in analytical standard. d8 Advanced X-ray diffractometer with Cu Kα radiation (λ = 0.154 nm) was used for the measurement of XRD patterns. TECNAI G2 (ACI) equipment (Hillsboro, OR, USA), with an accelerating voltage of 200 kV was used for Transmission electron microscopy (TEM) analysis and FEI Quanta FEG 250 was used for Scanning electron microscopy (SEM) analysis. Perkin Elmer LS 45 fluorimeter and PerkinElmer λ20 UV–vis spectrophotometer was used to obtain the emission and absorption spectra respectively.

7.2 Synthesis of gC_3N_4

The graphitic carbon nitride powder was synthesized using a previously reported method. In brief, approximately 10.0 g of melamine powder (white color) was placed in a covered crucible. It was put inside the muffle furnace, which was maintained at a heating rate of 10 °C/min and 550 ºC for 4 h. The yellow lump produced at the end of the reaction was cooled and ground into powder (Ajiboye et al., 2020; Das et al., 2020).

7.3 Synthesis of Ag/gC_3N_4

Silver nitrate was mixed and ground with the graphitic carbon nitride in the ratio of 1:2 ($AgNO_3$: gC_3N_4) using a mortar and pestle. The product was calcinated at 350 °C for 2 h at a heating rate of 10 °C/min. The obtained product was cooled, dispersed in distilled water and stirred continuously for 6 h. This was followed by centrifugation at 4000 rpm for 5 min to purify the product, which was dried at 80 °C for 8 h.

7.4 Photocatalytic reduction of Cr(VI) using gC_3N_4 and Ag/gC_3N_4 nanocomposite

The photocatalytic activities of gC_3N_4 and Ag/gC_3N_4 were carried out using hexavalent chromium as the model pollutant under visible light. The photoreactor fitted with a 28 W LED light was used for the investigation. In a typical experiment, 50 mL of 100 mg/L Cr(VI) solution was measured into a 100 mL beaker. To this solution, 50 mg of gC_3N_4 photocatalyst was introduced at pH of 2, 4, 7 and 12. The solution was stirred for 30 min in the dark to attain adsorption-desorption equilibrium. After this, the solution was irradiated with visible light while stirring was maintained for 120 min. During the illumination, 5 mL aliquots of the heavy metal solution were taken at 20 min intervals. The concentration of each aliquot was measured at λ_{max} = 350 nm with a UV–vis spectrophotometer. The percentage of hexavalent chromium that has been photocatalytically reduced was obtained by using **Equation (i).**

$$\% \, removal = \frac{C_o - C}{C_o} x \, 100 \qquad \text{(i)}$$

Where C_o and C are the concentration of hexavalent chromium before and after the photocatalytic process respectively. The rate of photocatalytic reduction was obtained by fixing the data obtained from the photocatalytic process into the linear plot of pseudo-first order kinetics following **Equation (ii)**.

$$-\ln(\frac{C}{C_o}) = K_1 t \qquad \text{(ii)}$$

Where Co and C are the concentration of hexavalent chromium before and after the photocatalytic process respectively; K_1 is the pseudo-first order rate constant and t is the time

7.5 RESULTS AND DISCUSSION

7.5.1 *X-ray diffraction (XRD) studies of Ag/gC_3N_4 nanocomposite*

The formation of graphitic carbon nitride was confirmed by the appearance of a prominent peak at 2θ = 27.4°, which was indexed to the (002) plane. This peak appears due to the presence of conjugated aromatic rings with interlayer stacking (Gogoi et al., 2021). The peaks at 77.5°, 64.4°, 44.3°, and 38.1° are indexed to (311), (220), (200) and (111) crystal planes respectively

(JCP2 04-0783) (Fig. 7. 1) (Gogoi et al., 2021). A reduction in the intensity of the peak at 2θ = 27.4° occurred upon the formation of the nanocomposite, compared to the intensity of the pristine graphitic carbon nitride, indicating that a rearrangement occurred by the incorporation of silver into graphitic carbon nitride(Thorat et al., 2021). There was a shift in the position of the (002) peak by about 0.2 ºC after the incorporation of the silver which showed a change in the interlayer distance compared to the pristine graphitic carbon nitride and the growth of the gC_3N_4 crystal structure was restricted (Ge et al., 2011; Thorat et al., 2021). The absence of any un-indexed peak showed that the Ag/gC_3N_4 synthesized was pure. The diameter of the Ag/gC_3N_4 estimated from the Scherrer equation was 37.19 nm, while the size of pristine gC_3N_4 was 65.58 nm. This confirmed a reduction in the size of the silver functionalized gC_3N_4 reduced compared with the size of the pristine gC_3N_4.

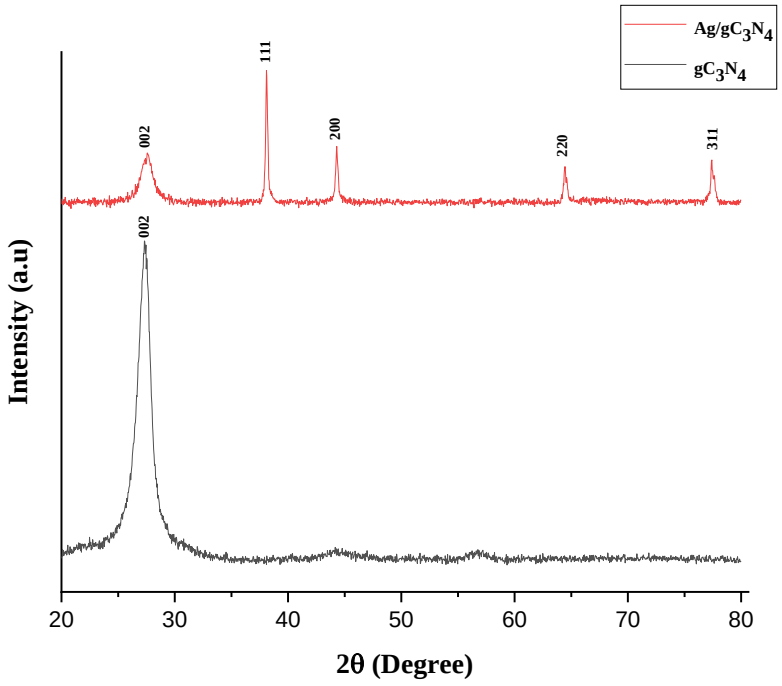

Figure 7.1: XRD patterns of graphitic carbon nitride and silver/graphitic carbon nitride nanoparticles.

7.5.2 *FTIR studies of Ag/gC_3N_4 nanocomposite*

In the FTIR spectrum (Fig.7. 2), sharp peaks that appeared at 1617 and 794 cm^{-1}, which are the characteristic peak of the C=N bond and the vibrational peak of the triazine unit respectively (Thang et al., 2021). The peaks in the range1317-1400 cm^{-1} were due to the aromatic rings in the structure of gC_3N_4.The peaks around 3071 cm^{-1} are attributed to the vibration of the N-H from the free amino group of the gC_3N_4 and O-H group of the adsorbed water molecules on the

surface of the nanocomposite (Elavarasan et al., 2021). The sharp peak at 794 cm^{-1} could be ascribed to the vibrational frequency of the bond between silver and non-metals (Gharibshahi et al., 2017).

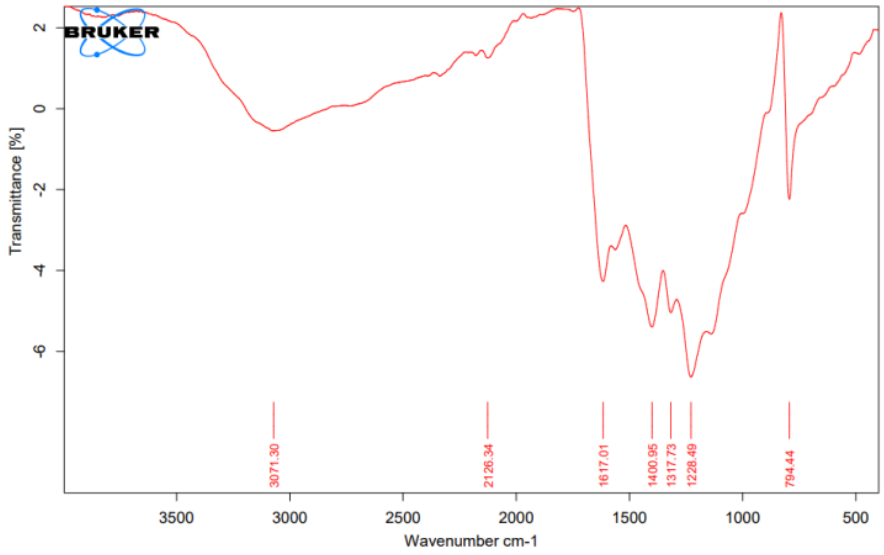

Figure 7.2: FTIR spectrum of Ag/gC_3N_4

7.5.3 *Optical study*

The wavelength of maximum absorption for the gC_3N_4 appears at 337 nm and this is because of unsaturated n-π∗ transitions with the atoms of nitrogen, and the second maximum at 396 nm was a result of poly conjugated heteroaromatic π− π∗ transition (Mohanraj et al., 2021). The wavelength of maximum absorption for the silver functionalized gC_3N_4 was found at 245 nm, as shown in Fig.7.3 (a and b), indicating a blue shift in the absorption maxima upon the incorporation of silver nanoparticles into gC_3N_4. Evaluation of the indirect bandgap energy was achieved by plotting $(ahv)^{1/2}$ against the energy of the photon (*hv)* as shown in Figures 7.3 (a and c), given the band gap energy of gC_3N_4 and Ag/gC_3N_4 as 2.60 eV and 3.60 eV respectively.

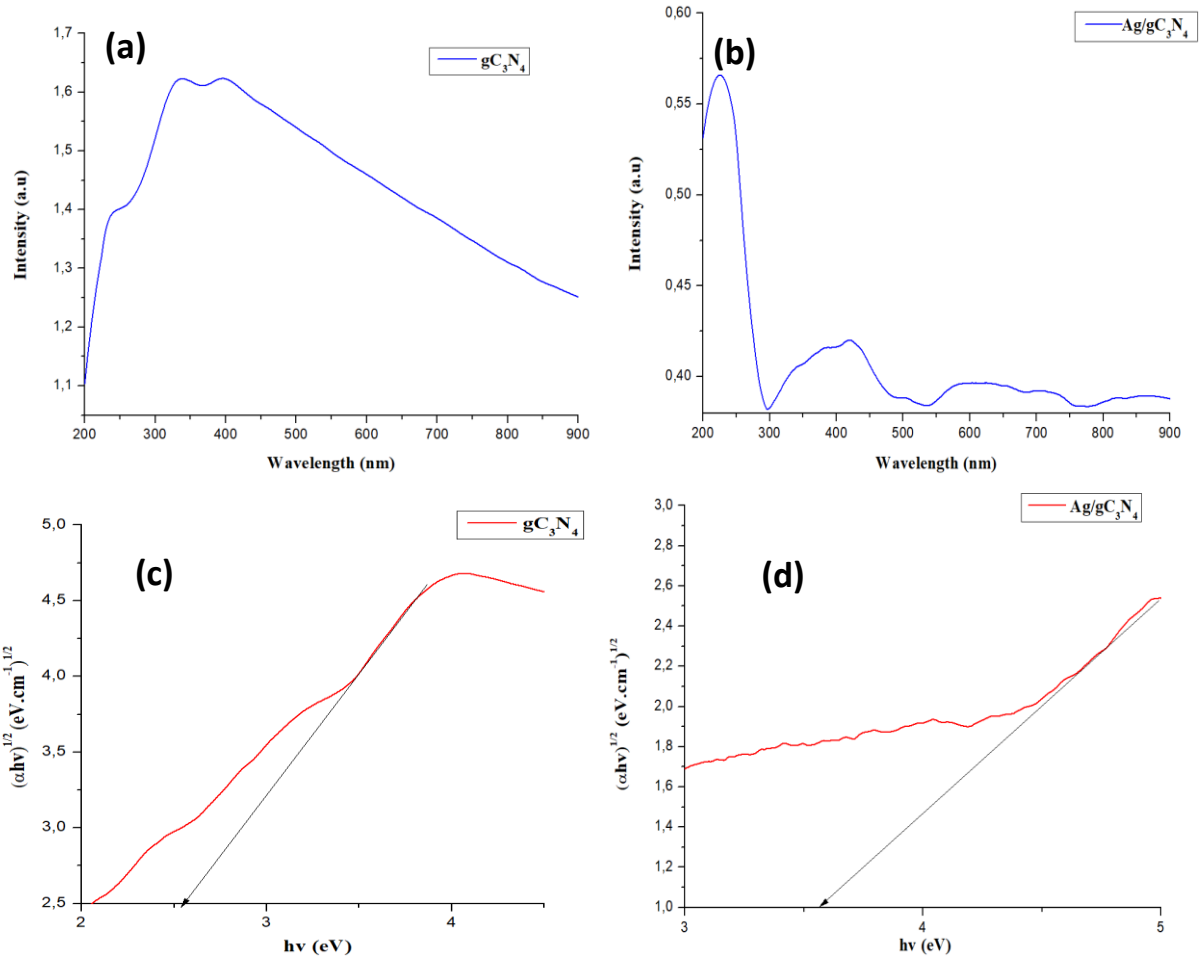

Figure 7.3: UV spectra of gC_3N_4 and Ag/gC_3N_4 (a and b respectively) and their Tauc plot (c and d respectively).

The bandgap energy of the silver-functionalized and the pristine graphitic carbon nitride are 3.60 and 2.60 eV respectively. The band positions were estimated from **Equations (iv)** and **(v)** (Dai et al., 2014) using these bandgap energies, and were obtained as -1.35 and +1.25 eV for the conduction band (E_{CB}) and valence band (E_{VB}) energies respectively. These band positions respectively changed to -1.64 eV and +1.96 eV in the composite of Ag and gC_3N_4. This implies that the incorporation of silver into the g-C_3N_4 increased the valence band but reduced the conduction band.

$$E_{CB} = X - 0.5Eg - 4.5 \quad \textbf{(iv)}$$

$$E_{VB} = X + 0.5Eg - 4.5 \quad \textbf{(v)}$$

Where X = absolute electronegativity which is usually derived from the geometric mean of the absolute electronegativities of all the elements in the semiconductor while Eg is the bandgap energies.

7.5.4 *Morphological study*

Figure 7.4a presents the SEM micrograph of the Ag/gC_3N_4 nanocomposite, which showed an aggregated surface structure, while the TEM image revealed the morphology of the Ag/gC_3N_4 is spherical (Fig. 7.4b). The particle size distribution histogram shows an average diameter of 34 nm (Fig.7. 4c) and the area distribution revealed an average area of approximately 700 nm^2 (Fig.74d). The size obtained with Ag-functionalized gC_3N_4 was in the range of the value obtained from the XRD image. Silver loaded on different carbon-based materials has been reported to have a smaller diameter between 0 -100 nm (Wang et al., 2017; Mangalam et al., 2019; Thorat et al., 2021). For instance, the diameter of silver nanoparticles loaded on nanofibers was determined to be 6.1 nm (Thorat et al., 2021), while the diameter of silver functionalized reduced graphene oxide and cyclodextrin were found to be approximately 80 nm (Wang et al., 2017; Mangalam et al., 2019). Therefore, the value obtained is within the range of other values reported for silver functionalized nanocomposites.

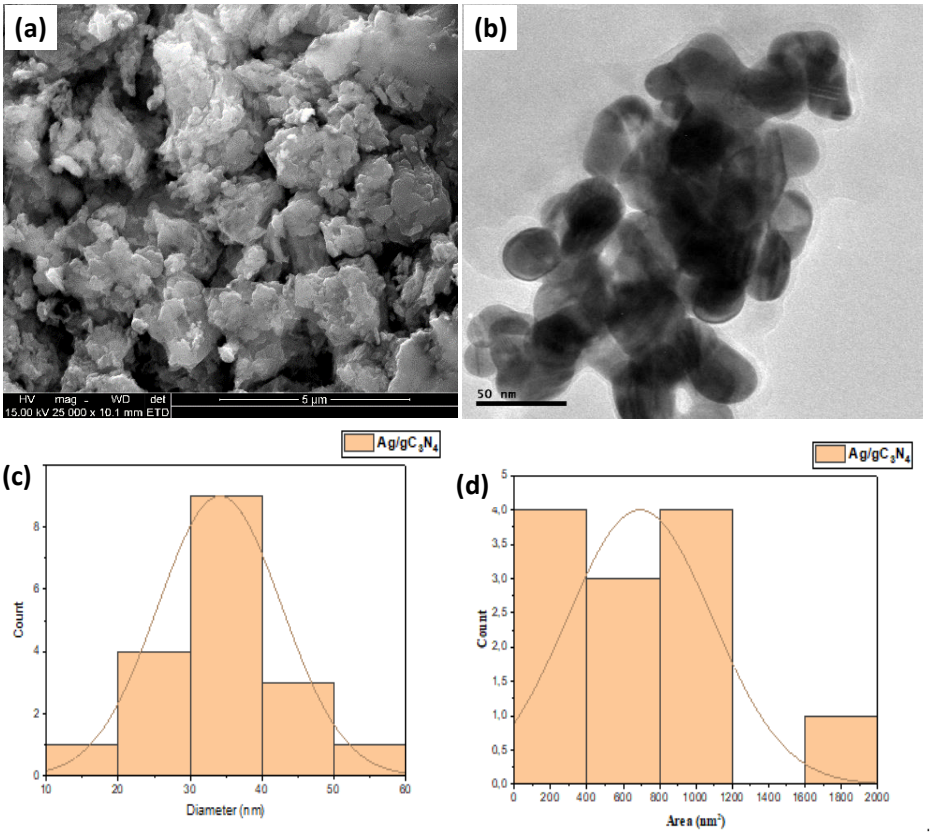

Figure 7.4: (a) SEM image (b) TEM image, (c) Particle size distribution histogram and (d) Area distribution histogram of Ag/gC_3N_4

The EDX spectrum of the Ag/gC_3N_4 nanocomposite showed that it is mainly composed of carbon and nitrogen without any impurities (Fig.7. 5a). In addition, the elements found in the EDX of Ag/gC_3N_4 were silver, carbon and nitrogen without any impurities (Fig.7. 5b). The absence of impurities in the EDX spectra shows that the materials were prepared without contamination. From the atomic weight ratio of the element, presented as inset in the EDX spectra, the ratio of carbon-to-nitrogen before and after incorporating the Ag into gC_3N_4 were 0.68 and 0.70 respectively, which were lower than the ideal ratio of 0.75 (Wang et al., 2019). This reduced ratio could be indicative that the melamine precursor was not completely condensed in the presence of the thermal energy demonstrating that there are uncondensed –NH- and $–NH_2$ (Gogoi et al., 2021)**.** The increase in the carbon-to-oxygen ratio from 0.68 to 0.70 when silver was introduced was an indication that the introduction of silver created some nitrogen vacancies. These nitrogen vacancies slow down the electron-hole pair recombination and extend the absorption of visible light (Li et al., 2012a; Putri et al., 2018; Shen et al., 2018; Wang et al., 2019).

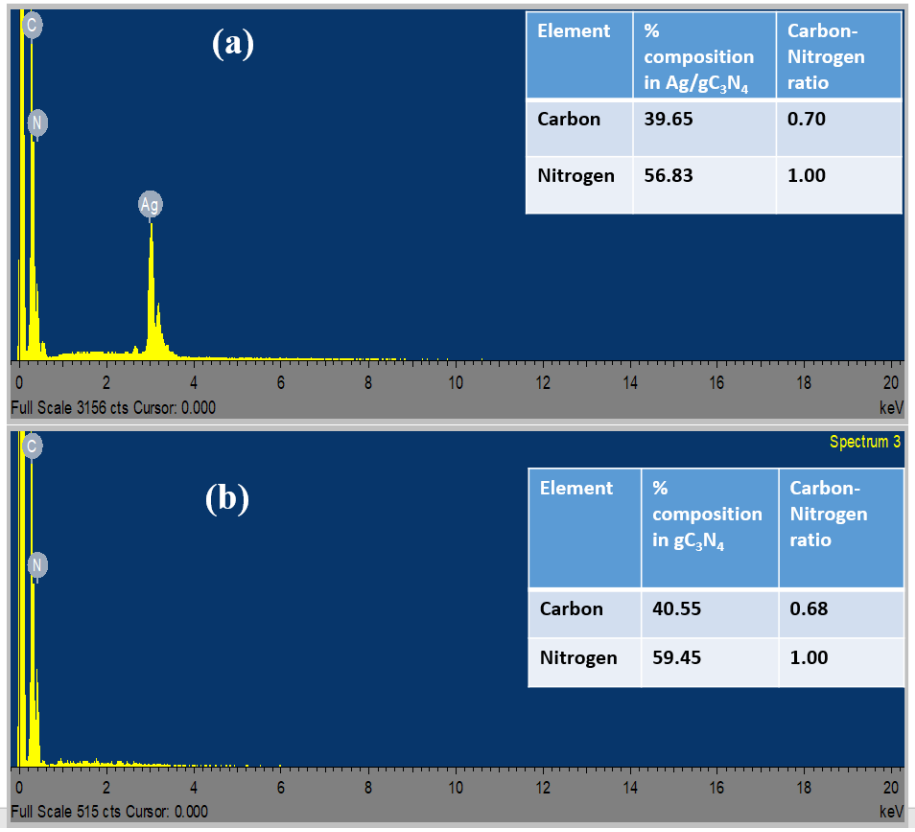

Figure 7.5: EDX spectra of (a) silver-functionalized graphitic carbon nitride (Ag/gC_3N_4) (b) graphitic carbon nitride.

7.5.5 *Photocatalytic activity of g-C_3N_4 and Ag/gC_3N_4 nanocomposite*

The plot of absorbance against wavelength for the photocatalytic reduction of hexavalent chromium using pristine gC_3N_4 and Ag/gC_3N_4 is shown in Fig. 7.6(a-c). The plot showed that the wavelength of maximum absorption of the prepared 100 mg/L of Cr(VI) solution was at 350 nm. The percentage of Cr(VI) that was reduced when pristine gC_3N_4 was used as the photocatalyst was 13.41% within 120 min of visible LED light irradiation but a marked increase occurred up to 35.3% when the Ag/gC_3N_4 was used as the photocatalyst under the same condition. The maximum photocatalytic reduction of 66.87% was achieved within 120 min of visible LED light irradiation when the concentration of hexavalent chromium pollutant was reduced from 100 mg/L to 20 mg/L as shown in Fig.7.6d.

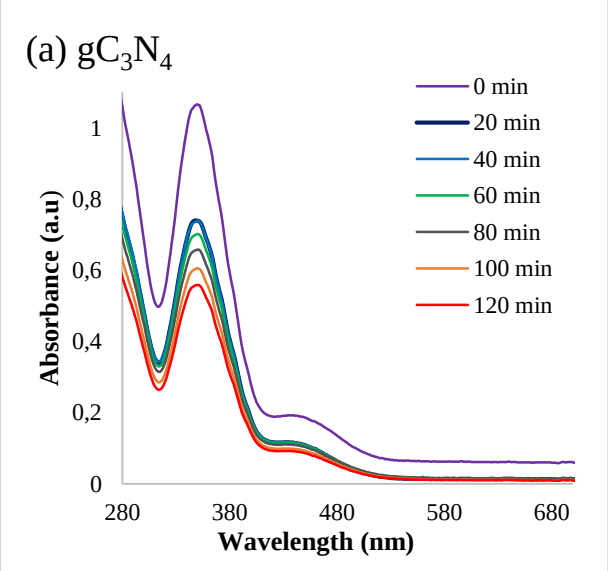

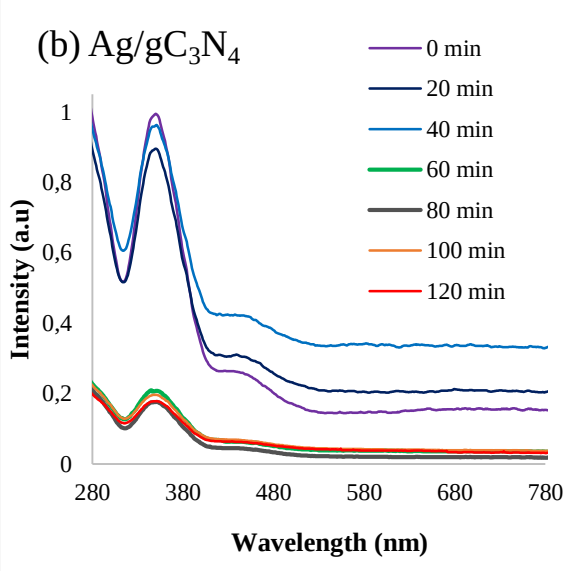

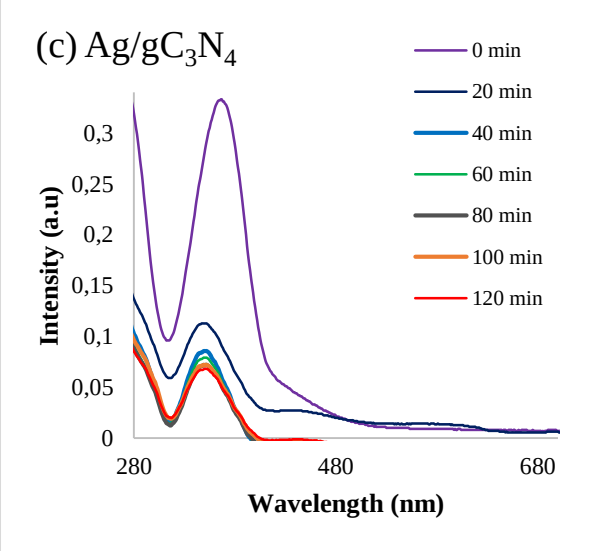

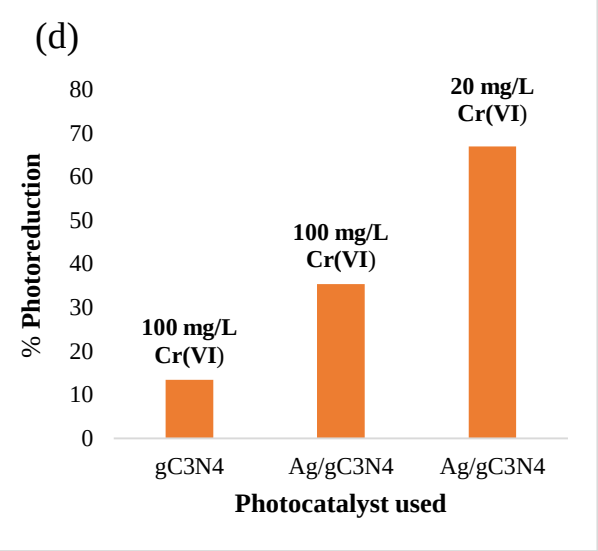

Figure 7. 6: Absorption spectra of the photocatalytic reduction of Cr(VI) ions using 50 mg dosage of:(a) pristine gC_3N_4, (b) Ag/ gC_3N_4 (100mg/L of Cr(VI) at pH 2), (c) Ag/ gC_3N_4 and 20mg/L of Cr(VI) at pH 2 under LED light, (d) Histogram showing the percentage Cr(VI) reduction at constant pH of 2 under 28W LED light.

7.6 Effect of various parameters on photocatalytic activity

7.6.1 *Effect of Cr(VI) concentration on the photocatalytic performance of Ag/gC_3N_4*

The rate of photocatalytic reduction of pollutants varies with their initial concentration. Hence, by using Cr(VI) with initial concentration of 100 mg/L, the rate of photocatalytic reduction was found to be 0.0008 min^{-1} and there was no significant increase in the rate of photocatalysis when the concentration of Cr(VI) was reduced to 50 mg/L. However, when the concentration was reduced from 100 mg/L to 20 mg/L, the rate of photocatalytic reduction increased from 0.0008 min^{-1} to 0.0033 min^{-1} (Fig.7. 7). The reduction in the removal rate with an increase in the concentration of hexavalent chromium could be attributed to the accumulation of generated excess trivalent chromium on the surface and pore of the composite photocatalyst, which culminated into the reduction of the rate of separation of trivalent chromium from the electrons and holes pairs (Li et al., 2019). Bankole et al., reported similar variation in photocatalytic removal of Cr(VI) with change in the initial concentration of Cr(VI) (Bankole et al., 2021).

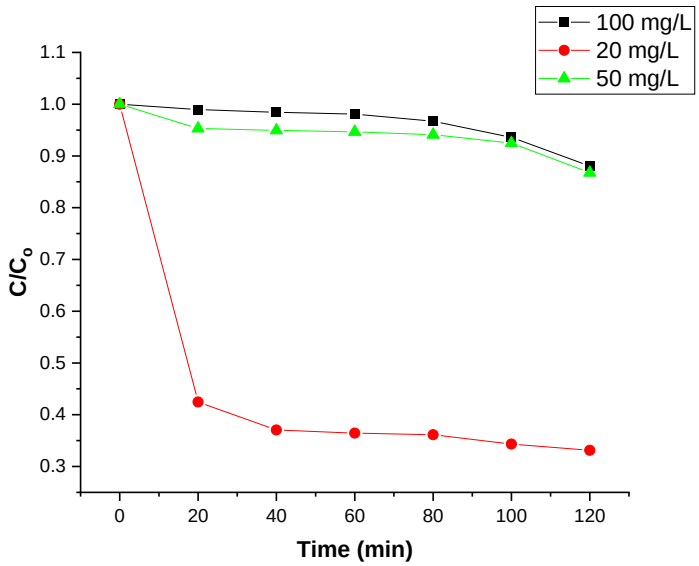

Figure 7.7: Effect of initial concentration on hexavalent chromium reduction at 100 mg/L, 50 mg/L and 20 mg/L (constant pH of 2 and 50 mg photocatalyst dosage).

7.6.2 *Effect of pH of Cr(VI) solution on the photocatalytic performance of Ag/gC_3N_4*

Hexavalent chromium exists in the form of CrO_4^{2-} (at pH slightly above 6). It is an oxo compound with a tetrahedral shape, while $HCrO_4^-$ is the dominant species under alkaline conditions. However, under high acidic conditions, trivalent chromium is the dominant species because it is thermodynamically stable (Hasija et al., 2021). Using Ag/gC_3N_4 as the photocatalyst, there were 0.0033 min^{-1} and 0.0029 min^{-1} removal rates at pH 2 and 4 respectively, which are the acidic conditions unlike 0.0009 min^{-1} and 0.0011 min^{-1} removal rates that were obtained at pH 7 (neutral) and pH 12 (alkaline) conditions respectively as shown in Fig. 7.8.

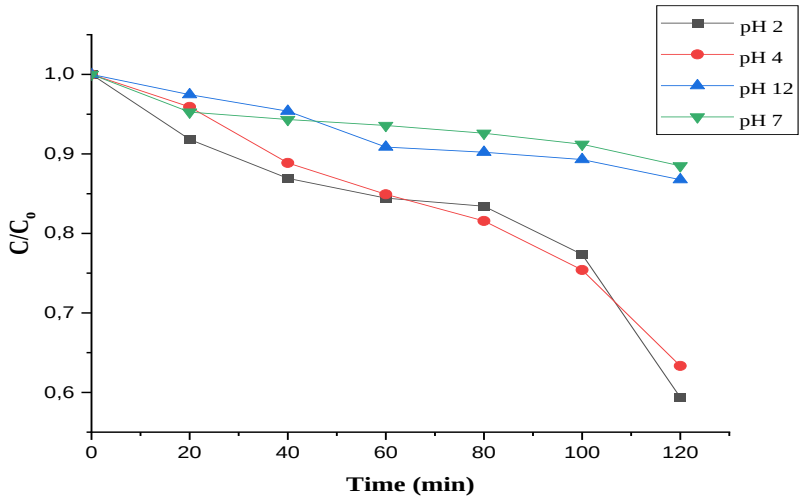

Figure 7.8: Comparative studies of hexavalent chromium reduction at pH 2, 4, 7 and 12 at a constant Cr(VI) concentration (100mg/L and 50 mg photocatalyst dosage).

It has been previously reported that photogenerated electrons play significant roles in the photocatalytic reduction of Cr(VI) to Cr(III); and this happens when the reduction potential of the chromium species is more positive than the position of the conduction band (Liang et al., 2016). The E^o of (CrO_4^{2-}/Cr^{3+}) =-0.13 V, E^o of ($HCrO_4^-/Cr^{3+}$) = 1.35 V and E^o of ($Cr_2O_7^{2-}/Cr^{3+}$) = 1.23 V vs. NHE (Liang et al., 2016). The observed hexavalent chromium removal was due to the action of photogenerated electrons, which were promoted by the presence of positively charged protons (H^+) in the system as shown in **Equation (vi)**. The existence of electrostatic repulsion between the Ag/gC_3N_4 and the hexavalent chromium in an alkaline solution subdued the reaction of photogenerated electrons, thereby leading to the low rate of conversion of Cr(VI) to Cr(III). However, the addition of dilute acid to the system causes the participation of the proton in the reaction which results in the formation of Cr(III) as shown in **Equation (xii)**. In the neutral condition, the high electron density of oxygen atoms prevents

the photogenerated electrons from reducing Cr(VI) to Cr(III) (Hasija et al., 2021) as shown in **Equation (xiii).**

$3e^-_{CB} + 7H^+ + HCrO_4^- \rightarrow Cr^{3+} + 4H_2O$…… (vi)

$10H^+ + 2e^- + Cr_2O_7^{2-} \rightarrow 2Cr^{3+} + O_2 + 5H_2O$……..…… (xii)

$4e^- + 2Cr_2O_7^{2-} \rightarrow 3O_2 + 4CrO_4^{2-}$ …… (xiii)

7.6.3 *Effect of addition of easily oxidizable organic acid on the photocatalytic performance of Ag/gC_3N_4*

In previous studies, the introduction of hole scavengers such as different organic acids has been reported (Zhng et al.,2019). These organic acids are easily oxidizable and they mediate the photocatalytic reduction leading to enhanced reduction reaction (Litter, 2017). In this study, oxalic acid was used as the hole scavenger and an enhanced photocatalytic reduction in the presence of oxalic acid was observed compared with the rate of hexavalent chromium reduction without oxalic acid as shown in Fig. 7.9. Within 20 min of visible light irradiation, the rate of photocatalytic reduction changed from 0.01517 to 0.02896 min^{-1} when oxalic acid was introduced into the system. This could be ascribed to the reaction between the photogenerated holes and the easily oxidizable organic, which is more feasible than when water was present as the hole scavenger. The oxidation of water to oxygen by photogenerated holes involves the transfer of four electrons in the rate-determining step (Litter, 2017; Hasija et al., 2021). Since holes have been depleted by the photogenerated holes scavenger, as shown in **Equation (ix)**, photogenerated electrons are more available for the reduction of hexavalent chromium and the rate of recombination of photogenerated holes and electrons is reduced (Iliev et al., 2006; Hasija et al., 2021).

$RCOOH + h_{vb}^+(HO^{\cdot}_{ads.}) \rightarrow RCOO^{\cdot} + H^+(H_2O) \rightarrow CO_2 + R^{\cdot}$……..(ix)

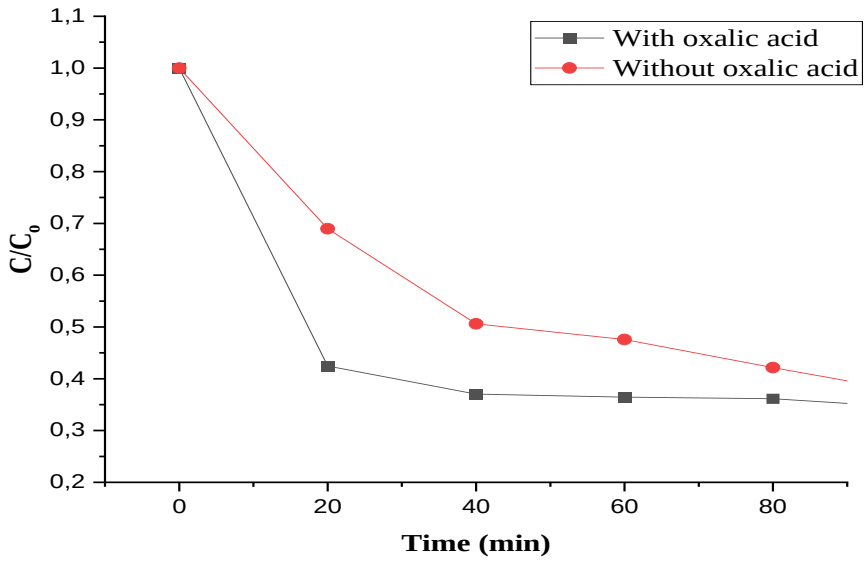

Figure 7.9: Comparative studies of hexavalent chromium reduction in the presence and absence of easily oxidizable organics (oxalic acid) (Cr(VI) concentration of 20mg/L, 50 mg photocatalyst dosage and pH of 2).

7.6.4 *Effect of catalyst dosage on the photocatalytic performance of Ag/gC_3N_4*

The concentration of Ag/gC_3N_4 photocatalyst was increased from 20 to 50 mg while maintaining a constant pH of 2, the concentration and volume of Cr(VI) were also kept constant. A change in the maximum rate of degradation from 0.0034 to 0.0056 min^{-1} occurred (as shown in Fig.7.10). This increase in the rate of photoreduction was due to an increase in the number of surface-active sites with an increase in photocatalyst dosage and the route of charge transfer which became more effective (Song et al., 2019). When the photocatalysis was carried out in the absence of catalyst (light only) under the same condition, only minimal photoreduction rate (0.0017 min^{-1}) occurred, which could be attributed to the self-photoreduction of the hexavalent chromium (Hasija et al., 2021).

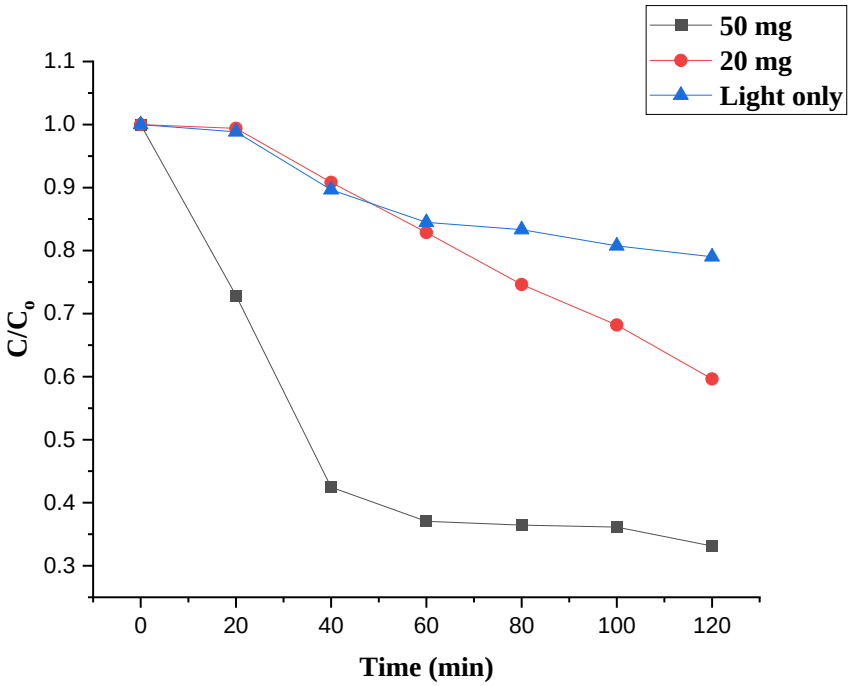

Figure 7.10: Comparative studies of hexavalent chromium reduction in the presence of visible light only and varied Ag/gC_3N_4 photocatalyst dosage (Cr(VI) concentration of 20mg/L and pH of 2).

The silver-functionalized graphitic carbon nitride displayed a better scavenging activity in DPPH than the ascorbic acid, which was used as the positive control, indicating that the nanocomposite is a better hydrogen donor to the radicals than the primary control (Adeyemi et al., 2021). The adsorption of DPPH on the nanocomposite was enhanced by the presence of silver nanoparticles. The adsorbed radicals of DPPH have ability to abstract atoms of hydrogen from the hydrated surface of the silver metal to give DPPH-H molecules (Pu et al., 2019).

CONCLUSION

The silver-functionalized graphitic carbon nitride was successfully prepared through the thermal condensation of melamine and silver salt. The obtained Ag/gC_3N_4 displayed improved photocatalytic activity towards the reduction of hexavalent chromium under visible light. The percentage reduction improved with an increase in photocatalyst dosage, a decrease in the concentration of hexavalent chromium under acidic conditions. The Ag/gC_3N_4 showed an

improved photocatalytic performance better than that of pristine gC_3N_4. The enhanced photocatalytic performance was due to reduction in the rate of recombination of photogenerated holes and electron pairs.

REFERENCES

Abass Sofi, M., Sunitha, S., Ashaq Sofi, M., Khadheer Pasha, S.K., Choi, D., 2022. An overview of antimicrobial and anticancer potential of silver nanoparticles. Journal of King Saud University - Science 34, 101791.

Adeyemi, J.O., Saibu, G.M., Olasunkanmi, L.O., Fadaka, A.O., Meyer, M., Sibuyi, N.R.S., Onwudiwe, D.C., Oyedeji, A.O., 2021. Synthesis, computational and biological studies of alkyltin(IV) N-methyl-N-hydroxyethyl dithiocarbamate complexes. Heliyon 7, e07693.

Aggarwal, R., Saini, D., Sonkar, S.K., Sonker, A.K., Westman, G., 2022. Sunlight promoted removal of toxic hexavalent chromium by cellulose derived photoactive carbon dots. Chemosphere 287, 132287.

Ajiboye, T.O., Kuvarega, A.T., Onwudiwe, D.C., 2020. Graphitic carbon nitride-based catalysts and their applications: A review. Nano-Structures & Nano-Objects 24, 100577.

Ajiboye, T.O., Oyewo, O.A., Onwudiwe, D.C., 2021. Conventional and Current Methods of Toxic Metals Removal from Water Using g-C_3N_4-Based Materials. Journal of Inorganic and Organometallic Polymers and Materials 31, 1419-1442.

Anwar, A., Abdalla, S.A.O., Aslam, Z., Shah, M.R., Siddiqui, R., Khan, N.A., 2019. Oleic acid–conjugated silver nanoparticles as efficient antiamoebic agent against Acanthamoeba castellanii. Parasitology Research 118, 2295-2304.

Bankole, O.M., Olorunsola, T.D., Ogunlaja, A.S., 2021. Photocatalytic decontamination of toxic hexavalent chromium in water over graphitic carbon nitride supported sulfur nanoparticles. Journal of Photochemistry and Photobiology A: Chemistry 405, 112934.

Barnhart, J., 1997. Occurrences, Uses, and Properties of Chromium. Regulatory Toxicology and Pharmacology 26, S3-S7.

Dai, X., Xie, M., Meng, S., Fu, X., Chen, S., 2014. Coupled systems for selective oxidation of aromatic alcohols to aldehydes and reduction of nitrobenzene into aniline using CdS/g-C_3N_4 photocatalyst under visible light irradiation. Applied Catalysis B: Environmental 158-159, 382-390.

Das, R.S., Warkhade, S.K., Kumar, A., Gaikwad, G.S., Wankhade, A.V., 2020. Graphitic carbon nitride @ silver zirconate nanocomposite (gC_3N_4@Ag_2ZrO_3): A Type-II heterojunction for an effective visible light photocatalysis and bacterial photo-inactivation. Journal of Alloys and Compounds 846, 155770.

Elavarasan, N., Vignesh, S., Srinivasan, M., Palanisamy, G., Bhuvaneswari, K., Venkatesh, G., Pazhanivel, T., Ramasamy, P., 2021. Integrating gC_3N_4 nanosheet with MoS_2 and ZnO-Ag: Remarkably enhanced photocatalytic performance under visible-light irradiation. Colloid and Interface Science Communications 44, 100474.

Emadian, S.S., Ghorbani, M., Bakeri, G., 2020. Magnetically separable $CoFe_2O_4$/ZrO_2 nanocomposite for the photocatalytic reduction of hexavalent chromium under visible light irradiation. Synthetic Metals 267, 116470.

Ge, L., Han, C., Liu, J., Li, Y., 2011. Enhanced visible light photocatalytic activity of novel polymeric g-C_3N_4 loaded with Ag nanoparticles. Applied Catalysis A: General 409-410, 215-222.

Gharibshahi, L., Saion, E., Gharibshahi, E., Shaari, A.H., Matori, K.A., 2017. Structural and optical properties of Ag nanoparticles synthesized by thermal treatment method. Materials 10, 402.

Gogoi, D., Shah, A.K., Qureshi, M., Golder, A.K., Peela, N.R., 2021. Silver grafted graphitic-carbon nitride ternary hetero-junction Ag/gC_3N_4(Urea)-gC_3N_4(Thiourea) with efficient charge transfer for enhanced visible-light photocatalytic green H_2 production. Applied Surface Science 558, 149900.

Hasija, V., Raizada, P., Singh, P., Verma, N., Khan, A.A.P., Singh, A., Selvasembian, R., Kim, S.Y., Hussain, C.M., Nguyen, V.-H., Le, Q.V., 2021. Progress on the photocatalytic reduction of hexavalent Cr (VI) using engineered graphitic carbon nitride. Process Safety and Environmental Protection 152, 663-678.

Iliev, V., Tomova, D., Bilyarska, L., Eliyas, A., Petrov, L., 2006. Photocatalytic properties of TiO_2 modified with platinum and silver nanoparticles in the degradation of oxalic acid in aqueous solution. Applied Catalysis B: Environmental 63, 266-271.

Ismael, M., 2020. A review on graphitic carbon nitride (g-C_3N_4) based nanocomposites: Synthesis, categories, and their application in photocatalysis. Journal of Alloys and Compounds 846, 156446.

Kadi, M.W., Mohamed, R.M., Ismail, A.A., Bahnemann, D.W., 2020. Decoration of g-C_3N_4 nanosheets by mesoporous $CoFe_2O_4$ nanoparticles for promoting visible-light photocatalytic Hg(II) reduction. Colloids and Surfaces A: Physicochemical and Engineering Aspects 603, 125206.

Lakra, R., Kiran, M.S., Korrapati, P.S., 2021. Furfural mediated synthesis of silver nanoparticles for photocatalytic reduction of hexavalent chromium. Environmental Technology & Innovation 21, 101348.

Li, J., Shen, B., Hong, Z., Lin, B., Gao, B., Chen, Y., 2012a. A facile approach to synthesize novel oxygen-doped g-C_3N_4 with superior visible-light photoreactivity. Chemical communications 48, 12017-12019.

Li, K., Huang, Z., Zhu, S., Luo, S., Yan, L., Dai, Y., Guo, Y., Yang, Y., 2019. Removal of Cr(VI) from water by a biochar-coupled g-C_3N_4 nanosheets composite and performance of a recycled photocatalyst in single and combined pollution systems. Applied Catalysis B: Environmental 243, 386-396.

Li, K., Liang, A., Jiang, C., Li, F., Liu, Q., Jiang, Z., 2012b. A stable and reproducible nanosilver-aggregation-4-mercaptopyridine surface-enhanced Raman scattering probe for rapid determination of trace Hg^{2+}. Talanta 99, 890-896.

Liang, Z., Wen, Q., Wang, X., Zhang, F., Yu, Y., 2016. Chemically stable and reusable nano zero-valent iron/graphite-like carbon nitride nanohybrid for efficient photocatalytic treatment of Cr(VI) and rhodamine B under visible light. Applied Surface Science 386, 451-459.

Litter, M.I., 2017. Last advances on TiO_2-photocatalytic removal of chromium, uranium and arsenic. Current Opinion in Green and Sustainable Chemistry 6, 150-158.

Mangalam, J., Kumar, M., Sharma, M., Joshi, M., 2019. High adsorptivity and visible light assisted photocatalytic activity of silver/reduced graphene oxide (Ag/rGO) nanocomposite for wastewater treatment. Nano-Structures & Nano-Objects 17, 58-66.

Mohanraj, J., Durgalakshmi, D., Saravanan, R., 2021. Water-soluble graphitic carbon nitride for clean environmental applications. Environmental Pollution 269, 116172.

Patel, G.M., Rohit, J.V., Singhal, R.K., Kailasa, S.K., 2015. Recognition of carbendazim fungicide in environmental samples by using 4-aminobenzenethiol functionalized silver nanoparticles as a colorimetric sensor. Sensors and Actuators B: Chemical 206, 684-691.

Pu, S., Li, J., Sun, L., Zhong, L., Ma, Q., 2019. An in vitro comparison of the antioxidant activities of chitosan and green synthesized gold nanoparticles. Carbohydrate Polymers 211, 161-172.

Putri, L.K., Ng, B.-J., Ong, W.-J., Lee, H.W., Chang, W.S., Chai, S.-P., 2018. Engineering nanoscale p–n junction via the synergetic dual-doping of p-type boron-doped graphene hybridized with n-type oxygen-doped carbon nitride for enhanced photocatalytic hydrogen evolution. Journal of Materials Chemistry A 6, 3181-3194.

Samadi, Z., Yaghmaeian, K., Mortazavi-Derazkola, S., Khosravi, R., Nabizadeh, R., Alimohammadi, M., 2021. Facile green synthesis of zero-valent iron nanoparticles using

barberry leaf extract (GnZVI@BLE) for photocatalytic reduction of hexavalent chromium. Bioorganic Chemistry 114, 105051.

Shen, M., Zhang, L., Shi, J., 2018. Converting CO_2 into fuels by graphitic carbon nitride-based photocatalysts. Nanotechnology 29, 412001.

Song, W., Ge, P., Ke, Q., Sun, Y., Chen, F., Wang, H., Shi, Y., Wu, X.-L., Lin, H., Chen, J., Shen, C., 2019. Insight into the mechanisms for hexavalent chromium reduction and sulfisoxazole degradation catalyzed by graphitic carbon nitride: The Yin and Yang in the photo-assisted processes. Chemosphere 221, 166-174.

Thang, N.Q., Sabbah, A., Chen, L.-C., Chen, K.-H., Hai, L.V., Thi, C.M., Viet, P.V., 2021. Localized surface plasmonic resonance role of silver nanoparticles in the enhancement of long-chain hydrocarbons of the CO_2 reduction over Ag-gC_3N_4/ZnO nanorods photocatalysts. Chemical Engineering Science 229, 116049.

Thorat, N., Borade, S., Varma, R., Yadav, A., Gupta, S., Fernandes, R., Sarawade, P., Bhanage, B.M., Patel, N., 2021. High surface area Nanoflakes of P-gC_3N_4 photocatalyst loaded with Ag nanoparticle with intraplanar and interplanar charge separation for environmental remediation. Journal of Photochemistry and Photobiology A: Chemistry 408, 113098.

Wang, K., Ji, Q., Li, H., Guan, F., Zhang, D., Feng, H., Fan, H., 2017. Synthesis and antibacterial activity of silver@carbon nanocomposites. Journal of Inorganic Biochemistry 166, 64-67.

Wang, X., Wu, L., Wang, Z., Wu, H., Zhou, X., Ma, H., Zhong, H., Xing, Z., Cai, G., Jiang, C., 2019. C/N Vacancy Co-Enhanced Visible-Light-Driven Hydrogen Evolution of g-C_3N_4 Nanosheets Through Controlled He+ Ion Irradiation. Solar Rrl 3, 1800298.

Wang, Y., Bao, S., Liu, Y., Yang, W., Yu, Y., Feng, M., Li, K., 2020. Efficient photocatalytic reduction of Cr(VI) in aqueous solution over CoS_2/g-C_3N_4-rGO nanocomposites under visible light. Applied Surface Science 510, 145495.

Zafar, Z., Fatima, R., Kim, J.-O., 2021. Effect of HCl treatment on physico-chemical properties and photocatalytic performance of Fe–TiO_2 nanotubes for hexavalent chromium reduction and dye degradation under visible light. Chemosphere 284, 131247.

Zhang,Q., Ge, Y., Yang, C.,Zhang B.,, K. Deng K.,2019., Enhanced photocatalytic performance for oxidation of glucose to value-added organic acids in water using iron thioporphyrazine modified SnO_2, Green Chemistry, 21 ,5019.

Zhai, Z., Zhang, F., Chen, X., Zhong, J., Liu, G., Tian, Y., Huang, Q., 2017. Uptake of silver nanoparticles by DHA-treated cancer cells examined by surface-enhanced Raman spectroscopy in a microfluidic chip. Lab on a Chip 17, 1306-1313.

Zhao, J., Liu, P., Ma, J., Li, D., Yang, H., Chen, W., Jiang, Y., 2019. Enhancement of radiosensitization by silver nanoparticles functionalized with polyethylene glycol and aptamer As1411 for glioma irradiation therapy. International Journal of Nanomedicine 14, 9483.

CHAPTER EIGHT

8.0 Conclusion and recommendations

Overall, the performance of the functionalized graphitic carbon nitride nanocomposites in the elimination of Ag(I), Cr(VI) and Pb(II) through photocatalytic reduction were found to be more efficient than using pristine graphitic carbon nitride as the photocatalyst. As shown in the reusability studies of $Ni_3Bi_2S_2$/O-gC_3N_4, the functionalized graphitic carbon nitride photocatalysts were found to retain over 80% of their efficiencies even after three cycles. Finally, the scavenging experiments showed that the main active species for the photocatalytic reduction of these metal ions are electrons (e^-), hydroxyl radicals ($\cdot OH^-$) and superoxide ($\cdot O_2^-$).

In chapter three, the suitability of dithiocarbamate complexes for generating metal sulphides under an inert atmosphere through the heat-up method in oleylamine as the capping agent was acheived. The studies clearly showed that the Acanthite phase of Ag_2S was successfully prepared from the silver(I) complex of *N*-methyl-*N*–phenyl dithiocarbamate at a relatively low temperature of 180 ^oC.

In chapter four, photocatalytic reduction of hexavalent chromium using graphitic carbon nitride functionalized with rod-like $Cu_{3.21}Bi_{4.79}S_9$ photocatalyst was acheived. The results revealed that over 90% of Cr(VI) was photocatalytically reduced within 1 h at a pH of 2, using the photocatalyst dosage of 10 mg and Cr(VI) concentration of 10 mg/L. The presence of bisphenol A, Ag(I) and Pb(II) in the photocatalytic system exhibited inhibitory effects on the photocatalytic reduction of Cr(VI).

In chapter five, visible light-driven photocatalytic reduction of monovalent silver using a composite of $Ni_3Bi_2S_2$ incorporated into O-doped gC_3N_4 was investigated. The studies revealed that the $Ni_3Bi_2S_2$ composited with oxygen-doped functionalized graphitic carbon nitride was effective for Ag(I) reduction under visible light. The addition of persulfate, Cr(VI) solution and a mixture of organic pollutants such as pharmaceuticals and dyes significantly reduced the rate of the photocatalytic reduction of silver(I). The optimum conditions obtained for the photocatalytic reduction process were pH 6, using 10 mg/L Ag^+ concentration, 25 mg of photo-catalyst's dosage, and a 28 W LED lamp.

In chapter six, the dye matrix effects on the photocatalytic reduction of heavy metals were obtained. This was done via the synthesis of $AgBiS_2$/gC_3N_4 and its application in the photocatalytic reduction of Pb(II) in the matrix of methyl orange, crystal violet and methylene

blue dyes. The removal rate of Pb(II) was 0.0045 min^{-1} in the absence of another dye contaminant, but changed to 0.0016, 0.0036 and 0.0096 min^{-1} in the presence of methylene blue, methyl orange and crystal violet.

In chapter seven, photocatalytic potency for chromium(VI) reduction by silver functionalized gC_3N_4 was investigated. The performance of the nanocomposite was better than that of pristine graphitic carbon nitride. Although silver possesses high plasmonic resonance compared to most metals, its performance in the reduction of Cr(VI) under visible light was lower than that of $Cu_{3.21}Bi_{4.79}S_9$–functionalized graphitic carbon nitride. However, the performance of Ag/gC_3N_4 was better than that of pristine gC_3N_4.

8.1 Future work

All the specific objectives stated in the study have been met, however, there are many issues, which may require further investigation:

1. There should be further studies on the comparative performance of these functionalized graphitic carbon nitrides in the degradation of each heavy metal ions investigated in this study.
2. The identification of products obtained from the organic pollutants that co-existed with the heavy metal ions in the contaminated water for better understanding.
3. The performance of these synthesized photocatalysts in real industrial water treatment requires further research for the optimization on the commercial scale.
4. Simultaneous photocatalytic microbial inactivation along with photocatalytic reduction of heavy metal ions using functionalized graphitic carbon nitride demands further investigation.

Appendix

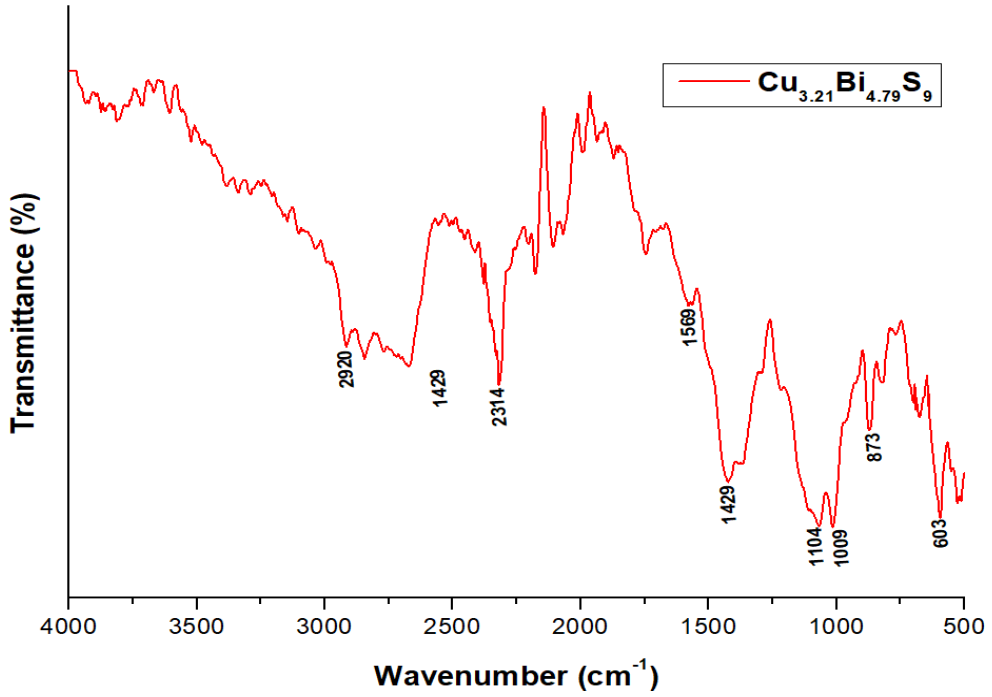

Figure S1: The FTIR spectrum of oleylamine-capped $Cu_{3.21}Bi_{4.79}S_9$

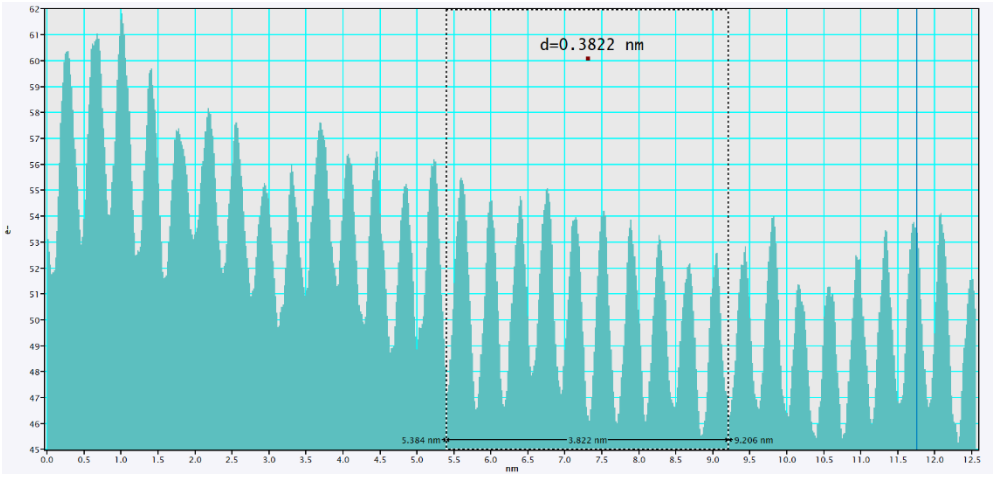

Figure S2: d-spacing from the HRTEM micrograph of $Cu_{3.21}Bi_{4.79}S_9$

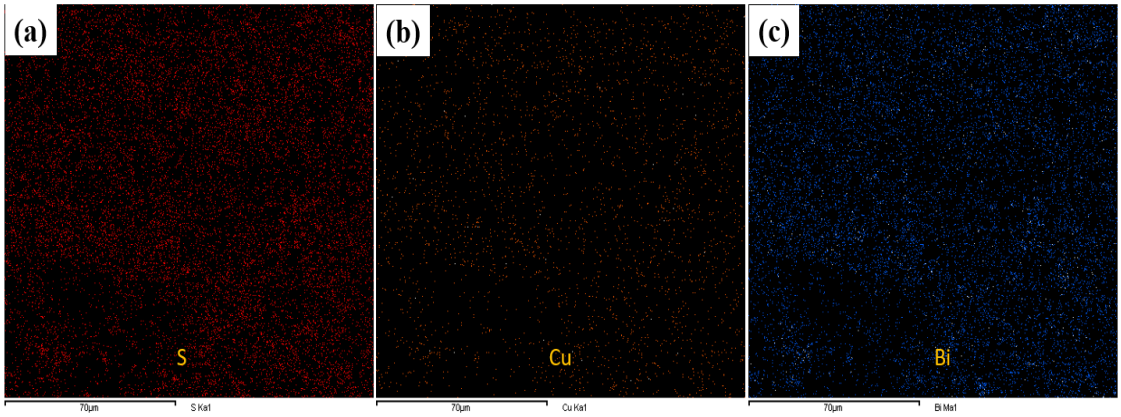

Figure S3: Elemental mapping of $Cu_{3.21}Bi_{4.79}S_9$

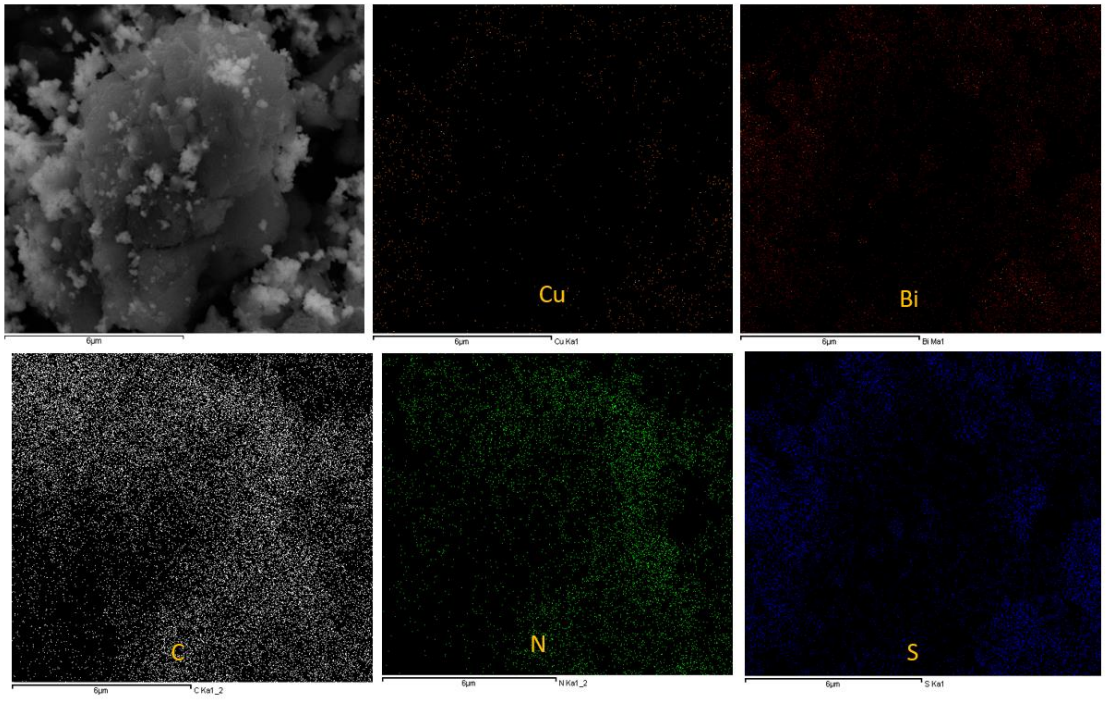

Figure S4: Elemental mapping of $Cu_{3.21}Bi_{4.79}S_9$/g-C_3N_4 nanocomposite

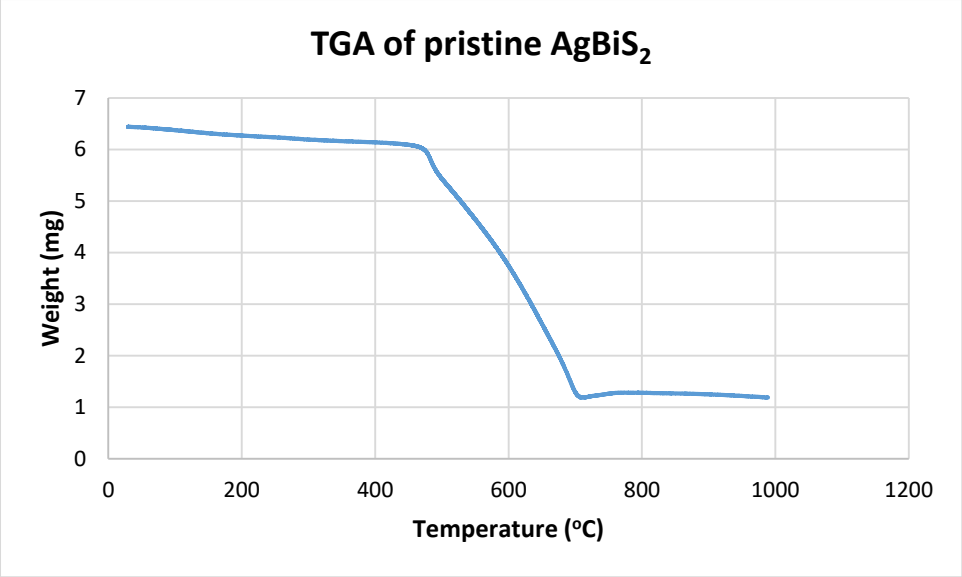

Figure S5: The thermal-gravimetry analysis (TGA) thermogram of pristine silver bismuth sulphide carried out under inert atmosphere.

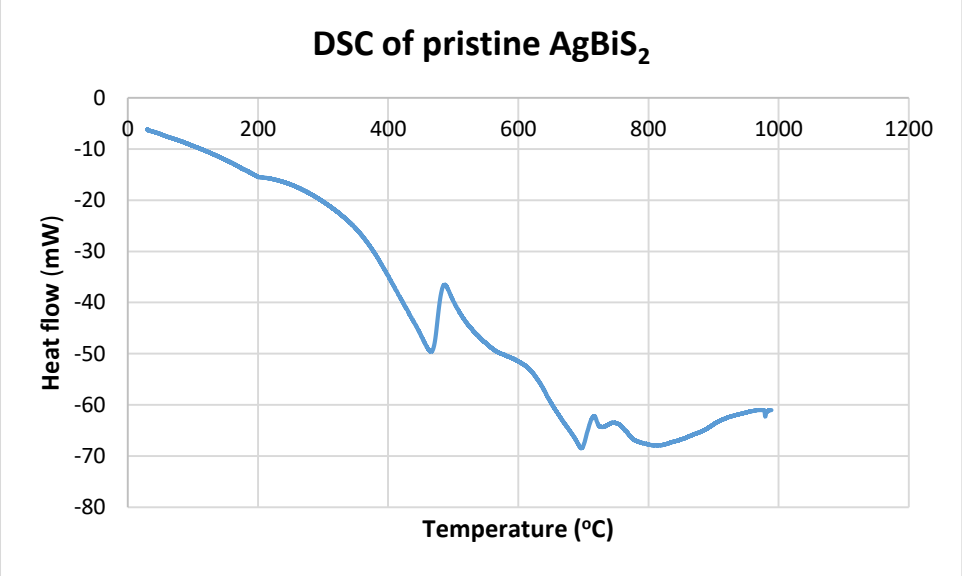

Figure S6: The Differential scanning calorimetry (DSC) thermogram of pristine silver bismuth sulphide carried out under inert atmosphere.